MAGNETOCALORIC, MAGNETORESISTANCE AND MAGNETODIELECTRIC EFFECTS IN UNDOPED AND DOPED $EuTiO_3$

KM RUBI

(*M. Tech., Indian Institute of Technology* - *Delhi, India*)

A THESIS SUBMITTED FOR
THE DEGREE OF DOCTOR OF PHILOSPHY

DEPARTMENT OF PHYSICS
NATIONAL UNIVERSITY OF SINGAPORE
2016

Supervisors:
Associate Professor Ramanathan Mahendiran, Main Supervisor
Professor Sow Chorng Haur, Co-Supervisor

Examiners:
Associate Professor Ariando
Assistant Professor Andrivo Rusydi
Professor A. Sundaresan (JNCSAR, India)

Declaration

I hereby declare that this thesis is my original work and it has been written by me in its entirety. I have duly acknowledged all the sources of information, which have been used in the thesis.

This thesis has also not been submitted for any degree in any university previously.

Rubi

Km Rubi

17 August 2016

Acknowledgements

The achievement and final outcome of thesis work required a lot of assistance and support from many people and I am extremely fortunate to have them all around me during my Ph.D. studies. Whatever I have achieved over the past four years is all because of their support and assistance and I would not forget them all to acknowledge.

First and foremost I would like to express my deepest gratitude to my supervisor, *Assoc. Prof. R. Mahendiran* for his continuous support and expert guidance. I am very thankful to him for his constant motivation, fruitful suggestions, continuous encouragement and kind support in all aspects that made my candidature a truly enriching experience at National University of Singapore.

I also would like to express my wholehearted thanks to my co-supervisor and Head of Physics Department *Prof. Sow Chorng Hour* for his kind support. I am very thankful to *Prof. Jian-Seng Wang* for fruitful discussion and generous help to complete my research projects. My sincere thanks to *Assoc. Prof. R. V. Ramanujan*, *Prof. T. Venkatesan* and *Prof. B. V. R. Chowdary* for allowing me to use their lab facilities.

I would like to thank all my colleagues in lab for their kind help during my Ph.D. studies. I appreciate *Dr. Pawan Kumar* and *Dr. Maheswar Repaka* for their moral support during my initial days in NUS and immense help provided throughout the period of my research work. I thank *Amit Chanda*, *Himadri Roy Dakua*, *Arindam Midya* and *Ushnish Chaudhary* for creating a cheerful and cooperative working atmosphere in the lab.

A special thanks to physics department workshop staff, especially *Late Mr. Tan*, *Mr. Goh*, *Mr. Fong* and *Mr. Suradi* and general office staff for their continuous help.

I would like to acknowledge National University of Singapore for giving me opportunity to pursue Ph. D. degree and providing financial support through graduate student research fellowship.

I would like to thank my friends in NUS and NTU comprising *Dr. Rupesh Rohan*, *Dr. Kapil Pareek*, *Akankshita Dash*, *Mahima Sharma*, *Ira Agrawal*, *Lakshmi Jothinathan*, *Dr. Varun Chaudhary*, *Geeta Kumari* and *Neha Agarwal* for making my days in Singapore more enjoyable and refreshing. My heartfelt thanks to my close friends *Parvinder Kaur*, *Prachi Rastogi*, *Priyanka Chikara*, *Prerna Nain* and *Preeti Maan* for their continuous encouragement. I specially thank to my best friends and my backbones *Rahul Kumar* and *Anjali Sengar* for their unlimited support, encouragement and inspiration and also the affection shown to me.

Finally and most importantly, I feel a deep sense of gratitude to my father, *Bijendra Singh* and my mother, *Kanta Devi* for their indefinite love, support and encouragement since my childhood to till now. I feel great to dedicate this thesis to them. My heartfelt thanks to my sisters *Ritu* and *Rosy*, my nephews *Anjanya* and *Arpit*, my niece *Angel* and all my cousins for their continuous support.

Table of Contents

Summary

Rare-earth titanates ($RTiO_3$, R: Gd, Pr, La, Sm etc) containing trivalent Ti-ion with single d electron in triply degenerate state ($3d^1(t_{2g}^1e_g^0)$) are interesting materials among perovskite oxides to investigate emergence of strong electron correlation effect, orbital controlled spin ordering and changing magnetic structure with increasing orthorhombic distortion. While in most of the rare-earth titanates both R and Ti ions adopt trivalent states, Eu and Ti cations in $EuTiO_3$ tend to stabilize in 2+ and 4+ valence states, respectively, and also in a simple cubic structure at room temperature. The coexistence of magnetically active Eu^{2+}: $4f^7$ and ferroelectric active Ti^{4+}: $3d^0$ ions in $EuTiO_3$ is stimulating for investigating the magneto-dielectric effect due to possible coupling between localized 4f spin of Eu^{2+} ion and electrical dipole ordering that can be induced by off center displacement of Ti^{4+} ion. Bulk $EuTiO_3$ is a G-type antiferromagnet with $T_N = 5.5\pm1$ and quantum paraelectric down to 2 K. Although synthesis and magnetic structure of $EuTiO_3$ has been reported in late 1970's, $EuTiO_3$ attracted a significant research attention only in the past few years after the demonstration of magnetoelectric coupling in single crystal and strain-induced multiferroicity in thin film. Recent finding of antiferrodistortion around room temperature in $EuTiO_3$ which resembles that of structural distortion found in $SrTiO_3$ around 110 K adds another mystery. In this thesis, we investigate magnetocaloric effect (MCE), magnetoresistance (MR) and magnetodielectric effect (MDE) in polycrystalline $EuTiO_3$. We report a giant MCE and colossal negative MR in $EuTiO_3$ for the first time. The effect of isovalent Ba^{2+} and aliovalent La^{3+} substitution for Eu^{2+} on the magnetic, electrical, MCE, MR and MDE properties of $EuTiO_3$ is also studied in details through $Eu_{1-x}Ba_xTiO_3$ and $Eu_{1-x}La_xTiO_3$ systems, respectively. All the samples were synthesized using the solid-state reaction method under reducing atmosphere (95% Ar + 5%H_2).

$EuTiO_3$ in which Eu^{2+} spins order antiferromagnetically below $T_N = 5.4$ K exhibits large values of magnetic entropy change ($-\Delta S_m = 49$ J/kg.K), adiabatic temperature change ($\Delta T_{ad} = 21$ K) and refrigeration cooling power ($RCP = 540$ J/kg) for a field change of 7 T at T_N. The giant MCE in this compound arises from the field induced suppression of the spin fluctuations associated with Eu^{2+}:$4f^7$ electrons. In view of the observed large values of $-\Delta S_m$, ΔT_{ad} and RCP, this compound may be of great interest for cryogenic magnetic refrigeration below 30 K.

While $EuTiO_3$ is an insulator under zero magnetic field, application of a magnetic field drives an insulator to metal (I-M) transition in paramagnetic region. The I-M transition shifts towards higher temperature ($T = 22$ K >> T_N for $\mu_0 H = 7$ T) with increasing strength of the magnetic field. $EuTiO_3$ shows a colossal negative MR ($\Delta\rho/\rho(0) = -99.15\%$ under a small magnetic field of $\mu_0 H = 0.5$ T at $T = 2$ K and $\Delta\rho/\rho(0) = -45\%$ under 7 T at $T = 45$ K (>>T_N)). This is first observation of colossal negative MR among the rare earth titanates. The negative MR in $EuTiO_3$ is suggested due to the suppression of $4f^7$ spin fluctuations by magnetic field that reduces the spin-disorder scattering. A simultaneous occurrence of large positive MDE ($\Delta\varepsilon/\varepsilon(0) = 670$ %) and negative ac MR ($\Delta\rho_{ac}/\rho_{ac}(0) = -99.9\%$) is also observed in polycrystalline $EuTiO_3$. A quadratic dependence of MDE on magnetization for low fields ($\mu_0 H \leq 1.7$ T) indicates that the MDE in this compound is due to the spin-lattice coupling.

While $EuTiO_3$ is an antiferromagnetic (AFM) and quantum paraelectric (PE), $BaTiO_3$ is non-magnetic and ferroelectric (FE) with $T_{FE} \sim 400$ K. The solid solution of these two compounds ($Eu_{1-x}Ba_xTiO_3$) shows ferromagnetism and ferroelectricity in single phase. While the compounds $Eu_{1-x}Ba_xTiO_3$ ($x \leq 0.2$) exhibit AFM interaction, the ferromagnetic (FM) interaction is observed in $Eu_{0.5}Ba_{0.5}TiO_3$ below $T_C = 1.7$ K. Ferroelectricity transition is observed in $Eu_{1-x}Ba_xTiO_3$ for $x \geq 0.4$. While the magnetic transition temperature in $Eu_{1-x}Ba_xTiO_3$ shifts to lower temperature with increasing Ba content, the FE transition temperature T_{FE} shifts towards higher temperature (T_{FE} = 150 K for x = 0.40 to T_{FE} = 396 K for x = 1.0). Including magnetic and FE transition temperatures; a phase diagram is constructed for $Eu_{1-x}Ba_xTiO_3$ ($0.00 \leq x \leq 1.0$). The two end compounds x = 0.0 ($EuTiO_3$) and x = 1.0 ($BaTiO_3$) are AFM+PE and PM+FE, respectively. As x increases from 0.0 to 1.0, $Eu_{1-x}Ba_xTiO_3$ transforms from AFM to FM and PE to FE at x = 0.4 and a multiferroic phase (FM + FE) is realized for $Eu_{1-x}Ba_xTiO_3$ ($0.4 \leq x \leq 0.95$).

$Eu_{1-x}Ba_xTiO_3$ also provides a great opportunity to study the effect of dilution of Eu^{2+} spins on the MCE, MR and MDE phenomena in $EuTiO_3$. The magnetic entropy change of $EuTiO_3$ reduces with Ba doping and varies from $-\Delta S_m$ = 40 J/kg.K to 6.7 J/kg.K at T = 4.5 K for $\mu_0 \Delta H$ = 5 T as x increases from 0.1 to 0.9 in the $Eu_{1-x}Ba_xTiO_3$ series. Half doped compound $Eu_{0.5}Ba_{0.5}TiO_3$ exhibits $-\Delta S_m$ = 31.32 J/kg.K, ΔT_{ad} =18.68 K and RCP = 343 J/kg at T = 2 K for $\mu_0 \Delta H$ = 7 T. We observed a drop in MR value of $EuTiO_3$ with Ba^{2+} substitution for Eu^{2+}. In $Eu_{1-x}Ba_xTiO_3$ series, the negative MR varies from MR = –85% (x = 0.1) to –20% (x = 0.6) at T = 20 K and $\mu_0 H$ = 7 T. The compounds of $Eu_{1-x}Ba_xTiO_3$ series also show large positive MDE together with negative ac MR up to x = 0.6. The MDE and ac MR decreases with increasing Ba doping from x = 0.02 (MDE = 120% and ac MR = – 94%) to x = 0.60 (MDE = 7.6% and ac MR = –13.5%) at T = 10 K and $\mu_0 H$ = 7 T. While MDE versus –ac MR curves for x = 0.10 and 0.30 are highly non-linear, they are almost linear at all temperatures for x = 0.50 and 0.60. We observed a linear relation in MDE and MR for the first time.

While the substitution of isovalent Ba^{2+} for Eu^{2+} does not dope a charge carrier in system, the substitution of aliovalent La^{3+} for Eu^{2+} dopes electrons into t_{2g} orbital of Ti-3d band of $EuTiO_3$. The ground state of $Eu_{1-x}La_xTiO_3$ changes from AFM for x = 0.01 to FM for $x \geq 0.03$. In $Eu_{1-x}La_xTiO_3$, the FM Curie temperature increases as x increases from x = 0.03

(T_C = 5.7 K) to x = 0.13 (T_C = 8.8 K) and then decreases with further increasing x (T_C = 7.2 K for x = 0.30). Here, the introduced t_{2g} electrons in the empty Ti-3d band seems to suppress AFM coupling and promote FM interaction between 4f spins of neighboring Eu^{2+} through RKKY like interaction. The compound x = 0.01 shows a large $-\Delta S_m$ = 41.5 J/kg.K and ΔT_{ad} = 17.2 K around 6.7 K for a field change of $\mu_0 \Delta H$ = 5 T. Although the peak value of $-\Delta S_m$ and ΔT_{ad} decreases as La content increases, it is impressive in x = 0.2 ($-\Delta S_m$ = 31.41 J/kg.K and ΔT_{ad} = 16 K at T = 7.5 K for $\mu_0 \Delta H$ = 5 T). The negative MR decreases drastically with increasing La contents in $Eu_{1-x}La_xTiO_3$ series. For $Eu_{0.99}La_{0.01}TiO_3$, MR = –75 % at T = 2 K for $\mu_0 H$ = 7T. For $x \geq 0.10$, the sign of MR changes to positive as temperature increases above 5 K. While the negative colossal magnetoresistance in $Eu_{1-x}La_xTiO_3$ is suggested due to the suppression of $4f^7$ spin fluctuations by magnetic field, the occurrence of positive MR in $Eu_{1-x}La_xTiO_3$ ($x \geq 0.10$) could be due to the increasing hybridization of Eu-4f and Ti-3d bands that enhances spin splitting of Ti-3d band.

Overall, magnetocaloric properties of the doped and undoped $EuTiO_3$ is easily understandable than the magnetoresistance and magnetodielectric effect in these materials. Due to time limitation of 4 years for completion of the Ph.D and closure of the lab for nearly 1 year due to renovation, certain measurements such as Hall effect and thermopower could not be done, which would have yielded information regarding carrier density and mobility to have better understanding of the electronic transport in these materials. I intend to complete the pending work after submission of the thesis.

List of Publications

Published

1. **Km Rubi**, P. Kumar, D V Maheswar Repaka, R. Chen, J-S. Wang and R. Mahendiran, "*Magnetocaloric effect in magnetoelectric* $Eu_{1-x}Ba_xTiO_3$", Applied Physics Letters **104**, 032407 (2014).

2. Midya, P. Mandal, **Km Rubi**, R. Chen, J.-S. Wang, R. Mahendiran, G. Lorusso and M Evangelisti, **"***Large adiabatic temperature and magnetic entropy changes in* $EuTiO_3$", Physical Review B **93**, 094422 (2016).

3. **Km Rubi** and R. Mahendiran, "*Magnetic field dependence of dielectric constant and resistivity in* $Eu_{0.98}Ba_{0.02}TiO_3$", IEEE Transaction on Magnetics **52**, 2500804 (2016).

4. **Km Rubi**, A. Midya, R. Mahendiran, D. V. Maheswar Repaka and R. V. Ramanujan, "*Magnetocaloric properties of* $Eu_{1-x}La_xTiO_3$ $(0.01 \leq x \leq 0.2)$ *for cryogenic magnetic cooling*", Journal of Applied Physics **119**, 243901 (2016).

5. Pawan Kumar, **Km Rubi** and R. Mahendiran, "*Room temperature giant magnetoimpedance in polycrystalline* $La_{0.75}Ba_{0.25}MnO_3$", AIP Advances **6**, 055913 (2016).

In preparation for submission

1. **Km Rubi**, R. Mahendiran, G. Lorusso, A. Camon, M Evangelisti and R. Matheiu "*Magnetocaloric and magnetodielectric effects in multiferroic* $Eu_{0.5}Ba_{0.5}TiO_3$"

2. **Km Rubi** and R. Mahendiran, "*Colossal magnetoresistance in* $Eu_{1-x}Ba_xTiO_3$ $(x = 0.0$ *and* $0.1)$"

3. **Km Rubi** and R. Mahendiran, "*Crossover from negative to positive magnetoresistance in* $Eu_{1-x}La_xTiO_3$ $(0.01 \leq x \leq 0.3)$".

4. **Km Rubi** and R. Mahendiran, "*Colossal magnetocapacitance and ac magnetoresistance in polycrystalline* $EuTiO_3$".

List of Conference Presentations

1. **13th Joint MMM-Intermag Conference** Jan 11-15, 2016, San Diego, California, USA
   Poster presentation - Magnetic field dependence of dielectric constant and resistivity of $Eu_{0.98}Ba_{0.02}TiO_3$.

2. **Multiferroic & Magnetoelectric Materials, Gordon Research Conference 2016,** Bates College, Lewiston, ME, USA
   Poster presentation – Magnetodielectric and magnetoresistance phenomena in $Eu_{1-x}Ba_xTiO_3$.

3. **IEEE Magnetic Society Summer School 2015,** University of Minnesota, Minneapolis USA
   Poster presentation – Large magnetodielectric effect and magnetocaloric effects in $Eu_{0.4}Ba_{0.6}TiO_3$. **(*Silver Poster Award*)**

4. **ICMAT2015 & IUMRS-ICA2015 Conference,** Suntec Singapore
   Poster presentation – Giant magnetocaloric effect and colossal magnetoresistance in antiferromagnet $EuTiO_3$.

5. **IEEE Magnetic Symposium 2015,** Nanyang Technological University, Singapore
   Oral Presentation – Giant magnetocaloric effect in magnetoelectric $EuTiO_3$ and $Eu_{0.5}Ba_{0.5}TiO_3$

6. **IPS Meeting 2015, Institute of Physics in Singapore,** Nanyang Technological University, Singapore
   Poster presentation - Large magnetodielectric effect and magnetocaloric effects in $Eu_{0.4}Ba_{0.6}TiO_3$. **(*Outstanding Poster Award*)**

7. **IPS Meeting 2014, Institute of Physics in Singapore,** National University of Singapore, Singapore
   Poster presentation – Giant magnetocaloric effect and colossal magnetoresistance in antiferromagnet $EuTiO_3$. **(*Outstanding Poster Award*)**

8. **9th Mathematics and Physical Sciences Graduate Congress 2014,** University of Malaya, Kuala Lumpur, Malaysia
   Poster presentation – Giant Magnetocaloric effect in magnetoelectric $Eu_{1-x}Ba_xTiO_3$ **(*Best Presentation Award*)**

9. **Magnetic Symposium Best Presentation Contest 2013, IEEE Magnetic Society Singapore Chapter**, National University of Singapore, Singapore
   Oral presentation – Giant Magnetocaloric effect in magnetoelectric $Eu_{1-x}Ba_xTiO_3$

List of Figures

List of Tables

Chapter 1 Introduction

Transition metal oxides are a fascinating class of materials due to their wide range of physical properties such as electronic transport, magnetism, and thermal response. The electron correlations in transition metal oxides constrain the number of electrons at a lattice site and induce coupling among the charge, spin and orbital degrees of freedom, which gives rise to a variety of phenomena, for example, metal-insulator transition, multiferroicity and superconductivity. A renewed interest in transition metal oxides was caused by the discovery of high temperature superconductivity in cooper oxides.[1] Since then, tremendous efforts have been made to enhance the temperature at which the material turns into superconductor and the superconductivity is achieved around 130 K in Hg-Ba-Ca-Cu-O system.[2] One most important phenomenon investigated in transition metal oxide is colossal magnetoresistance effect, i.e. huge change in resistivity with applying magnetic field. This phenomenon has been detected in several manganese-based oxides since the 1990s.[3, 4] Hole doped manganites exhibit an insulator-metal transition around paramagnetic to ferromagnetic transition temperature and the resistivity can be changed by several orders of magnitude with application of magnetic field. Manganites ($La_{1-x}Sr_xMnO_3$)[5] was the first family of transition metal oxides discovered to show the ferromagnetism and metallic behavior in single phase. Later, the ferromagnetism and colossal magnetoresistance were also investigated in cobalt-based oxides.[6, 7] The magneto-thermodynamic phenomenon known as the magnetocaloric effect is also investigated in several transition metal oxides over wide temperature range.[8-10] Because of nontoxic and high chemically stable nature, these materials are considered as potential magnetic refrigerants.

Many of the transition metal oxides have a very large dielectric permittivity, making them suitable for the dielectric layer of capacitors. Especially $BaTiO_3$ and $SrTiO_3$ have had many technological applications as dielectric materials. The coexistence of ferroelectricity and ferromagnetism- termed multiferroicity in transition metal oxides made these materials more interesting towards device applications such as electronic memory storage and magnetic field sensors. While the multiferroicity and magnetodielectric coupling have been studied extensively in manganites ($YMnO_3$[11]and $BiMnO_3$[12]) and ferrites ($BiFeO_3$[13]) since last few decades, $EuTiO_3$ [14, 15] attracted substantial research interest only in recent years.

The aim of this thesis is to investigate the magnetocaloric, magnetoresistance and magnetodielectric effects in an exceptional rare-earth titanate, $EuTiO_3$. Moreover, we study the substitution effect of divalent alkaline-earth and trivalent rare-earth ions on the physical phenomena in $EuTiO_3$. In this chapter, we present an overview of titanates especially $EuTiO_3$ and investigated phenomena (magnetocaloric effect, magnetoresistance and magnetodielectric effect).

1.1Perovskite structure oxides: Titanates

Perovskite is the name of calcium titanium oxide; $CaTiO_3$ mineral named after Russian mineralogist L. A. Perovski. Perovskite oxides having general formula ABO_3 are some of the most fascinating and technologically important class of materials in condensed material research. Fig. 1.1 shows an ideal cubic unit cell structure of perovskite oxide ABO_3,

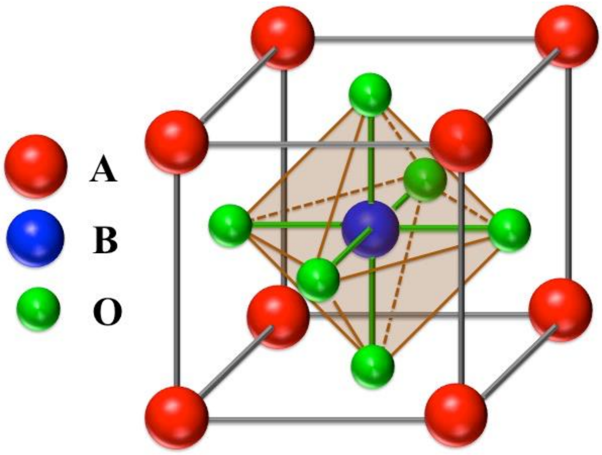

Figure 1.1 Crystal structure of perovskite oxide ABO_3.

where B is transition metal ion (Mn, Fe, Co, Ti etc.) and A is a divalent alkaline earth ion (Sr, Ba, Ca etc.) or trivalent rare earth ion (La, Pr, Gd etc.). In ABO_3 structure, the B-site cation occupies the body center position with oxygen octahedral cage as BO_6, whereas A-site cation occupies a corner position. The A, B and O sites are associated with 12, 6 and 8 coordination numbers, respectively. These materials have high structure stability and the A and B- site cation can be substituted by any foreign cation having different ionic radius or oxidation state. However, the degree of substitution at the A and B-site cation is not liberal, as it would create the deviation in the framework and destroy the crystal structure. The stability and the degree of distortion for the crystal structure can be estimated from the tolerance factor (t) of the crystal. The tolerance factor is defined as

$$t = \frac{\langle r_A \rangle + r_O}{\sqrt{2}(\langle r_B \rangle + r_O)} \tag{1.1}$$

where $\langle r_A \rangle$, $\langle r_B \rangle$ and r_O are the radii of the A cation, B cation and O ion, respectively.

The perovskite oxides have been of interest for their magnetic, electrical and optical properties. These materials have great use in the fabrication of various microelectronics and optoelectronic components like ferroelectric random access memories, thermistors, capacitors, microsensors and microactuators. Titanates are classified into two categories: alkaline-earth titanates and rare-earth titanates.

1.1.1 Alkaline-earth titanates

Alkaline earth titanates ($ATiO_3$, A: Ca, Ba and Sr) are important materials for the electronics industry. Among these titanates, $BaTiO_3$ (BTO) is most widely used because of its large dielectric constant (ε ~ 7000), ferroelectric and piezoelectric properties and photorefractive effect. BTO was discovered during World War II in 1941. H. D. Megaw[16] (1945) proposed the first detailed description of the crystal structure of BTO in the high temperature ferroelectric phase. Later, A. von Hippel [17, 18] revealed that BTO crystal

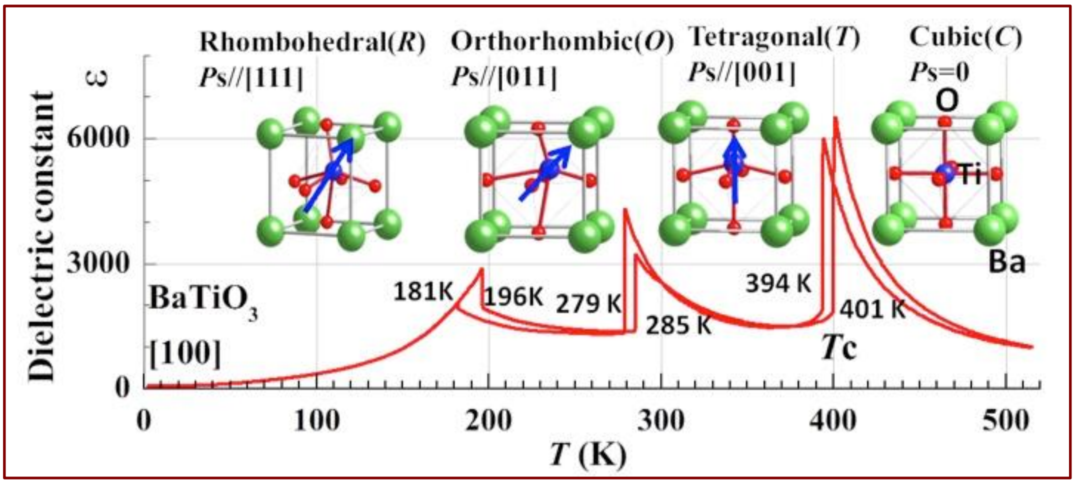

Figure 1.2 Temperature dependence of dielectric constant of BTO single crystal. Insets show the schematics of Ti displacement in the oxygen octahedron of the perovskite structure. T_C represents the paraelectric-to-ferroelectric phase transition. Figure from Ref. [19]

undergoes a series of phase transitions: (i) cubic to tetragonal (~400 K), (ii) tetragonal to orthorhombic (~278 K) and orthorhombic to rhombohedra (~183 K). In cubic form, all the Ba^{2+} ions occupy eight corners of an elementary cubic cell, whereas single Ti^{4+} ion resides at the center of the cube and the O^{2-} ions at the center of each surface of that cube (Fig. 1.2). However, below ferroelectric transition temperature T_{FE} ~ 400 K, BTO exhibits distorted tetragonal structure with a mutual displacement of the centers of positive and negative charges within the sublattice. Consequently, a dipole moment arises parallel to one of the cubic areas of the original phase. Such a spontaneous polarization generated in the tetragonal structure is the origin of its ferroelectric and piezoelectric behavior.

In contrast to BTO, $CaTiO_3$ (CTO) and $SrTiO_3$ (STO) remain paraelectric down to the lowest temperatures measured as a result of quantum fluctuations and so they are called quantum paraelectrics. The dielectric constant of a regular ferroelectric shows divergence near room temperature, while for quantum paraelectrics it begins to diverge in the regular manner but levels off at low temperatures (See Fig. 1.3(a)). In ferroelectric materials with high T_{FE}, the transition is governed by thermal fluctuations and the dielectric susceptibility χ_E follows a Curie-Weiss behavior,

$$\chi_E = \frac{C}{T - T_{FE}} \tag{1.2}$$

where C is a constant. The ferroelectric transition is driven by instability of the crystal lattice against a soft optical phonon mode. The softening of the mode is caused by the competition of short-range and long-range Coulomb forces and it can be modified by varying parameters such as temperature, pressure or field. From the Drude-Lorentz relation, the dielectric constant is inversely proportional to the square of soft mode frequency ω, i.e.

$$\varepsilon = \chi_E + 1 \approx \frac{\omega_p^2}{\omega^2} \tag{1.3}$$

where $\omega_p^2 = Ne^2/(\varepsilon_0 m)$ is the plasma frequency for free electron gas. For low T_{FE} materials, quantum fluctuations stabilize the system and the soft mode saturates at a given frequency. These systems are barely stable against their ferroelectric soft mode at 0 K. So, they are called incipient ferroelectrics or quantum paraelectrics. At high temperature, ε of quantum paraelectrics follows the Curie Weiss law, which fails to describe the saturation of ε at low temperature. Below the temperature T_1, where quantum fluctuation becomes discernible, ε can be well described by the Barrett formula, which is derived from a model based on

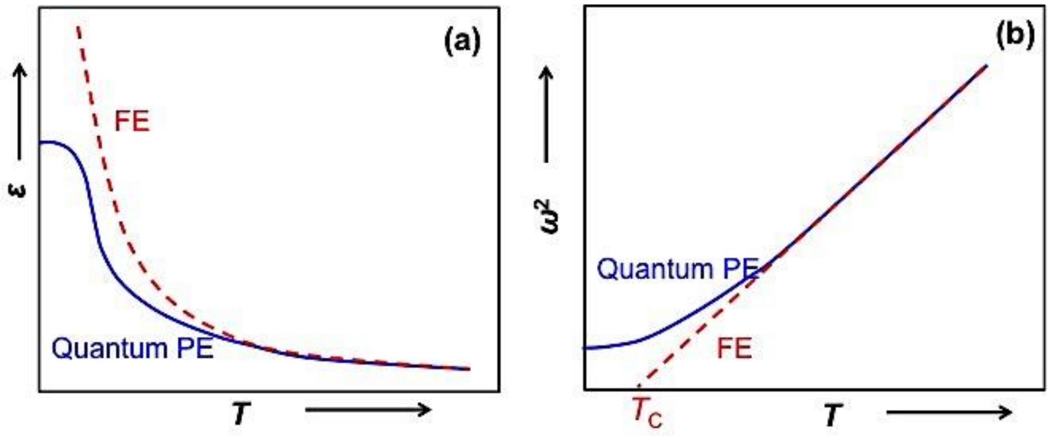

Figure 1.3 (a) Temperature dependence of dielectric constant of a FE material (dashed line) and quantum PE (solid line). (b) Soft mode frequency as a function of temperature for FE (dashed line) and quantum PE (solid line).

mean-field quantum-statistical ensemble of anharmonic oscillators,

$$\varepsilon(T) = A + \frac{B}{(T_1/2)\coth(T_1/2T) - T_0} \tag{1.4}$$

where T_0 is the Curie-Weiss temperature in the classical limit.

STO, having a cubic perovskite structure at room temperature with lattice constant a = 3.905 Å, is a band insulator with a band gap of ~ 3.2 eV. Oxygen deficient STO shows superconducting transition below 1 K.[20] Similar to BTO, STO also undergoes various low symmetry structural phase transition at lower temperatures: a cubic to tetragonal at ~ 110 K, a tetragonal to orthorhombic at ~ 60 K and orthorhombic to rhombohedra at ~ 30 K.[21-23] STO shows an unusual dielectric response. It has a large dielectric constant (~ 300) at room temperature, which increases to a few thousands at low temperatures (Fig. 1.4).[24] Further, the dielectric response is also shown to be tunable with electric field.[25] The exciting dielectric property of STO made it an ideal material as a gate dielectric in oxides based field effect transistors. Although STO undergoes structural transitions at low temperatures, it does not show ferroelectricity. The paraelectric state of STO is very sensitive to lattice perturbations, thus a subtle change in the lattice structure would create a ferroelectric behavior in STO. The ferroelectricity in STO is shown to be

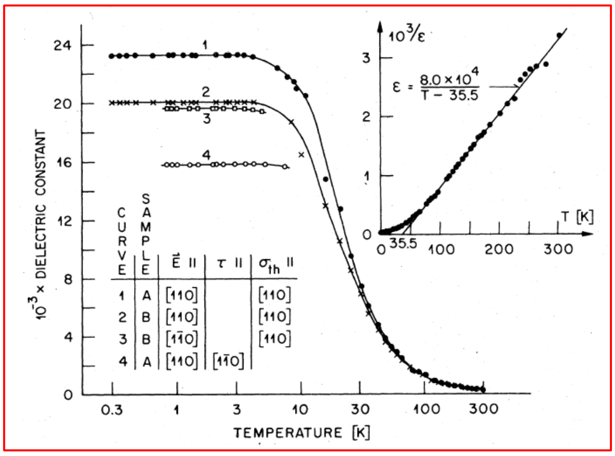

Figure 1.4 Temperature dependence of dielectric constant for various STO samples. Figure from Ref. [24].

induced by chemical substitution[26, 27] and strain[28, 29]. However, the relaxor ferroelectricity is also observed in unstrained STO thin film and bulk crystal recently, where ferroelectricity arises from minute amount of unintentional Sr deficiency in nominally stoichiometric samples.[30]

1.1.2 Rare-earth titanates

Perovskite rare-earth titanates ($RTiO_3$, R: La, Pr, Gd, Sm, Eu etc) having Ti ion in trivalent state ($3d^0$:$t_{2g}^1e_g^0$) are interesting class of materials to investigate the emergence of strong correlation electrons, orbital order driven spin configuration and change in magnetic ground state with increasing orthorhombic distortion. Excluding $EuTiO_3$, these compounds have rare earth and Ti ions in trivalent state. In $EuTiO_3$, Ti is tetravalent and Eu is divalent with large spin moment (S = 7/2) due to the stable $4f^7$ electronic configuration. Trivalent $RTiO_3$ exhibits a pseudocubic perovskite crystal structure with an orthorhombic distortion ($GdFeO_3$-type distortion) in which the TiO_6 octahedra forming the perovskite lattice tilt alternatingly (Fig. 1.5). The magnitude of the distortion depends on the ionic radii of the R

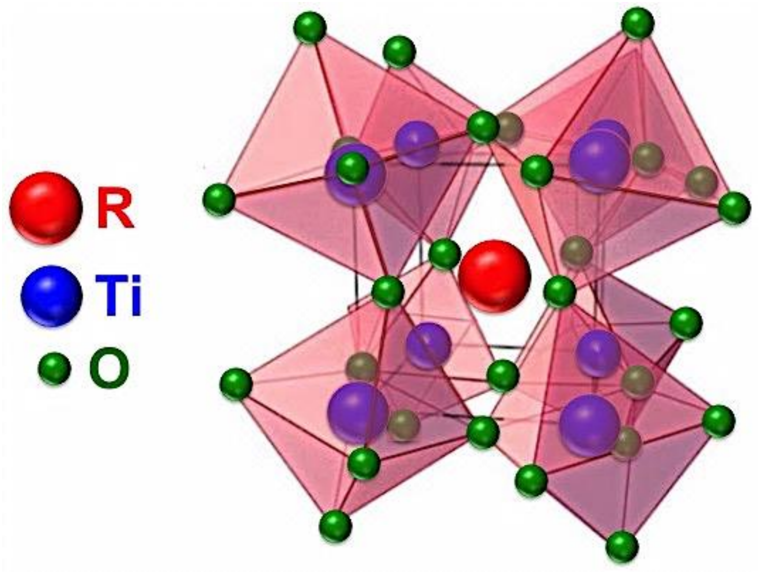

Figure 1.5 Crystal structure of $RTiO_3$ with $GdFeO_3$-type distortion.

ions. With a small ionic radius of the R ion, the lattice structure is more distorted and the Ti-O-Ti bond angle is decreased more significantly from 180°. The ionic radii of La and Y ions are 117 pm and 104 pm, respectively. Therefore, the bond angle in LaTiO$_3$ is 157° (ab-plane) and 156°(c-axis), but 144° (ab-plane) and 140° (c-axis) in YTiO$_3$.[31] However, the magnitude of distortion could be controlled using solid-solution system. In RTiO$_3$, this bond angle distortion controls the interplay of the orbital, spin and lattice degrees of freedom.

Greedan *et. al.*[32] and Katsufuji *et.al.*[33] studied the magnetic and electrical properties of RTiO$_3$ as a function of ionic radius of rare earth ions independently. Fig. 6(a) shows the magnetic phase diagram of trivalent RTiO$_3$, which exhibits an antiferromagnetic-to-ferromagnetic (AFM-FM) phase transition. LaTiO$_3$ with smallest distortion shows a G-type AFM ground state below ~ 140 K. With increasing GdFeO$_3$-type distortion, T_N decreases and it is strongly depressed at SmTiO$_3$ (T_N ~ 53 K), subsequently a FM ordering appears. In the significantly distorted compounds such as GdTiO$_3$ (T_C ~ 30 K) and YTiO$_3$ (T_C ~ 27 K) a FM ground state accompanied by a large Jahn-Teller distortion is realized. In case

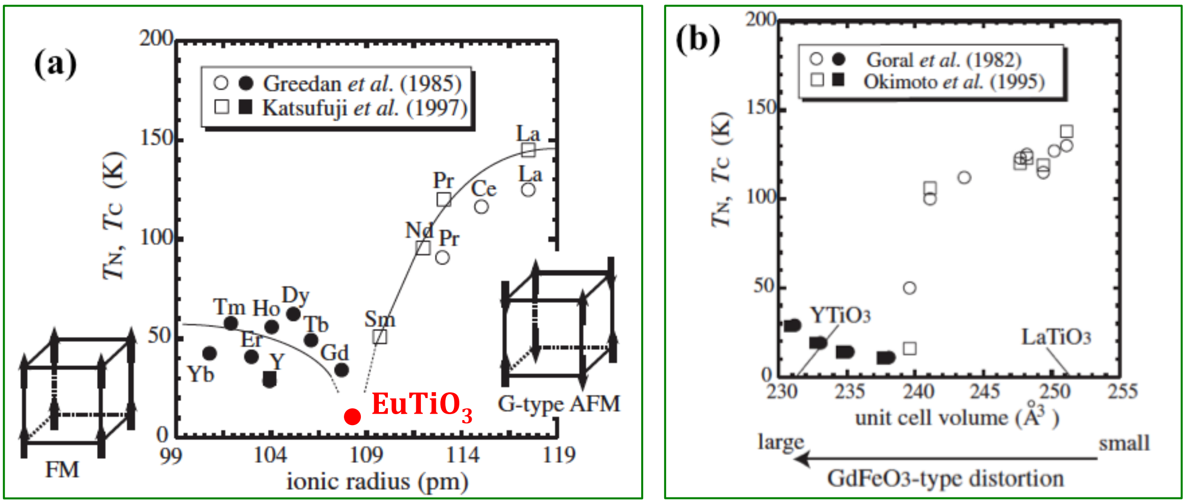

Figure 1.6 (a) A magnetic phase diagram of RTiO$_3$ as a function of ionic radius of R-ions and (b) A magnetic phase diagram for La$_{1-x}$Y$_x$TiO$_3$ as a function of unit-cell volume proportional to the Y concentration and GdFeO$_3$ type distortion. T_N (Open symbols) and T_C (closed symbols) represent the transition temperature for antiferromagnetic and ferromagnetic ordering, respectively. Figures from Ref. [34, 35].

of $EuTiO_3$, the ionic radii of Eu^{2+} and Ti^{4+} are 117 pm and 56 pm, respectively. Since the ionic radius of Ti^{4+} is smaller than that for Ti^{3+} (81 pm), the position of $EuTiO_3$ in the magnetic phase diagram of $RTiO_3$ can be assumed between $GdTiO_3$ and $SmTiO_3$, where both T_N of lighter rare earths and T_C of heavier rare earths vanish (see Fig. 6(a)). This demonstrates the instability between the formation of AFM and FM phase in $EuTiO_3$. A magnetic phase diagram with varying ionic radius was also found for $La_{1-x}Y_xTiO_3$ (Fig. 6(b)).[36, 37]

Trivalent $RTiO_3$ are strongly correlated Mott insulators, with a single electron occupying Ti t_{2g} orbitals. Divalent alkaline ions substituted $RTiO_3$ ($R_{1-x}A_xTiO_3$) shows a transition from insulating to metallic state upon carrier doping achieved by increasing x.[33, 38, 39] The resistivity of $R_{1-x}Ca_xTiO_{3+y/2}$ with R = La, Pr, Nd and Sm and various hole concentrations

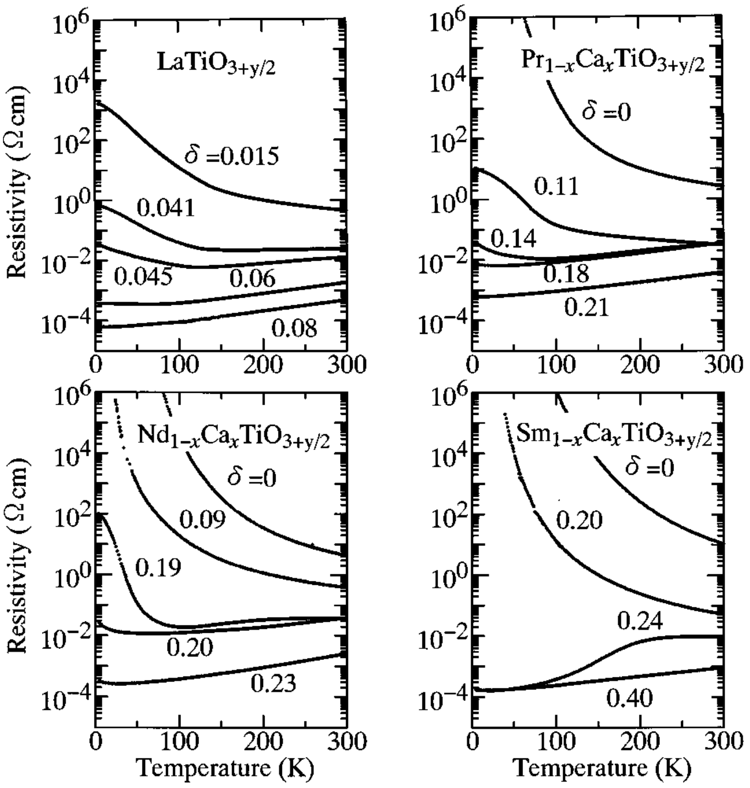

Figure 1.7 Temperature dependence of resistivity for $R_{1-x}Ca_xTiO_{3+y/2}$ (R = La, Pr, Nd and Sm) crystals with various hole concentrations $\delta = x + y$.[33]

reported by Katsufuji *et. al*.[33] is shown in Fig. 7. For all R, the change in resistivity with hole doping is similar. With an increase of hole concentration δ, the temperature dependence of resistivity varies from insulating to metallic.

1.2 $EuTiO_3$

1.2.1 Crystal and magnetic structure of $EuTiO_3$

$EuTiO_3$ (ETO), in which europium is apparently divalent, was successfully synthesized first time by J. Brous *et. al*.[40] in 1953. It was noticed that the ETO is isostructral with STO (cubic pervoskite structure) and has almost identical lattice constant (a = 3.905 Å). ETO can be considered as magnetic relative to STO because of Eu^{2+}: $4f^7$ spins. Fig. 1.8(a) shows the crystal structure of ETO, where arrows depict the Eu^{2+} spins. T. R. McGuire *et. al*.[41] and C.-L. Chien *et. al*.[42] studied the magnetic properties of ETO and revealed that ETO exhibits antiferromagnetic ordering below T_N = 5.5 K (Fig. 1.8(b)). In spite of AFM ordering, ETO shows a positive Curie Weiss temperature (θ = 3.17 K). From powder neutron

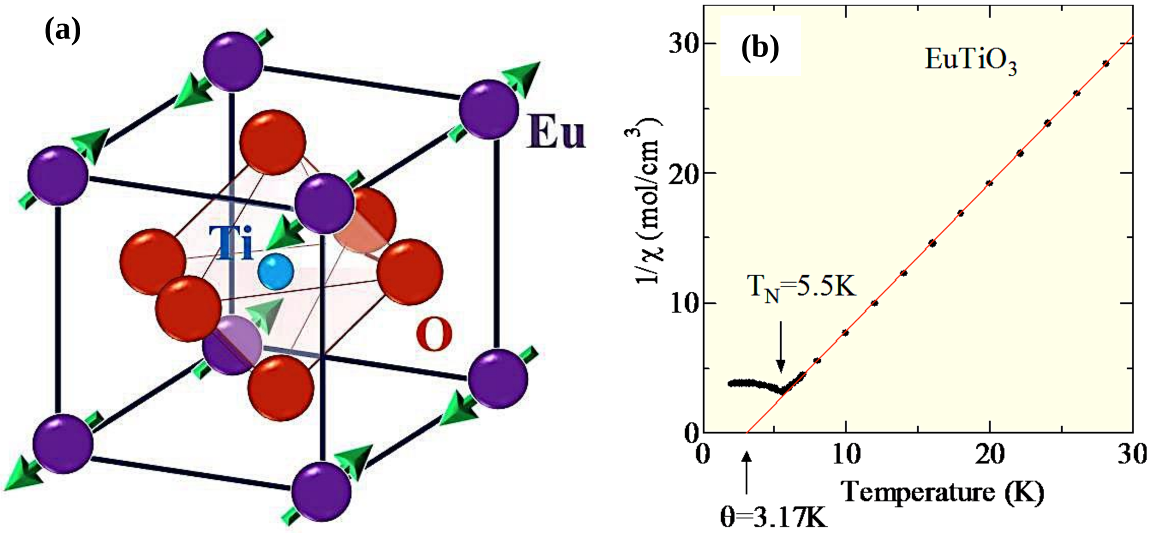

Figure 1.8 (a) Crystal structure of perovskite $EuTiO_3$. Arrows represent the Eu spins. (b) Temperature dependence of inverse susceptibility of $EuTiO_3$, which indicates a positive Curie Weiss temperature (θ = 3.17 K) despite antiferromagnetic transition at T_N = 5.5 K.

diffraction pattern, it was concluded that ETO has G-type antiferromagnetic structure, in which a given Eu^{2+}-spin has 6 nearest neighbor Eu^{2+}-spins in antiparallel and 12 next nearest neighbor Eu^{2+}-spins in parallel.[41] The nearest and next-nearest neighbors exchange interaction coefficient evaluated using mean field theory are $J_1 = -0.021k_B$ K and $J_2 = +0.040k_B$ K, respectively.

The exchange coefficient of nearest-neighbor interactions, J_1 is the key factor in AFM-FM switching. The possible exchange mechanisms for J_1 are: (i) a direct exchange between Eu 4f states, (ii) an indirect exchange via Eu 5d states, (iii) a superexchange via O 2p states and (iv) a superexchange via Ti 3d states. However, the AFM superexchange via Ti 3d states is more favorable for an AFM exchange mechanism competing with the indirect FM exchange via Eu 5d states. The competition between AFM superexchange and FM exchange leads to a delicate balance between AFM and FM phases in ETO.[43]

Although the crystal and magnetic structures of ETO were reported few decades ago, this material has gained considerable attention only in recent years after the demonstration of magnetoelectric coupling in 2001. Fig. 1.9(a) and (b) display the number of publications and citations per year related to ETO. As one can see from Fig.1.9(a), there were only few reports on ETO until 2010, while the number of publications per year rapidly increases in 2012.

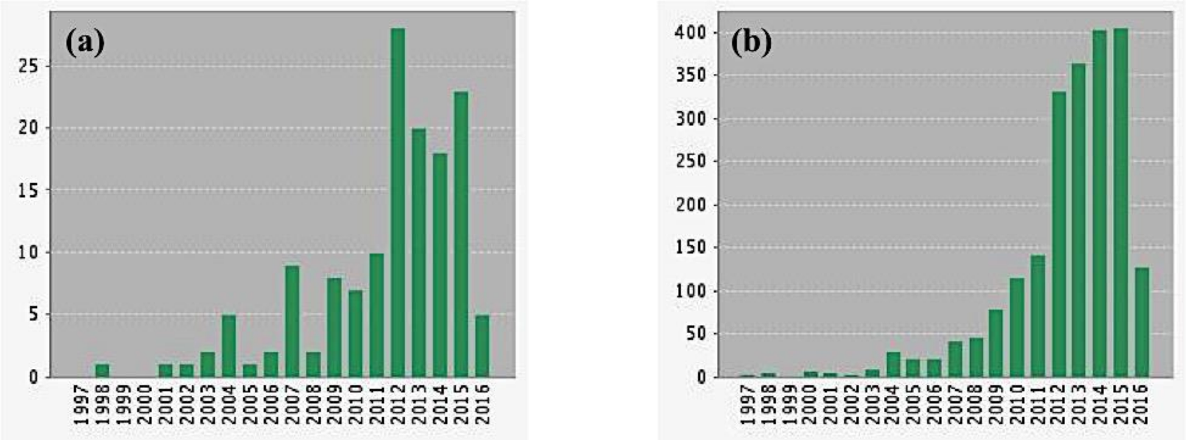

Figure 1.9 (a) Number of publications per year and (b) number of citation per year related to $EuTiO_3$. Source: Web of Science.

1.2.2 Electronic structure of $EuTiO_3$

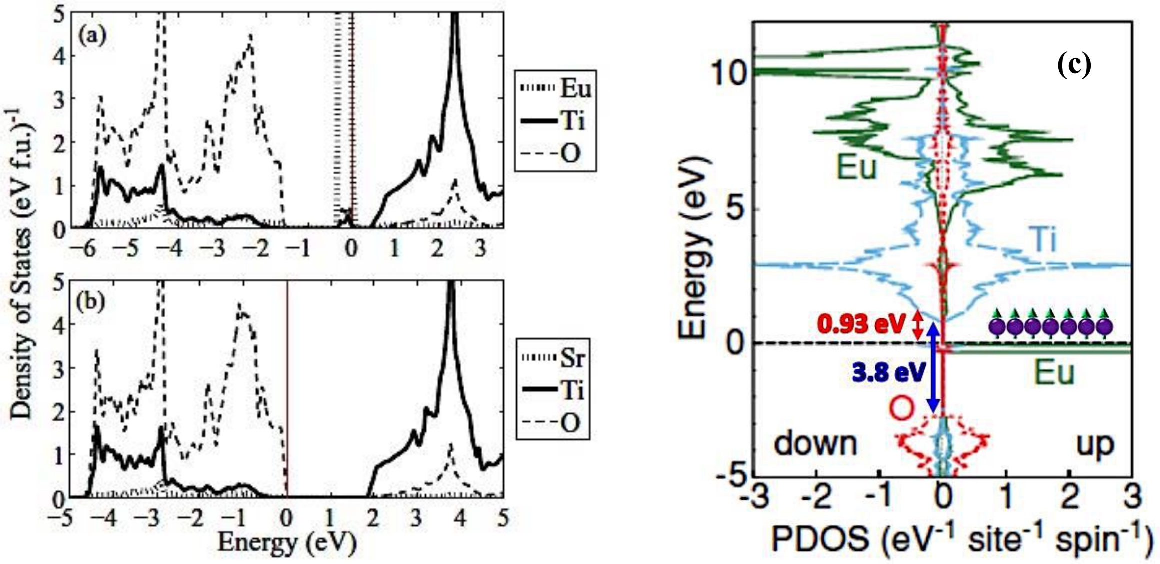

Figure 1.10 Density of states (DOS) of (a) $EuTiO_3$ and (b) $SrTiO_3$ calculated from first principle, figure from ref. [44] (c) Partial density of states (PDOS) of $EuTiO_3$ calculated through hybrid Hatree-Fock density functional calculations, figure from Ref. [43].

While Akamatsu *et. al*.[43] studied the band structure of ETO using Hatree Fock density functional calculations, Birol and Fennie [44] performed First-principle calculations within density functional theory. Fig. 1.10 (a) and (b) show the density of states (DOS) of ETO and STO, respectively, calculated from first principle. The ETO and STO have quite similar band structure, where valence band has occupied O-p states and conduction band consists of unoccupied Ti d states. However, the half-occupied Eu-4f states in ETO form narrow bands below Fermi level. There is very little hopping between the Eu 4f orbitals and the neighboring cations, since the radii of the 4f orbitals are much smaller than that of the 5s or 5p orbitals. From Fig. 1.10 (c), the band gap is determined to be 0.85 eV, which is in good agreement with that estimated from an optical absorption spectrum *i.e.* 0.93 eV[45] for ETO thin film.

1.2.3 Magnetoelectric coupling in $EuTiO_3$

First time, T. Katsufuji and H. Takagi [14] demonstrated the magnetoelectric coupling in ETO single crystal. The reported temperature dependences of dielectric constant and inverse susceptibility of ETO are shown in Fig. 1.11(a) at left and right y-axes, respectively. Even though ETO is quantum paraelectric, the dielectric constant increases with decreasing temperature and shows a large value at low temperature ($\varepsilon \sim 400$ at $T = 30$ K). Fig. 1.11 (b) shows the variation of the dielectric constant of ETO under various magnetic fields. In absence of magnetic field, the dielectric constant shows a sharp decrease due to the antiferromagnetic ordering below $T_N = 5.3$ K. For increasing magnetic field, the dielectric constant at low temperature gradually increases and the sharp peak occurs at low field (1T), which eventually disappears at higher fields. The magnetodielectric effect was observed around 7 % at $T = 2$ K and $\mu_0 H = 1.5$ T.[14] The magnetodielectric effect was suggested to arise from coupling of the transverse optical phonon modes to magnetic fields via spin-spin correlation $\langle S_i \cdot S_j \rangle$ of the localized 4f electrons on the nearest neighbor Eu^{2+} ions. The

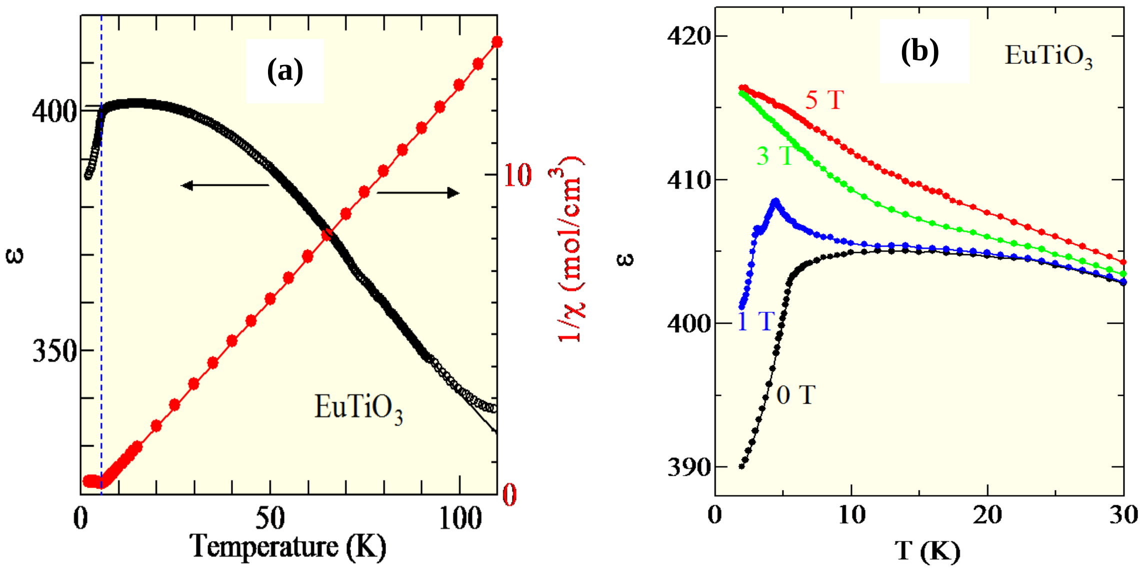

Figure 1.11 (a) Temperature dependence of dielectric constant (left y-axis) and inverse magnetic susceptibility (right y-axis). (b) Temperature dependence of dielectric constant under different magnetic fields. Figure from Ref. [14]

experimental data of the temperature and magnetic field dependence of the dielectric constant fits to the relation

$$\varepsilon(T,H) = \varepsilon_0(T)(1+\alpha\langle S_i \cdot S_j\rangle_H) \tag{1.5}$$

where $\varepsilon_0(T)$ is the spin independent part of the dielectric constant and α is the coupling constant between spin correlation and dielectric constant. It was suggested that hybridization between the Eu-4f orbitals and O-2p orbital is varied depending on the configuration of Eu spins, which modifies the frequency of the T_{1u} mode that contains Eu-O-Eu stretching motion. The magnitude of the change in phonon-frequency with magnetic field can be estimated from the change in dielectric constant.[14]

The dielectric constant associated with one optical phonon was given

$$\varepsilon(\omega) = \varepsilon_1(\omega) - i\varepsilon_2(\omega) = \varepsilon_\infty + \frac{4\pi N e^2/\mu}{(\omega_0^2-\omega^2)+i\Gamma\omega} \tag{1.6}$$

where N is the number of the unit cells per unit volume, e the effective charge of ions, □ the effective mass of ions and □□is the scattering rate of phonon.

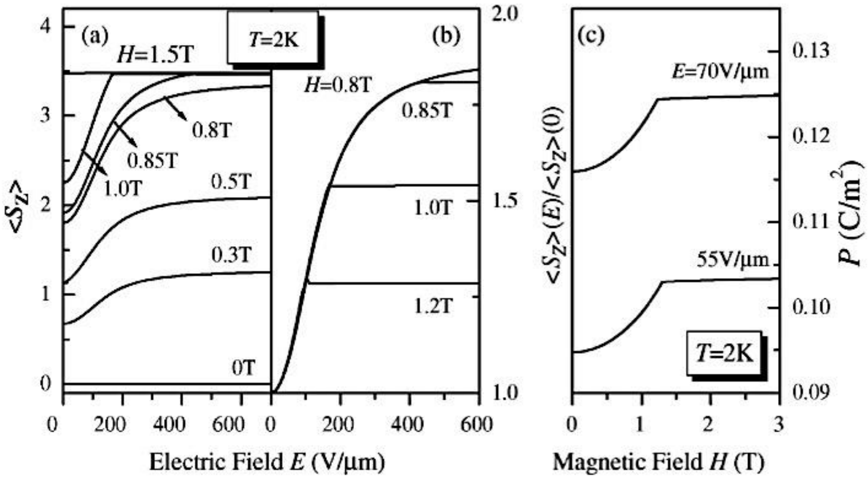

Figure 1.12 (a) Electric-field dependence of the spin momentum along z-axis under various magnetic fields at *T* = 2 K. (b) The normalized electrical field dependence of the magnetization to the zero field value in various magnetic field at 2 K. (c) Magnetic field dependence of the electric-field-induced polarization in ETO at *T* = 2K. Figure from Ref. [46].

H. Wu *et. al.*[47] have studied the magnetoelectric coupling in ETO theoretically and confirmed the magnetodielectric properties of ETO and $Eu_{1-x}Ba_xTiO_3$ reported by Katsufuji. Wu and Shen[46] demonstrated magnetodielectric effect by mutual dependence of electric and magnetic properties. This dependence is revealed by the variation of the electric-field-induced polarization with applied magnetic field as well as the change of magnetic-field-induced spin moment under application of electric field. Fig. 1.12(a) displays the variation in spin moment along z –axis ($\langle S_z \rangle$) as a function of applied electric field for different external magnetic fields, whereas Fig. 1.12 (b) shows the variation of normalized $\langle S_z \rangle$ value to their values for zero electric field. The $\langle S_z \rangle$ does not show any electric field dependence in two cases: (i) zero magnetic field and (ii) high magnetic field ($H > 1.5$ T). In the first case, the antiferromagnetic ordering remains unperturbed by the electric field and the magnetization is zero, whereas in the second case the parallel spin alignment remained unperturbed by the electric field and the magnetization is saturated. For $0\ \mathrm{T} < H < 1.0\ \mathrm{T}$, the magnetization increases with increasing electric field, approaching a saturation value which depends on the applied external magnetic field. This effect is explained through the nature of antiferromagnetic ordering in ETO crystal. The presence of a magnetic ground state in ETO is due to superexchange interaction. The superexchange interaction in ETO is mediated not only by Ti ions but also by O ions. Therefore, under the electric field parallel to the magnetic field, O ions will be displaced from its equilibrium, resulting in the reduction of the antiferromagnetic ordering, which is proportional to the square of the electric polarization. As a result, except for the ferromagnetic ordering induced by magnetic field, an additional electric-field-induced ferromagnetic ordering will appear and increase with the electric field due to the antiferromagnetic exchange energy reduction as a consequence of the increasing polarization. The results present in Fig. 1.12 (a) and (b) provide clear evidence that the magnetization in ETO can be controlled by the electric field. In addition to the dielectric

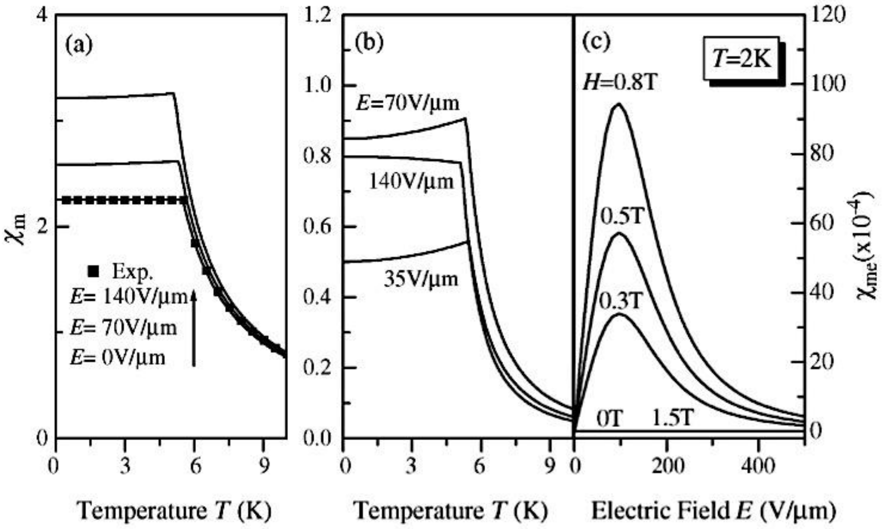

Figure 1.13 Temperature dependence of (a) magnetic susceptibility and (b) magnetoelectric susceptibility under different electric fields. (c) Electric field dependence of magnetoelectric susceptibility under various magnetic fields at *T* = 2 K. Figure from Ref. [46]

properties, the magnetic field has an effect on the electric-field-induced polarization as shown in Fig. 1.12 (c).

Wu and Shen[46] also discuss the magnetoelectric effect in ETO in relation with the magnetic field, electric field and temperature. Fig. 1.13 (a) and (b) show the temperature dependence of the magnetic susceptibility and magnetoelectric susceptibility under various electric fields, respectively. The magnetoelectric susceptibility is given as

$$\chi_{me} = \frac{\delta\langle S_Z\rangle}{\delta E} \tag{1.7}$$

The magnetic susceptibility increases in magnitude below T_N with application of electric field. The magnetoelectric susceptibility in the AFM phase does not display monotonic behavior with the applied electric field. In Fig. 1.13(c), the electric field dependence of magnetoelectric susceptibility is displayed under different magnetic fields at 2 K. No magnetoelectric effect is observed for 0 T field. However, with increasing magnetic field the magnetoelectric effect arises and then vanishes again as the field approaches the saturation

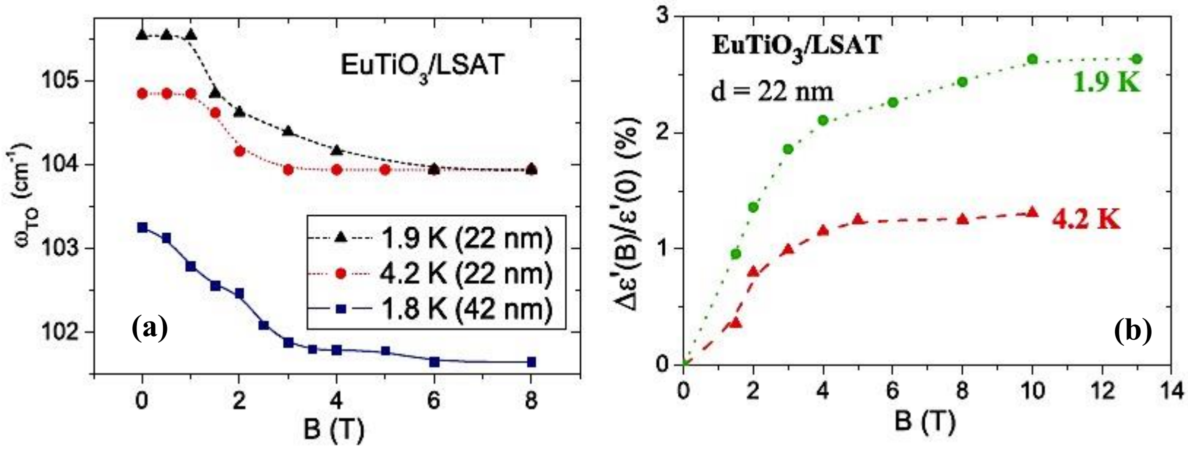

Figure 1.14 Magnetic field dependence of (a) the lowest-frequency phonon and (b) the relative changes of static permittivity obtained from the fits of IR reflectance of ETO thin films deposited on LSAT substrate. Figures from Ref. [48]

magnetic field (1.5 T). On the other hand, the magnetoelectric susceptibility shows a maximum for a fixed magnetic field.

The magnetodielectric properties of ETO thin films deposited on LSAT substrate were studied through the temperature and magnetic field dependences of polar phonons using infrared reflectance spectroscopy.[48] The phonon frequencies exhibit gradual softening with decreasing temperature, leading to an increase in static permittivity. In antiferromagnetic phase, a remarkable softening of the lowest-frequency polar phonon was observed under an applied magnetic field (Fig. 1.14(a)). Fig. 1.14 (b) show the reported magnetic field dependence of relative dielectric permittivity obtained from the fit of IR reflectance spectra. It is noticed that the change in dielectric permittivity with magnetic field in ETO thin film (~ 2.5 %) is almost three times smaller than that in the single crystal (~ 7 %), because the phonons are stiffened in the strained thin films.

S. Kamba *et. al.*[49] studied the magnetodielectric effect of ETO ceramics by measuring the dielectric permittivity under the magnetic field as well as using infrared reflectivity spectroscopy. Fig. 1.15(a) shows the real part of dielectric permittivity of ETO ceramic as a function of temperature under various magnetic fields. It is noticed that the

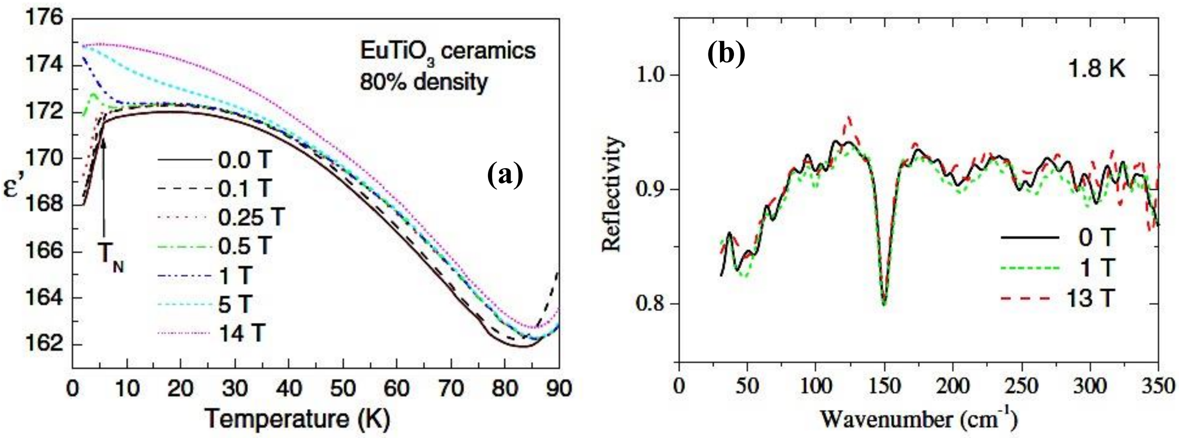

Figure 1.15 Temperature dependence of dielectric permittivity of ETO ceramic under various magnetic fields and (b) FIR reflectivity spectra of ETO ceramic taken at 1.8 K and various magnetic fields. Figures from Ref. [49].

temperature and field dependences of dielectric permittivity for ETO ceramic is quite similar those for ETO single crystal. However, the value of dielectric permittivity at low temperature is smaller than that of single crystal. The infrared reflectivity spectra under various magnetic fields are shown in Fig. 1.15 (b). No spectral change with magnetic field is observed because of the low IR signal, high noise and limited accuracy of measurements.

1.2.4 Multiferroicity in $EuTiO_3$

Since bulk ETO is AFM at temperature lower than 5.5 K and paraelectric at all temperature, many efforts have been made to induce the ferroelectricity and ferromagnetism

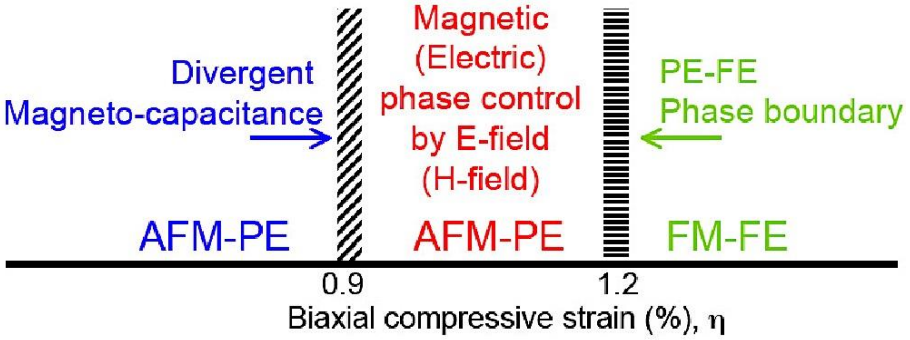

Figure 1.16 Compressive epitaxial strain phase diagram for ETO. Figure from Ref. [50].

in ETO. Using first-principle density functional calculation, Fennie and Rabe[50] predicted that the magnetic (electric) phase can be controlled by an applied electric (magnetic) field in epitaxially strained ETO. According to their theory, the ground state of ETO changes from AFM-PE state to FM-FE one with increasing compressive strain (Fig. 1.16). Lee *et. al.*[15] experimentally demonstrated that the magnetoelectric coupling in ETO can be controlled through epitaxial strain. The (001)-oriented $EuTiO_3$ thin films were grown on three different substrates (001) $SrTiO_3$ (STO), (001) $(LaAlO_3)_{0.29}$-$(SrAl_{0.5}Ta_{0.5}O_3)_{0.71}$ (LSAT) and (110) $DyScO_3$. These substrates produce biaxial strains of 0.0 %, -0.9 %and +1.1%, respectively in thin film. Fig. 1.17 (a) show the temperature dependence of second harmonic generation

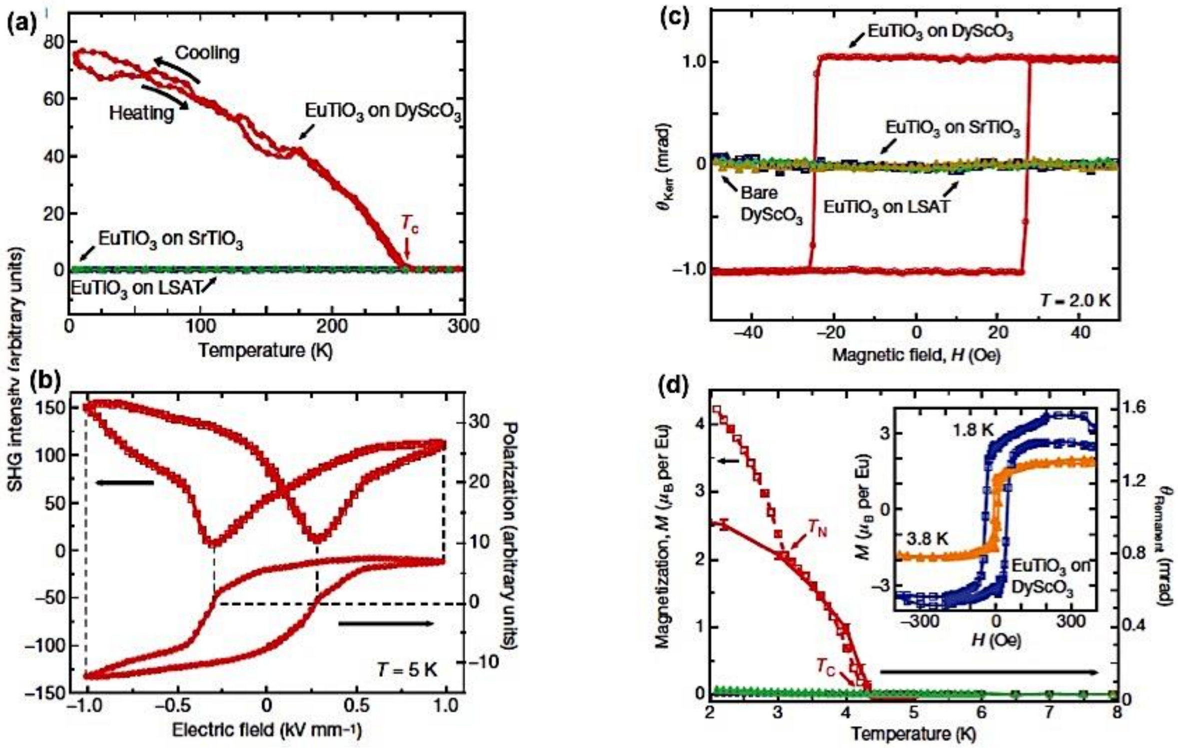

Figure 1.17 (a) Temperature dependence of second harmonic generation (SHG) signal of ETO on $DyScO_3$ (red), ETO on STO (blue) and ETO on LSAT (green). (b) SHG hysteresis loop (top) and corresponding polarization loop (bottom) for ETO on $DyScO_3$ at T = 5 K. (c) MOKE measurements at T = 2 K of ETO on $DyScO_3$ (red), ETO on STO (blue), ETO on LSAT (green) and bare $DyScO_3$ substrate (gold). q_{Kerr} is the Kerr-induced polarization rotation in the optical probe beam and is proportional to the in-plane magnetization. (d) Temperature dependence of the magnetization measured using MOKE and SQUID. Inset shows the isothermal SQUID magnetization curves at T = 1.8 and 3.8 K. Figures from Ref. [15].

(SHG) signal of ETO on $DyScO_3$ (red), ETO on STO (blue) and ETO on LSAT (green). ETO on $DyScO_3$ film only exhibited the second harmonic generation (SHG) signals and sharp maxima in temperature dependent dielectric measurements. Therefore, ETO thin film with +1.1 % strain showed paraelectric to ferroelectric transition around 250K. As can be seen from Fig. 1.17 (b), the strained thin film exhibits a clear SHG and P-E loops at T = 5K. Fig. 1.15 (c) show the MOKE response as a function of magnetic field of ETO on $DyScO_3$ (red), ETO on STO (blue), ETO on LSAT (green) and bare $DyScO_3$ substrate (gold). The ETO thin film with + 1.1 % strain has a clear ferromagnetic hysteresis loop, with sharp switching to full saturation. From the temperature dependence of the MOKE (Fig. 1.17(d)), strained ETO thin film on $DyScO_3$ substrate was confirmed to be ferromagnetic with Curie temperature T_C = 4.24 K.

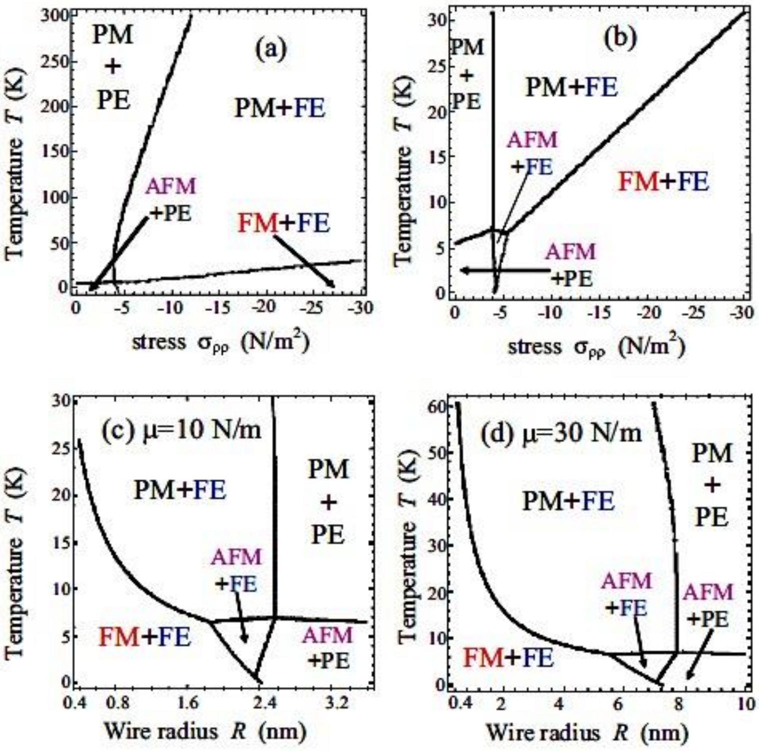

Figure 1.18 Phase diagram of EuTiO3 nanowire in coordinates of temperature and radial stress: (a) 0 K < *T* < 300 K and (b) 0 K < *T* < 30 K. Phase diagram of the EuTiO3 nanowire in coordinates temperature and wire radius calculated for different surface stress coefficients: (c) 10 N/m and (d) 30 N/m. Figures from Ref. [51].

The coexistence of ferroelectricity and ferromagnetism has been also predicted for ETO nanowires using Landau-Ginzburg-Devonshire theory with phenomenological parameters extracted from reported experimental data and first principle calculations.[51] According to theory, intrinsic surface stress induces ferroelectric spontaneous polarization of ~ 0.1-0.5 C/m^2 in ETO nanowires. The spontaneous polarization in turn induces the ferromagnetism at low temperature due to the strong magnetoelectric coupling. Fig. 1.18 (a) and (b) display the phase diagrams of ETO nanowire generated in coordinates of temperature and radial stress. The FE+PM, FE+FM and FE+AFM phases appear in the ETO nanowires subjected to the intrinsic surface stress. The FE and FM phase transition temperatures increase with increasing surface stress, which is inversely proportional to the nanowire radius. The phase diagrams of ETO nanowire in coordinates of temperature and wire radius are illustrated in Fig. 1.18 (c) and (d) for surface tension coefficients μ = 10 N/m and 30 N/m, respectively. For μ = 10 N/m, the FE+FM phase is induced in ETO nanowire of a radius less than 3 lattice constant (~ 1nm) at temperatures lower than 10 K. For μ = 30 N/m, the radius dependent FE+FM appears in a nanowire of a radius less than 3 lattice constant at temperature lower than 30 K. Thus, higher the surface tension coefficient, wider the region of the multiferroic FE+FM phase. The region of multiferroic phase increases with decreasing wire radius. Regarding the applications, ETO nanowire can perform better than strained ETO thin film, since the FM interaction in nanowire could be induced at higher temperature (~ 30 K) than that in thin film (~ 4 K). However, the multiferroicity in ETO nanowires is needed to verify experimentally.

1.2.5 Antiferrodistortive transition in EuTiO$_3$

Although the crystallographic structure of the magnetoelectric ETO had been considered to remain cubic down to low temperature, Bussmann-Holder *et. al.*[52] suggested an antiferrodistortive phase transition at the temperature T_S = 282 K based on an anomaly in

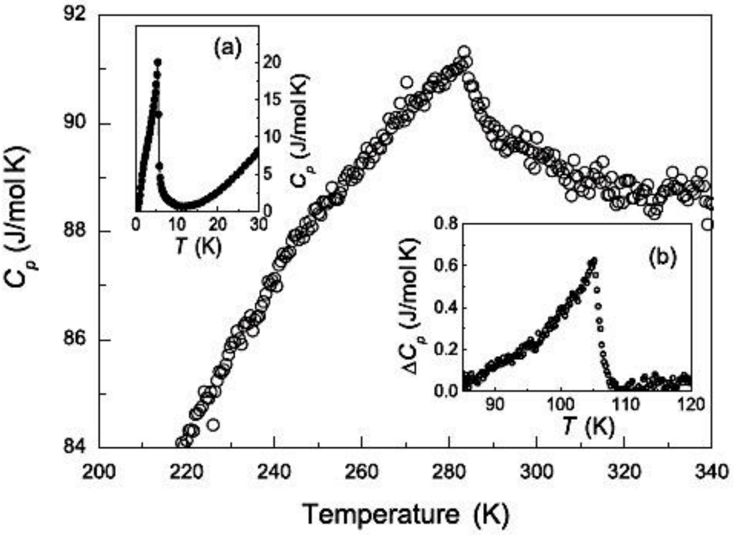

Figure 1.19 Main panel: Temperature dependence of specific heat of ETO in the temperature range around structural phase transition. Insets: (a) specific heat of ETO as a function of temperature in low temperature region and (b) specific heat of STO around phase transition (T_A ~ 105 K). Figure from Ref. [52]

specific heat data. They suggested that the high temperature structural transition found in ETO is analogous to cubic-tetragonal transition that occurs around 105 K in STO. The main panel and inset (b) of Fig. 1.19 show the temperature dependence of specific heat (C_p) of bulk ETO and STO, respectively, in the temperature range around phase transition. In ETO, an anomaly similar in shape to that of STO is seen at 282 K, which is close to the theoretically expected phase transition temperature (~ 298 K). M. Allieta *et. al.*[53] persented high-resolution synchrotron X-ray powder-diffraction pattern, which shows cubic (Pm-3m) to tetragonal (I4/mcm) structural phase transition at T_S = 235 K, involving TiO_6 octahedra tilting. While measuring phonon dispersion in ETO single crystal using inelastic X-ray scattering, D. S. Ellis *et. al.*[54] found a structural transition to an antiferrodistortive phase at temperature ~ 285 K. In addition, the first principle calculations for ETO also predict that its ground state consists of rotation and tilting of the oxygen octahedra.[55]

V. Goian *et. al.*[56] also revealed an antiferrodistortive phase transition in ETO ceramics at ~ 300 K by means of X-ray diffraction, dynamical mechanical analysis and

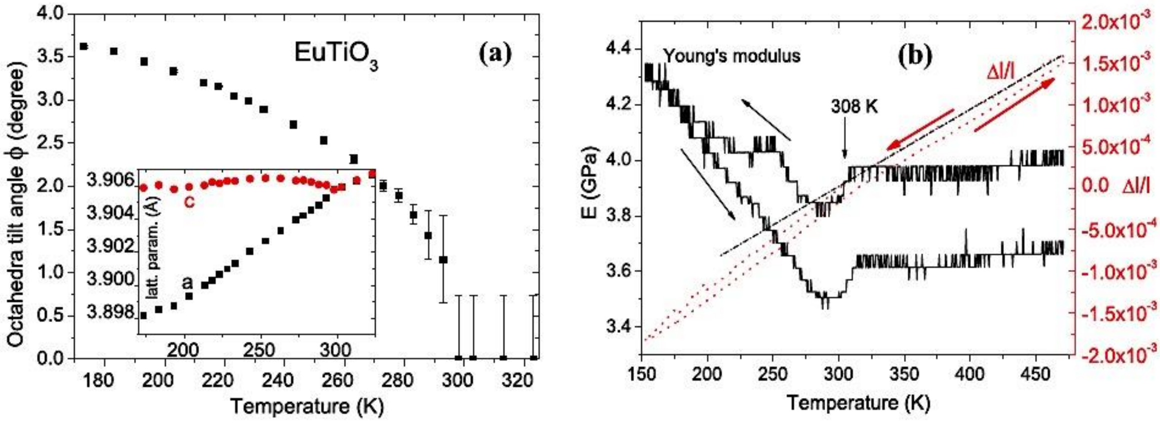

Figure 1.20 (a) Temperature dependence of tilt angle of oxygen octahedra from the c-axis. Inset displays the pseudocubic lattice parameters *a* and *c* as a function of temperature. (b) Temperature dependence of Young's modulus *E* and thermal expansion Δ*l*/*l* in bulk ETO. Figures from Ref. [56]

infrared reflectivity spectroscopy. It was noticed that the lattice parameter splits (see inset of Fig. 1.20 (a)) around 300 K due to the tetragonal distortion. The reported temperature dependence of the tilting angle of oxygen octahedra is shown in the main panel of Fig. 1.18 (a). The antiferrodistortive phase transition arises between 295 and 320 K, and the tilt angle reaches a value of 3.6° at 173 K. Fig. 1.20 (b) shows the temperature dependence of the Young's modulus and thermal expansion measured while cooling and heating. The thermal expansion depends linearly on temperature below and above 308 K, indicating that the phase transition is of second order. This is also consistent with the observed anomaly in the Young's modulus, which shows a negative dip at 308 K followed by a linear increase with decrease in temperature. Later, Reuvenkamp *et. al*.[57] investigated the structural phase transition by temperature and magnetic field dependence of linear thermal expansion of ETO and claimed that the structural phase transition in ETO is of first order in nature. A distinct anomaly was seen in thermal expansion coefficient of ETO (see Fig. 1.21 (a)) at T_S = 282 K, which is similar to the anomaly seen at the cubic-tetragonal phase transition in STO at 105 K. The anomaly was well described by the thermal displacement correlation function, which exhibits an abrupt change at the structural phase transition caused by a double-well potential

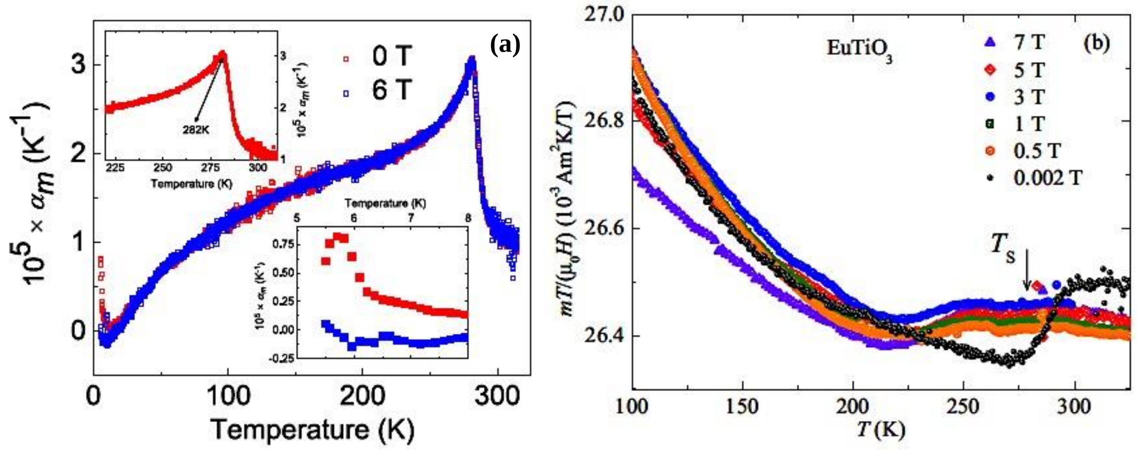

Figure 1.21 (a) Temperature dependence of thermal expansion coefficient of ETO for 0 T (red line) and 6 T (blue line) magnetic fields. The upper inset displays the enlarged scale to enable a better determination of TS. The lower inset shows the low-temperature thermal expansion coefficient for 0 T and 6 T. Figure from Ref. [57] (b) Temperature dependence of the quantity mT/(μ_0H) of ETO for various magnetic fields, where m is magnetic moment. Figure from Ref. [58].

in the oxygen- oxygen interaction. The structural phase transition is also observed from the temperature dependence of magnetic moment under low magnetic field (0.002 T) when it was plotted as the product *mT* normalized by the magnetic field $\mu_0 H$ versus T (see Fig. 1.21 (b)).[58] Spalek *et. al.* [59] studied the elastic and inelastic properties of ETO crystal using resonant ultrasound spectroscopy at frequencies in the vicinity of 1 MHz. It was seen that the softening of the shear elastic constants C_{44} and ½(C_{11}-C_{12}) occurs by ~ 20 – 30 % with falling temperature in a narrow temperature interval through the structural transition T_S = 284 K. Here, we conclude that the reported structural phase transition in ETO varies from 235 K to 310 K and the deviation probably depends on the density of sample or oxygen stoichiometry and/or defects in sample.

1.2.6 Magnetostriction in $EuTiO_3$

Reuvekamp *et. al.*[60] performed the magnetostriction experiment for polycrystalline ETO in low temperature range between 1.3 K and 12 K with varying the magnetic field from 0 T to 6 T. Fig. 1.22 (a) show the reported results of the change in sample length with respect to the reference length at T = 10 K, $\Delta L/L$(10 K) as a function of temperature under different magnetic fields. Under zero magnetic field, the $\Delta L/L$ shows an unusual drop at T_N = 5.7 K. With increasing magnetic field, this anomaly shifts to lower temperature. For $\mu_0 H$ > 0.625 T, the $\Delta L/L$ becomes positive with a well-resolved peak at 1 T, where the AFM state is completely suppressed. For $\mu_0 H$ > 1 T, $\Delta L/L$ continuously increases with decreasing temperature and increasing magnetic field. This behavior of magnetostriction for ETO is reminiscent of the dielectric constant behavior at low temperature, where a strong drop is observed at T_N.[14] Since the dielectric constant of ETO $\varepsilon(T) \propto \frac{1}{\omega(T)^2}$, where ω is the soft optical mode frequency which hardens at T_N and softens with increasing magnetic field. Therefore, the magnetostriction data from Fig. 1.22(a) implies that the field induced lattice expansion above 1 T supports the mode softening and stabilizes true multiferroic ordering. The thermal coefficient $\alpha = \frac{1}{L}\frac{dL}{dT}$ as a function of temperature under different magnetic field is shown in Fig. 1.22(b). Under zero magnetic field, a sharp cusp like anomaly is observed at T_N similar to the sharp anomaly in temperature dependent specific heat data. The sharp anomaly shifts towards lower temperature and broadens with increasing magnetic field. Under $\mu_0 H$ = 1 T, the anomaly completely vanishes and its sign changes for field higher

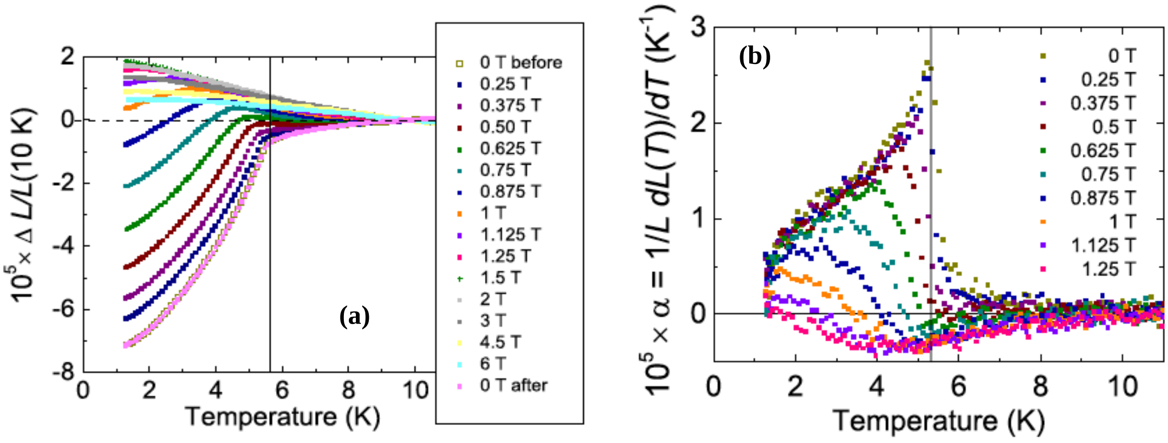

Figure 1.22 Temperature dependence of (a) relative length changes and (b) average linear coefficient of thermal expansion of ETO for different magnetic fields. Figures from Ref. [60].

than the threshold field 1 T. Later, P. Reuvekamp *et. al*.[61] combined the polarizability model with magnetostriction data and showed that the tiny changes in the lattice parameter at the onset of AFM order hugely affect the polarizability coordinates, lattice dynamics and dielectric permittivity.

1.3. Other Eu^{2+}-based perovskite oxides

Besides $EuTiO_3$, $EuMO_3$ (M = Zr, Hf, Si and Ge) also accept europium in divalent state. Akamatsu *et. al*.[43] calculated the exchange interaction constants for $EuMO_3$ (M = Ti, Zr, Hf, Si and Ge). For $EuZrO_3$ and $EuHfO_3$, the nearest neighbor's exchange constant (J_1) is negative and the magnetic ground state is G-type AFM similar to $EuTiO_3$. Whereas, for $EuSiO_3$ and $EuGeO_3$, J_1 is positive and the magnetic ground state is FM. The electronic structure of $EuZrO_3$ and $EuHfO_3$ is also different than that of $EuSiO_3$ and $EuGeO_3$. In the case of $EuZrO_3$ and $EuHfO_3$, conduction band consist of Zr-4d and Hf-5d states, respectively, while for $EuSiO_3$ and $EuGeO_3$, conduction band is composed of the Si-3s and Ge-4s states, respectively.

It is noticed that the magnetic ground state of $EuTiO_3$ can be tuned by chemical substitution at Eu, Ti or O sites. Several studies on chemical substitution effects on $EuTiO_3$ have been made so far. Ferromagnetic and metallic behavior is observed in oxygen deficient $EuTiO_3$ ($EuTiO_{3-\delta}$) thin film[62] as well as hydride substituted $EuTiO_3$ ($EuTiO_{3-x}H_x$)[63]. In case of Ti site substitution, $EuTi_{1-x}M_xO_3$ (M = Nb^{4+},[64] Al^{3+}, Ga^{3+}[65] and Cr^{3+}[66]) show FM interaction beyond a certain x value, whereas an AFM interaction is observed in $EuTi_{1-x}Zr_xO_3$ ($0.0 < x < 1.0$)[64]. For $EuTi_{1-x}Al_xO_3$ and $EuTi_{1-x}Ga_xO_3$, the Eu^{2+}/Eu^{3+} mixed valence state is suggested to contribute to the emergence of the FM behavior. However, the itinerant electrons introduced by Nb^{4+} ($4d^1$) doping are suggested to be responsible for FM interaction and metallic behavior in $EuTi_{1-x}Nb_xO_3$.[64, 67] The effect of chemical substitution at Eu-site

S. No.	Material	Magnetic property	T_N (K)	T_C (K)	Electrical property	Ref.
1.	$EuTiO_3$	AFM	5.5		Insulator	[42]
2.	$EuZrO_3$	AFM	4.1		Insulator	[68]
3.	$EuHfO_3$	AFM	3.9		Insulator	[69]
4.	$EuTiO_{3-\delta}$*	FM		~ 6	Metal	[62]
5.	$EuTiO_{2.93}H_{0.07}$	FM		12	Metal	[63]
6.	$EuTi_{0.5}Nd_{0.5}TiO_3$	FM		6	Metal	[64]
7.	$EuTi_{0.9}Al_{0.1}TiO_3$	FM		4	-	[65]
8.	$EuTi_{0.9}Ga_{0.1}O_3$	FM		4	-	[65]
9.	$EuTi_{0.9}Cr_{0.1}O3$	FM		9.7	-	[66]
10.	$Eu_{0.9}La_{0.1}TiO_3$	FM		8	Metal	[70]
11.	$Eu_{0.5}Gd_{0.5}TiO_3$	FM		~ 4	Metal	[70]
12.	$Eu_{0.5}Dy_{0.5}TiO_3$	FM		~ 12	Metal	[71]
13.	$Eu_{0.5}Sr_{0.5}TiO_3$	AFM	3.5		Insulator	[72]
14.	$Eu_{0.5}Ba_{0.5}TiO_3$	AFM	1.9		Insulator	[73]

Table 1.1 List of Eu^{2+}-based perovskite oxides with their magnetic and electrical properties. T_N and T_C are the AFM and FM transition temperatures, respectively.

*** $EuTiO_{3-\delta}$ with charge carrier concentration $n > 1.5 \times 10^{-19} cm^{-3}$ shows FM and metallic behavior.**

of $EuTiO_3$ is impressive, as Eu:$4f^7$ spins are diluted. In case of isovalent substitution, e.g. $Eu_{1-x}Sr_xTiO_3$[72], $Eu_{1-x}Ca_xTiO_3$ [74] and $Eu_{1-x}Ba_xTiO_3$[75], the ground state remains AFM until high doping level ($x \leq 0.5$) and T_N decreases with increasing x. On the other hand, the effect of trivalent rare earth doping is quite contrastive. The substitution of La^{3+} or Gd^{3+} for Eu^{2+} dopes electrons into t_{2g} orbitals of Ti-3d band and renders the samples ferromagnetic and metallic. Katsufuji and Takura[70] reported FM interaction in $Eu_{0.9}La_{0.1}TiO_3$ and $Eu_{0.5}Gd_{0.5}TiO_3$ at T_C = 8 K and 4 K, respectively. We listed the magnetic and electrical properties of Eu^{2+}-based perovskite oxides with magnetic transition temperatures in Table 1.1.

1.4 Magnetocaloric effect

The magnetocaloric effect (MCE) is described as the reversible temperature change (ΔT_{ad}) of a material during magnetization and demagnetization in adiabatic conditions or the reversible change in magnetic entropy (ΔS_m) when the field change takes place in an isothermal condition. MCE is one of the most exciting phenomena of magnetic materials and has potential applications in solid-state refrigeration technology. Debye and Giauque independently proposed to use reversible temperature change in paramagnetic salts to obtain low temperature by adiabatic demagnetization. In 1933, Giauque and MacDougall[76] constructed a magnetic refrigerator and achieved a temperature of 250 mK using gadolinium salt $Gd_2(SO_4)_3.8H_2O$. Magnetic refrigeration was the first method developed for cooling below liquid helium. Researchers used paramagnetic salts such as ferric ammonium alum, chromic potassium alum and cerous magnesium nitrate to achieve cryogenic temperature. In recent years, ferromagnetic materials such as Gd[77], $Gd_5(Si_xGe_{1-x})$[10], $LaFe_{1-x}Si_x$[78], $MnFe_{1-x}P_xAs$[79], Ni based Heusler alloys[80] and Mn-based oxides[81] have received much attention for magnetic cooling near room temperature. There is also growing interest to find new cheap and efficient materials that can be useful for magnetic refrigeration to cover the temperature interval between the boiling points of liquid nitrogen (T_b = 77 K) and Helium-3 (T_b= 3.19 K) or Helium-4 (T_b = 4.23 K).

High interest in hydrogen as a clean fuel for the future demands production, storage and transportation of hydrogen in liquid form, which, in turn, requires cooling hydrogen gas below 20.3 K.[82] Rare earth alloys ($Er_{1-x}Dy_xAl_2$, $(Dy,Gd)Ni_2$) and intermetallic alloys are considered to be promising materials for magnetic refrigeration for T = 20 -80 K.[83, 84] Nevertheless, decomposition of $ErAl_2$ due to hydrogenation posses problems that need to be solved.[85] Gadolinium Gallium garnet (GGG, $Gd_5Ga_3O_{12}$) and its derivatives have excellent magnetocaloric properties for magnetic refrigeration between 2 K and 20 K.[86] ABO_3

oxides of perovskite structure possessing transition metal ion (B) and rare earth or alkaline earth ion (A) are usually chemically stable at cryogenic temperatures in inert atmosphere. They are easy to synthesize and cheaper than intermetallic alloys. If they are also stable under hydrogen atmosphere, they could be exploited for magnetic refrigeration. Rare earth titanates ($RTiO_3$, R= Gd, Ho, Dy etc.)[87-89] that undergo second-order phase transitions exhibit significant magnetocaloric properties.

The magnetocaloric effect directly depends on the magnitude of the magnetic entropy change of the material. Figure 1.23 shows the schematic diagram of the whole cyclic process of adiabatic demagnetization in typical ferromagnetic material during magnetic refrigeration. The magnetic refrigeration cycle is analogous to the Carnot cycle where the magnetic field is applied and removed instead of pressure. Initially, all spins of the magnetic material are randomly oriented under zero magnetic field at a given temperature *T*. When the magnetic field (*H*) is applied in adiabatic condition, the spins align in the field direction. Therefore, the

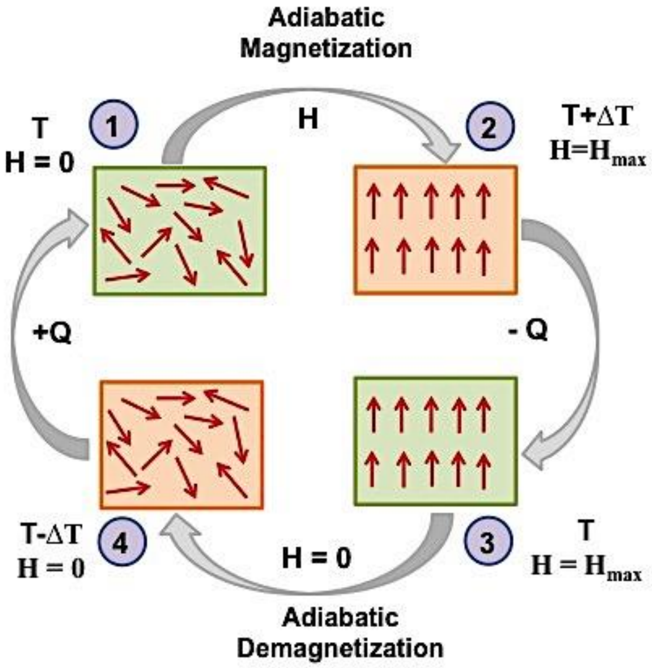

Figure 1.23 Schematic of adiabatic demagnetization of a magnetic material.

magnetic entropy of the material decreases and causes an increase in the lattice and electronic entropy, since the total entropy change in adiabatic process is zero. The temperature of the material increases from T to $T + \Delta T$. The added heat is removed (-Q) through the gas or fluid bringing it backs to the temperature T under the magnetic field H. When the magnetic field is removed (demagnetization) in adiabatic conditions, the magnetic spin system returns to its original alignment by capturing energy from the lattice. Therefore, temperature of the material decreases by an amount ΔT. Finally; the magnetic material with temperature $T - \Delta T$ is placed in the thermal contact with the environment to be refrigerated. The heat transfers (+Q) from the refrigerated environment to the working material. Thus, the decrease in the temperature of the magnetic material helps to remove heat from the load (refrigerator).

1.4.1 Thermodynamics of the MCE

Considering two joint principles of thermodynamics on a ferromagnetic sample under a magnetic field and the sample as a thermodynamic system, the internal energy (U) of the system can be represented as a function of the entropy (S), the volume (V) and the magnetization (M):

$$dU = TdS - pdV - HdM \tag{1.8}$$

where p, T and H are the pressure, temperature and magnetic field, respectively.

The free energy (F) is defined as:

$$F = U - TS \tag{1.9}$$

and its total differential form is

$$dF = dU - TdS - SdT \tag{1.10}$$

or

$$dF = -SdT - pdV - MdH \tag{1.11}$$

The Gibbs free energy (*G*) is a function of *T*, *p* and *H* and is used for the system under constant pressure. *G* is defined as

$$G = U - TS + pV - MH \tag{1.12}$$

the differential form is

$$dG = Vdp - SdT - MdH \tag{1.13}$$

For the Gibbs free energy, the internal parameters *S*, *p* and *M* conjugated to the external variables can be determined by following equations

$$S(T, H, p) = -\left(\frac{\partial G}{\partial T}\right)_{H,p} \tag{1.14}$$

$$M(T, H, p) = -\left(\frac{\partial G}{\partial H}\right)_{T,p} \tag{1.15}$$

$$V(T, H, p) = -\left(\frac{\partial G}{\partial p}\right)_{T,H} \tag{1.16}$$

Using Eqs. (1.14) and (1.15), one can obtain so-called Maxwell equation

$$\left(\frac{\partial S}{\partial H}\right)_{T,p} = \left(\frac{\partial M}{\partial T}\right)_{H,p} \tag{1.17}$$

The heat capacity at constant parameter y is defined as

$$C_y = \left(\frac{dQ}{dT}\right)_y \tag{1.18}$$

where dQ is the required heat quantity for changing the system temperature dT. From the second law of thermodynamics

$$dS = \frac{dQ}{T} \tag{1.19}$$

Using Eqs. (1.18) and (1.19), the heat capacity as a function of entropy is

$$C_y = T\left(\frac{dS}{dT}\right)_y \tag{1.20}$$

The total entropy change of the system can be represented as

$$dS = \left(\frac{\partial S}{\partial T}\right)_H dT + \left(\frac{\partial S}{\partial H}\right)_T dH \tag{1.21}$$

Introducing Eqs. (1.17) and (1.20) into Eq. (1.21), the entropy is expressed as

$$dS = \left(\frac{C_p}{T}\right) dT + \left(\frac{\partial M}{\partial T}\right) dH \tag{1.22}$$

When the sample undergoes in an adiabatic process of magnetization, $dS = 0$ and the reversible change in temperature (ΔT_{ad}) is given as

$$\Delta T_{ad} = -\int_0^H \left(\frac{T}{C_p}\right)\left(\frac{\partial M}{\partial T}\right)_H dH \tag{1.23}$$

The magnetic entropy S_m of a paramagnet is given as[90]

$$S_m(T,H) = Nk_B\left[\ln(2J+1) - \frac{1}{2}\frac{C_J H^2}{T^2}\right] \tag{1.24}$$

Where C_J is the Curie constant. The S_m of a ferromagnet above the Curie temperature T_C is

$$S_m(T,H) = Nk_B\left[\ln(2J+1) - \frac{1}{2}\frac{C_J H^2}{(T-T_C)^2}\right] \tag{1.25}$$

The magnetic entropy reaches at maximum in a completely disordered state, which could be realized for conditions $T \to \infty$ and $H = 0$. The maximum magnetic entropy value per mole of magnetic atoms is

$$S_m(T, H) = Nk_B \ln(2J + 1) = R \ln(2J + 1) \tag{1.26}$$

where J is the quantum number of the total angular momentum of an atom and R (= Nk_B) is the gas constant.

1.4.2 Methods to estimate the MCE

There are two ways to estimate the magnetocaloric effect experimentally.

(i) Direct Method

The change in the adiabatic temperature (ΔT_{ad}) of a magnetic material can be measured directly during application and removal of magnetic field under adiabatic conditions. Thermocouple is used to measure the ΔT_{ad} of the sample in different modes. These measurements are very complicated and errors in measurement are very common. The measurement error mainly depends on the thermal contact between the sample and thermocouple. Measurements need to be carried out under adiabatic conditions. The measurements are more time consuming and difficult to perform with materials of low thermal conductivity. The quality of the results can be improved using pulse magnetic field where the magnetic field varies promptly.

(ii) Indirect method

To estimate the MCE, the indirect method is considered more accurate and used extensively. In this method, the isothermal magnetic entropy change (ΔS_m) and adiabatic temperature change (ΔT_{ad}) are calculated from the heat capacity measured with and without magnetic field or from the isothermal field dependent magnetization using the thermodynamic Maxwell's equations.

The temperature dependence of magnetic entropy can be obtained from the experimental heat capacity (C_p) after subtracting the lattice contribution. The magnetic entropy S_m can be calculated using the equation

$$S_m(T) = \int_0^T \frac{C_p(T)}{T} dT \tag{1.27}$$

If S_m is known for $\mu_0 H = 0$ T and $\mu_0 H > 0$T, the ΔS_m and ΔT_ad can be calculated. The principle of the calculation of ΔS_m and ΔT_ad can be understood from the Fig. 1.24 (a).

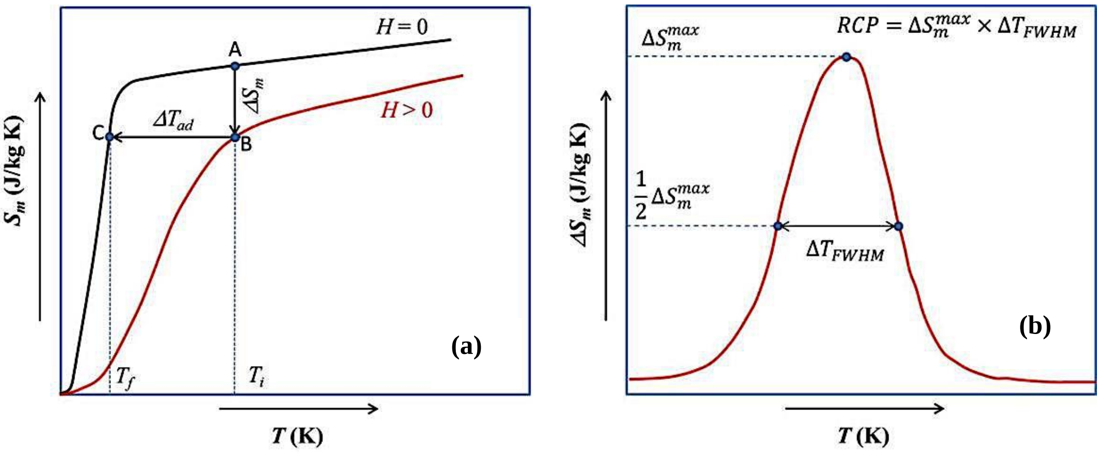

Figure 1.24 Schematic for the calculation of (a) magnetic entropy change and adiabatic temperature change, and (b) relative cooling power.

Initially, the system is in state A (T_i, $H = 0$) at temperature T_i and field $H = 0$. If the magnetic field is applied in isothermal condition, the system goes to state B ($\mathrm{T_i}$, $H > 0$) with magnetic entropy change $\Delta S_m = S_m(\mathrm{H}) - S_m(0)$ as depicted by a vertical arrow in Fig. 1.24 (a). The adiabatic demagnetization (removal of the magnetic field from $H > 0$T to $H = 0$ T) takes the system from the state B (T_i, $H > 0$) to C (T_f, $H = 0$T) with the temperature change $\Delta T_\mathrm{ad} = T_i - T_f$ as showed by a horizontal arrow in Fig. 1.24 (a).

The magnetic entropy change can also be evaluated from the magnetization isotherms. According to thermodynamic Maxwell's relation

$$\left(\frac{\partial S_m(T,H)}{\partial H}\right)_T = \left(\frac{\partial M(T,H)}{\partial T}\right)_H \tag{1.28}$$

After integrating Eq. (2) for an isothermal process, we obtain

$$\Delta S_m(T,H) = \int_{H_1}^{H_2} \left(\frac{\partial M(T,H)}{\partial T}\right)_H dH \tag{1.29}$$

where H_1 and H_2 are the applied fields and $H_2 > H_1$.

Eq. (1.29) can be simplified by the conversion of integration into summation when the isothermal of magnetization are measured at very close temperature interval. Therefore, the Eq. (1.29) can be written as

$$|\Delta S_m(T,H)| = \sum_i \frac{M_{i+1} - M_i}{T_{i+1} - T_i} \Delta H_i \tag{1.30}$$

where M_i and M_{i+1} are the magnetization measured with a field H_i at T_i and T_{i+1} temperatures, respectively .

To achieve giant MCE, ΔS_m and ΔT_{ad} should be large. Since ΔS_m is directly proportional to $\left(\frac{\partial M}{\partial T}\right)$, a large change in the magnetization of the materials with respect to temperature gives rise to a large ΔS_m and ΔT_{ad}. Except ΔS_m and ΔT_{ad}, the relative cooling power (*RCP*) is also an important physical parameter that has been used to characterize the MCE properties of the materials. *RCP* is an important practical quantity that determines heat transfer between the hot and cold ends separated by the temperature difference ΔT_{FWHM}. *RCP* can be estimated from the temperature dependent ΔS_m curves as shown in Fig. 1.24 (b). It is defined as

$$RCP = \Delta S_m^{max} \times \Delta T_{FWHM} \tag{1.31}$$

where $\Delta S_m^{max}$is the maximum value of magnetic entropy change.

1.4.3 Types of MCE

The MCE is more pronounced in the vicinity of magnetic ordering temperature (ferromagnetic or antiferromagnetic transition) where the spin entropy decreases by application of the magnetic field and increases by removal of the field. The MCE are classified into two categories: one is normal MCE and another inverse MCE.

(i) Normal magnetocaloric effect (NMCE): The temperature of the magnetic material decreases with adiabatic demagnetization, where the magnetic entropy decreases with applied magnetic field *i.e.* $\Delta S_m = S_m(\mathrm{H}) - S_m(0)$ shows a negative sign. Generally, the NMCE has been found in the materials, which show the ferromagnetic or antiferromagnetic ordering.

(ii) Inverse magnetocaloric effect (IMCE): The temperature of the material decreases with adiabatic magnetization and ΔS_m increases with application of magnetic field in isothermal condition *i.e.* $\Delta S_m = S_m(H) - S_m(0)$ shows a positive sign.

1.5 Colossal magnetoresistance

The magnetoresistance (*MR*) is the property of a material where the electrical resistivity changes upon application of an external magnetic field. First time, William Thomson discovered the ordinary *MR* in the pieces of iron and nickel.[91] The main application of *MR* is the magnetic field sensors, which are used to read the data in hard disk drivers and another devices. Generally, it is defined as

$$MR(\%) = \frac{\rho(H) - \rho(H = 0)}{\rho(H = 0)} \times 100 \tag{1.32}$$

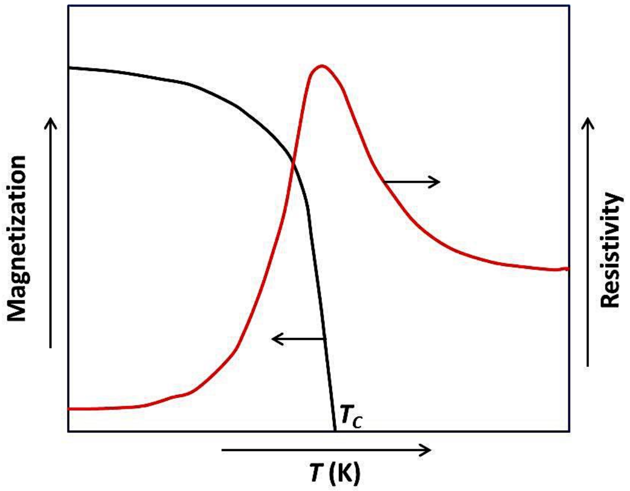

Figure 1.25 Representation of magnetic phase transition and insulator metal transition from temperature dependence of magnetization (left y-axis) and resistivity (right y-axis), respectively.

The colossal *MR* is the large change in the electrical resistance of a material in presence of magnetic field. The term colossal was used to make distinction with giant magnetoresistance (GMR), which was found earlier in thin film structure composed of alternating ferromagnetic and non-magnetic conductive layers.[92] A. Fert and P. Grunberg received the 2007 Nobel Prize in physics for the discovery of GMR. First time, the negative magnetoresistance was observed in bulk ferromagnetic semiconductor $Eu_{1-x}Gd_xSe$ by S. Von Molnar and Methfessel in 1967.[93] Later, colossal *MR* was studied extensively in manganese-based perovskite oxides. The large negative magnetoresistance in these materials is associated with ferromagnetic (FM) ordering accompanied by insulator-metal (I-M) transition as shown in Fig. 1.25. The large negative *MR* is observed in the family of doped perovskite manganites with chemical formula $R_{1-x}A_xMnO_3$, where R = (La, Pr, Sm…) trivalent rare earth ions and A = (Ca, Ba, Sr…) are divalent alkaline-earth ions. The colossal MR (– 60 %) was reported in ferromagnetic $La_{2/3}Ba_{1/3}MnO_x$ thin film at room temperature.[94] Later, Jin *et. al*. reported maximum value of the *MR* (~100000 %) in $La_{0.67}Ca_{0.33}MnO_x$ thin film near 77 K under the magnetic field of 6T.[95]

1.5.1 Colossal magnetoresistance in Eu^{2+} based materials

Among Eu^{2+} based compounds, Europium monochalcogenides (EuX, X = O, S, Se and Te) have attracted special attention in 20th century because of their wide verity of electronic and magnetic properties. EuX crystallize in cubic rock-salt structure and the lattice parameters increases from 5.141 Å (EuO) to 6.598 Å (EuTe). These compounds are model systems for Heisenberg magnet with spin ordering dominated by indirect nearest neighbor interaction (J_1) and next-nearest-neighbor interaction (J_2) between the localized magnetic moment of the Eu^{2+}:$4f^7$ ($S = 7/2$). Depending on the sign and magnitudes of J_1 and J_2, EuX exhibit different magnetic ground states. While EuO and EuS are ferromagnetic in the ground state with T_C = 69 K[96] and 16 K[97], respectively, EuTe is antiferromagnetic below T_N = 9.7 K[98] and EuSe is a metamagnetic with T_N = 4.6 K[99]. EuX are magnetic semiconductors and the experimental electronic energy band gaps are 1.12, 1.65, 1.80 and 2.0 eV in EuO, EuS, EuSe and EuTe, respectively at room temperature.[100] The schematic of the band structures of EuX is displayed in Fig. 1.26. The valence band is composed of

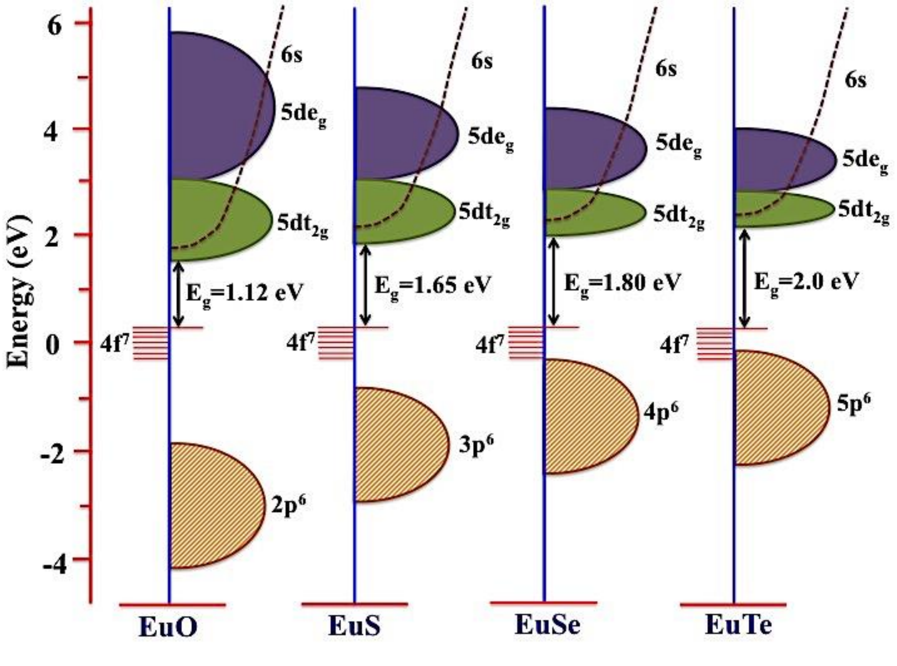

Figure 1.26 Schematic of the electronic band structure of EuO, EuS, EuSe and EuTe. The values of energy band gap are taken from Ref. [100].

oxygen-p filled orbital and the conduction band consists of Eu-5d and 6s orbitals. The Eu:$4f^7$ level lies within the forbidden band gap. The 5d and 6s electrons are considered to be itinerant and the4f electrons are localized. The $4f^7$ level shifts downward with increasing atomic number of X ion in EuX and it overlaps with the $5p^6$ valance band in case of EuTe. The band gap between 4f and the bottom of conduction band increases with increasing mass of X ion in EuX.

While EuO is a ferromagnetic semiconductor, oxygen deficient and Eu-rich EuO becomes metallic below T_C and the I-M transition is very impressive, *i.e.* the resistivity drops nearly 8 orders of magnitude.[101],[102] Moreover, an applied magnetic field shifts the I-M transition temperature towards higher temperature, resulting in colossal *MR* with decrease in resistivity of up to 6 orders of magnitude.[102] Several mechanisms such as formation of bound magnetic polaron, conduction band splitting, have been proposed to explain the origin of I-M transition and colossal *MR* in EuO.[102-105] It was found that electron doping in EuO arises 100 % polarization of the conduction electrons, and the material has a colossal MR

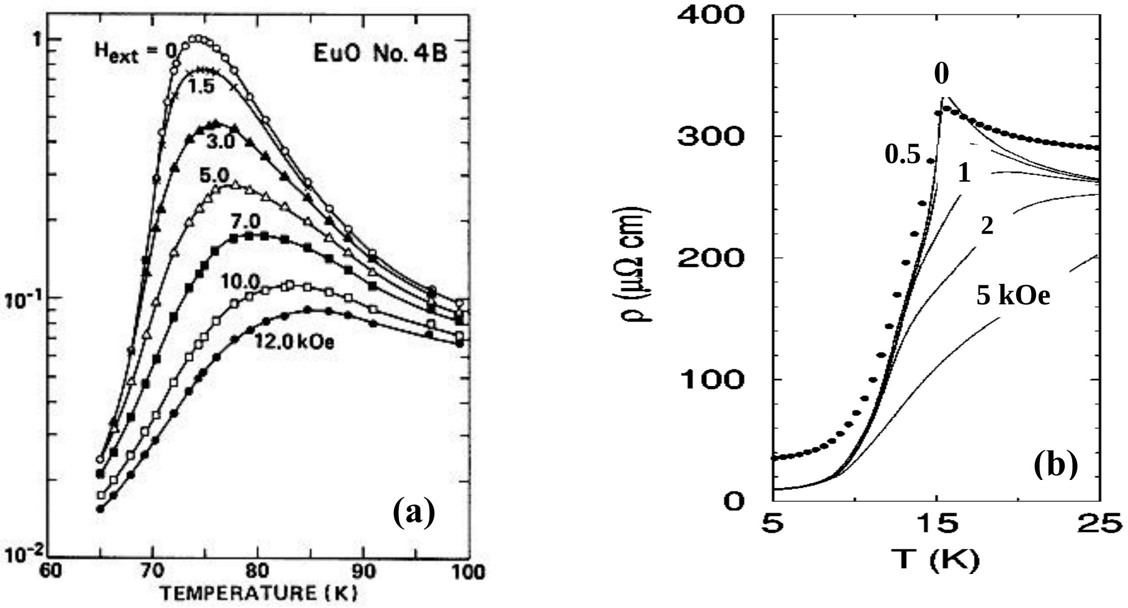

Figure 1.27 Temperature dependence of resistivity under various magnetic fields for (a) EuO and (b) EuB_6. Figures are from Refs. [102] and [106].

effect stronger than well-known manganites.[107] Unlike EuO, n-type EuSe and EuTe exhibit positive *MR*, which was explained by the effect of spin-splitting of the conduction band on nonmagnetic scattering.[108, 109] A large magnetoresistance and I-M transition in Gd doped EuSe was attributed to a hopping mechanism and a trapping of electrons in polarized spin clusters, in which an applied magnetic field decreases the spin disorder and allows more hopping.[93]

Europium hexaboride (EuB_6), in which Eu ions are divalent, is a ferromagnetic semimetal with T_C ~ 13 K.[110, 111]. Sullow *et. al*.[106] found that EuB_6 shows colossal *MR*, which is not associated with its T_C but with a second phase transition at T_m = 15.5 K. The I-M transition in EuB_6 at T_m was suggested due to the percolation of magnetic polarons. $Eu_{14}MnBi_{11}$ having antiferromagnetic ordering below T_N = 32 K also shows colossal negative *MR* (–67 % at T = 20 K and $\mu_0 H$ = 5T).[112] In this material, the colossal *MR* was suggested due to ferromagnetic spin fluctuations, a conclusion which is consistent with the relatively strong ferromagnetic Mn-Mn exchange.

1.5.2 Proposed mechanism for magnetoresistance

Several mechanisms have been proposed to explain the I-M transition and colossal magnetoresistance in europium monochalcogenides and other magnetoresistive materials. Here, we throw a light on few of them.

1.5.2.1 Formation of magnetic polaron

In magnetic semiconductors, charge carriers are coupled with localized spins of magnetic ions by a strong exchange interaction. If the magnetic exchange interaction between the carriers and localized spins is larger than that between the localized spins themselves, the carrier tend to align the localized spins to its own spin within the spatial extent of its wavefunction. The resulting cloud of polarized spins can be considered as a magnetic

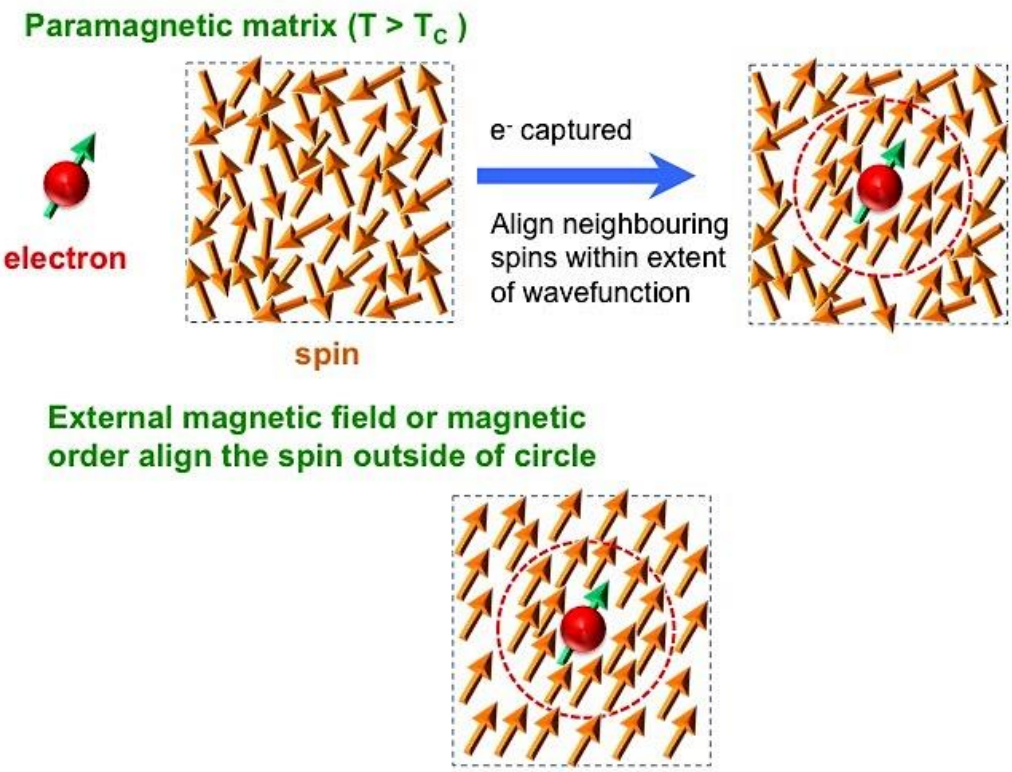

Figure 1.28 Schematic of polaron formation in paramagnetic and ferromagnetic region.

molecule and this spin-organized system is called magnetic polaron. A simple schematic of the formation of magnetic polaron is displayed in Fig. 1.28. In paramagnetic region ($T > T_C$), the free energy of magnetic polaron inside of the disordered lattice produces a localized state. If this state is isolated, the charge transport can only occur by hopping from one site to another site. When a material goes through ferromagnetic ordering temperature or an external magnetic field is applied, the disordered spins become ordered and size of magnetic polarons increases. The magnetic binding energy of polaron disappears and the carriers are able to move through lattice diffusively resulting as a drop in resistivity. Hence, the formation and percolation of magnetic polarons is one of the possible origins of magnetically driven I-M transition.

Torrance *et. al.*[103] predicted the I-M transition in EuO using the concept of bound magnetic polaron. In nonstoichiometric EuO, small numbers of electrons are excited to the conduction band. These electrons essentially move over the Eu ions and couple with the 4f electrons on the same ion through s-f exchange interaction. The interaction energy is of the order of 0.1 eV. Because of the s-f interaction, the spins of 4f electrons near the conduction electrons tend to order even in the paramagnetic state. These conduction electrons are then trapped in an exchange potential set up by the aligned 4f spins and form magnetic polaron. C. S. Snow *et al.*[113] provided direct spectroscopic evidence that the I-M transition in EuO as and EuB_6 are preceded by the formation of magnetic polarons. Recently, Storchak *et. al.*[114] also confirmed the formation of magnetic polaron at room temperature in EuX (X= O, S, Se and Te) thin films using low-energy muon spin relaxation and magnetization measurements techniques. The origin of colossal *MR* in the manganite compound $La_{2/3}Ca_{2/3}MnO_3$ has also been attributed to the presence of magnetic polarons.[115] Teresa *et. al.*[115] performed volume thermal expansion, magnetic susceptibility and small angle neutron scattering measurements for $La_{2/3}Ca_{2/3}MnO_3$ and revealed the evidence for the existence of magnetic polaron in paramagnetic regime. The localized magnetic clusters of size ~ 12 Å were detected above T_C, which grow in size and decrease in number on application of magnetic field. Unlike in EuO, magnetic polaron in manganites also produce local lattice distortion.

1.5.2.2 Spin-disorder scattering

While the resistivity in nonmagnetic materials is due to the scattering of charge carriers by impurities or phonons, in magnetic materials it could be due to the scattering of charge carriers by spin disorder. De Gennes and Friedel[116] theoretically predicted the anomaly in resistivity around magnetic ordering temperature through spin disorder scattering. It was noticed that the atomic spins are random at high temperature and the conduction electrons have a finite mean free path. At low temperature (near magnetic phase transition), the atomic spins are aligned and no scattering can occur, resulting a decrease in resistivity. In 1968, C. Haas[117] explored the spin disorder scattering effect considering the exchange interaction between free charge carriers and localized magnetic moment and calculated *MR* of a ferromagnetic semiconductor. The *MR* of a ferromagnetic semiconductor due to a change of the mobility and a constant carrier concentration was given as

$$\frac{\rho(H)}{\rho(0)}=\frac{\chi(H)}{\chi(0)} \tag{1.33}$$

where $\rho(H)$ and $\rho(0)$ are the resistivity with and without magnetic field, respectively. $\chi(H)$ and $\chi(0)$ are the susceptibility with and without magnetic field, respectively.

Using Born approximation in scattering theory, Majumdar and Littlewood[118] derived a similar relation between resistivity and magnetic susceptibility, which is given as

$$\frac{\rho(H)-\rho(0)}{\rho(0)}=\frac{\Delta\rho}{\rho(0)}\approx 1-\frac{\chi(2k_F,T,H)}{\chi(2k_F,T,0)} \tag{1.34}$$

where k_F is the Fermi momentum and $k_F = (3\pi^2 n)^{1/3}$, n is the density of electron gas.

Using Ginzburg-Landau approximation, the low field magnetic susceptibility is

$$\chi^{-1}(q,T,H)\propto A(T)+(q\xi_0)^2+\left(\frac{m(H)}{m_{sat}}\right)^2 \tag{1.35}$$

where $A(T)$ is zero and the correlation length $\xi(T)=\xi_0/A(T)^{1/2}$ diverges at $T = T_C$. m_{sat} is the saturation magnetization .

Using Eq. (1.34) and (1.35), the magnetoresistance at low field was given as

$$\frac{\Delta\rho}{\rho(0)}=C\left(\frac{m(H)}{m_{sat}}\right)^2\approx\left(\frac{1}{2k_F\xi_0}\right)^2\left(\frac{m}{m_{sat}}\right)^2 \tag{1.36}$$

However, this relation was first calculated by Kubo and Ohata[119] using the Drude formula with the quasiparticle lifetime estimated from the thermal spin fluctuations. Majumdar and Littlewood[118] predicted a relation between scaling constant *C* and charge carrier density *n*. According to their theory,

$$C \propto n^{-2/3} \tag{1.37}$$

Therefore, the coupling coefficient *C* decreases with increasing charge carrier concentration *n*. It has been shown that a large number of systems including manganites, manganese pyrochlore and magnetically doped semiconductors follow this relation.[118] For manganites ($La_{1-x}Sr_xMnO_3$), the experimental values of scaling constant *C* are in the range of 0.5 – 5[4], while it is large as 75 for EuB_6 [106] and 15 for pyrochlore $Ti_2Mn_2O_7$[120]. While Eq. (1.36) is consistent with the qualitative features of negative MR at low fields, the quantitative disagreement exist with the calculations based on the second-order perturbation expansion of the exchange Hamiltonian. Khosla and Fischer[121] proposed a modified theory in which the higher order perturbation terms were included. The negative magnetoresistance is then given by an empirical expression

$$\frac{\Delta\rho}{\rho(0)} = a^2 \ln(1 + b^2 H^2) \tag{1.38}$$

where *a* and *b* are the physical characteristics of the exchange interaction and *H* is the applied magnetic field. The parameters *a* and *b* are given as

$$a = A_1 J D(\varepsilon_F)[S(S+1) + \langle M \rangle^2] \tag{1.39}$$

and

$$b^2 = \left[1 + 4S^2\pi^2 \left(\frac{2JD(\varepsilon_F)}{g}\right)^4\right] \left(\frac{g\mu_B}{\alpha k_B T}\right)^2 \tag{1.40}$$

where J is exchange interaction energy, $D(\varepsilon_F)$ the density of states at the Fermi level, S the spin of localized magnetic moment, g Lande factor and $\langle M\rangle$ the average magnetization. α is a numerical constant lies between 0.1 and 10.

Eq. (1.38) has been used to explain the negative magnetoresistance originated from the spin dependent scattering of charge carriers with localized magnetic moments in various magnetic semiconductors such as CdS[121], InMnAs[122] and InMnSb[123].

1.5.2.3 Spin splitting of conduction band

Using perturbation theory, C. Haas[117] predicted that the exchange interaction between charge carriers and localized magnetic moment in magnetic semiconductors causes a splitting of conduction band into two subbands for spin parallel and antiparallel to the magnetization. For ferromagnetic semiconductors, the splitting occurs below T_C when no external magnetic field is applied. However, in case of applied magnetic field, band splits above T_C. For antiferromagnetic semiconductors, band splitting occurs only in an applied magnetic field. The conduction band splitting influences the electrical resistivity of magnetic

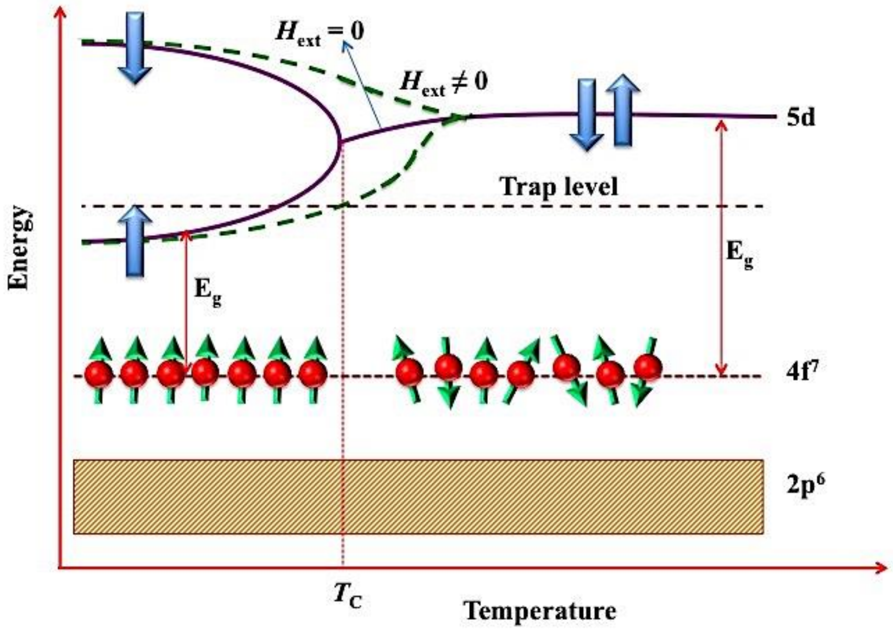

Figure 1.29 Splitting of Conduction band (Eu-5d) in EuO.

semiconductors around magnetic phase transition temperature. When the band splitting is large than k_BT, the origin of the MR above and below T_C is different. For $T < T_C$, the number of charge carriers in the lower subband increases because of large separation between the subbands. With an application of magnetic field, the spin flip scattering decreases and the mobility of these carrier increases, leading to a lower resistivity. For $T > T_C$, the charge carriers are present in both subbands. The mobilities of the charge carriers are different and depend on the magnetic field.

Oliver *et. al*.[101] studied electrical and optical properties of EuO and observed a red shift (shift in optical absorption edge to longer wavelength with decreasing temperature and increasing magnetic field). Shapira *et. al*.[102] performed resistivity and Hall effect experiments for various samples of EuO and proposed a model for IMT. It was assumed that the oxygen vacancies in nonstoichiometric EuO form a defect level (trap level) below the conduction band edge and the IMT is due to the presence of electron traps. Steeneken *et al*.[107] reported large changes in the electronic band structure across T_C in EuO thin film using spin-resolved X-ray absorption spectroscopy. These changes are caused by large exchange splitting of conduction band (~0.6 eV) in the ferromagnetic state. It was attributed that the band splitting is due to direct exchange interaction between the localized Eu-4f moments and the delocalized 5d-6s conduction band states. The bottom of the conduction band consists mainly of majority spins, i.e., doped charge carries are practically fully spin polarized. Further, these measurements suggested that the red shift of the optical edge was due to spin-splitting of the conduction band rather than to a broadening of the conduction band. The schematic spin splitting of conduction band in EuO is displayed in Fig. 1.29. The I-M transition was explained as follows: above T_C, defect or impurity states have their energy levels located just below the bottom of the conduction band and the material behaves like a semiconductor, i.e., the resistivity increasing with decreasing temperature as a result of thermal activation of carriers from the impurity states to the conduction band. Below T_C, the conduction band splits due to the exchange interactions, and the defect states now fall into the conduction band. The electrons of these defects can now propagate in the spin-polarized bottom of the conduction band without any activation energy, and the system behaves like a metal.

In case of diluted magnetic semiconductors, hybridization of p and d bands or s and d bands gives rise to band splitting under the application of magnetic field due to giant Zeeman effect. These two bands consist of spin-polarized carriers with different conductivity and mobility. A two-band model was proposed to explain the magnetoresistance in magnetic semiconductors due to spin splitting.[121, 124] According to the two-band model, the positive *MR* is given as

$$MR = \frac{c^2H^2}{(1 + d^2H^2)} \tag{1.41}$$

where c and d are related to the conductivity and mobility of carriers in the two spin-split bands and are given as

$$c^2 = \frac{\sigma_1\sigma_2(\mu_1 + \mu_2)^2}{(\sigma_1 + \sigma_2)^2} \tag{1.42}$$

and

$$d^2 = \frac{(\sigma_1\mu_2 - \sigma_2\mu_1)^2}{(\sigma_1 + \sigma_2)^2} \tag{1.43}$$

where σ_1 (σ_2) and μ_1(μ_2) are the conductivity and mobility of the majority spin (minority spin) carriers in two band, respectively.

The occurrence of positive magnetoresistance in diluted magnetic semiconductors InMnAs[122], GaMnAs[125], ZnMnO[126] and InMnSb[123] has been suggested due to

Zeeman spin-splitting of the band states. However, the positive magnetoresistance in EuS and EuTe was explained by the effect of spin splitting of conduction band on nonmagnetic scattering.[109, 127, 128]

1.6 Multiferroics and magnetoelectrics

A ferroic is a material that possesses a spontaneous and switchable alignment: In ferroelectrics, the alignment of electric dipole moment switched by an electric field (*E*); in ferromagnetics, the electron spin alignment switched by a magnetic field (*H*); and in ferroelastics, strain alignment switched by a stress (σ). A multiferroic combines any two or more primary ferroic ordering in same phase (Fig. 1.30). However, current convention uses the term "multiferroic" to materials that exhibit ferroelectricity and ferromagnetism in single phase. Multiferroics hold great potential for applications as the magnetoelectric coupling allows switching of the ferroelectric state with a magnetic field or switching of magnetization

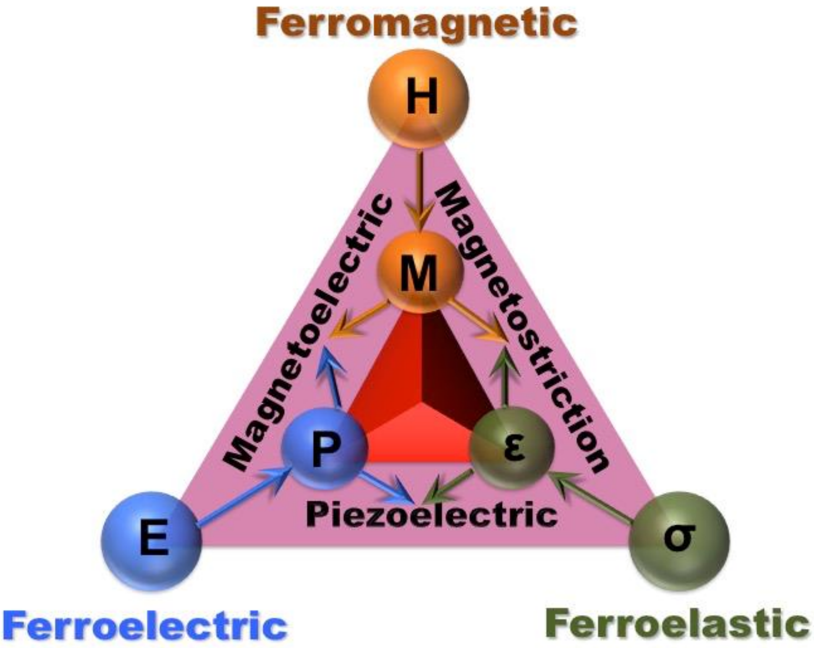

Figure 1.30 Phase control in ferroics and multiferroics. The electric field *E*, magnetic field *H* and stress σ control the electric polarization *P*, magnetization *M* and strain ε, respectively. In a multiferroic, the coexistence of at least two ferroic forms of ordering leads to additional interactions magnetoelectric, piezoelectric and magnetostrictive.

with electric field.[129-131] Multiferroics offer the possibility to combine the best qualities of ferroelectric random access memories (FeRAMs) and magnetic random access memories (MRAMs) i.e. fast low-power electrical write and non-destructive magnetic read operations.[132] Significantly, these materials could yield entirely new device paradigms, such as electric field controlled magnetic data storage.

The first ferromagnetic ferroelectric material to be discovered was nickel iodine boracite, $Ni_3B_7O_{13}I$.[133] Later, many more multiferroic boracite compounds with complex structure have been synthesized.[134, 135] The search for other ferromagnetic ferroelectrics began in Russia in 1950s with mixed pervoskites. However, multiferroism in ABO_3 type pervoskite oxides is scarce due to contradicting origins of ferroelectricity and ferromagnetism.[131, 136] While ferroelectricity in ABO_3 type perovskite oxides is favored by the presence of d^0 ion at the B-site and strong hybridization of $B(d^0)$-O(2p) orbitals, magnetic ordering requires B ion with partially filled d orbitals or A ion with partially filled f orbitals. Replacement of the d^0 B cation in ferroelectric perovskite oxides by magnetic d^n cations is considered an approach to synthesize multiferroics. Using this approach, the first synthetic ferromagnetic ferroelectric material, $(1-x)Pb(Fe_{2/3}W_{1/3})O_3$-$xPb(Mg_{1/2}W_{1/2})O_3$ was produced in the early 1960s.[137] However, the complex compounds $PbFe_{1/2}Nb_{1/2}O_3$ and $PbFe_{2/3}W_{1/3}O_3$ are ferroelectric antiferromagnets with Curie temperature 387 K and 178 K and with the Neel temperature at 143 K and 363 K, respectively.[138] Here, the Mg and W ions are diamagnetic and cause the ferroelectricity, whereas the Fe^{3+} (d^5) ion is responsible for the magnetic ordering. A number of other perovskite materials, such as $BiMnO_3$[139, 140], $YMnO_3$[11] and $BiFeO_3$[13, 141, 142], are also known to have ferroelectric and magnetic (mostly antiferromagnetic type) ordering.

Multiferroics having simultaneous ferroelectric and magnetic ordering, exhibit unusual physical properties such as magnetoelectric coupling (magnetoelectric effect). The magnetoelectric effect is the phenomenon of inducing electric polarization (magnetization) by applying an external magnetic field (electric field). This allows an electric field to control the magnetic properties of a material and a magnetic field to control the electric properties. However, magnetoelectric effect may exist in ferroelectric-paramagnet ($Tb_2(Mo_4)_3$)[143] or paraelectric-antiferromagnet ($EuTiO_3$)[14], i.e whatever the nature of magnetic and electrical order parameters. The materials, which show magnetoelectric effect, are called magnetoelectrics. Magnetoelectric effect can arise directly between the two order parameters or could be induced indirectly via strain. Fig. 1.31 shows the relationship between multiferroic and magnetoelectric materials. Ferromagnets (ferroelectrics) form a subset of magnetically (electrically) polarizable materials such as paramagnets and antiferromagnets (paraelectrics). The intersection of ferromagnets and ferroelectrics (red hatching region) represents materials that are multiferroic. Magnetoelectric coupling (small circle of red color) is an independent phenomenon that can arise in any materials, which are both magnetically and electrically polarizable.

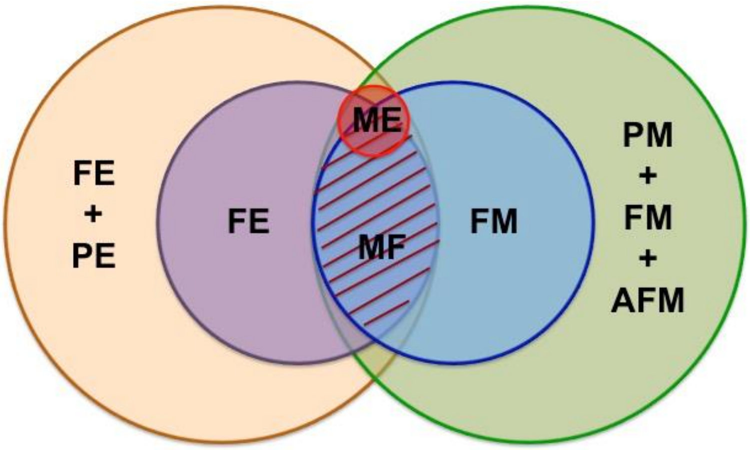

Figure 1.31 Relationship between multiferroics and magnetoelectrics. FE: ferroelectric, PE: paraelectric, FM: ferromagnet, AFM: antiferromagnet, PM: paramagnet, MF: multiferroic and ME: magnetoelectric.

1.6.1 Magnetodielectric effect

The coupling between magnetism and dielectric properties in magnetic insulator is called magnetodielectric effect, where magnetic ordering produces the anomalies in temperature dependent dielectric constant or low frequency dielectric constant is sensitive to an external magnetic field.

The magnetoelectric effect was first presumed to exist by Pierre Curie, and subsequently attracted a great deal of interest in the 1960s and 1970s. In 1957, the magnetoelectric effect was predicted to occur in rhombohedral antiferromagnet Cr_2O_3 [144] and then, it was experimentally observed below the Neel temperature (T_N = 307 K) in 1960.[145] However, magnetodielectric effect is also observed in the materials, which does not so any spontaneous polarization i.e. no ferroelectricity. Various mechanisms have been proposed to explain the origin of magnetodielectric effect.

1.6.2 Magnetodielectric effect with magnetoelectric Coupling

Magnetism is associated with spin degrees of freedom while the dielectric properties depends on the charge degree of freedom. However electron has both charge and spin, so there are number of mechanisms that gives rise to spin-charge coupling. The free energy (F) can be written in terms of magnetization (M), polarization (P) and electric field (E) as:

$$F = (1/2\varepsilon_0)P^2 - PE - \alpha PM + \beta PM^2 + \gamma P^2 M^2 \tag{1.44}$$

where ε_0 is the dielectric constant in vacuum and α, β, and γ are the coupling constants. Since P and M are the polar and axial vectors respectively, so αPM term will not be scalar and vanish from the free energy expression. The term βPM^2 is also forbidden by the symmetry in many cases. So only the term $\gamma P^2 M^2$ gives rise solely to the magnetodielectric effect. This expression is sufficient to understand the dielectric properties observed in many non-ferroelectric magnetodielectrics. Since the effective dielectric constant is the second derivative of free energy with respect to polarization, Therefore,

$$\varepsilon = (1/\varepsilon_0) + \gamma M^2 \tag{1.45}$$

Eq. (1.45) is suitable for investigating the magnetodielectric coupling in ferromagnetic systems, which develop a non zero M in the ordered phase, but this expression is not sufficient for describing the magnetodielectric coupling in antiferromagnetic systems, where M is zero in ordered phase. To discuss the magnetodielectric coupling in antiferromagnetic system, G. Lawes *et. al.*[146] proposed a model coupling the uniform polarization P to the q dependent magnetic correlation function $\langle M_q M_{-q}\rangle$, M_q is the magnetization at wave vector q. The lowest order free energy is

$$F = (1/2\varepsilon_0)P^2 - PE + P^2 \sum_q g(q)\langle M_q M_{-q}\rangle\,(T) \tag{1.46}$$

where $g(q)$ is the q-dependent coupling constant and $\langle M_q M_{-q}\rangle$ is the thermal average of the instantaneous spin-spin correlation, which obeys sum rule.

$$\sum_q \langle M_q M_{-q}\rangle = Ng^2\,\mu_B^2 S(S+1) \tag{1.47}$$

The dielectric constant is

$$\varepsilon = \frac{\varepsilon_0}{1 + 2\varepsilon_0 I(T)} \tag{1.48}$$

where $I(T) = \sum_q g(q)\langle M_q M_{-q}\rangle(T)$

One possible origin of magnetodielectric coupling is spin-phonon coupling. The dielectric response of insulators is determined by optical phonon frequencies, expressed by the Lyddane-Sachs-Teller relation, $\frac{\omega_L^2}{\omega_T^2} = \frac{\varepsilon_{st}}{\varepsilon_\infty}$, where ω_L and ω_T are the natural frequencies of longitudinal acoustic and transverse optical lattice vibration respectively. The lattice

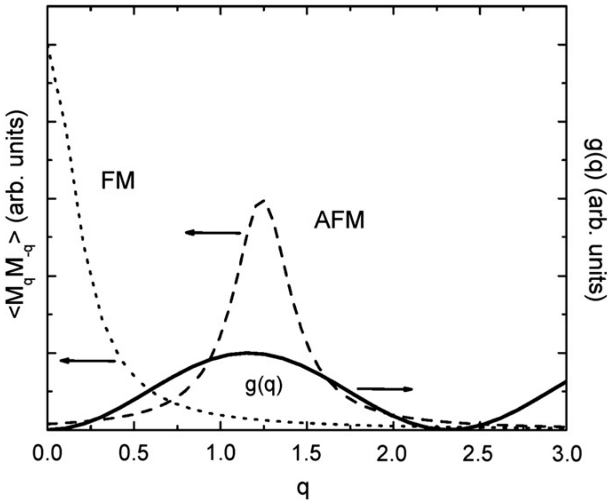

Figure 1.32 Schematic curves illustrating the magnetodielectric coupling constant g(q) (solid line), computed assuming spin-phonon coupling, together with the spin-spin correlation functions for ferromagnetic order (dotted line) and antiferromagnetic order (dashed line). Figure from Ref. [147].

distortions are normally insensitive to magnetic order. In a system with a strong spin-lattice coupling the development of the magnetic order shifts the optical phonon frequencies, which change the dielectric constant. The spin-phonon induced magnetodielectric coupling term is plotted for ferromagnetic and antiferromagnetic system in Fig. 1.32.

The shift in static dielectric constant with magnetic field is determined by the product of $g(q)$ with $\langle M_q M_{-q} \rangle$. In case of antiferromagnetic order, this product will be very large when the maximum value in $g(q)$ coincides with spin-spin correlation peak and in case of ferromagnetic order, it will vanish as there is no overlap. In the paramagnetic phase, the correlation function is constant, so Eq. (1.46) expects that there will be small shift in static dielectric constant with magnetic field. However, the possibility of having a large overlap between $g(q)$ and $\langle M_q M_{-q} \rangle$ in antiferromagnets suggests that magnetodielectric effect may be expected to be much larger in antiferromagnets than ferromagnets.

1.6.2.1 Magnetoelectric Coupling in non-polar Systems

In these systems there is no spontaneous polarization i.e. no ferroelectric transition. The two systems $SeCuO_3$ and $TeCuO_3$, which are ferromagnetic (T_C = 25 K) and antiferromagnetic

(T_N = 9 K), respectively, are the good systems to explain the magnetodielectric effect due to magnetoelectric coupling. Under zero magnetic field, the dielectric constant of $SeCuO_3$ drops sharply below T_C and the dielectric constant of $TeCuO_3$ increases gradually at temperature well above T_N. At high temperatures, the net magnetization of $SeCuO_3$ is approximately zero, so the magnetodielectric shift in the dielectric constant arises solely from spin correlations in the paramagnetic phase. Below T_C, a spontaneous magnetization develops which couples to the electric polarization and changes the dielectric constant, as expressed in Eqs. (1.46) and (1.48). From Fig. 1.32, increasing ferromagnetic correlations decrease the overlap between g (q) and $\langle M_q M_{-q} \rangle$, which decreases the magnitude of $I(T)$. This decrease in the size of the magnetodielectric shift associated with ferromagnetic order then produces a change in the dielectric constant. With increasing magnetic field, the decrease in dielectric constant shifts to higher temperatures and shows broadening, consistent with the behavior of the magnetization in the ferromagnetic materials.

More detailed investigations show that the field dependent change in dielectric constant in $SeCuO_3$ can be fit by a term proportional to M^2 (Fig. 1.33(b)). While considering a magnetodielectric effect proportional to M^2 is sufficient to explain the coupling in non-polar

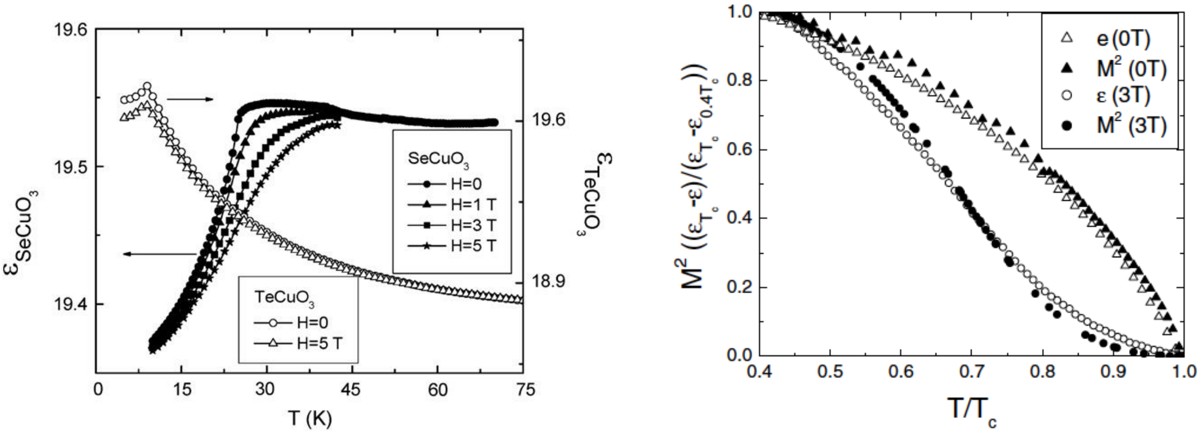

Figure 1.33 (a) temperature dependence of dielectric constant under various magnetic fields for the ferromagnetic $SeCuO_3$ (left y-axis) and the antiferromagnetic $TeCuO_3$ (right y-axis). (b) Comparison of the shift in ε (scaled to the value at $T = 0.4T_C$) to M^2 (scaled in the same way) for $SeCuO_3$ below T_C. Figure from Ref. [146].

ferromagnets, a full q-dependent analysis is necessary to interpret measurements on antiferromagnetic systems.

The magnetodielectric shift given in Eq. (1.48) can also be used to explain the temperature and magnetic field dependence of the dielectric constant of antiferromagnetic $TeCuO_3$, which is shown at right hand scale of Fig. 1.33(a) for different fixed magnetic fields. At a relatively high temperature, above the antiferromagnetic transition, $\langle M_q M_{-q} \rangle$ develops a peak at a non-zero q vector, corresponding to short-range antiferromagnetic correlations. The coupling term $g(q)$ is expected to have a maximum near this same q vector for magnetic ordering leading to an increase in the dielectric constant as $\langle M_q M_{-q} \rangle$ gets larger approaching T_N. This is in contrast to $SeCuO_3$, where the spin-spin correlation function does not develop a peak at the maximum of $g(q)$, so $\varepsilon(T)$ remains almost flat at higher temperatures. Applying a large magnetic field to $TeCuO_3$ is expected to suppress antiferromagnetic order, leading to a smaller value of $\langle M_q M_{-q} \rangle$ at the q vector for antiferromagnetic ordering. As can be seen in Fig. 1.33(a), the shift in dielectric constant in $TeCuO_3$ is slightly smaller for $\mu_0 H = 5$ T than for $\mu_0 H = 0$ T, which is consistent with additional spectral weight being concentrated at the $q = 0$ ferromagnetic spin-spin correlation forced by the applied field.

1.6.2.2 Magnetoelectric Coupling in polar Systems

Magnetodielectric effect can also be observed at the magnetic transition temperatures in the systems having ferroelectric transition. These systems have a finite polarization, so the free energy given in Eq. (1.44) is used to determine the magnetoelectric coupling. However, for some materials, the ferroelectric transition temperature occurs at far above magnetic transition temperature, so change in dielectric constant associated with the ferroelectric transition can typically be neglected and Eq. (1.48) is sufficient to explain the

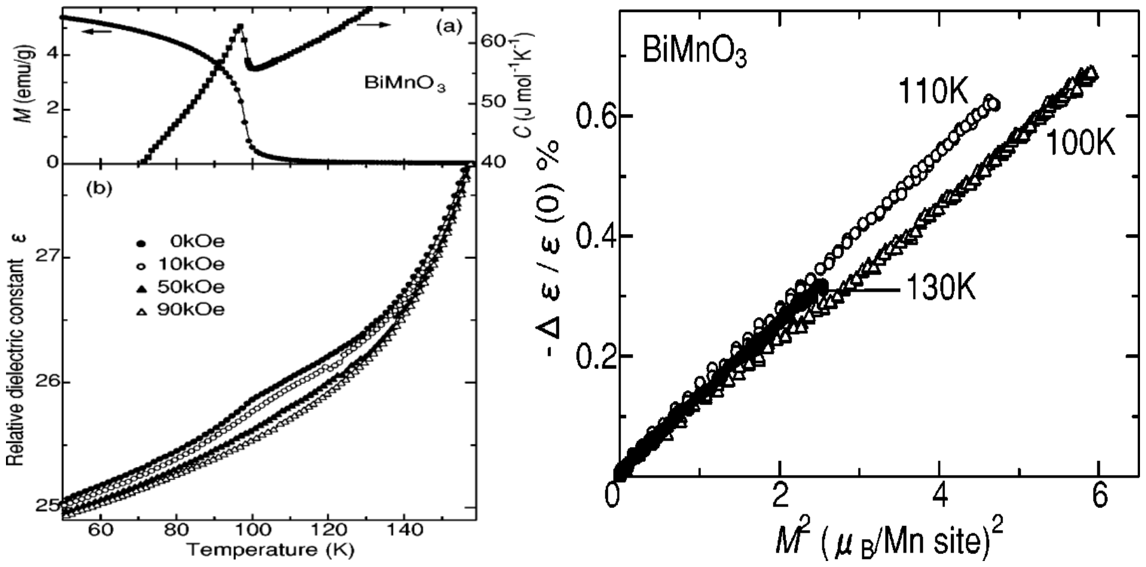

Figure 1.34 Temperature dependence of (a) magnetization (left hand scale) and heat capacity (right hand scale), and (b) relative dielectric constant of $BiMnO_3$ with different fixed magnetic field. (c) Magnetodielectric effect as a function of square magnetization at temperatures near T_C. Figure from Ref. [12].

magnetoelectric coupling. In these systems, the magnitude of magnetodielectric coupling is relatively small. $BiMnO_3$ is ferromagnetic below T_C = 105 K and ferroelectric near structural transition 750 K. It shows a dielectric anomaly at T_C and a magnetic field induced change in dielectric constant (Fig 1.34(b)).[12] At temperature below T_C, the magnitude of magnetodielectric effect is small, although the magnetization has reached greater than 80 % of its value by 10 kOe. This suggests that the magnetic domain rotation least affects the dielectric constant at low temperature. The maximum magnetodielectric effect is 0.6 % around 100 K. The magnetodielectric effect in $BiMnO_3$ is directly proportional to the square magnetization as shown in Fig.1.34(c). These observed results leads to the conclusion that the origin of the magnetodielectric effect is attributed to the magnetoelectric coupling.

1.6.3 Magnetodielectric effect without magnetoelectric coupling

G. Catalan proposed that magnetodielectric can also be observed through the combination of Maxwell Wagner relaxation and magnetoresistance, unrelated to the magnetoelectric coupling.[148] The calculation was done for manganite based magnetoresistive materials with charge depleted interfacial region (grain boundaries). The *MR* in these materials arises due to two different contributions; (i) the spin polarized tunneling of electrons across the grain boundaries in polycrystalline samples and (ii) enhancement of double exchange in the core of the sample in case of single crystal or thin films. In polycrystalline insulating samples, the difference in conductivity of grains and grain boundaries yields the charge accumulation at their interfaces by applying electric field, which is known as Maxwell-Wagner relaxation (MWR)[149, 150]. The dielectric permittivity of these samples can be calculated considering a series circuit of two RC elements as shown in Fig. 1.35, one corresponding to grains and other for grain boundaries (Fig. 1.35).[148, 151] In RC elements, the capacitor (*C*) defines the charge storage capacity of the material and resistor (*R*) in parallel of capacitor describes the leakage current due to untrapped charges carriers.

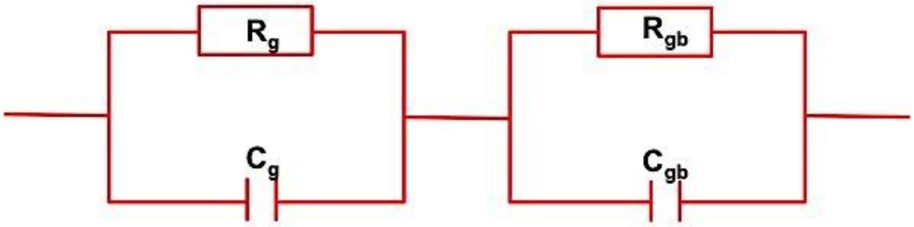

Figure 1.35 Equivalent series circuit of RC elements of grains (R_g, C_g) and grain-boundaries (R_{gb}, C_{gb}).

The real and imaginary parts of permittivity of this circuit are [152]

$$\varepsilon'(\omega) = \frac{1}{C_0(R_g + R_{gb})} \frac{\tau_g + \tau_{gb} - \tau + \omega^2 \tau_g \tau_{gb} \tau}{1 + \omega^2 \tau^2} \tag{1.49}$$

and

$$\varepsilon''(\omega) = \frac{1}{\omega C_0(R_g + R_{gb})} \frac{1 - \omega^2 \tau_g \tau_{gb} + \omega^2 \tau(\tau_g + \tau_{gb})}{1 + \omega^2 \tau^2} \tag{1.50}$$

where $C_0 = \frac{\varepsilon_0 A}{t}$, A and t are the cross section area and thickness of the sample respectively. $\tau_g = R_g C_g$, $\tau_{gb} = R_{gb} C_{gb}$, $\tau = \frac{\tau_g R_{gb} + \tau_{gb} R_g}{R_g + R_{gb}}$, $\omega = 2\pi f$, where f is the ac frequency and $\frac{1}{C} = \frac{1}{C_g} + \frac{1}{C_{gb}}$, where C is the measured capacitance of the sample.

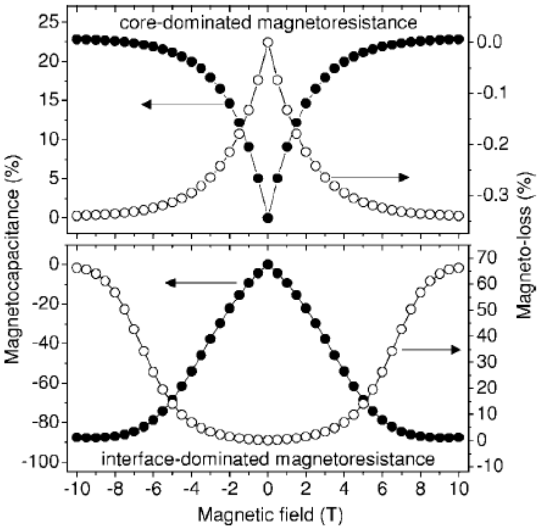

Figure 1.36 Magnetocapacitance and magnetodielectric loss of a depleted boundary layer material where *MR* is core and interface based. Figure from Ref. [148]

The calculated magnetocapacitance (MC) and magnetodielectric loss of magnetoresistive samples are shown in the left and right y-axes of Fig. 1.36. It is noticed that the magnetodielectric loss shows an opposite behavior of magnetocapacitance, i.e. positive (negative) magnetocapacitance material gives negative (positive) magnetodielectric loss, if magnetodielectric effect results from the magnetoresistance and Maxwell Wagner effect. Several materials such as $BaTiO_3$:Fe single crystal[153], γ-Fe_2O_3 polycrystalline sample[151], spinal MnZn ferrite[154], shows the magnetodielectric effect due to the combination of Maxwell Wagner effect and magnetoresistance.

1.7 Motivation

In this thesis, we investigate three systems: (i) $EuTiO_3$, (ii) $Eu_{1-x}Ba_xTiO_3$ and (iii) $Eu_{1-x}La_xTiO_3$.

1.7.1 $EuTiO_3$

In the past few years, a lot of attention has been focused to investigate the magnetoelectric properties[14, 48, 50] and multiferroicity[15, 51] in ETO. Additionally, the appearance of an antiferrodistortive transition near room temperature in this compound generated a significant research interest and it has been studied extensively.[52, 56, 57] Since ETO contains Eu^{2+} with seven unpaired spins in 4f level, it has a potential to show a large magnetocaloric effect (MCE). The mainstream in the field of MCE is to find new materials exhibiting a large MCE close to room temperature for domestic and industrial applications. However, low-temperature refrigeration is important not only for basic research but also for cooling superconducting magnets used in magnetic resonance imaging and liquefaction of hydrogen. Therefore, we investigate the magnetic entropy change as well as adiabatic temperature change in ETO experimentally, for the first time.

Although EuO was the first oxide discovered to exhibit colossal *MR* under a high magnetic field[102, 155], the *MR* in transition metal oxides rarely attracted attention before 1980. The discovery of a large negative *MR* in mixed valent manganites in 1990 spurred interest to explore magnetoresistive properties of other transition metal oxides.[3, 4] Very recently, T. Ito *et. al.*[156] reported a positive *MR* in rare earth titanates $RTiO_3$ (R = Pr and Ce). However, there is no report of *MR* in other titanates including ETO.

All the previous reports on the magnetodielectric effect in ETO focused only on the change in real part of the dielectric constant under magnetic field. The imaginary part (ac resistivity or dielectric loss) was overlooked. Here, we perform a systematic study of dielectric constant, ac-resistivity and dielectric loss as the function of temperature, frequency and magnetic field. The impedance spectroscopy is utilized to understand the relaxation phenomenon in ETO.

1.7.2 $Eu_{1-x}Ba_xTiO_3$

While ETO is an antiferromagnetic (T_N = 5.5 K) and quantum paraelectric, BTO is non-magnetic and ferroelectric (T_{FE} ~ 400 K). Both Ba and Eu are isovalent. The solid solution of these two compounds may exhibit ferromagnetism and ferroelectricity in single phase. Additionally, the lattice expansion in $Eu_{1-x}Ba_xTiO_3$ due to larger size of Ba^{2+} ions compared to that of Eu^{2+} ions can change the strength of exchange interactions (J_1 and J_2) between Eu:4f spins. In this context, it is worth to investigate the magnetic and ferroelectric properties of $Eu_{1-x}Ba_xTiO_3$ over wide range of composition ($0.00 < x < 1.0$) and establish a phase-diagram in temperature-doping (T-x) space. $Eu_{1-x}Ba_xTiO_3$ also provides a unique opportunity to study how the magnetocaloric, magnetoresistance and magnetodielectric properties change systematically with the spin dilution of rare earth site (Eu^{2+}:$4f^7$).

1.7.3 $Eu_{1-x}La_xTiO_3$

The magnetic ground state of ETO thin film was shown to be tune from AFM to FM via biaxial compressive strain. However, the substitution of trivalent rare earth ion at Eu site could be an effective method to control the magnetic phase of ETO. Unlike Ba^{2+}, the substitution of La^{3+} for Eu^{2+} can dope electrons into t_{2g} orbital of Ti-3d band of ETO, which can suppress antiferromagnetic coupling and promote ferromagnetic interaction between 4f spins on neighboring Eu^{2+} ions through RKKY interaction. We study the magnetic interaction in $Eu_{1-x}La_xTiO_3$ through magnetization and heat capacity measurements. Since the end compound $LaTiO_3$ of $Eu_{1-x}La_xTiO_3$ series is an antiferromagnetic semiconductor with T_N ~ 140 K[157], it will be interesting to study how the magnetocaloric property and magnetoresistance of ETO are affected by La^{3+} substitution for Eu^{2+}. While there is no report on the magnetocaloric effect in $Eu_{1-x}La_xTiO_3$ series so far, a negative MR has been reported in a ferromagnetic metal $Eu_{0.9}La_{0.1}TiO_3$[70]. Here, we investigate the magnetocaloric properties and MR in $Eu_{1-x}La_xTiO_3$ over wide composition range ($0.01 \leq x \leq 0.3$).

1.8 Organization of thesis

The present thesis is organized as follows:

Chapter 1: In chapter 1, I have presented a brief description of titanates and reported exotic properties of $EuTiO_3$. The background and basics of phenomena investigated in this thesis (magnetocaloric effect, colossal magnetoresistance, multiferroicity and magnetodielectric effect) are discussed briefly.

Chapter 2: Chapter 2 mainly focuses on the brief description of various experimental techniques that were employed to prepare and characterize the samples. I also discuss the methods and instruments used for magnetization, heat capacity and electrical transport (dc and ac) measurements.

Chapter 3: Chapter 3 mainly presents detailed study of magnetocaloric, magnetoresistance and magnetodielectric effects in $EuTiO_3$ compound. The powder X-ray diffraction (XRD) pattern and thermogravimetric (TGA) trace are presented to characterize the $EuTiO_3$ sample. To study the dielectric properties of $EuTiO_3$, a detailed analysis of impedance spectroscopy data is reported.

Chapter 4: In this chapter, we present magnetic and ferroelectric properties of $Eu_{1-x}Ba_xTiO_3$ ($0.02 \leq x \leq 1.0$) and establish a phase diagram. The impact of non-magnetic Ba^{2+} substitution for magnetic cation (Eu^{2+}) on the magnetic entropy change, magnetoresistance and magnetodielectric effect of $EuTiO_3$ is discussed.

Chapter 5: Chapter 5 focuses on the magnetic, magnetocaloric and magnetoresistance properties of $Eu_{1-x}La_xTiO_3$ ($0.01 \leq x \leq 0.3$) compounds. Substitution of La^{3+} for Eu^{2+} dopes electron in t_{2g} band unlike in $Eu_{1-x}Ba_xTiO_3$. The magnetoresistance data is analyzed using proposed model such as spin-disorder scattering and two-band model.

Chapter 6: Finally, in chapter 6, we presented a summary of main results obtained in this thesis work and outline of future research direction.

Chapter 2 Experimental Methods and Techniques

In this chapter, the experimental methods and techniques used to prepare and characterize the undoped and doped $EuTiO_3$ samples during the course of this thesis are described in detail. Conventional solid-state reaction method was adopted to prepare the samples. X-ray diffraction was used to determine the structure and phase purity of the prepared samples. To investigate the magnetic, electrical and thermal properties, we used Physical Property Measurement System (PPMS) supplied by Quantum Design Inc. (USA).

2.1 Sample preparation

Several methods have been demonstrated so far to synthesize the perovskite oxide materials. The most widely used methods are solid-state reaction, sol-gel combustion, co-precipitation etc. Solid-state reaction route is the most convenient synthesis method for preparing polycrystalline samples. This method involves grinding and heating of mixed raw materials to obtain a single-phase due to ionic diffusion. In a typical solid-state reaction method, the precursors in the form of oxides or carbonates are weighed in the stoichiometric proportions and mixed thoroughly. After mixing and grinding, the powder is initially annealed at high temperature (1000°C – 1500°C) and further at high temperature for 24 hours with two intermediate grinding in order to ensure homogeneity of the mixed powders.

All the samples studied in this thesis were prepared using solid-state reaction method. While most of the perovskite oxide can be prepared after annealing in ambient atmosphere, perovskite $EuTiO_3$ can be prepared only in reduced atmosphere. Since the precursor Eu_2O_3 contains Eu^{3+}, we used reduced atmosphere (95%Ar + 5% H_2) that reduces Eu^{3+} in to Eu^{2+}. We used a tube furnace (MTI – GSL1500X) where the gas can be flowed easily during annealing. A schematic diagram of sample preparation is displayed in Fig. 2.1. For preparing $EuTiO_3$, the stoichiometric ratio of Eu_2O_3 and TiO_2 powders were mixed with pestle in an

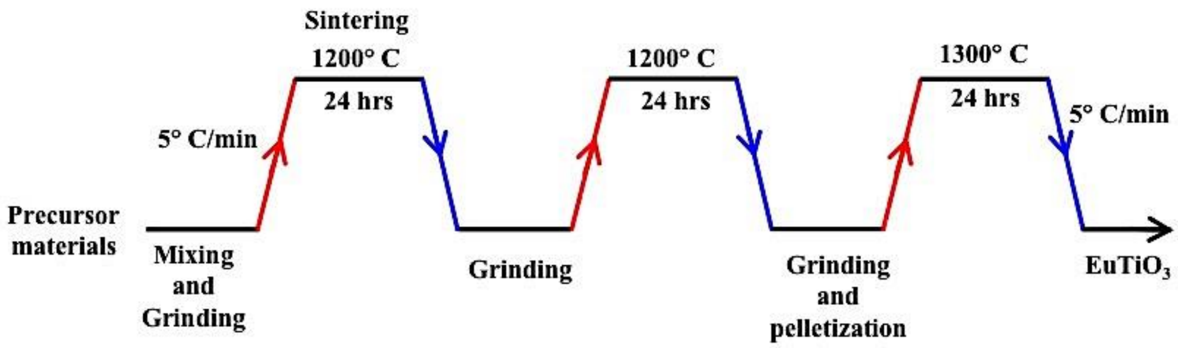

Figure 2.1 Schematic diagram of $EuTiO_3$ sample preparation using solid-state reaction method.

agate mortar. After mixing and grinding, the powder was sintered at temperature 1200°C for 24 hours twice under 95% Ar and 5% H_2 atmosphere. After sintering, powder was ground again and pressed in a uniaxial press into a disc shaped pellet. The pellet was sintered at 1300°C for 24 hours in same atmosphere. The additional precursors $BaCO_3$ and La_2O_3 were used for preparing Ba and La doped $EuTiO_3$, respectively.

2.2 Characterization techniques

2.2.1 X-ray powder diffractometer

The powder X-ray diffractometer is widely used technique for phase identification of crystalline samples. This is the most common technique to study the crystal structure, atomic spacing, and grain size of materials. X-ray diffraction (XRD) is based on the principle of Bragg's law of diffraction:

$$2dSin\theta = n\lambda \tag{2.1}$$

where d is the spacing between the crystalline lattice planes, θ is the glancing angle between the incident X-ray beam and crystalline plane, n is the order of diffraction and λ is the wavelength of the incident X-ray beam.

The X-ray diffractometer consists of three main components: (i) X-ray tube, (ii) sample stage and (iii) X-ray detector, as shown in Fig. 2.2. X-rays are generated in a cathode ray tube by heating a filament to produce electrons, accelerating the electrons toward a target by applying voltage, and bombarding the target material with electrons. When electrons have sufficient energy to remove inner shell electrons of the target material, characteristic X-ray spectra are produced. The most common target material is copper with CuKα radiation (1.5418 Å). These X-rays are collimated and directed onto the sample. X-ray detector records the X-rays reflected from the sample. When the geometry of the incident X-rays impinging the sample satisfies the Bragg Eq. (2.1), constructive interference occurs and diffraction pattern shows a peak.

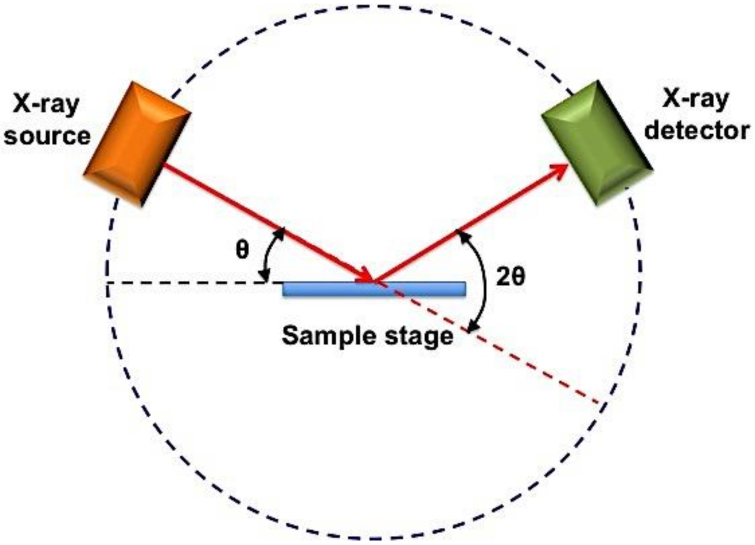

Figure 2.2 Schematic diagram of X-ray diffractometer.

In the present study, Philips X'PERT MPD powder X-ray diffractometer with CuKα radiation was used for the structural characterization of the samples. The Rietveld refinement method was used to fit the powder XRD pattern and evaluate the lattice parameters. We used FULLPROF software to do the Rietveld refinement of XRD pattern. In a typical XRD experiment, the sample was scanned from $2\theta = 20°$ to 80° with a scan rate 0.5°/min.

2.2.2 Thermogravimetric analyzer

Thermogravimetric analysis (TGA) is commonly used method to determine the mass gain or loss as a function of increasing temperature due to decomposition or oxidation. TGA can also provide information about physical phenomena, such as second-order phase transition, as well as chemical phenomena such as dehydration, chemisorption. Thermogravimetric analyzer consists of a precision balance with a pan loaded with sample and a programmable furnace. The furnace can be programmed for a constant heating rate. The precision balance continuously weighs the sample as it is heated to a specific temperature.

In this thesis, we utilized TGA to determine the oxygen contents in prepared sample. Perovskite $EuTiO_3$ oxidizes and converts into the pyrochlore phase $Eu_2Ti_2O_7$ after heating up in air. $Eu_2Ti_2O_7$ did not show any observable weight gain in wide temperature range (600°C – 1200°C). Therefore, the oxygen nonstoichiometry parameter δ can be evaluated from the weight gain during oxidation using equation given below.

$$2EuTiO_{3-\delta} + (0.5 - \delta)O_2 \rightarrow Eu_2Ti_2O_7 \tag{2.2}$$

A Discovery Thermogravimetric Analyzer from TA Instruments was employed to collect the TGA traces (mass gain as a function of temperature or time) while heating the sample in air from room temperature to 1000°C at a rate of 5°C/min. A discovery TGA provides an isothermal temperature precision of ± 0.1°C and weighing precision of ±0.01 %.

2.3 Measurement techniques

2.3.1 Magnetic measurements

The magnetization measurements were done using a Physical Property Measuring System (PPMS, Quantum Design Inc. USA) equipped with a vibrating sample magnetometer (VSM) probe. The PPMS is a cryogenic platform that can be used to carry out temperature (1.8 K to 400 K) and magnetic field (–7 T to +7T) dependent physical measurements. Fig. 2.3

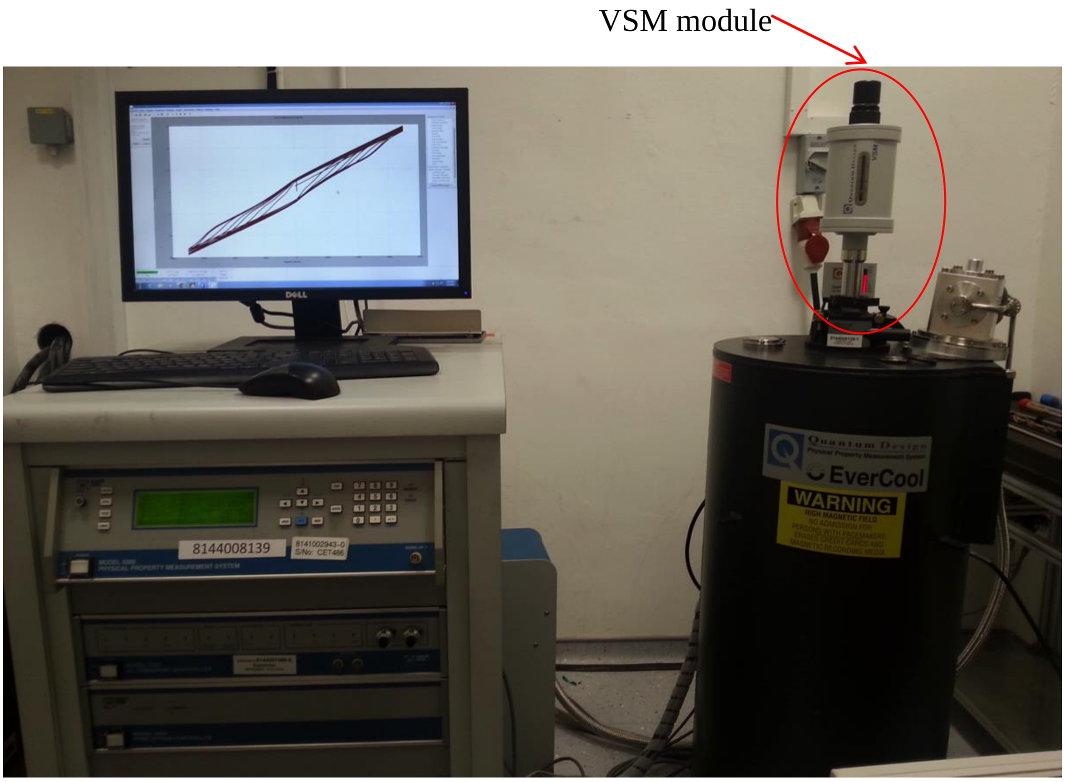

Figure 2.3 Photograph of Physical Property Measurement System (PPMS) equipped with Vibrating Sample Magnetometer (VSM) module.

displays the PPMS equipped with VSM module used for the present study. The VSM consists of a linear motor for vibrating the sample and pickup coil for detecting the response. It works on the principle of Faraday's law of electromagnetic induction. When a magnetic material vibrates sinusoidally inside a uniform magnetic field, it introduces an oscillating magnetic flux. According to Faraday's law, this oscillating magnetic flux will induce an electromotive force (emf), which is detected by a pickup coil. The time dependent induced voltage is given as

$$V_{emf} = \frac{d\phi}{dt} = \frac{d\phi}{dz}\frac{dz}{dt} \tag{2.3}$$

where ϕ is the magnetic flux enclosed by the pickup coil, z is the vertical motion of magnetic material with respect to coil and t is the time. For a sinusoidally oscillating sample position, the voltage developed is given as:

$$V_{emf} = 2\pi f CmAsin(2\pi ft) \tag{2.4}$$

where C is the coupling constant, m is the magnetic moment, A and f are the amplitude and frequency of oscillation. Frequency of vibration of VSM is 40 Hz and sensitivity is 10-6 emu. In the PPMS-VSM system, the magnetic field can be applied up to 7 T with help of superconducting magnets. PPMS used MultiVu software for automation and control the measurement.

2.3.2 Heat capacity measurements

The heat capacity of samples was measured using heat capacity option in PPMS, Quantum Design Inc. (USA). The PPMS heat capacity option uses a relaxation technique to measure the heat capacity at constant pressure. The front and back views of sample puck used for this measurement are shown in Fig. 2.4 (a) and (b), respectively. The puck consists of three elements: (i) heater, (ii) thermometer and (iii) sample platform. The heater and thermometer are attached to the bottom side of the sample platform. The sample is mounted to the platform using a thin layer of Apiezon grease, which provides thermal contact of

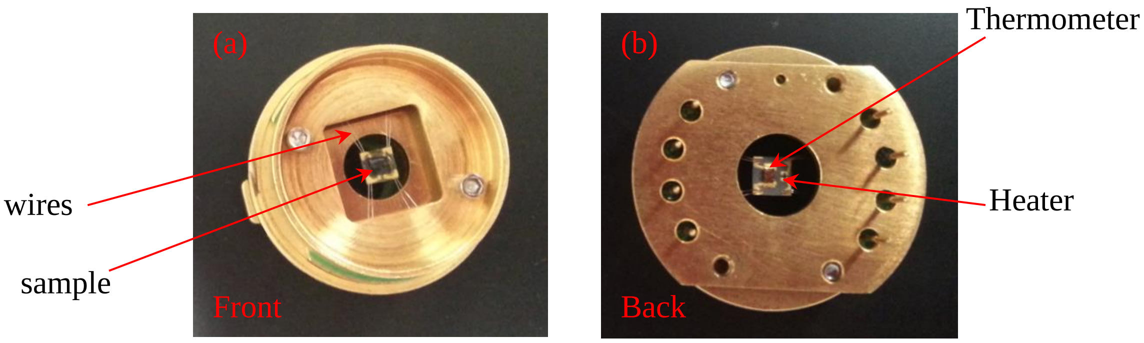

Figure 2.4 Heat capacity puck (a) front view and (b) back view.

sample to the platform. The Apiezon N grease shows a spurious behavior at temperature ~ 280 K. Therefore, we used N grease for low temperature (250 K – 2K) measurements and H grease for high temperature (250 K – 350 K).

The heat capacity of a sample in PPMS is calculated using a simple model, which is the most basic analysis of the raw measurement data, assuming that the temperatures of sample and sample platform are same during measurements. In this model, the temperature T of the platform as a function of time t obeys the equation

$$C_{total}\left(\frac{dT}{dt}\right) = K_W(T - T_b) - P(t) \tag{2.5}$$

where C_{total} is the total heat capacity of the sample and sample platform, K_{W} is the thermal conductance of the supporting wires, T_{b} is the temperature of the thermal bath and $P(t)$ is the power applied by the heater. The heater power is equal to P_0 while heating the sample during measurement, which is equal to zero while cooling. The solution of Eq. (2.4) is given by an exponential function with a characteristic time constant τ equal to $C_{\text{total}}/K_{\text{W}}$.

2.3.3 DC resistivity measurements

Various methods have been suggested to measure the dc resistance. However, the precision of the methods depends on the contact resistance and shape of the sample (single crystal, thin film or polycrystalline samples). For polycrystalline samples, two methods can be used: (i) four-probe and (ii) two-probe. While four-probes method is used for low resistive samples, two-probes method is suitable for high resistive samples.

2.3.3.1 Four-probe method

Four-probes is the most widely used method for resistivity measurements of low resistive samples. Using four probes, one can eliminate the probe resistance, contact resistance and spread resistance in the measurement. The resistivity of sample is typically evaluated by sourcing a constant current and measuring the voltage drop.

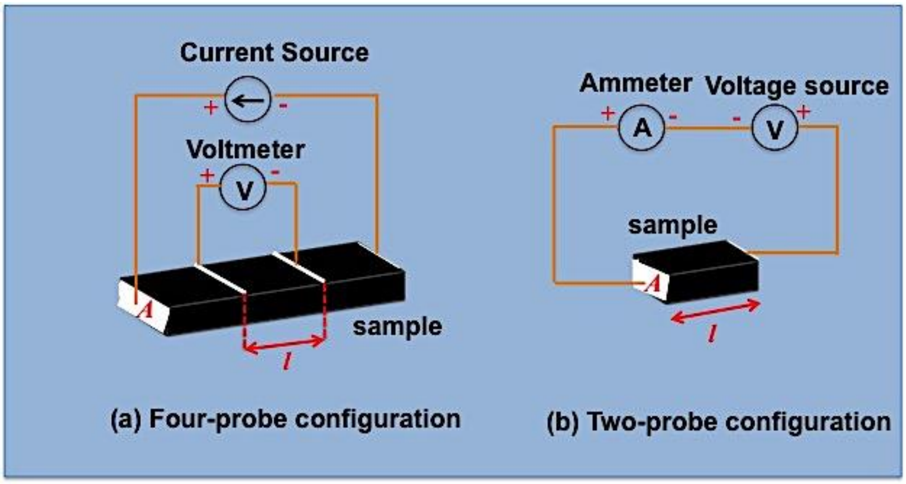

Figure 2.5 Four-probe and two-probe configurations for dc resistivity measurements.

Fig. 2.5(a) illustrates the resistivity measurement of bulk samples using the four-probe configurations. In order to measure the resistivity with four-probe method, the sample is cut in a bar shape (~12mm × 4 mm × 2 mm). A current source is connected to both ends of the sample and voltmeter leads are placed a known distance apart (~ 3 mm) on its surface. The resistivity (ρ) of sample can be calculated from the magnitude of the source current (I), measured voltage (V), the cross-sectional area (A) and the distance between the voltmeter leads (l), using equation

$$\rho = \frac{V}{I} \times \frac{A}{l} \tag{2.6}$$

We performed dc resistivity measurements for low resistive samples using an inbuilt dc resistivity measurement option in PPMS, Quantum Design Inc. (USA). The dc resistivity in PPMS is measured in the temperature range T = 400 K – 10 K under external magnetic fields up to $\mu_0 H$ = 7 T. While PPMS is widely used for the resistivity measurements for metallic and semiconducting samples, the resistivity of insulating samples cannot be measured using PPMS due to the limitation of current source ($I_{\min}$ = 500 nA).

2.3.3.2 Two-probe method

Two-probe is simple method for measuring resistivity and is illustrated in Fig. 2.5(b). This method is useful for insulting samples, where the sample resistance is much higher than the contact resistance. In this method, the resistance of sample can be evaluated by measured voltage drop (*V*) across the sample and current through the sample (*I*). However, we determined the resistivity of an insulator by applying a voltage to the sample for a specific period of time and measuring the resulting current with an electrometer. In order to evaluate the resistivity with two-probe method, the sample is cut in a rectangular shape (~6 mm × 4 mm × 2 mm). The two-probe resistivity measurements under magnetic fields were performed using PPMS and Keithley 6517A electrometer controlled with LabVIEW program.

2.2.4 AC electrical transport measurements

We used Agilent 4294A impedance analyzer for ac electrical transport (capacitance, ac resistance, dielectric loss and impedance) measurements throughout this thesis. The capacitance and ac resistance or dielectric loss measurements are performed simultaneously on parallel plate capacitor geometry sample as shown in Fig. 2.6. The capacitance of a

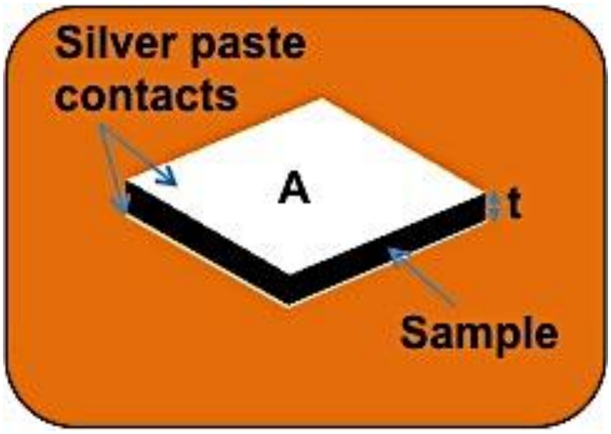

Figure 2.6 A schematic of parallel plate capacitor geometry sample for capacitance measurements.

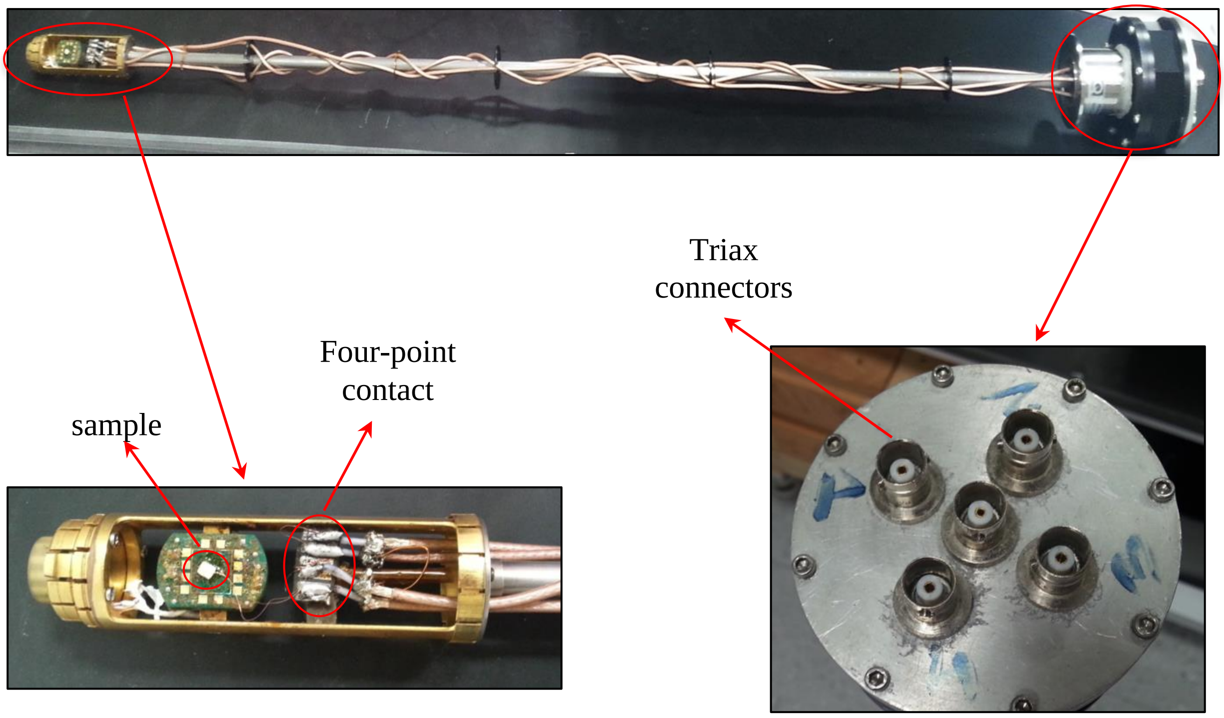

Figure 2.7 Top: Full view of multifunctional probe wired with coaxial cables for ac electrical transport measurements using PPMS. Bottom left: zoom view of sample holder and connections and bottom right: top view of probe head.

dielectric in parallel plate capacitor geometry is given by

$$C = \varepsilon\varepsilon_0 \frac{A}{t} \tag{2.7}$$

where ε is the dielectric constant, ε_0 is vacuum permittivity, A is the area of the contacts and t is the thickness of the sample.

In order to form a parallel plate capacitor, electrodes were made on the largest surfaces of the samples using silver paint. The samples were polished before making contacts in order to obtain a smooth surface and better sample-electrode interface.

For temperature dependent capacitance measurements under zero field, we used a closed cycle refrigerator cryostat (Sumitomo Cryogenics) and a temperature controller (Lake Shore Cryotronics, Inc.). However, the capacitance under magnetic field was measured in PPMS. The PPMS and Agilent 4294A both were controlled by the LabVIEW program. A home-built multifunctional probe was used to measure the capacitance of the samples in PPMS. Although this probe was design to perform both two-point and four point ac transport measurements, we used two-point method. Fig. 2.7 shows the photograph of the multifunctional probe. The probe head contains four triax connectors, which are connected to coaxial wires below the head. The sample was stacked to sample holder with GE varnish.

2.2.5 Pyroelectric current measurements

Measurement of pyroelectric current is commonly used method to determine the spontaneous polarization as well as paraelectric to ferroelectric transition temperature. All materials that exhibit spontaneous polarization are pyroelectric and their electric polarization changes with varying temperature in zero electric field. A typical pyroelectric current measurement first involves poling while cooling the sample in an applied electric field through the transition temperature where the sample becomes pyroelectric or ferroelectric. When the temperature at which the measurement will be started is reached, the electric field is removed and sample is heated at a constant rate. The current is measured continuously as the sample is heated to a specific temperature. A maximum in pyroelectric current is expected at the transition temperature. The polarization can be obtained by integrating the pyroelectric current with respect to time.

$$P = \frac{1}{A}\int i\, dt \tag{2.8}$$

We performed pyroelectric current measurements in PPMS for few-selected ferroelectric samples to confirm the ferroelectric transition temperature. A Keithley 6517A electrometer was used to pole the sample and measure the pyroelectric current. We used multifunctional probe shown in Fig. 2.7 for applying high electric field and measuring the current. The sample was cooled down to the temperature 10 K with rate 4 K/min in PPMS. At T = 10 K, the electric field was removed and the top and bottom electrodes were shorted to eliminate the surface charge. Then, the sample was heated at a constant rate 4 K/min. A strong peak was seen at phase transition temperature.

Chapter 3 Magnetic, Magnetocaloric, Magnetoresistance and Magnetodielectric Properties of $EuTiO_3$

3.1 Introduction

$EuTiO_3$ is unique among the rare-earth titanates of the formula $RTiO_3$ because Eu and Ti cations stabilize in 2+ and 4+ valence states, contrary to trivalent state adopted by both R and Ti ions in other rare-earth titanates.[158] The coexistence of magnetically active Eu^{2+} ($4f^7$, S = 7/2, L= 0) ion and ferroelectric active $Ti^{4+}(d^0)$ ion in $EuTiO_3$ is provocative for investigating cross coupling (magneto-electric interaction) between electrical and magnetic polarizations. Antiferromagnetic superexchange interaction between localized 4f moments on nearest neighbhor Eu^{2+} ions drive $EuTiO_3$ to be antiferromagnetic (G-type) below T_N = 5.5±0.1 K.[41] Although ferroelectric transition was not realized in bulk $EuTiO_3$ down to 2 K, magneto-electric coupling is manifested through a dielectric anomaly- a sudden decrease of dielectric constant (ε) at T_{N} in the absence of magnetic field.[14] Magnetic and dielectric properties of $EuTiO_3$ can also be tuned with lattice strain and electric field. While the bulk sample of $EuTiO_3$ is antiferromagnetic and paraelectric, it turns into ferromagnetic and ferroelectric, i.e., multiferroic, in a tensile strained thin film.[15]

The insulating $EuTiO_3$ is also interesting from the perspective of magnetic refrigeration since the half filled 4f shell of the Eu^{2+} has a large total angular momentum ($J = S = 7/2$ and $L = 0$), it may show a large isotropic magnetic entropy change. Although P. J. von Ranke *et al.* studied the magnetic entropy change in $EuTiO_3$ theoretically;[159] we investigate magnetic entropy change as well as adiabatic temperature change of this compound experimentally for the first time. Nevertheless, the impact of external magnetic field on electrical resistivity of neither bulk nor thin film samples of $EuTiO_3$ has been reported so far. Here, we study the magneto transport in polycrystalline $EuTiO_3$ as a function of temperature and magnetic field.

While the impact of magnetic field on the real part of dielectric permittivity is studied for $EuTiO_3$ single crystal, thin film and ceramic as well extensively, the imaginary part (ac resistivity or dielectric loss) is overlooked. The magnetically tunable spin-phonon coupling was suggested the most likely origin of the magnetodielectric effect in $EuTiO_3$. On the other hand, G. Catalan[148] suggested that the positive magnetocapacitance effect could also occur due to negative magnetoresistance or magnetodielectric loss in the presence of Maxwell-Wagner relaxation. Therefore, investigation of magnetoresistance, magnetodielectric loss with magnetodielectric effect is pertinent to understand the origin of the positive magnetodielectric effect. Here, we perform a systematic study of dielectric constant, ac-resistivity and dielectric loss as the function of temperature, frequency and magnetic field. In this chapter, we report the impact of magnetic field on electrical (ac and dc resistivity and dielectric constant) and thermal properties of polycrystalline $EuTiO_3$ measured using different experimental techniques.

3.2 Experimental details

Polycrystalline $EuTiO_3$ sample was prepared using conventional solid-state reaction method. The powders of Eu_2O_3 and TiO_2 were mixed in the stoichiometric ratio. After mixing and grinding, the powder was sintered at temperature 1200^oC for 24 hours twice under reduced atmosphere (95% Ar and 5% H_2). After sintering, powder was ground again and pressed in a uniaxial press into a disc shaped pellet. The pellet was sintered at 1300^oC for 24 hours in same atmosphere. Philips X'PERT MPD powder X-ray diffractometer was employed for structure characterization at room temperature using Cu$K\alpha$ radiation. Thermo gravimetric analysis (TGA) technique was used to evaluate the oxygen nonstoichiometry. Magnetization was measured using a Physical Property Measurement System (PPMS) equipped with vibrating sample magnetometer (VSM) probe. The heat capacity from 300 K to 300 mK was measured by a relaxation technique in PPMS equipped with the ^3He option.

The temperature dependence of direct current (dc) resistivity under zero magnetic field was measured using four-probe configuration in PPMS. Two-probe dc-resistivity below 120 K as a function of temperature and magnetic field was carried out in a superconducting cryostat (Quantum Design Inc. USA) using a Keithley 6517A electrometer with applied dc voltage of 10 volt. The magnetic field was applied perpendicular to electric field direction. The temperature and field dependent capacitance and ac resistance measurements were performed simultaneously on a parallel-plate capacitor like structure sample in PPMS using Agilent 4294A impedance analyzer with applying 1 V excitation voltage. Impedance measurements as a function of frequency (100 Hz – 1MHz) were performed for same sample at various temperatures. Silver paste was used to make the electrical contacts. The EIS Spectrum Analyzer software was used for fitting the impedance data.

3.3 Results and discussion

3.3.1 Structure characterization: X-ray diffraction

Room temperature X-ray powder diffraction (XRD) pattern was analyzed using the Rietveld refinement method. Fig. 3.1 shows the XRD pattern of $EuTiO_3$, in which open

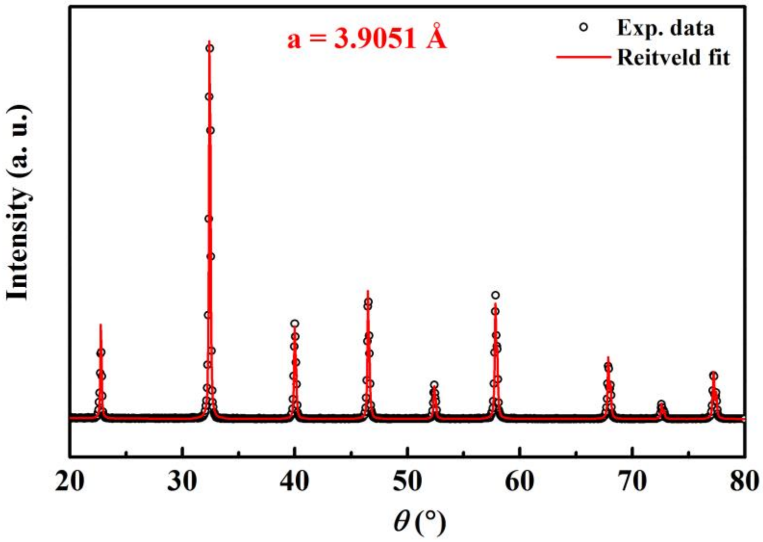

Figure 3.1 Powder XRD pattern of $EuTiO_3$ (symbol) and Rietveld refine data (solid line).

symbol and solid line represent the experimental data and Reitveld fit, respectively. The XRD pattern reveals the single phase of sample and the Reitveld refinement fit demonstrates the cubic structure with space group Pm$\overline{3}$m and lattice constant a = 3.9051 Å. The calculated lattice constant value nearly matches with reported value a = 3.9058 Å. [56]

3.3.2 Thermogravimetric analysis

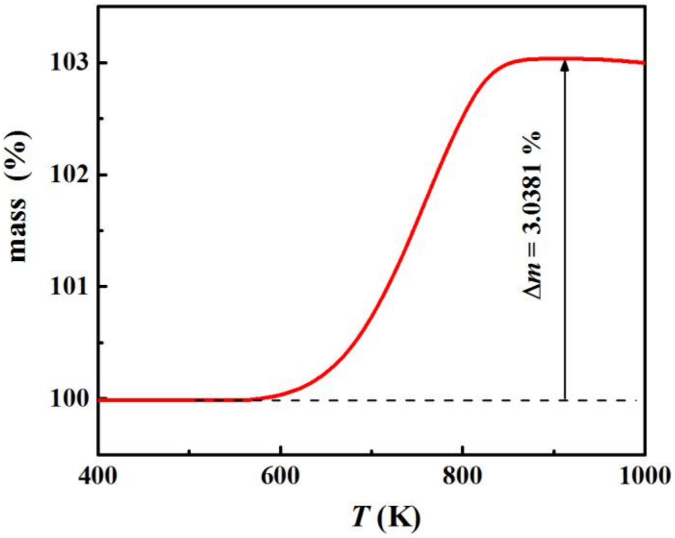

Figure 3.2 TGA trace of $EuTiO_3$ during oxidation in air.

The perovskite $EuTiO_3$ oxidizes and converts into the pyrochlore phase $Eu_2Ti_2O_7$ after heating up in air.[160] $Eu_2Ti_2O_7$ did not show any observable weight gain in wide temperature range (900 K – 1500 K). Therefore, the oxygen nonstoichiometry parameter δ can be evaluated from the weight gain during oxidation using equation given below. [160]

$$2EuTiO_{3-\delta} + (0.5-\delta)O_2 \rightarrow Eu_2Ti_2O_7 \tag{3.1}$$

From Eq. (3.1), the molar mass of $EuTiO_{3-\delta}$ can be written as

$$2M(EuTiO_{3-\delta}) = \frac{M(Eu_2Ti_2O_7)}{100\% + \Delta m\%} \tag{3.2}$$

and

$$M(EuTiO_{3-\delta}) = M(Eu) + M(Ti) + (3-\delta)M(O) \tag{3.3}$$

Fig. 3.2 shows the mass gain of $EuTiO_3$ during oxidation process in air. The molar mass of $EuTiO_{3-\delta}$ and oxygen content δ can be calculated using Eq. (3.2) and (3.3).

The calculated $\delta = -0.028$ corresponding to $\Delta m = 3.0381\%$ is very small indicating the low tolerance for deviation in oxygen stoichiometry in the $EuTiO_{3-\delta}$ perovskite phase.

3.3.3 DC magnetization and susceptibility

The main panel of Fig. 3.3 (a) shows the temperature dependent magnetization (M) of $EuTiO_3$ measured while cooling from 300 K to 2.5 K under the magnetic field of H = 1kOe. $M(T)$ increases smoothly with decreasing temperature from 300 K to 20 K and show a rapid increase below 20 K. The inset of Fig. 3.2 (a) shows expanded view of $M(T)$ data from 20 K to 2.5 K. $M(T)$ increases rapidly below 20 K and shows a peak at T = 5.42 K (= T_N), which corresponds to the onset of antiferromagnetic interaction among Eu^{2+}:$4f^7$ spins. Fig. 3.3 (b) shows the temperature dependence of inverse susceptibility ($\chi^{-1}=H/M$) from 300 K to 2.5 K. Fitting of $\chi^{-1}(T)$ with the Curie-Weiss (CW) law $\left(\chi = \frac{C}{T-\theta_p}\right)$ yields an effective magnetic

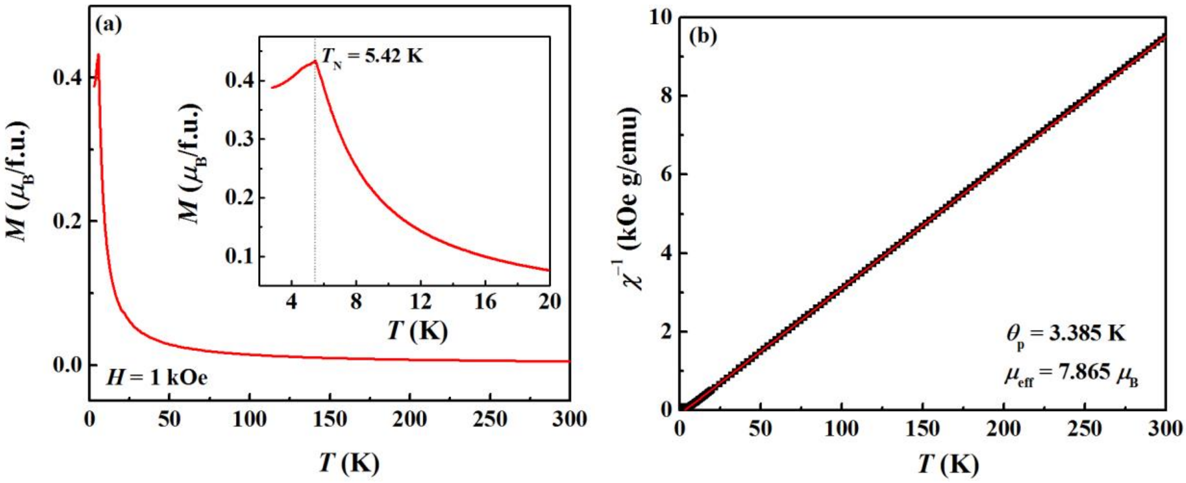

Figure 3.3 (a) Main panel: Temperature dependence of dc magnetization (M) measured under 1kOe (0.1 T) magnetic field. Insets show the $M(T)$ curve below 20 K. (b) Inverse susceptibility versus temperature, where symbol and solid line represent the experimental data and Curie-Weiss fit, respectively.

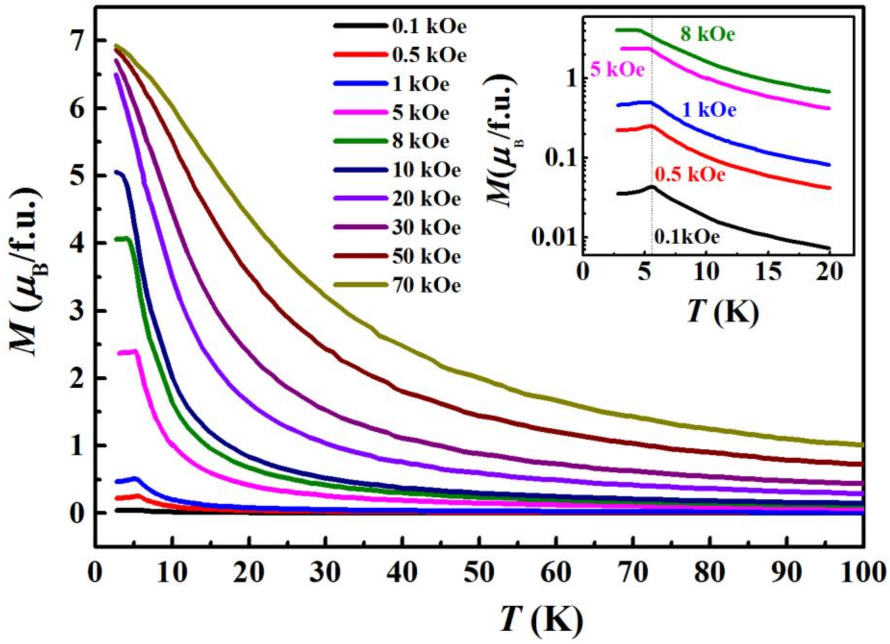

Figure 3.4 Main panel: Temperature dependence of dc magnetization (*M*) measured under various magnetic fields. Inset shows the *M*(*T*) in low temperature range (20 K -2 K) under low magnetic fields.

moment $\mu_{eff} = \left(\frac{3k_B C_M}{N}\right)^{1/2}$ = 7.86 μ_B and Curie temperature θ_p = 3.38 K. The experimentally observed μ_{eff} value is close to the theoretically expected value $\mu_{eff} = g\mu_B\sqrt{J(J+1)}$ = 7.94 μ_B, for non- interacting Eu^{2+} ions with $J = S = 7/2$.

The main panel of Fig. 3.4 shows the temperature dependence of magnetization *M*(*T*) for T = 100 K - 2 K under various magnetic fields ($\mu_0 H$ = 0.01 to 7 T). As can be seen from the inset of Fig. 3.4, *M*(*T*) peak at T_N shifts down and flattens with increasing magnetic field from 0.01 to 0.8 T. Finally, the peak disappears for fields higher than 1 T. The magnetization reaches a value of 7 μ_B/f.u. at 2 K for $\mu_0 H$ = 7 T, which is the expected value for full spin polarization of $4f^7$ spins ($M_s = g\mu_B S = 7\mu_B$, where g = 2 and S = 7/2) of Eu^{2+} :$4f^7$ ions.

Fig. 3.5 (a) shows the field dependence of *M* at T = 2.5 K while sweeping the field in direction ($\mu_0 H$ = 0 → +5T and +5T → – 5 T→ +5 T). No hysteresis is observed even at low magnetic field. The magnetization increases linearly below 1 T and shows tendency towards saturation at higher fields. The linear increase of *M(H)* below 1 T is due to spin flopping in

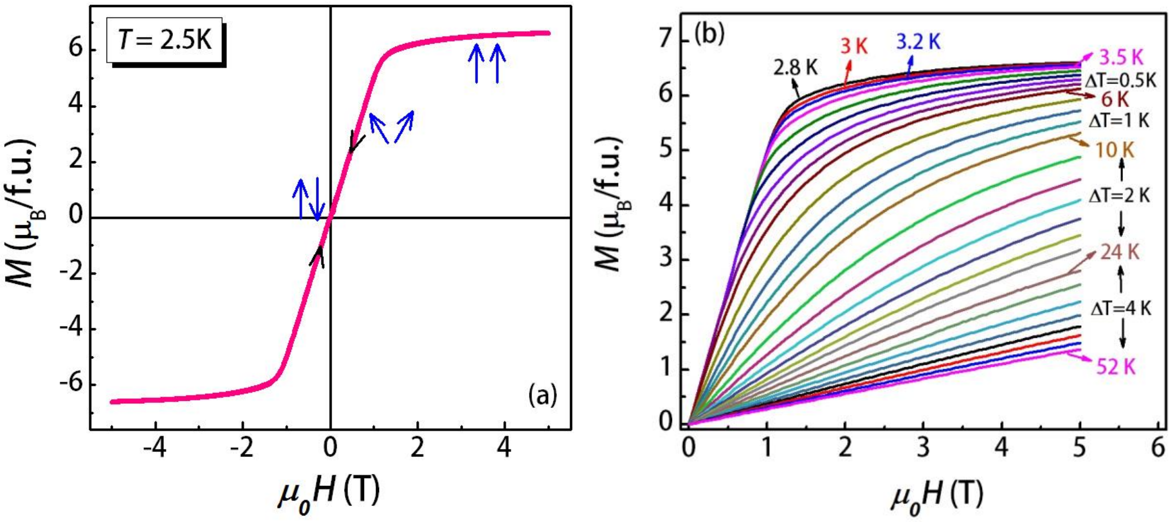

Figure 3.5 (a) Field dependence of magnetization *M*(*H*) at temperature *T* = 2.5 K measured while sweeping the field (0 - +5T - –5 T - +5T). (b) *M*(*H*) at different temperature measured while sweeping the field 0 - +5 T - 0T.

the antiferromagnetic state. The M reaches 6.6μ_B/f.u. at the highest field which is slightly lower than saturation magnetization $M_S = g\mu_B S = 7\mu_B$ expected for complete alignment of all Eu^{2+}spins. Fig. 3.5 (b) shows $M(H)$ isotherms at different temperatures. We have measured $M(H)$ isotherm at a close temperature interval from 2.8 K to 52 K. Interestingly, $M(H)$ shows nonlinear behavior at several kelvins above T_N and they become linear only for $T > 28$ K. For temperatures below 5.5 K, a peculiar behavior of magnetization has been observed. The magnetization in the linear field region for different temperatures ($T <$ 5 .5 K) overlaps each other up to certain field range in the linear regime. This is different from the behavior of a paramagnet or ferromagnet for which the magnitude of M in the low field-range should increase with lowering temperature. Above 5.5 K, the magnetization is decreasing with increasing the temperature for all magnetic field intervals. Fig. 3.6 shows the Arrott plot (M^2 versus $\mu_0 H/M$ isotherms) of the EuTiO$_3$ compound. If the magnetic transition is second order, the slope of the isotherm will be positive and the slope is negative if the phase transition is first order.[161] From Fig 3.6, the positive slope of the Arrott plot confirms that

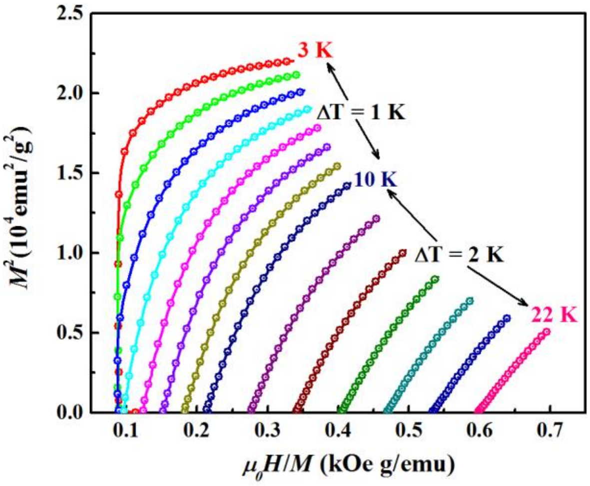

Figure 3.6 Arrott plot (M^2 versus *H/M* curves) of $EuTiO_3$ at various temperatures.

the $EuTiO_3$ undergoes a second order magnetic transition from paramagnetic to antiferromagnetic with decreasing temperature.

3.3.4 Heat capacity

The temperature dependence of the heat capacity (C_p) for $EuTiO_3$ measured upon cooling from 300 K to 2 K under zero magnetic field is displayed in Fig. 3.7(a). C_p decreases down to 10 K below which it increases rapidly and exhibits a very sharp λ- like peak at T_N, which is clearly shown in inset of Fig. 3.7(a). In the high temperature range (20-300 K), the

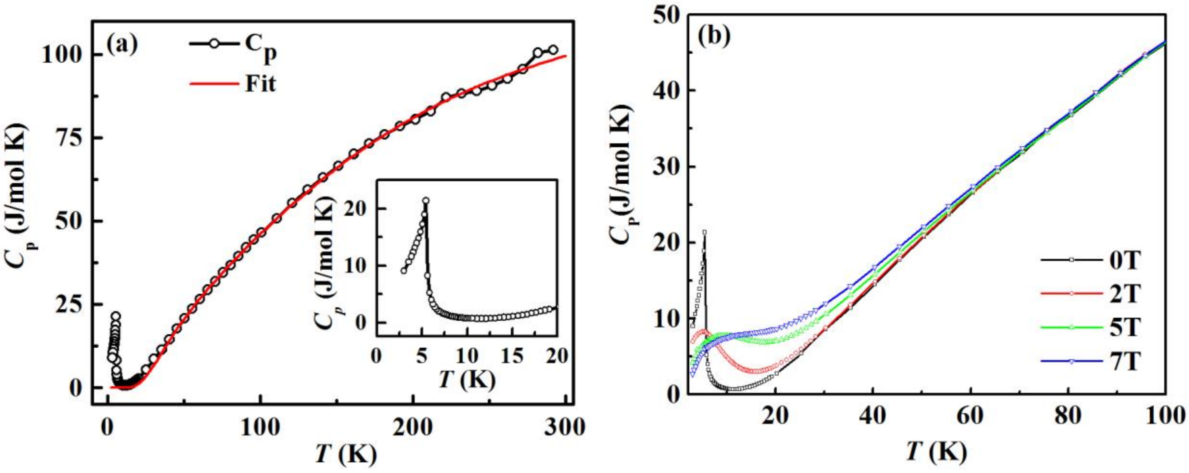

Figure 3.7 (a) Main panel: Temperature dependence of heat capacity (C_p) at constant pressure under zero magnetic field. Symbol and solid line represent the experimental data and fit to Eq. 3.4, respectively. Insets show the *M*(*T*) curve below 20 K. (b) Temperature dependence of heat capacity under various magnetic fields.

heat capacity data is fitted with lattice heat capacity obtained from the Einstein model:

$$C_{lat} = R\sum_{i=1}^{3}\frac{\left(\theta_{E_i}/T\right)^2 e^{\theta_{E_i}/T}}{\left(e^{\theta_{E_i}/T}-1\right)^2} \tag{3.4}$$

where θ_{E1}(= 153 K), θ_{E2} (= 425 K), and θ_{E3} (= 802 K) are the Einstein temperatures.

The heat capacity as a function of temperature from 100 K to 2 K under $\mu_0 H$ = 0, 2, 5 and 7 T is shown in Fig. 3.7(b). The zero-field data show a clear peak at T_N = 5.4 K. The heat capacity peak suppresses in magnitude, smears and shifts to higher temperature with increasing strength of the external magnetic field.

3.3.5 Magnetocaloric effect

3.3.5.1 Magnetic entropy change

The magnetic entropy change (ΔS_m) can be calculated from the magnetization isotherms as well as heat capacity data. The ΔS_m from the magnetization isotherms can be obtained using the Maxwell equation: $-\Delta S_m(T,H) = \int_0^H (\partial M/\partial T)_H \, dH$. We used numerical approximation to the integral for small temperature $\Delta Sm = \sum_i \frac{M(H_{i+1},T_{i+1})-M(H_i,T_i)}{T_{i+1}-T_i}\Delta H_i$, where$M_i$ and M_{i+1} are the experimentally measured values of magnetization for a magnetic field H_i at temperatures T_i and T_{i+1}, respectively. The main panel of Fig 3.8 shows the temperature dependence of $-\Delta S_m$ for $\mu_0\Delta H$ = 0.5 T to 5 T calculated from magnetization isotherms shown in Fig. 3.5(b). The $-\Delta S_m$ for $\mu_0\Delta H$ = 0.5 T is almost zero at T = 50 K and it gradually increases with decreasing temperature and goes through a peak value around T_N. While the peak position is not affected, the magnitude of the peak increases with increasing value of ΔH. The maximum value of $-\Delta S_m$ at the peak ($-\Delta S_m^{max}$) reaches 10 J/kg.K for $\mu_0\Delta H$ = 1 T, 30 J/kg.K for $\mu_0\Delta H$ = 3 T and 40.27 J/kg.K for $\mu_0\Delta H$ = 5 T. The $-\Delta S_m$ versus temperature for $\mu_0\Delta H$ < 1 T is shown in the inset of Fig 3.8. Below T_N and under low

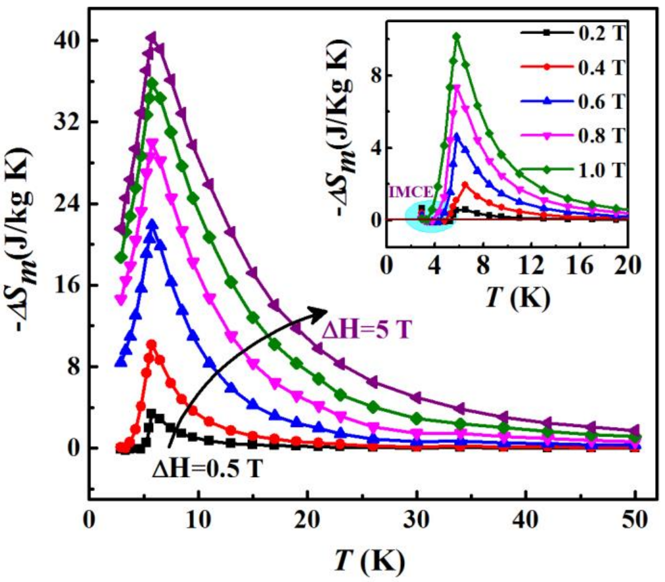

Figure 3.8 Main panel: Temperature dependence of magnetic entropy change ($-\Delta S_m$) for field changes from 0.5 T to 5 T. Inset: $-\Delta S_m$ as a function of temperature for low field changes from 0.2 T to 1.0 T.

magnetic fields ($0.2\ \mathrm{T} < \mu_0\Delta H < 0.8\ \mathrm{T}$), we observe a small inverse magnetocaloric effect,i.e., $-\Delta S_m$ is negative. The negative value of $-\Delta S_m$ means the magnetic entropy $S_m(H,T)$ increases under the magnetic field. This behavior was predicted by von Ranke *et al*. when the spins are not initially aligned along the anisotropy axis.[162] As the magnetic field increases above 1T, the inverse MCE vanishes.

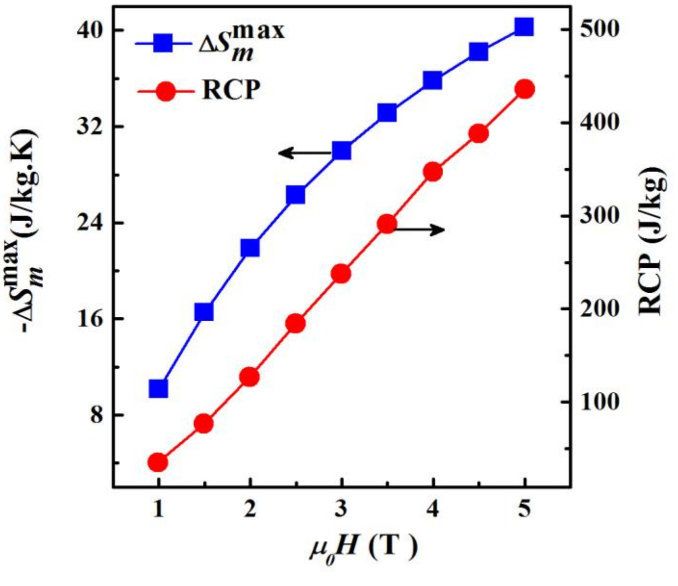

Figure 3.9 Magnetic field dependences of maximum magnetic entropy change ($-\Delta S_m^{max}$) on left y-axis and refrigeration cooling power (*RCP*) on right y-axis.

Besides a large ΔS_m value, a good magnetic refrigerator should show a large adiabatic temperature change (ΔT_{ad}) and relative cooling power (*RCP*). The *RCP* quantifies the amount of heat transferred between the cold and the hot reservoirs separated by a temperature difference δT_{FWHM} in an ideal Carnot cycle and it is defined as $RCP = -\Delta S_m^{max} \times \delta T_{FWHM}$, where δT_{FWHM} is the temperature span corresponding to the full width at half maximum of the ΔS_m versus T curve. The field dependences of $-\Delta S_m^{max}$ and *RCP* are shown in Fig. 3.9 at left and right hand scales, respectively. The *RCP* increases with increasing magnetic field and reaches 440 J/kg for $\mu_0\Delta H$ = 5T.

3.3.5.2 Adiabatic temperature change

The adiabatic temperature change as well as magnetic entropy change can be obtained from the temperature dependence of magnetic entropy data under different magnetic fields. The temperature dependence of magnetic entropy (S_m) at a constant field H is estimated directly from the heat capacity data, measured under a magnetic field H using the relation$S(H,T) = \int_{T_1}^{T_2} \frac{C_p(H,T)}{T} dT$, where T_1 and T_2 are the lowest and highest temperatures of interest. After subtracting the lattice contribution, the heat capacity data plotted as C_p/R, where R is the gas constant, is shown in inset of Fig. 3.10(a). The main panel of Fig. 3.10 (a) shows the normalized magnetic entropy (S_m/R) calculated from the heat capacity under different magnetic fields. For temperatures above 8K, the zero field S_m/R approaches a temperature independent value 2.08, which is the same as the maximum magnetic entropy [S_m/R = ln(2S+1) = ln(8) = 2.079] expected for complete randomization of 4*f* spins. The zero-field magnetic entropy drops rapidly below T_N and S_m decreases in value with increasing magnetic field strength. The magnetic entropy change (ΔS_m) and adiabatic temperature change (ΔT_{ad}) are shown in Fig. 3.10 (b) and (c), respectively, for field changes of $\mu_0\Delta H$ = 2, 5 and 7 T. The values of -ΔS_m and ΔT_{ad} are 40(47.32) J/kg.K and 16.6(20) K for $\mu_0\Delta H$ = 5 T

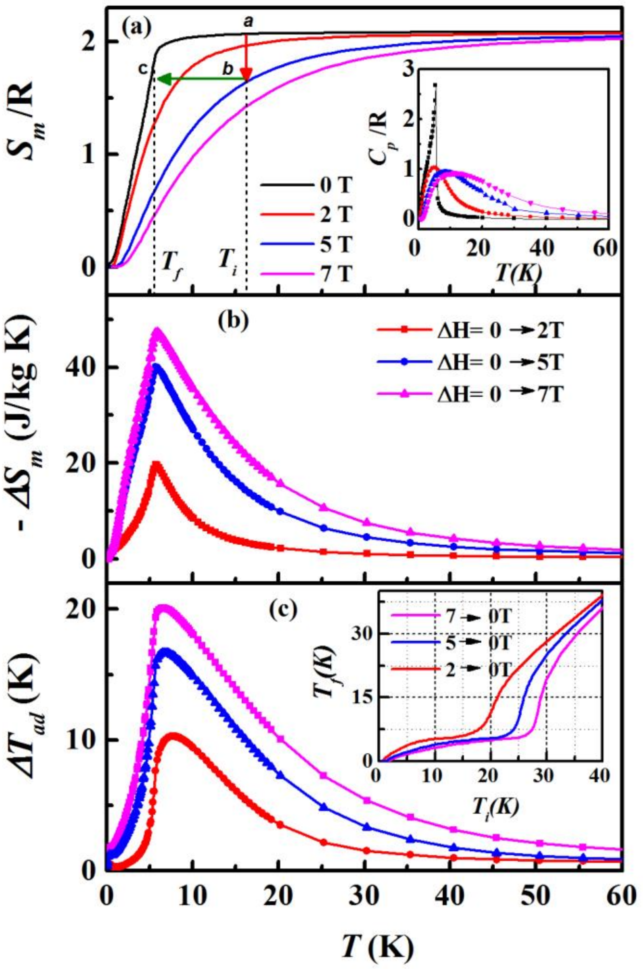

Figure 3.10 (a) Main panel: Temperature dependence of magnetic entropy (S_m) calculated from heat capacity data. The inset shows the temperature dependence of the heat capacity under different fields after subtracting the lattice contribution. (b) Magnetic entropy change ($-\Delta S_m$) and (c) adiabatic temperature change (ΔT_{ad}). Inset: Final temperature T_f as a function of initial temperature T_i in the adiabatic demagnetization process for different values of the magnetic field.

and 7 T, which are comparable to the values obtained for the $EuTiO_3$ single crystal.[163] The temperature dependence of ΔT_{ad} in the main panel of Fig. 3.10 (c) indicates the temperature rises upon adiabatic magnetization. The dependence of the final temperature (T_f) that can be reached by an adiabatic removal of magnetic field at temperature T_i is more intuitive and it is shown in the inset of Fig. 3.10 (c). If the sample is initially at 30 K and magnetized by 7 T, decreasing the magnetic field adiabatically to zero causes the sample temperature drop to 19.5 K. The lower the T_i, the lower is the T_f. An adiabatic removal of magnetic field from T_i =

20 (5) K leads to 5 (0.17) K. For comparison of the magnetocaloric properties of $EuTiO_3$ with other materials, we list the maximum values of $-\Delta S_m$, ΔT_{ad}, *RCP* and the magnetic transition temperature for other potential magnetic refrigerant materials having a phase transition below 40 K along with $EuTiO_3$ in Table 3.1. EuO and $DyTiO_3$ have a magnetic ordering temperature above 40 K. It can be noted that ΔT_{ad} observed in $EuTiO_3$ is higher than other promising magnetocaloric materials for refrigeration from 1 to 40 K. Only the metal-organic framework material $Gd(HCOO)_3$ shows a comparable value. Therefore, $EuTiO_3$ has a great potential as a refrigerant material below 40 K.

Compound	**ΔT_{ad} (K)**	**$-\Delta S_m$ (J/kg.K)**	***RCP* (J/kg)**	**$\mu_0\Delta H$ (T)**	**T_N/T_C (K)**	**Ref.**
$EuTiO_3$ (PC)	16.5	40.4	440	5	5.4	This work
$EuTiO_3$ (SC)	16.6	42.4	450	5	5.6	[163]
$DyTiO_3$	6.79	16	360	5	65	[87]
EuO	6.8	17.5	-	5	69	[164]
Eu_3O_4	7.8	12.7	-	5	5.3	[165]
EuSe	-	37.5	435	5	4.6	[166]
$EuHo_2O_4$	11.6	22.5	260	5	5	[167]
$ErAl_2$	12	36	-	5	13	[168]
$Gd_3Ga_5O_{12}$	24	25	-	5	1	[169]
$Gd_3Al_5O_{12}$	-	29	-	5	-	[170]
$Gd(HCOO)_3$	22	55	-	7	2	[171]

Table 3.1 Maximum values of $-\Delta S_m$, ΔT_{ad}, *RCP* and magnetic transition temperature for $EuTiO_3$ with other potential magnetic refrigerant materials. SC: single crystal and PC: polycrystal.

3.3.6 DC resistivity

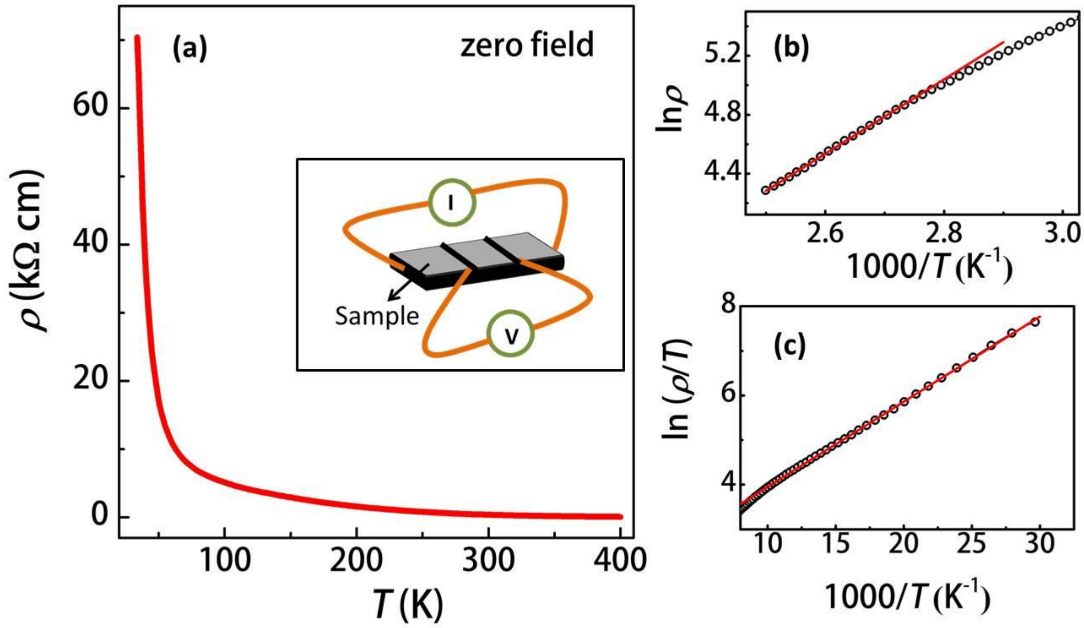

Figure 3.11 (a) Main panel: Temperature dependence of dc resistivity of $EuTiO_3$ measured using four-probe method. Inset shows the four probes configuration of the sample. (b) ln(ρ) versus 1/T curve and (c) ln(ρ/T) versus 1/T curve.

The main panel of Fig. 3.11(a) shows the temperature dependence of the four-probe dc resistivity (ρ_{dc}) for $EuTiO_3$ under zero field measured while cooling from 400 K to 30 K. The current flow in the sample was kept low enough (~ 500 nA) to avoid Joule heating. The resistivity keeps increasing with lowering temperature. A gradual increase between 400 K and 50 K is followed by a rapid increase below 50 K. The value of resistance below 30 K exceeds the instrument limit. The four-probe resistivity in the high temperature regime follows thermally activated behavior $\rho = \rho_0 \exp\left(\frac{E_a}{k_B T}\right)$. Fig. 3.11(b) shows ln($\rho$) versus 1/$T$ plot with a linear fit in temperature region 400 K < T < 345 K for four-probe resistivity data under zero field. The activation energy E_a calculated from the linear fit of ln(ρ) versus 1/T plot is 217 meV, which is comparable to the reported E_a value for polycrystalline $EuTiO_{3-\delta}$ sample.[172] The nature of electrical conduction changes from thermal activation at high temperature to small polaron hopping $\rho = \rho_0 T \exp\left(\frac{E_p}{k_B T}\right)$ at lower temperature range (100K – 35K). Fig. 3.11(c) shows ln(*ρ/T*) versus 1/T curve with linear fit (red line). The polaron hopping energy (E_p) calculated from the linear fit of ln(*ρ/T*) versus 1/*T* curve is 16.45 meV, which is much smaller than the E_a = 217 meV.

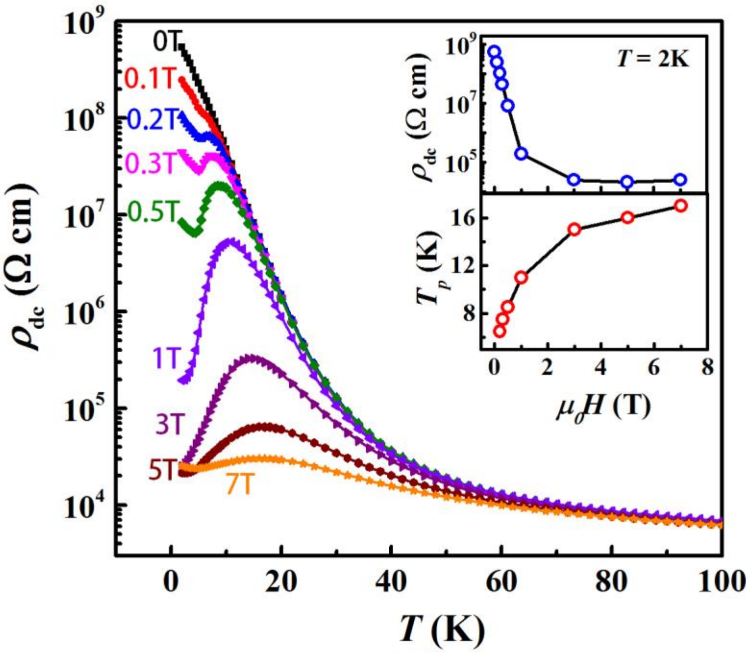

Figure 3.12 Main panel: Temperature dependence of two-probe dc resistivity (ρ_{dc}) under zero and different magnetic fields. Top inset: ρ_{dc} at T = 2K as a function of magnetic field. Bottom inset: The peak position in $\rho_{dc}(T)$ as a function of magnetic field.

Since four-probe resistivity was not reliably measurable below 30 K, we measured two-probe dc resistivity from 100 K down to 2 K using a Keithley 6517A electrometer. The main panel of Fig. 3.12 shows the temperature dependence of two-probe dc-resistivity (ρ_{dc}) under different magnetic fields. In zero field, $\rho_{dc}(T)$ increases by five orders of magnitude as temperature decreases from 100 K to 2 K. However, $\rho_{dc}(T)$ shows a kink at T = 5.5 K under a small magnetic field of 0.1 T which transform into a peak at $T = T_p$ under higher magnetic fields (0.2 T ≤ $\mu_0 H$ ≤ 7 T) in paramagnetic state. The peak broadens and T_p shifts toward higher temperature with increasing field strength. The peak in $\rho_{dc}(T)$ represents an insulator to metal (I-M) transition. The upper and lower insets of Fig. 3.12 show the field dependence of ρ_{dc} at T = 2K and I-M transition temperature (T_p), respectively. The ρ_{dc} decreases by 4 orders of magnitude as magnetic field increases from 0 T ($\rho_{\mathrm{dc}} \sim 10^9\ \Omega$ cm) to 1 T ($\rho_{\mathrm{dc}} \sim 10^5\ \Omega$ cm), while the change is incremental in the field range 1 T $\leq \mu_0 H \leq$ 7 T. The peak position T_p increases rapidly for $\mu_0 H \leq$ 4T and gradually at higher fields.

We already discussed that $\rho_{\mathrm{dc}}(T)$ follows the thermal activation behavior at high temperature range (400 K-325 K) and small polaron hopping for low temperature range (100 K - 35 K). The low-temperature $\rho_{\mathrm{dc}}(T)$ can also be described by the three-dimensional Mott

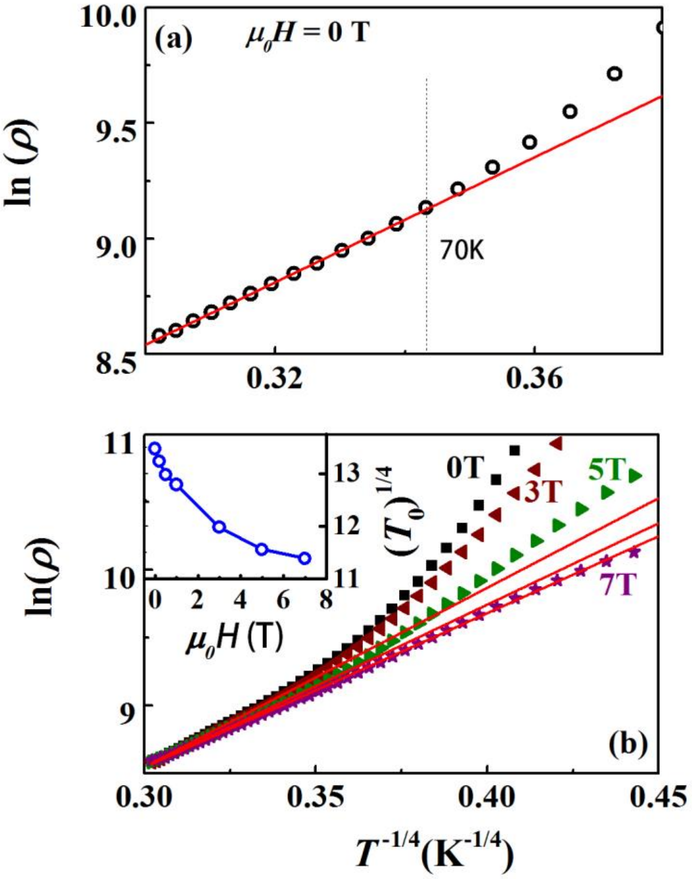

Figure 3.13 (a) ln(ρ) versus $(1/T)^{1/4}$ curve with linear fit for four-probe resistivity data for $\mu_0 H$ = 0 T, and (b) Main panel: ln(ρ) versus $(1/T)^{1/4}$ curve with linear fit for two-probe resistivity data under different magnetic fields. Symbol and red line represents the experimental data and linear fit. Inset: The value of $(T_0)^{1/4}$ as a function of magnetic field.

VRH model: $\rho = \rho_0 exp\left(\frac{T_0}{T}\right)^{1/4}$ where T_0 is the characteristic temperature given by $T_0 = \frac{1.5}{k_B\alpha^3 N(E_F)}$, where $N(E_F)$ is the density of states and α is decay length of localized wave function.[173] The value of T_0 can be calculated from the slope of linear fit of ln(ρ) verses $T^{-1/4}$ plot. The ln(ρ) versus $T^{-1/4}$ curve with linear fit for four-probe resistivity is shown in the inset of Fig. 3.13(a). The value of $T_0^{1/4}$ is 16.19 $K^{1/4}$, which closely matches with the reported $T_0^{1/4}$ value for $EuTiO_3$ prepared under 30% H_2 atmosphere.[11] The main panel of Fig. 3.13 (b) shows the ln(ρ) verses $T^{-1/4}$ plot with linear fit for temperatures 120 K < T < 25 K under selected magnetic fields for the two-probe resistivity data. In zero field, $\rho(T)$ below T ~ 70 K deviates from the VRH behavior. However, VRH mechanism fairly fits to the data for $\mu_0 H$ = 7T down to 25 K in the insulating state. The value of $T_0^{1/4}$ decreases with increasing magnetic field from 13.47 $K^{1/4}$ for $\mu_0 H$ = 0T to 11.39 $K^{1/4}$ for $\mu_0 H$ = 7T (inset of Fig. 3.13(b)). The decrease in T_0 value indicates that α increases and localization length ξ (inversely proportional to α) decreases as magnetic field increases. It means that the hopping distance R increases with increasing magnetic field.

To find the possible connection with I-M transition and magnetic property, we plot ρ(T) and inverse susceptibility (χ^{-1}) in Fig. 3.14 (a), (b), (c) and (d) for $\mu_0 H$ = 0.1, 1, 3 and 7 T, respectively. The left and right scales represent the $\chi^{-1}(T)$ and $\rho(T)$ data, respectively. The $\chi^{-1}(T)$ is fitted with Curie-Weiss law, $= \frac{C}{T+\theta_{CW}}$, where θ_{CW} is Curie-Weiss temperature and C is the Curie-Weiss constant. From Fig. 3.14(a), the $\chi^{-1}(T)$ follows the Curie-Weiss law for T > 7 K under $\mu_0 H$ = 0.1 T and a small kink appears in $\rho(T)$. For higher magnetic fields $\mu_0 H$ = 1 T, 3 T and 7 T, the $\chi^{-1}(T)$ deviates from the Curie-Weiss behavior below $T \approx T_p$ and the deviation shifts to higher temperature with increasing magnetic field. The deviation of inverse susceptibility from the Curie-Weiss behavior below $T \approx T_p$ in paramagnetic state

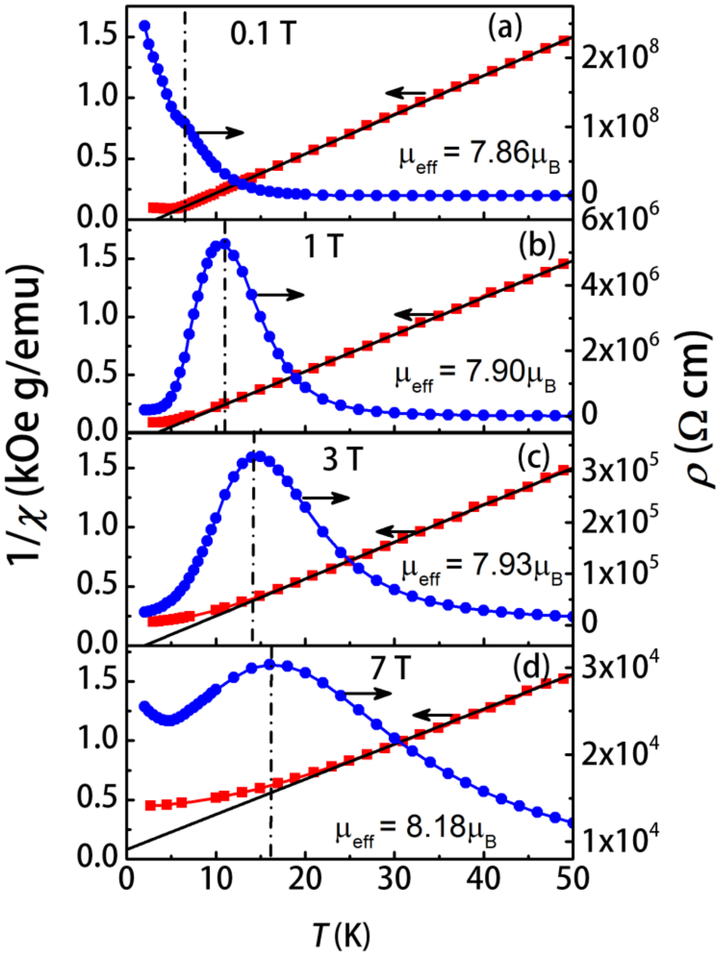

Figure 3.14 Temperature dependence of inverse susceptibility (χ^{-1} on the left scale) and dc-resistivity (ρ on the right scale) under the magnetic fields of (a) 0.1 T, (b) 1 T, (c) 3 T and (d) 7 T. Solid line represents the Curie-Weiss law fit.

indicates the possibility of ferromagnetic clusters formation above T_C indicates the possibility of ferromagnetic clusters formation above T_C.[174, 175] Therefore; the insulator-metal transition in paramagnetic region might be due to the formation of local ferromagnetic clusters. The effective magnetic moment (μ_{eff}) is calculated using the relation $\mu_{eff} = \left(\frac{3k_B C_M}{N}\right)^{1/2}$, where C_M is calculated from the linear fit of $\chi^{-1}(T)$. The μ_{eff} value is 7.86μ_B for $\mu_0 H$ = 0.1 T, which is slightly lower than the theoretically expected $\mu_{eff} = 2\sqrt{J(J+1)}\mu_B$ = 7.94μ_B, corresponds to the 4f^7 spin configuration of Eu^{2+} (J = 7/2). The μ_{eff} value increases with increasing field strength and reaches 8.18 μ_B for $\mu_0 H$ = 7 T. The Curie-Weiss temperature θ_{CW} is 3.38 K for $\mu_0 H$ = 0.1 T, decreases with increasing magnetic field and reaches – 0.91 K for $\mu_0 H$ = 7 T.

3.3.7 DC magnetoresistance

The main panel of Fig. 3.15 shows the temperature dependence of magnetoresistance (MR) calculated from the temperature dependent dc-resistivity using the formula, $MR = \frac{\rho(H,T)-\rho(0,T)}{\rho(0,T)}$, where $\rho(0,T)$ and $\rho(H,T)$ are the resistivity values under zero and H magnetic field, respectively at temperature T. The MR is negative for all the fields (0.1 T ≤ $\mu_0 H$ ≤ 7 T). When $\mu_0 H$ = 0.1 T, MR is negligible above 15 K but shows a rapid increase below 10 K. At T = 2 K, MR is ~ −58 % for 0.1 T and it increases to −99 % for 0.5 T. The MR shows a small increase at 2 K for $\mu_0 H$ > 0.5 T. However, as the strength of magnetic field increases, MR becomes appreciable at high temperature too and shows incremental increase for $\mu_0 H \geq$ 0.5 T. This trend is also reflected in the field dependence of MR measured at fixed temperatures shown in the inset of Fig. 3.15. A large MR (– 45 % for $\mu_0 H$ = 7 T) is seen at T = 44 K, far above T_N.

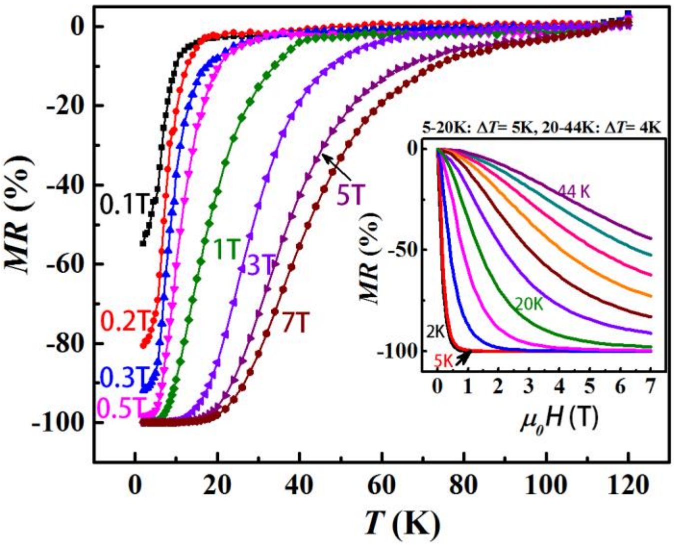

Figure 3.15 Main panel: Temperature dependence of magnetoresistance (*MR*) under different magnetic fields. Inset: Field dependence of *MR* at different temperatures.

According to theoretical model of spin disorder scattering, the relation between field dependent *MR* and *M* in paramagnetic region for low field regime (small *M*) is expressed by a scaling function[4],[176],[118]

$$\frac{\Delta\rho}{\rho_0} = -\,C\left(\frac{M}{M_{max}}\right)^2 = -Cm^2 \tag{3.5}$$

where $m = M/M_{max}$, M_{max} is the magnetization under $\mu_0 H = 5$ T and C is a scaling constant that depends on the density of charge carriers per magnetic unit cell. The Eq. (3.5) can be obtained from the expansion of empirical equation

$$\frac{\Delta\rho}{\rho_0} = a'[exp(-b'm^2) - 1] \tag{3.6}$$

into power series for low *M* values, where a' and b' are constants and $C = a'b'$.[177]

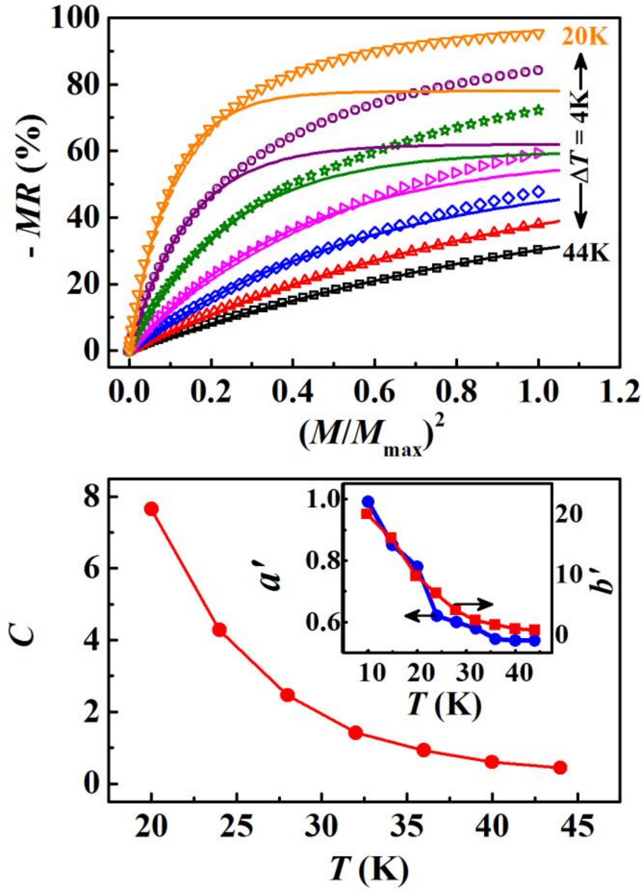

Figure 3.16 (a) Symbols: Negative *MR* versus $(M/M_{max})^2$ at different temperatures and Line: Fit to equation (3.6). (b) Temperature dependence of the coupling coefficient *C*. Inset shows the constants *a* (left scale) and *b* (right scale) as a function of temperature.

The $-MR$ versus $(M/M_{\max})^2$ curves show a linear behavior only for temperatures $T \geq$ 36 K and magnetization $m^2 \leq 0.1$. Therefore; we attempt to fit the MR versus M curves at different temperatures using Eq. (3.6). Fig 3.16(a) shows the field dependent $-MR$ versus $(M/M_{\max})^2$ curves fitted with Eq. (3.6). For $T = 40$ K and 44 K, the curves fit in the whole m regime but deviation occurs for $T \leq 36$ K. The deviation shifts to lower m value as temperature decreases from 36 K to 20 K. The values of fitting parameters a' and b' as a function of temperature are shown in inset of Fig. 3.16(b) at left and right scales, respectively. The C value calculated from the fitting parameters a' and b' of Eq. (3.6) as a function of temperature is shown in main panel of Fig. 3.16(b). The value of C increases with decreasing temperature and reaches from $C = 0.44$ at $T = 44$ K to $C = 7.8$ at $T = 20$ K. While a value of $C \sim 1$ represents a weak d-f coupling, for strong coupling C should be above 4. In manganites, close to the insulator-metal phase boundary, $C \approx 4$-5 and it decreases to 1 for metallic compositions away from the phase boundary.[178] The large C value for $EuTiO_3$ even in paramagnetic region represents the strong coupling between charge carriers and Eu^{2+}:$4f^7$ spins.

Eq. (3.5) was initially applied to explain negative MR observed in diluted magnetic alloys (eg. $Cu_{1-x}Mn_x$) at low temperatures in terms of the scattering of carriers by localized moments. The quantitative disagreement with the localized magnetic moment model exists, while the qualitative features of the negative MR at low fields were consistent. That is because the localized moment theory was based on calculation involving the second-order perturbation expansion of the exchange Hamiltonian. Even a theory of spin-disorder scattering by magnetic fluctuation developed by C. Hass for ordered magnetic semiconductor was based on the earlier theory of magnetic metal alloy and involved only second-order perturbation expansion.[117] A modified theory was proposed by Khosla and Fischer that takes higher order terms of the perturbation into account.[121] The negative magnetoresistance is then given by[123]

$$MR = -a^2 \ln(1 + b^2 H^2) \tag{3.7}$$

where a and b are the physical characteristics of the exchange interaction and H is the applied magnetic field. The a and b are given by

$$a = A_1 J D(\epsilon_F)[S(S+1) + \langle M \rangle^2] \tag{3.8}$$

and

$$b^2 = \left[1 + 4S^2\pi^2\left(\frac{2JD(\epsilon_F)}{g}\right)^4\right]\left(\frac{g\mu_B}{\alpha k_B T}\right)^2 \tag{3.9}$$

Here, J is the exchange interaction energy, $D(\varepsilon_F)$ is the density of states at Fermi level and $\langle M \rangle$ is the average magnetization.

Fig. 3.17 (a) shows the MR data fitted with Eq. (3.7). The experimental MR data fit very well in full field range for $T \geq 32$ K, while the deviation occurs around $\mu_0 H = 4$ T for $T = 28$ K and shifts to lower field value as temperature decreases. Fig. 3.17 (b) show the temperature dependence of the coefficients a and b at left and right scales, respectively. The value of b increases with decreasing temperature.

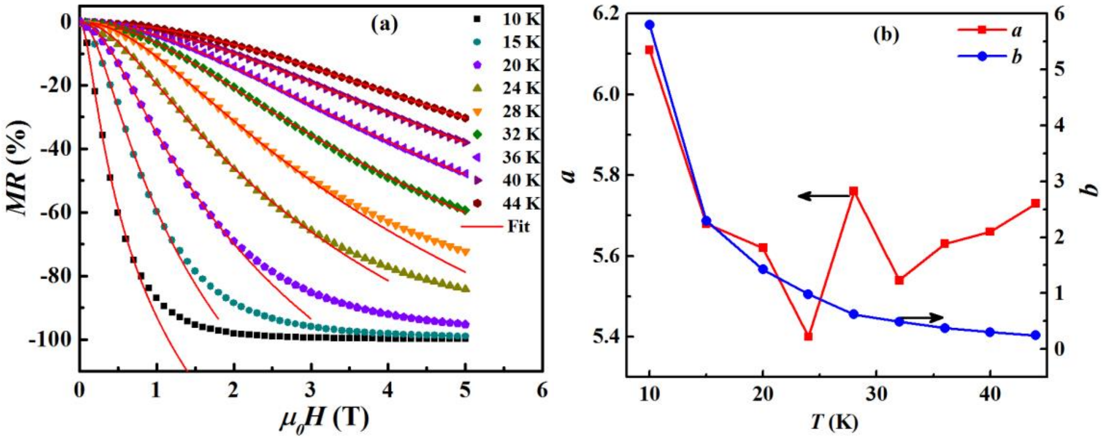

Figure 3.17 (a) Symbols: Experimental *MR* as a function of magnetic field at different temperatures. Solid line: Least-squares fit of experimental *MR* to Eq. (3.7). (b)Temperature dependence of coefficients *a* (left y-axis) and *b* (right y-axis) in Eq. (3.7).

Since MR of $EuTiO_3$ follows the proposed models describing the spin-disorder scattering at high temperatures ($T \geq 10$ K), the negative colossal magnetoresistance in $EuTiO_3$ occurs most likely due to the suppression of $4f^7$ spin fluctuations by magnetic field, which reduces the spin-disorder scattering as temperature decreases and magnetic field increases.

3.3.8 Dielectric constant and ac resistivity

We measured capacitance (C) and ac resistance (R_{ac}) of a thin parallel-plate capacitor like structure of polycrystalline $EuTiO_3$ sample simultaneously for different frequencies (f = 1 kHz – 1 MHz) of the ac voltage excitation while warming from 10 K to 400 K. The dielectric constant (ε) and ac resistivity (ρ_{ac}) are calculated using standard formulas $\varepsilon = \frac{Ct}{\varepsilon_0 A}$ and $\rho_{ac} = \frac{R_{ac}A}{t}$, respectively, where t is the thickness, A is the cross section area of the

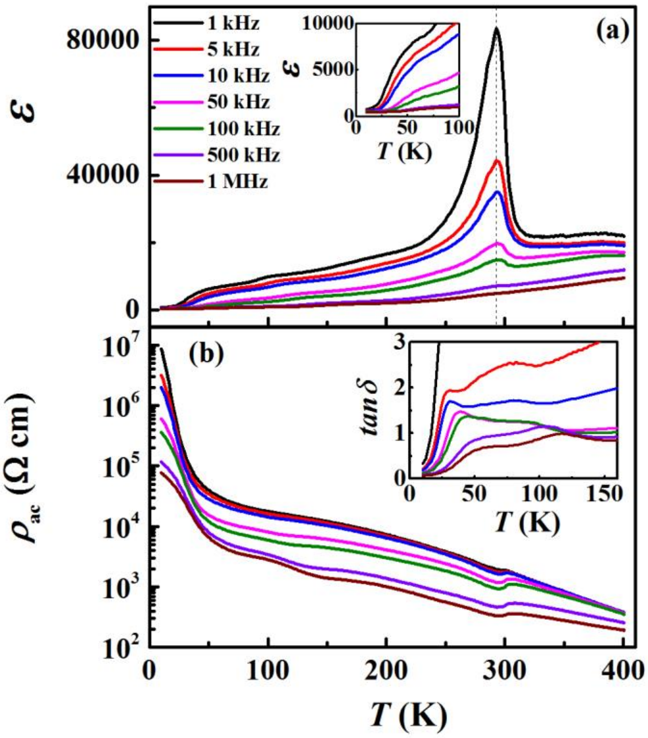

Figure 3.18 Main panels: Temperature dependence of (a) dielectric constant (ε) and (b) ac resistivity (ρ_{ac}) for various frequencies. Insets: (a) $\varepsilon(T)$ in low temperature range (10-100K) and (b) temperature dependence of dielectric loss ($tan\delta$).

sample and ε_0 is vacuum permittivity. The main panels of Fig. 3.18(a) and (b) show the temperature dependence of ε and ρ_{ac}, respectively, for different frequencies. $\varepsilon(T)$ at 1 kHz shows a pronounced peak at temperature of 292 K and a step like decrease in the temperature regime around 20 K. The peak in $\varepsilon(T)$ at T = 292 K decreases in amplitude as frequency increases from 1 kHz to 100 kHz and vanishes for $f \geq$ 500 kHz. The peak in $\varepsilon(T)$ is unlikely due to ferroelectric transition. However, J. F. Scott predicted that an anomaly in dielectric constant could be observed in the vicinity of antiferrodistortive transition.[179] Therefore, the pronounced peak in $\varepsilon(T)$ is most likely due to an antiferrodistortive phase transition that is investigated in $EuTiO_3$ in a temperature range, 250 K < T < 310 K, by means of various techniques.[56, 57, 180].

The enlarge view of $\varepsilon(T)$ at low temperature is shown in the inset of Fig. 3.18 (a). For f = 1kHz, the value of ε (~ 700) is temperature and frequency independent in a temperature regime 10 K < T < 20 K. However, it increases rapidly from ~ 700 at T = 20 K to ~10^4 at T = 75 K and shows a step like increase. We observed that the step like increase shifts toward higher temperature as frequency increases from 1 kHz to 100 kHz and there is no step like increase for $f \geq$ 500 kHz. The shift in step like increase provides a sign of dielectric relaxation, which could be responsible for strange increase in ε above 30 K. Recently, S. Kamba et al. also noticed a huge increase in ε (T) of $EuTiO_3$ ceramic above 80 K and suggested a Maxwell-Wagner relaxation responsible for this unusual increase. However, they did not present the dielectric constant data above 100 K.

In contrast of $\varepsilon(T)$, $\rho_{ac}(T)$ for 1kHz increases smoothly with decreasing temperature from 400 to 60 K and rapidly below 60 K. An anomaly is observed at T = 292 K for all frequencies, exactly at same temperature, where the strong peak is found in $\varepsilon(T)$. At T = 400 K, the ρ_{ac} value for 1 kHz (370 Ω cm) is larger than the ρ_{dc} value (74 Ω cm). The ρ_{ac} value is frequency dependent throughout temperature range and decreases with increasing frequency. The $\rho_{ac}(T)$ is quite similar to $\rho_{dc}(T)$ (Fig. 3.11 (a)) except an anomaly at T = 292 K. To examine the step like increase in $\varepsilon(T)$, we also measured capacitance (C) and dielectric loss ($tan\delta$) simultaneously as a function of temperature. The temperature dependence of $tan\delta$ is shown in the inset of Fig. 3.18(b). While $tan\delta(T)$ for f = 1kHz increases rapidly with increasing temperature, $tan\delta(T)$ for $f \geq 5$ kHz shows a peak. As frequency increases, the peak position in $tan\delta$ shifts to higher temperature and it is found exactly at same temperature where the step like increase starts in $\varepsilon(T)$. The step like increase in $\varepsilon(T)$ and the peak in $tan\delta(T)$ indicate the possibility of dielectric relaxation in this material at temperatures much above magnetic transition temperature.

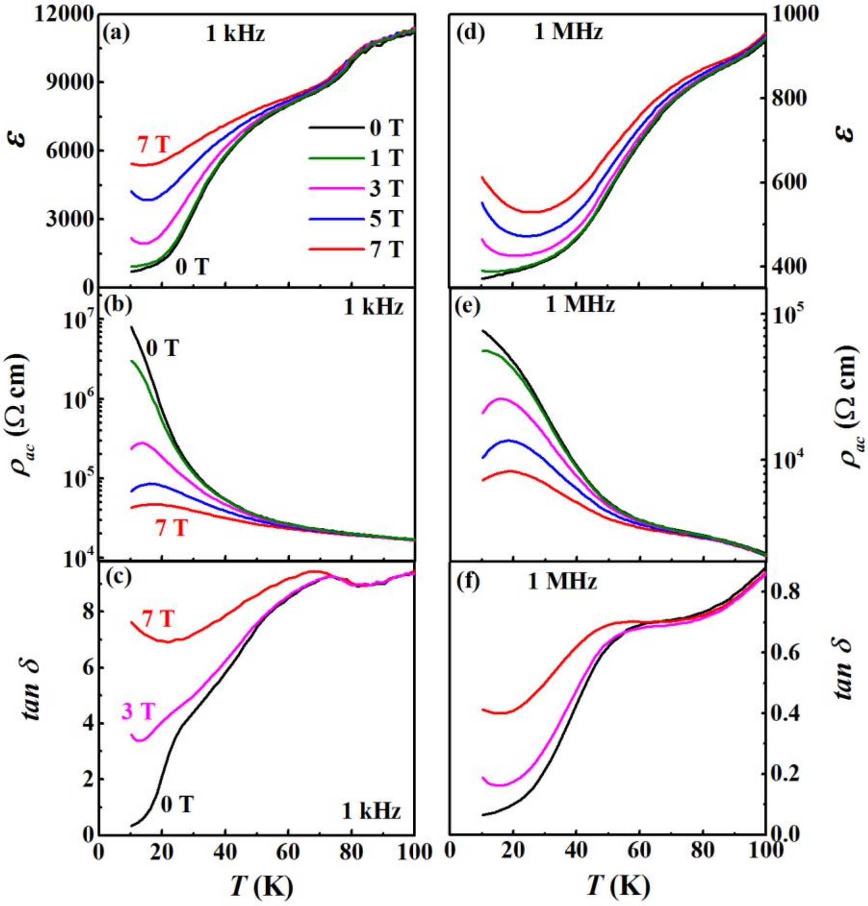

Figure 3.19 Temperature dependence of (a) dielectric constant (ε), (b) ac resistivity (ρ_{ac}) and (c) dielectric loss ($tan\delta$) for f = 1 kHz under various magnetic fields. (d) ε (e) ρ_{ac} and (f) $tan\delta$ for f = 1 MHz.

Fig. 3.19 (a), (b) and (c) show the temperature dependence of ε, ρ_{ac} and $tan\delta$ respectively, for f = 1 kHz measured upon cooling from 100 K to 10 K under different magnetic fields. The $\varepsilon(T)$ in zero field decreases rapidly between 100 K and 20 K and shows a weak temperature dependence below 20 K. Note that 20 K is much above the Neel temperature (T_N = 5.4 K). While $\varepsilon(T)$ under 1 T is field independent above 25 K, it increases in magnitude relative to zero field value below 25 K. Under the field of 3 T, $\varepsilon(T)$ increases in magnitude relative to zero field value below 50 K and also shows an upturn around 15 K. The upturn shifts towards higher temperature with increasing magnetic field strength. For f = 1MHz (Fig. 3.19 (d)) the weakly temperature dependent behavior of $\varepsilon(T)$ in zero field extends until 35 K and an upturn in $\varepsilon(T)$ under 3 T field occurs at 21 K. As magnetic field increases, the upturn shifts to higher temperature and occurs at 26 K for μ_0H = 7 T.

The ρ_{ac}(T) in zero field and for 1 kHz increases rapidly below 50 K and it decreases in magnitude under 1 T below 30 K. Under higher magnetic fields, ρ_{ac}(T) decreases more in magnitude and shows insulator-metal like transition. The insulator-metal transition shifts towards higher temperature as magnetic field increases and it occurs at T = 13 K for μ_0H = 3 T and at T = 17 K for μ_0H = 7 T. For f = 1 MHz, the transition occurs at T = 16 K for μ_0H = 3 T and T = 19 K for μ_0H = 7 T (Fig. 3.19(e)). The value of $tan\delta$ under field is larger than the zero field value for both frequencies f = 1 kHz and 1 MHz. However, the zero field $tan\delta$ exhibits complex temperature dependence.

Fig 3.20 (a), (b) and (c) show the frequency dependence of ε, ρ_{ac} and $tan\delta$, respectively, under different magnetic fields at T = 10 K measured while sweeping frequency from 100 Hz to 1 MHz. While $\varepsilon(f)$ decreases monotonically with increasing frequency under μ_0H = 0 and 1 T, a step like change is visible for $\mu_0H \geq 3$ T. The magnetic field has less impact on ε at $f \geq$ 1MHz and above. For $\mu_0 H$ = 0 T and 1 T, $\rho_{ac}(f)$ decreases monotonically with increasing frequency but shows a weak frequency dependence in low frequency region followed by a faster decrease above a certain frequency for $\mu_0 H \geq$ 3 T. The step like change in $\varepsilon(f)$ occurs around the frequency where $\rho_{ac}(f)$ undergoes a change of slope. While ε depends weakly on the magnetic field for f = 1 MHz, ρ_{ac} is still field dependent at f = 1 MHz. The $tan\delta(f)$ also decreases monotonically under $0 \leq \mu_0 H \leq 3$ T as frequency increases, but a change in slope is observed under higher magnetic fields. As like $\rho_{ac}(f)$, $tan\delta$ for f = 1 MHz is also field dependent. The frequency dependent *MC, ac MR* and *MDL* calculated from $\varepsilon(f)$, $tan\delta(f)$ are shown in Fig. 3.20(d), (e) and (f), respectively. The magnetodielectric effect

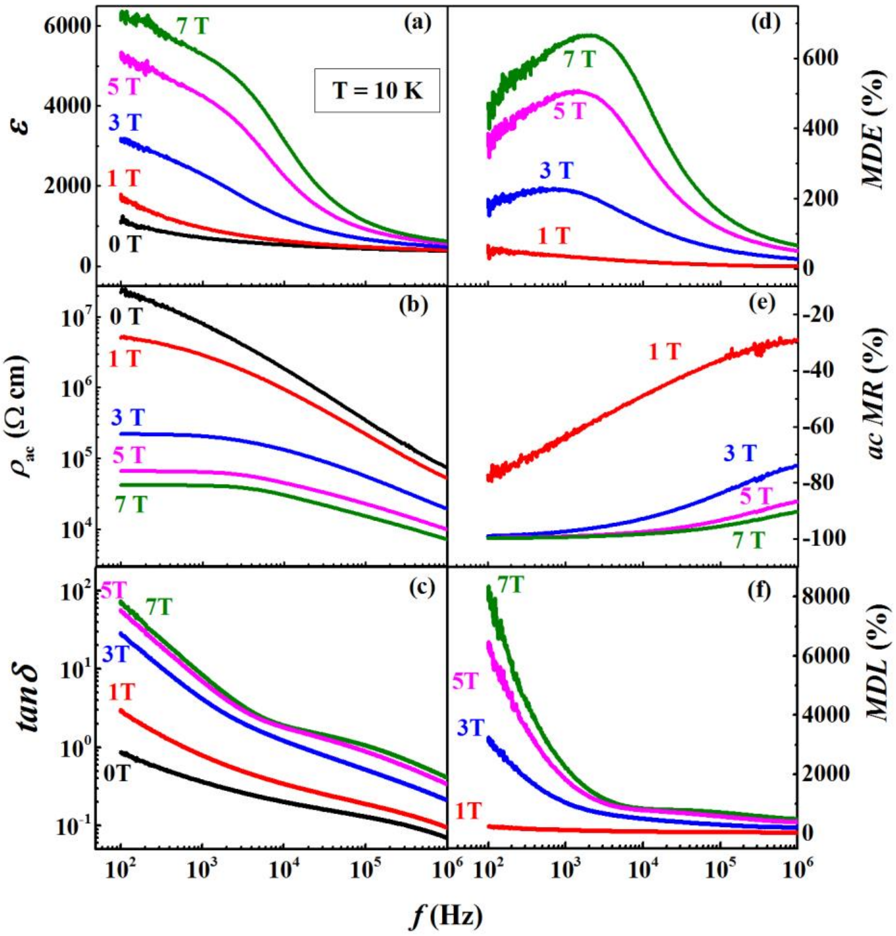

Figure 3.20 Frequency dependence of (a) dielectric constant (ε), (b) ac resistivity (ρ_{ac}), (c) dielectric loss (*tan*δ), (d) magnetodielectric effect (*MDE*), (e) magnetoresistance (*MR*) and (f) magnetodielectric loss (*MDL*) at T = 10 K under various magnetic fields.

(*MDE*), ac magnetoresistance (ac *MR*) and magnetodielectric loss (*MDL*) are calculated using formulas $MDE = \frac{\varepsilon(H,f)-\varepsilon(0,f)}{\varepsilon(0,f)}$, $ac\ MR = \frac{\rho_{ac}(H,f)-\rho_{ac}(0,f)}{\rho_{ac}(0,f)}$, and $MDL = \frac{tan\delta(H,f)-tan\delta(0,f)}{tan\delta(0,f)}$, respectively. A strong frequency dependence of *MDE*, *MR* and *MDL* is observed for all magnetic fields. For $\mu_0 H$ = 1 T, *MDE* decreases monotonically with increasing frequency from 52 % at 100 Hz to 6 % at 1 MHz. On the other hand, the *MDE* for 3 T goes through a peak value 230 % around 1 kHz. The peak position in *MDE* shifts to higher frequency as the field increases and the maximum *MDE* reaches 700 % at 5 kHz frequency for $\mu_0 H$ = 7 T. From Fig. 3.20 (e), *MR* is negative for all frequencies in contrast to the *MDE*. The *MR* under 1 T decreases rapidly in magnitude as frequency increases from 100 Hz (*MR* = –70 %) to 1 MHz (*MR* = –30 %). For higher magnetic fields ($\mu_0 H \geq$ 3 T), *MR* value decreases gradually with increasing frequency. At *f* = 100 Hz, the *MR* is –100 % for $\mu_0 H$ = 3, 5 and 7 T, but *MR* at *f* = 1 MHz increases as field increases. As can be seen from Fig. 3.20 (f), *MDL* is 3000 % at 100 Hz and under 3 T, it decreases rapidly between 100 Hz and 1 kHz and gradually at higher frequencies, while the change is gradual from 100 Hz to 1 MHz for 1 T. For $\mu_0 H$ = 7T, the *MDL* value exceeds 8000 % at *f* = 100 Hz and decreases rapidly as frequency increases and reaches 5 % at *f* = 1 MHz. Here, we noticed that the *MDE* and *MDL* both are positive for full frequency range (100 Hz- 1MHz), while *MR* is negative. The magnitude to *MDE*, *MR* and *MDL* are not same for all magnetic fields and frequencies.

To investigate the magnetic field dependence of *MDE*, *MR* and *MDL*, we measured ε, ρ_{ac} and $tan\delta$ while sweeping magnetic field from 0 T to 7 T at constant temperature and frequency. The *MDE*, ac *MR* and *MDL* are calculated using standard formulas $MDE = \frac{\varepsilon(H,T)-\varepsilon(0,T)}{\varepsilon(0,T)}$, $ac\ MR = \frac{\rho_{ac}(H,T)-\rho_{ac}(0,T)}{\rho_{ac}(0,T)}$, and $MDL = \frac{tan\delta(H,T)-tan\delta(0,T)}{tan\delta(0,T)}$, respectively. Fig. 3.21 (a), (b) and (c) show *MDE*, – ac *MR* and *MDL*, respectively, as a function of magnetic field at *f* = 1kHz for *T* = 10, 20 and 30 K. At 10 K, *MDE* increases monotonically with

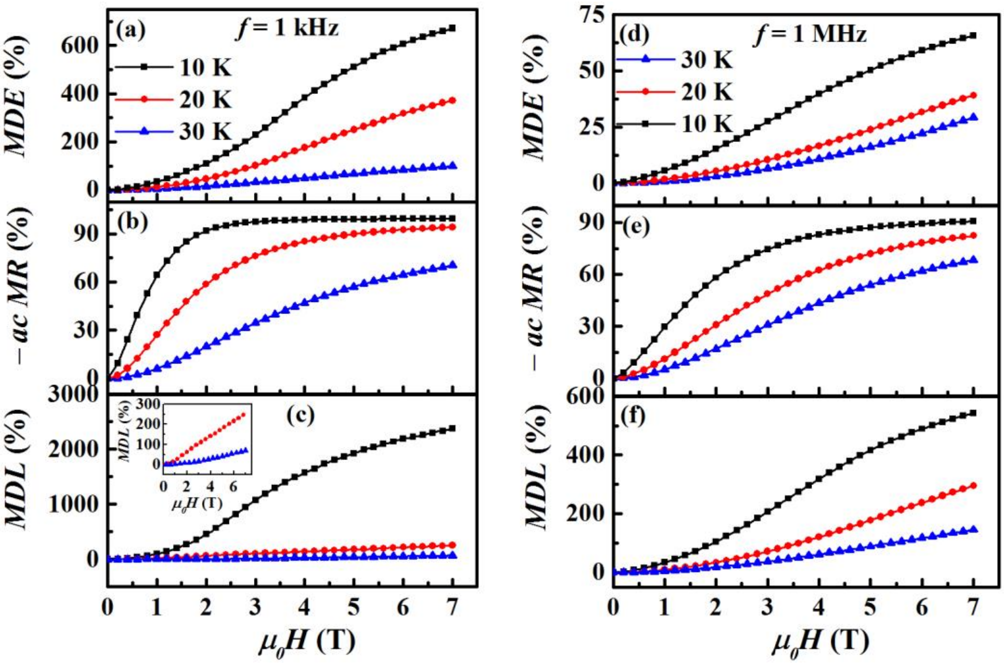

Figure 3.21 Magnetic field dependence of (a) magnetodielectric effect (*MDE*), (b) magnetoresistance (*MR*) and (c) magnetodielectric loss (*MDL*) for *f* = 1 kHz, and (d) *MDE*, (e) *MR* and (f) *MDL* for *f* = 1MHz at different temperatures.

increasing magnetic field and reaches 700% at 7 T and 10 K. This *MDE* value is much larger than 7% *MDE* found at 2 K and 7T, well below the Neel temperature in single crystalline $EuTiO_3$. The magnitude of *MDE* falls with increasing temperature (*MDE* = 700%, 300%, 50% at 7 T for *T* = 10, 20 and 30 K). In contrast to continuous gradual increase in *MDE*, *–MR* shows a dramatic increase of 90% at 2 T. It further increases by only 10 % as the field increases from 2 to 3 T and saturates for higher fields. Thus, the field dependence of *MR* is completely different from that of the *MDE*. As the temperature increases, *MR* also decreases (*MR* = –100%, –90% and –70% at *T* = 10, 20 and 30 K, respectively for μ_0H = 7 T). The field dependence of *MDL* is similar to that of *MDE* at *T* = 10 K, but the value of *MDL* is larger than that of *MDE*. The *MDL* is 2500 % at *T* = 10 K for μ_0H = 7 T and decreases drastically as temperature increases. As seen from inset of Fig. 3.21 (c), *MDL* is only 250 % and 35 % for *T* = 20 K and 30 K, respectively.

Fig. 3.21 (d), (e) and (f) show the magnetic field dependence of *MDE*, – ac *MR* and *MDL* for $f = 1$ MHz at different temperatures. While the field dependence of *MDE* and *MDL* for $f = 1$ MHz is quite similar to that for $f = 1$kHz, *MR* for 1 MHz increases monotonically with increasing magnetic field and does not show any saturation at high fields. The values of *MDE*, *MR* and *MDL* for $f = 1$MHz are smaller than those values for $f = 1$kHz. For $f = 1$ MHz, *MDE* = 70%, *MR* = –90% and *MDL* = 550 % at $T = 10$ K and $\mu_0 H = 7$ T. Fig. 3.22 (a) and (b) show the *MDE* versus MR curves for different temperatures and frequencies. A highly no-linear relation is realized between *MDE* and *MR* for all frequencies and temperatures. G. Catalon predicted that a combination of negative magnetoresistance and Maxwell-Wagner relaxation effect can also lead to a positive magnetocapacitance effect.[148] If the negative magnetoresistance arises from grains (core), *MDE* is expected to be positive and *MDL* is negative. However, the signs of *MDE* and *MDL* are positive for all the frequencies in our $EuTiO_3$ polycrystalline sample (Fig. 3.20 and 3.21).

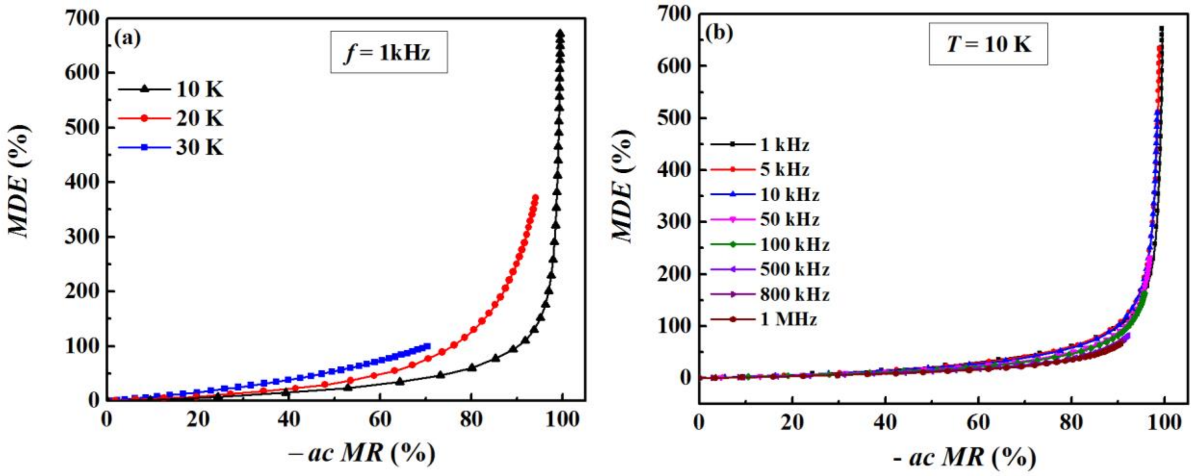

Figure 3.22 ***MDE*** **versus –ac** ***MR*** **curves for (a)** $f = 1$ **kHz at different temperatures and (b) at** $T = 10$ **K for different frequencies.**

The magnetocapacitance effect in $EuTiO_3$ was suggested to arise from coupling of the transverse optical phonon modes to magnetic fields via spin-spin correlation $\langle S_i \cdot S_j \rangle$ of the localized 4f electrons on the nearest neighbor Eu^{2+} ions.[14] The experimental data of the temperature and magnetic field dependences of the dielectric constant were found to fit the relation

$$\varepsilon(T,H) = \varepsilon_0(T)(1+\alpha\langle S_i \cdot S_j\rangle_H) \tag{3.10}$$

where $\varepsilon_0(T)$ is the spin independent part of the dielectric constant and α is the coupling constant between spin correlation and dielectric constant. Katsufuji *et. al.*[3] suggested that hybridization between the Eu-4f orbitals and O-2p orbital is varied depending on the configuration of Eu spins, which modifies the frequency of the T_{1u} mode that contains Eu-O stretching motion. The phonon frequency changes with magnetic field and so is the dielectric constant. Assuming α is positive, $\langle S_i \cdot S_j\rangle_H$ is negative in the antiferromagnetic state, *i.e.*, zero field but changes into positive in the ferromagnetic phase, thus resulting in positive magnetocapacitance. If the spin fluctuation is completely negligible in the paramagnetic state, we can replace $\langle S_i \cdot S_j\rangle_H$ by the square of the spin moment $|\langle S\rangle|^2$ which, in turn, is proportional to the square of magnetization, M^2. Since $M = 0$ when $H = 0$ in the paramagnetic phase, and the dielectric constant is given by

$$\frac{\varepsilon(T,H)}{\varepsilon(T,0)} - 1 = \alpha|\langle S\rangle|^2 = \alpha M^2 \tag{3.11}$$

However, this relation is not necessary to be followed if spin fluctuation is negligible, *i.e.*, $\langle S_i \cdot S_j\rangle_0 \neq 0$. In this case, magnetocapacitance should deviate from M^2 dependence.

The M^2 dependence of the dielectric constant is also predicted from the phenomenological expression for the free energy (F) for a multiferroic, which can be expressed in terms of magnetization (M), polarization (P) and electric field (E) as:

$$F = (1/2\varepsilon_0)P^2 - PE - \alpha PM + \beta PM^2 + \gamma P^2M^2 \tag{3.12}$$

where ε_0 is the dielectric constant in vacuum and α, β, and γ are the coupling constants. Therefore, the dielectric constant, which is second order derivative of the free energy with respect to polarization, is given by

$$\varepsilon = (1/\varepsilon_0) + \gamma M^2 \tag{3.13}$$

Eq. (3.11) is applied to investigate the magnetodielectric coupling in several materials such as $NiCr_2O_4$,[181] $SeCuO_3$ [146]and Mn_3O_4.[182]

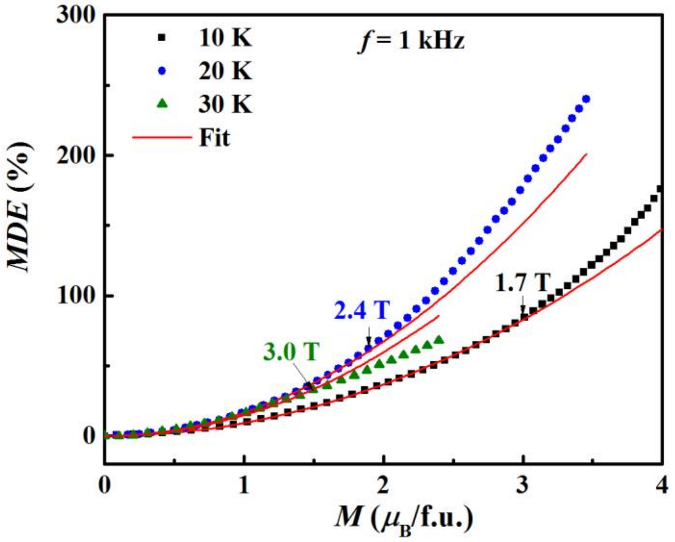

Figure 3.23 Magnetodielectric effect (*MDE*) versus magnetization (*M*) curves at temperatures *T* = 10, 20 and 30 K for *f* = 1kHz. Symbol represents experimental data and solid line represents the Fit to Eq. (3.11).

In Fig. 3.23, we plot *MDE* versus *M* for *T* = 10, 20 and 30 K at frequency *f* = 1 kHz. The *MDE* versus *M* curves are fitted with Eq. (3.11). The fitted *MDE* agrees very well with the experimental data only for low magnetization, *i.e.* low magnetic fields and deviates at high fields. The deviation shifts to lower field as temperature decreases and found at $\mu_0 H$ = 3.0 T, 2.4 T and 1.7 T for *T* = 30 K, 20 K and 10 K, respectively as depicted by arrows in Fig. 3.23.

3.3.9 Impedance spectroscopy

To investigate more quantitative vision into the dielectric response, complex impedance ($Z^* = Z' + iZ''$) spectroscopy was performed. The impedance of the dielectric sample can be represented by two-circuit element connected in parallel: one resistive (R) accounting for the leakage of current through the material and one capacitive (C) accounting for the dielectric character or charge storage capability. Valuable information of a dielectric sample can be obtained by plotting the negative imaginary part ($-Z''$) versus real part (Z') of complex impedance. In an ideal case of complex impedance plane, the $-Z''$ versus Z' curve should depict a semicircle of diameter R with a maximum at a frequency $\omega_{\max} = 1/RC$, where C is the capacitance of ideal capacitor. Moreover, to account the non-ideal dielectric response, C is commonly replaced by a constant phase element (CPE). The impedance of the R-CPE circuit is given by

$$Z^*_{R-\mathrm{CPE}} = \frac{R}{1 + RQ(i\omega)^n} \tag{3.14}$$

where Q and n are the amplitude and the phase of the CPE, respectively.[183] The value of n should be between 0 and 1 ($0 \leq n \leq 1$) and being $n = 1$ for an ideal capacitor.

In R-CPE circuit, the semicircle is slightly depressed depending on the value of n (i.e. how n deviates from the unity) and the depressed semicircle shows maximum at a frequency $\omega_{\max} = 1/(RQ)^{1/n}$. Therefore, the capacitance of the R-CPE circuit can be given by

$$C = (R^{1-n}Q)^{1/n} \tag{3.15}$$

We measured absolute impedance ($|Z|$) and phase (θ) of $EuTiO_3$ sample at various selected temperatures from 300 K to 10 K while sweeping the frequency from 100 Hz to 1 MHz. The real and imaginary parts of impedance are calculated using formulas $Z' = |Z|\cos\theta$ and $Z'' = |Z|\sin\theta$, respectively. The impedance data is fitted using the EIS Spectrum Analyzer

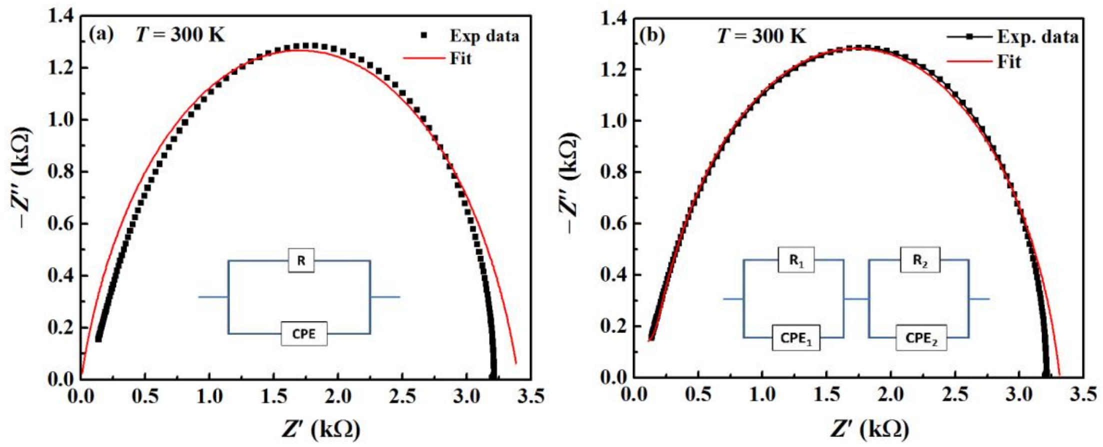

Figure 3.24 Impedance complex plane ($-Z''$ versus Z' curve) data at 300 K fitted using the model of (a) Eq. (3.11) and (b) Eq. (3.12). Symbol and solid line represent experimental data and fitting respectively. The inset sketch shows the equivalent circuit.

software. In Fig. 3.24 (a), we show $-Z''$ versus Z' curve of the impedance measured at 300 K, where symbol and solid line represent the experimental data and fit to an equivalent circuit model consisting of R-CPE element. The sketch of the equivalent circuit is shown in the inset of Fig. 3.24(a). As can be seen, the fitted data does not agree with experimental data for all frequencies. The extrinsic contribution to the dielectric properties could be the origin of this deviation. In polycrystalline samples, grain boundary effects may play an important role as the extrinsic contribution to dielectric properties and another element should be considered while accounting the extrinsic contribution. Therefore, an equivalent circuit model consisting two R-CPE elements connected in series has been employed to analyze the impedance data. Fig. 3.24 (b) shows the $-Z''$ versus Z' curve at T = 300 K fitted with an equivalent circuit model consisting two R-CPE elements. The sketch of the equivalent circuit is shown in inset of Fig. 3.24 (b). Here, the fit is in good agreement with experimental data at high frequency, while deviation is observed at low frequency. The low frequency data represent extrinsic contribution and high frequency data represent the intrinsic one. At 300 K, the low frequency

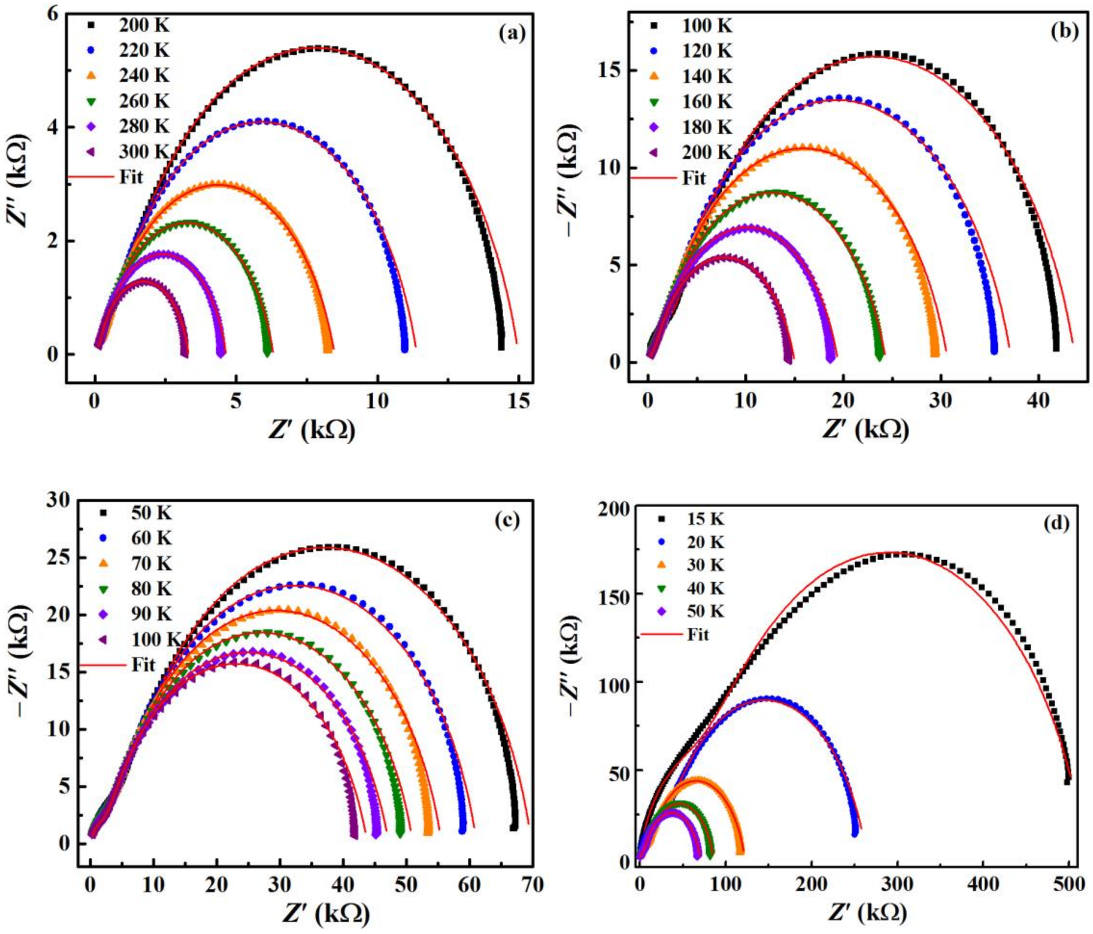

Figure 3.25 Impedance complex plane (–*Z*″ versus *Z*′ curve) data fitted with the model of equivalent circuit of two R-CPE elements for (a) T = 200 K – 300 K, (b) 100 K – 200 K, (c) 50 K – 100 K and (d) 15 K – 50 K. Symbol and solid line represent experimental data and fitting respectively.

contribution nearly dominates the experimentally available frequency range (100 Hz – 1 MHz). The similar fitting is applied to the impedance complex planes (–*Z*″ versus *Z*′ curves) for other temperatures.

Fig. 3.25(a), (b), (c) and (d) show the impedance complex planes with fitting for *T* = 200 K – 300 K, *T* = 100 K – 200 K, *T* = 50 K – 100 K and *T* = 50 K – 15 K, respectively. As temperature decreases, the radius of the semicircle increases and two incomplete semicircles are seen at high and low frequency, respectively, at *T* = 260 K. The radius of the low frequency semicircle is much larger than that of the high frequency one. This reflects that the low frequency contribution is more resistive than the high frequency one. It can be noted from Fig. 3.25 (b), (c) and (d) that the radius of high-frequency semicircle significantly increases with decreasing temperature. It means the resistivity of bulk increases as temperature decreases, which agree with temperature dependence of dc resistivity as well as ac resistivity. As can be seen from Fig. 3.25 (a)-(d), the impedance complex plane data fit nicely to the equivalent circuit model connecting two *R*-CPE elements in series for 300 K ≤ T ≤ 20 K, while the impedance at T = 15 K does not fit with same circuit. It means the Maxwell-Wagner relaxation exhibits in $EuTiO_3$ polycrystalline sample above 15 K. Lunkenheimer *et. al.*[184] suggested that the colossal dielectric constant might be due to a Maxwell-Wagner-type contribution of depletion layer at the interface between sample and contacts or at grain boundaries. Hence, the colossal dielectric constant in polycrystalline $EuTiO_3$ ($\varepsilon > 10^4$ for f = 1kHz) could be due to the Maxwell-Wagner contribution at grain boundaries.

Fig. 3.26 (a) show the $-Z''$ versus Z' curves at T = 40 K under different magnetic fields from 0 T to 7 T. The experimental data agree very well with the fit data obtained using

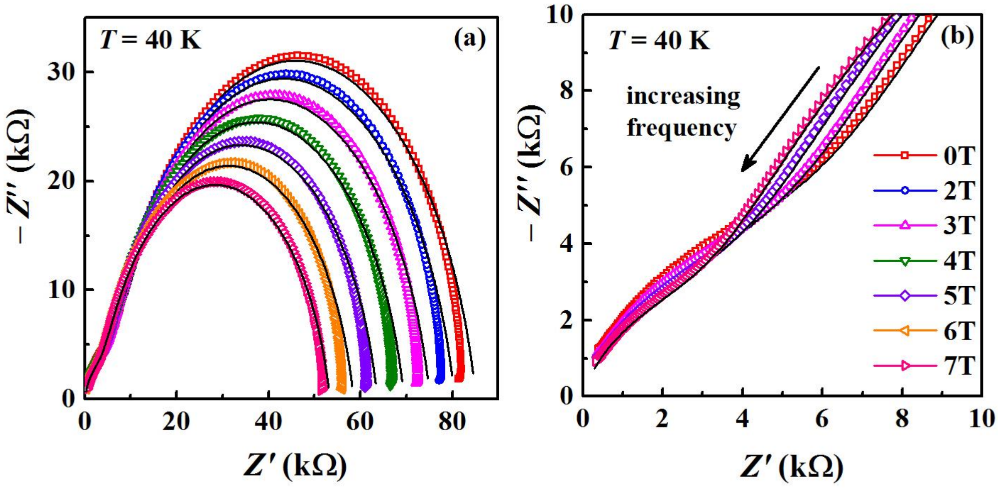

Figure 3.26 (a) Impedance complex plane ($-Z''$ versus Z' curve) data at T = 40 K under different magnetic fields. Symbol represents experimental data and solid line represents the fitting with an equivalent circuit model consisting of two *R*-CPE elements. (b) Enlarge view of Fig. (a) in high frequency region.

$\mu_0 H$ (T)	R_1 (Ω)	Q_1 (F)	n_1	R_2 (Ω)	Q_2 (F)	n_2	C_1 (F)	C_2 (F)
0	6147	8.45E-10	0.821	77897	1.66E-9	0.852	5.95E-11	3.50E-10
1	6044	8.53E-10	0.820	77271	1.68E-9	0.8518	5.89E-11	3.54E-10
2	5704	8.97E-10	0.819	73820	1.70E-9	0.8516	6.07E-11	3.55E-10
3	5231	9.60E-10	0.818	69023	1.72E-9	0.8517	6.36E-11	3.56E-10
4	4710	1.03E-9	0.817	63717	1.75E-9	0.8518	6.63E-11	3.58E-10
5	4199	1.09E-9	0.816	58497	1.78E-9	0.8517	6.81E-11	3.60E-10
6	3734	1.13E-9	0.815	53689	1.82E-9	0.8519	6.84E-11	3.65E-10
7	3325	1.15E-9	0.814	49409	1.85E-9	0.8513	6.85E-11	3.651E-10

Table 3.2 Fitting parameters of the impedance complex plane data at T = 40 K under different magnetic fields fitted with an equivalent circuit model consisting of two *R*-CPE elements. The subscripts 1 and 2 represent the grain and grain boundary contribution, respectively.

the equivalent circuit model consisting of two *R*-CPE elements except slight deviation at low frequency. As can be noticed, the radius of the low frequency semicircle decreases with increasing magnetic field strength. Fig. 3.26(b) shows the enlarge view of Fig. 3.26(a) in high frequency range. For clarity, we show data only for 0, 3, 5 and 7 T fields in Fig. 3.26(b). At high frequency, an incomplete semicircle can be seen, which radius decreases as field increases. The fitting parameters are listed in Table 3.2. The subscript 1 and 2 are related to intrinsic (grain) and extrinsic contribution (grain boundary), respectively. The capacitance is calculated using Eq. (3.12). The resistance of grain and grain boundary decreases with increasing magnetic field, while the capacitance increases for both.

The magnetoresistance and magnetocapacitance (magnetodielectric effect) for grain and grain boundary are shown in Fig. 3.27 (a) and (b), respectively. The magnetoresistance is negative, while *MDE* is positive for grain and grain boundary both. The *MR* from grain is –46 % for $\mu_0 H$ = 7T, which is nearly equal to the *MR* obtained from the dc resistivity. The *MDE* calculated from grain capacitance (*MDE* = 17 % for $\mu_0 H$ = 7T) is much larger than that calculated from grain boundary (*MDE* = 4 % for $\mu_0 H$ = 7T). The *MDE* is also calculated from the temperature dependent dielectric constant data and *MDE* at 40 K for different magnetic

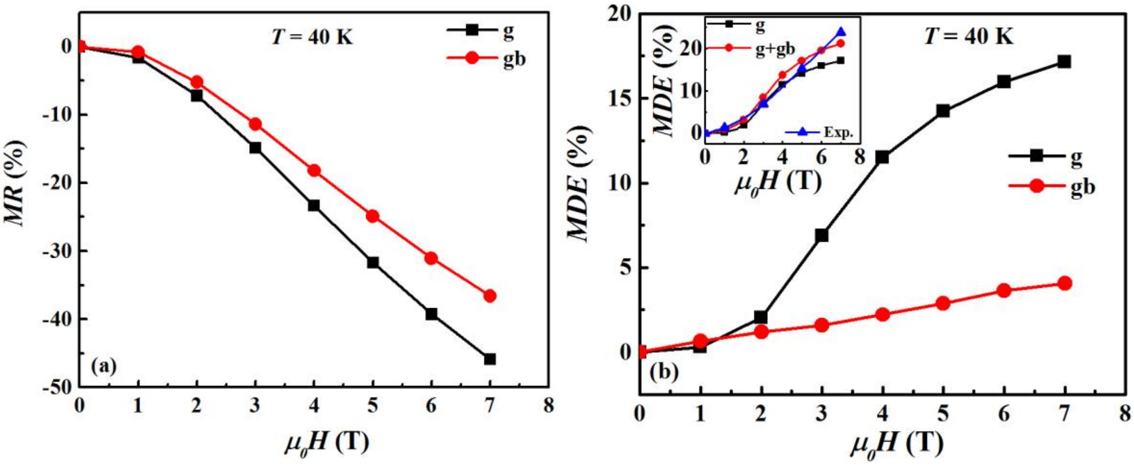

Figure 3.27 Magnetic field dependence of (a) magnetoresistance (MR) and (b) magnetodielectric effect (MDE) at *T* = 40 K for grain (g) and grain boundary (gb) calculated from the fitting parameters of impedance complex plane data.

fields (1, 3, 5 and 7T) is extracted. We show the field dependence of *MDE* calculated from the experimental data and fitting parameters in inset of Fig. 3.26(b). For low fields, the experimental *MDE* nearly matches with intrinsic *MDE* (grain), but the high field value exceeds the total *MDE* value (grain and grain boundary). The similar fitting is applied for

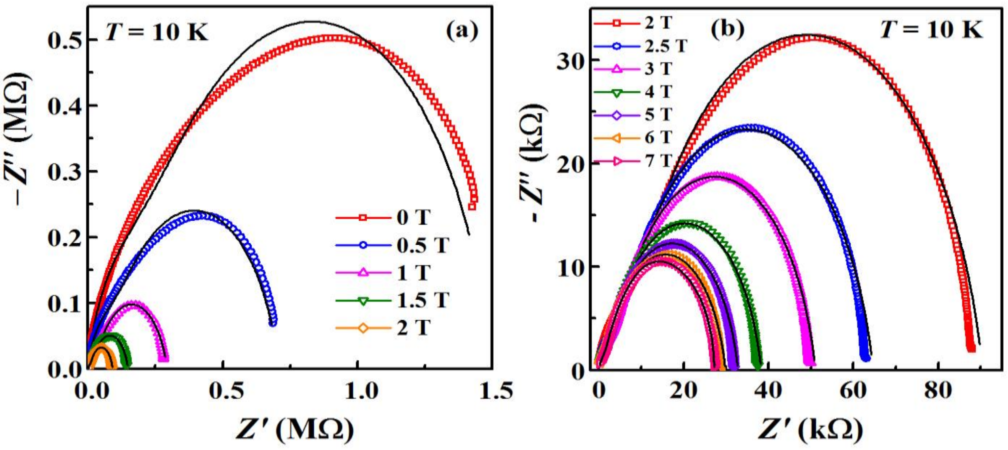

Figure 3.28 Impedance complex plane (–*Z*″ versus *Z*′ curve) data at *T* = 10 K under the magnetic fields (a) 0 T – 2 T and (b) 2 T – 7T. Symbol represents experimental data and solid line represents the fitting with an equivalent circuit model consisting of two *R*-CPE elements.

impedance data at T = 10 K for different magnetic fields (Fig. 3.28 (a) and (b)). The fit data agree quite well with experimental data for magnetic fields above 1 T, the large deviation occurs for zero and 0.5 T field data.

3.4 Summary

In summary, polycrystalline $EuTiO_3$ sample was prepared using conventional solid-state reaction method under reduced atmosphere. The most important findings are:

1. $EuTiO_3$ shows antiferromagnetic ordering due to Eu^{2+} magnetic moments below T_N = 5.42 K.
2. The magnetocaloric effect is investigated by magnetization and heat capacity measurements. $EuTiO_3$ shows a giant magnetocaloric effect around T_N. The isothermal magnetic entropy change is 49 J/kg.K, the adiabatic temperature change is 21 K and the refrigeration cooling power is 540 J/kg for a field change of 7 T at T_N.
3. The large magnetocaloric effect is due to suppression of the spin entropy associated with localized 4f moments of Eu^{2+} ions. The giant magnetocaloric effect together with negligible hysteresis, suggest that $EuTiO_3$ could be a potential material for magnetic refrigeration below 30 K.
4. $EuTiO_3$ is an insulator under zero magnetic field, while application of the magnetic field drives an insulator to metal transition at temperature $T = T_p$, where the resistivity shows a broad maximum. The T_p shifts towards higher temperature (T_p = 22 K >> T_N for $\mu_0 H$ = 7 T) with increasing strength of the magnetic field.
5. $EuTiO_3$ sample shows a colossal negative magnetoresistance ($\Delta\rho/\rho(0) = -99.15\%$) under a small magnetic field of $\mu_0 H$ = 0.5 T at T = 2 K and $\Delta\rho/\rho(0) = -45\%$ under 7 T at T = 45 K (>>T_N). It is suggested that small oxygen nonstoichiometry induces donor impurity states very close to the bottom of Ti-3d conduction band, which are strongly exchange coupled to localized $4f^7$ spins of Eu^{2+} ions. The negative colossal

magnetoresistance is suggested to be caused by suppression of fluctuations of $4f^7$ spins, which enhances carrier delocalization in the impurity states. The exact origin of insulator-metal transition and *MR* in $EuTiO_3$ has to be understood.

6. Polycrystalline $EuTiO_3$ also shows a giant positive magnetodielectric effect ($\Delta\varepsilon/\varepsilon(0)$ = 670 % under 7 T at T = 10 K), which is much larger than that observed in $EuTiO_3$ single crystal ($\Delta\varepsilon/\varepsilon(0)$ = 7 % under 1.5 T at T = 2 K) and thin film ($\Delta\varepsilon/\varepsilon(0)$ = 3 % under 1.5 T at T = 2 K).
7. The quadratic dependence of *MDE* on magnetization (*i.e. MDE* $\propto M^2$) for low fields indicates that the magnetodielectric effect is attributed to strong spin-lattice coupling in this material.
8. From the decent fitting of the impedance data with equivalent circuit model consisting of two *R*-CPE elements, it is confirmed that $EuTiO_3$ exhibits Maxwell Wagner relaxation above T = 15 K. However, the occurrence of positive magnetodielectric effect with positive magnetodielectric loss suggests that the *MDE* does not arise from the combination of Maxwell Wagner relaxation and negative magnetoresistance in this compound.

Chapter 4 Multiferroicity, Magnetocaloric, Magnetoresistance and Magnetodielectric Properties of $Eu_{1-x}Ba_xTiO_3$

4.1 Introduction

We have discussed magnetic, electrical and dielectric properties of $EuTiO_3$ in previous chapter. In this chapter, we focus our attention on $Eu_{1-x}Ba_xTiO_3$ series. Both Eu and Ba are divalent. $Eu^{2+}(4f^7)$ possess a large magnetic moment (7 μ_B) due to localized 4f electrons but Ba^{2+} ($5p^6$) is non-magnetic. While $EuTiO_3$ is antiferromagnetic and quantum paraelectric, $BaTiO_3$ is non-magnetic and ferroelectric at room temperature (T_{FE} ~ 402 K). Hence, the emergence of ferroelectricity with increasing Ba content in $Eu_{1-x}Ba_xTiO_3$ will be interesting. Besides, it is interesting to investigate the change in magnetic ground state of $EuTiO_3$ with Ba substitution. Also, $Eu_{1-x}Ba_xTiO_3$ provides a unique opportunity to study how the magnetocaloric effect and magnetoresistance change systematically with the spin dilution of rare earth site.

Half doped compound, $Eu_{0.5}Ba_{0.5}TiO_3$ was suggested to be ferroelectric below $T_{FE} \approx$ 215 K and ferromagnetic below 2 K almost thirty six years ago by D. L. Janes *et al.*[185] Rushchanskii *et. al.*[186] confirmed the coexistence of ferroelectricity and magnetism in this compound recently. V. Goian *et al.*[73] studied dielectric properties of bulk $Eu_{0.5}Ba_{0.5}TiO_3$ in zero field from few MHz to THz frequency range. J. M. Wesselinowa[187] predicted a steplike increase in the dielectric constant at the onset of magnetic order in $Eu_{0.5}Ba_{0.5}TiO_3$. T. Wei *et al.*[188] studied the dielectric properties of $Eu_{1-x}Ba_xTiO_3$ and found that the ferroelectric transition temperature (T_{FE}) increases from ~60 K ($x = 0.25$) to ~ 280 K ($x = 0.65$). Magnetoelectric coupling in ferroelectric compositions will be of great interest since it may allow tuning of ferroelectric hysteresis loop by magnetic field and vice versa. Earlier studies of the magnetodielectric effect in $Eu_{1-x}Ba_xTiO_3$ series was confined to compositions in the quantum paraelectric regime ($0 \leq x \leq 0.2$) and the *MDE* was found to drastically reduce with increasing Ba content (x). Here, we investigate the magnetodielectric effect in 2% to 60% magnetic site diluted $EuTiO_3$ sample. In addition to the magnetic field dependence of the real part of dielectric constant, we also report the field dependence of ac resistivity and loss tangent ($tan\delta$), which were not studied in the previous work. Therefore, in this chapter we study the magnetic, ferroelectric, magnetocaloric, magnetoresistance and magnetodielectric properties of $Eu_{1-x}Ba_xTiO_3$ ($0.02 \leq x \leq 1.0$).

4.2 Experimental details

Polycrystalline $Eu_{1-x}Ba_xTiO_3$ ($0.02 \leq x \leq 0.95$) samples were synthesized through solid-state reaction method. Stoichiometric proportion of Eu_2O_3, $BaCO_3$ and TiO_2 powder were mixed, ground and sintered at 1200° C for 24 hours in 95% Ar and 5 % H_2 atmosphere. After two intermediate grinding and annealing at 1200° C, powders were pressed in a uniaxial press into pellets and the pellets were sintered at 1300° C for 24 hours in same atmosphere. Polycrystalline $BaTiO_3$ sample was prepared using $BaCO_3$ and TiO_2 powders in stoichiometric ratio and annealing at 1200° C in air. Powder X-ray diffraction (XRD) using CuKα radiation was performed at room temperature to examine the phase and crystal structure of the samples. A Discovery Thermogravimetric analyzer from TA Instruments was employed to determine the oxygen contents in few selected samples. TGA trace was collected while heating the sample in air from room temperature to 1200 K at a rate of 5K/min. Magnetization for all the samples was measured using a Physical Property Measurement System (PPMS) equipped with vibration sample magnetometer (VSM) probe. Additional magnetization measurements were carried out for $x = 0.5$ sample using micro Hall probe (□HP) technique from $T = 10$ K to 0.35 K at the University of Zaragoza, Spain. The heat capacity was measured by a relaxation technique in PPMS. The dielectric properties under zero magnetic field were measured as a function of temperature using an Agilent

4294A Impedance Analyzer, a model 336 cryogenic temperature controller (Lake Shore Cryotronics, Inc.) and a closed cycle refrigerator cryostat (Sumitomo Cryogenics). For dielectric measurements, the samples were cut in the form of parallel-plate capacitor geometry. Pyroelectric current for few selected samples was measured in a superconducting cryostat (Quantum Design Inc. USA) using Keithley 6517A electrometer. Four-probe dc-resistivity in zero magnetic field was measured as a function of temperature in a closed cycle refrigerator cryostat using Keithley 6221 Current Source and Keithly 2700 Multimeter instruments. Two-probe dc-resistivity below 120 K as a function of temperature and magnetic field was carried out in a superconducting cryostat using a Keithley 6517A electrometer with applied dc voltage of 10 volt. The dielectric and ac resistivity measurements under magnetic fields were performed in PPMS interfaced with Agilent 4294A Impedance Analyzer.

4.3 Results and discussion

4.3.1 Structural characterization: X-ray diffraction

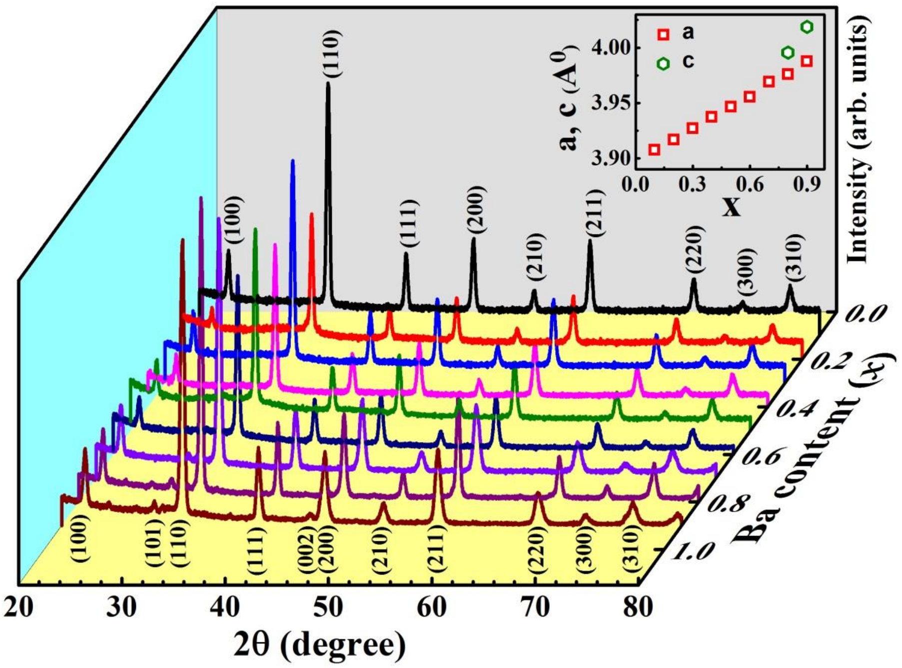

Figure 4.1 Powder X-ray diffraction pattern of $Eu_{1-x}Ba_xTiO_3$ ($0.1 \leq x \leq 0.9$). Inset shows variation of *a* and *c* lattice parameters with Ba content (*x*).

We show powder X-ray diffraction (XRD) pattern of $Eu_{1-x}Ba_xTiO_3$ ($0.1 \leq x \leq 0.9$) in the main panel of Fig. 4.1. Compositions $x = 0.1$ to 0.7 are cubic but $x = 0.8$ and 0.9 show tetragonal symmetry as evidenced by the splitting of (200) diffraction peak into (002) and (200) peaks in agreement with the results of T. Wei. *et. al.*[188] Reitveld analysis of XRD data was performed to obtain lattice parameters. Inset shows a and c lattice parameters as a function of compositions (x). The a parameter increases linearly from 3.9074 Å for $x = 0.1$ to 3.9751 Å for $x = 0.9$ as the bigger size Ba^{2+} ions (1.35 Å) replaces the smaller Eu^{2+} ions (1.17 Å). The c parameter is 3.977 Å and 4.021 Å for $x = 0.8$ and 0.9, respectively.

4.3.2 Thermogravimetric analysis

We performed Thermogravimetric analysis for few selected samples $x = 0.10$, 0.50 and 0.60 to determine the oxygen contents. In case of $Eu_{1-x}Ba_xTiO_3$, $EuTiO_3$ oxidizes to pyrochlore $Eu_2Ti_2O_7$ due to the oxidation of Eu^{2+} to Eu^{3+}, while $BaTiO_3$ is thermally stable. Therefore, the oxygen nonstoichiometry parameter δ for $Eu_{1-x}Ba_xTiO_{3-\delta}$ samples can be determined using Eq. (4.1) and (4.2).

$$2\mathrm{Eu}_{1-x}\mathrm{Ba}_x\mathrm{TiO}_{3-\delta} + (\delta + 0.5(1-x))\mathrm{O}_2 \longrightarrow (1-x)\mathrm{Eu}_2\mathrm{Ti}_2\mathrm{O}_7 + 2x\mathrm{BaTiO}_3 \tag{4.1}$$

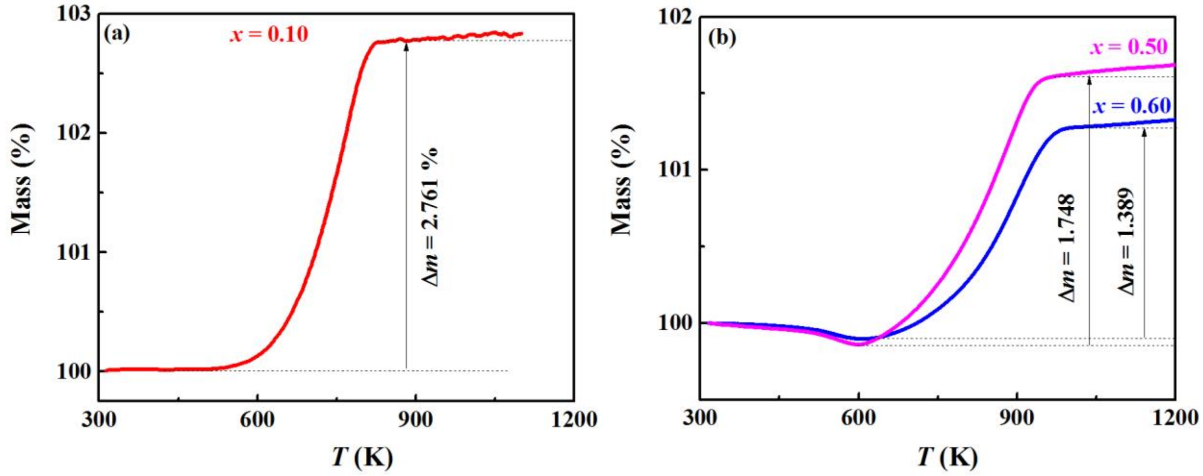

Figure 4.2 TGA traces for (a) $x = 0.10$ and (b) $x = 0.50$ and 0.60 during oxidation in air.

$$2M(\mathrm{Eu}_{1-x}\mathrm{Ba}_x\mathrm{TiO}_3) - 2\delta M(\mathrm{O}) = \frac{(1-x)M(\mathrm{Eu}_2\mathrm{Ti}_2\mathrm{O}_7) + 2xM(\mathrm{BaTiO}_3)}{100\% + \Delta m(\%)} \tag{4.2}$$

Where M represents the molar mass and Δm is the mass gain.

The molar mass of $\mathrm{Eu}_{1-x}\mathrm{Ba}_x\mathrm{TiO}_3$ can be calculated using Eq. (4.3).

$$M(\mathrm{Eu}_{1-x}\mathrm{Ba}_x\mathrm{TiO}_3) = (1-x)M(\mathrm{Eu}) + xM(\mathrm{Ba}) + M(\mathrm{Ti}) + 3M(\mathrm{O}) \tag{4.3}$$

Fig. 4.2 (a) and (b) present TGA trances of mass gain for x = 0.10 and x = 0.50, 0.60, respectively. For x = 0.10, the mass gain during oxidation is Δm = 2.761% and the calculated δ is −0.0241. However, the δ value is +0.0126 and +0.0075 for x = 0.50 and 0.60, respectively, corresponding to the weight gain Δm = 1.748 % and 1.389 %. The negative value of δ for x = 0.10 implies a slight excess of oxygen in this samples, while the positive values of δ for x = 0.5 and 0.6 indicate the presence of oxygen vacancies.

4.3.3 DC magnetization

The main panel of Fig. 4.3 (a) and (b) show the temperature dependence of the dc magnetization (M) for x = 0.00 – 0.20 and x = 0.30 – 0.90, respectively, measured upon cooling from 300 K to 2.5 K under a magnetic field of H = 1 kOe. We have shown the data

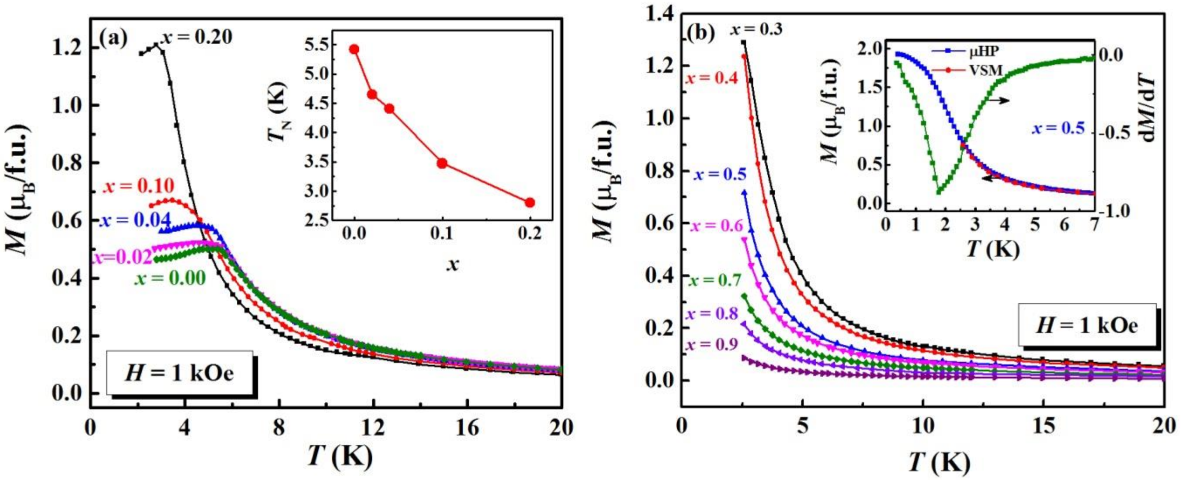

Figure 4.3 Main panels: Temperature dependence of magnetization (M) of $\mathrm{Eu}_{1-x}\mathrm{Ba}_x\mathrm{TiO}_3$ for (a) x = 0.0 – 0.20 and (b) x = 0.3 – 0.9, measured using VSM. Insets: (a) x dependence of T_N and (b) Left y-axis: Temperature dependence of magnetization (M) measured using a vibrating sample magnetometer (VSM) and a micro Hall probe (μHP) for x = 0.5 sample. Right y-axis: temperature dependence of dM/dT.

only in the low temperature range (T = 2.5 K – 20 K) for clarity. The prominent peak around $T = T_N$ = 5.42 K in x = 0.00 indicates the onset of antiferromagnetic ordering. As x increases from 0.00 to 0.2, the peak in $M(T)$ shifts towards lower temperature, i.e. T_N decreases and the magnitude of M below 4 K increases. The inset of Fig. 4.3 (a) shows the x dependence of T_N. For x = 0.2, T_N decreases to 2.79 K. From the main panel of Fig. 4.3(b), the magnitude of M at T = 2.5 K for x = 0.3 is higher than that for x = 0.2, but it decreases as the Ba contents increases further. As x increases above 0.2, T_N shifts below our measurement limit of T = 2.5 K. The inset of Fig. 4.3(b) shows the temperature dependence of magnetization (M) measured in a magnetic field of H = 1 kOe for x = 0.5. $M(T)$ for $T \geq 2.5$ K and for T = 7-0.35 K, was measured using a VSM and μHP technique, respectively. Since the μHP technique does not give absolute value of the magnetization,[189] the signal measured by the μHP was scaled to match the $M(T)$ data obtained from the VSM. The $M(T)$ increases rapidly as the temperature is decreased below 20 K and levels off below ~1.0 K. It is likely that sample is ferromagnetic at the lowest temperature. The corresponding susceptibility $\chi_0 = N_A \mu_B M_{0.1\mathrm{T}} / H$

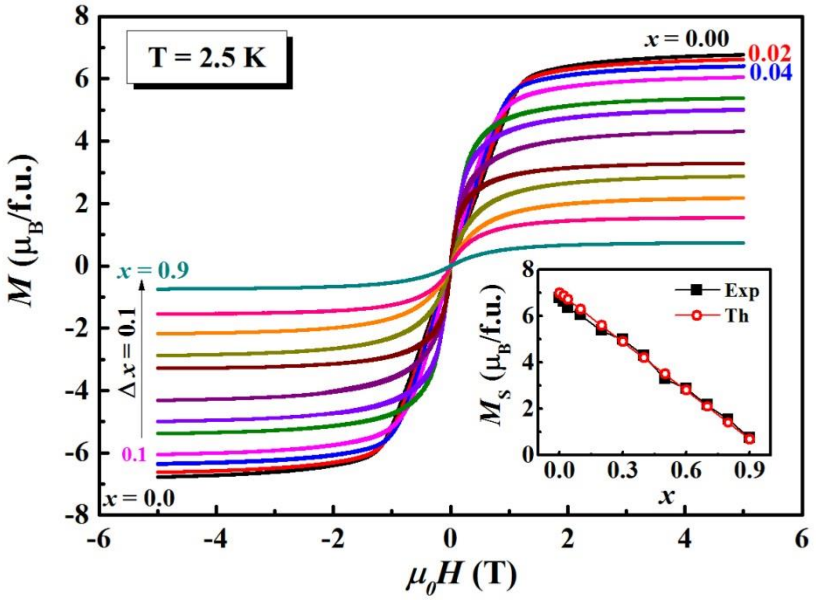

Figure 4.4 Main panel: $M(H)$ isotherms at T = 2.5 K for $Eu_{1-x}Ba_xTiO_3$ (0.00 ≤ x ≤ 0.9). Inset: Experimental values of the saturation magnetization (M_S) at 5 T (closed square) and theoretical value (open circle).

= 11.2 cm^3/mole for $\mu_0 H$ = 0.1 T is close to the calculated limit for a completely ferromagnetically ordered isotropic material below T_C, namely, 1/□ where □ is the demagnetizing factor (a rough estimate gives the value of 10.8 cm^3/mole). The temperature derivative of the magnetization (dM/dT) shows a minimum at $T = T_C = 1.7$ K, where T_C is taken as the ferromagnetic Curie temperature. Oxygen deficient $\mathrm{Eu_{0.5}Ba_{0.5}TiO_3}$ sample was reported to be ferromagnetic with $T_C = 1.85$ K.[190]

The main panel of Fig. 4.4 shows the field dependence of magnetization, $M(H)$ measured at T = 2.5 K while sweeping the field in direction ($\mu_0 H = 0 \rightarrow +5$T and +5T $\rightarrow -5$ T$\rightarrow +5$ T). None of the sample shows hysteresis. M increases linearly with H up to 1 T for x = 0.00, 0.02, 0.04 and 0.1 as the spin configuration changes from antiferromagnetic to spin flop state and the angle between the flopped spins decreases towards zero with further increasing field leading to an induced ferromagnetic state. $M(H)$ curves for $x > 0.2$ resemble that of a soft ferromagnet. However, absence of hysteresis and remanence suggests that these samples are most likely in the paramagnetic state in zero field, but ferromagnetic order is induced by the external magnetic field aided by low thermal energy. Inset of Fig. 4.4 compares the experimental value of M at 5 T with the theoretically expected saturation magnetization value according to $M_S = (1- x)gS\mu_B$/f.u., assuming $S = 7/2$ and $g = 2$. The saturation magnetization at 5 T, M_S, decreases gradually with increasing x from 6.62 μ_B/f.u. for x = 0.02 to 0.7 μ_B/f.u. for x = 0.9. The theoretical values of magnetization closely match with the experimental results.

Fig. 4.5 shows the temperature dependence of inverse susceptibility (χ^{-1}) for $\mathrm{Eu_{1-x}Ba_xTiO_3}$ ($0.1 \leq x \leq 0.9$) in low temperature (T = 2.5 K – 35 K). The χ^{-1}(T) is fitted with the Curie-Weiss law, $\chi^{-1} = (T + \theta_p)/C$, where θ_p is the paramagnetic Curie temperature and C is the Curie constant, which is related to the effective magnetic moment ($\mu_{\mathrm{eff}} = 2.83\sqrt{C_M}$, where C_M is the Curie constant per gram molecular weight) of Eu^{2+} ions in the paramagnetic

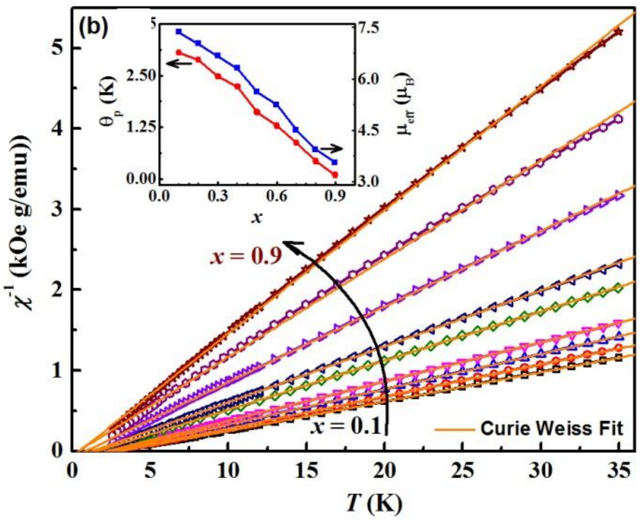

Figure 4.5 Temperature dependence of the inverse susceptibility (χ^{-1}) and the Curie Weiss fit in the low temperature range for $Eu_{1-x}Ba_xTiO_3$ ($0.1 \le x \le 0.9$). Inset: Composition (x) dependence of the paramagnetic Curie temperature (θ_p) on left y-axis and the effective magnetic moment (μ_{eff}) on right y-axis.

state. We show θ_p and μ_{eff} in the inset of Fig. 4.5. It is found that θ_p is positive and non-zero for all the compositions and the value of θ_p decreases with increasing x (θ_p = 3.05 K for x =0.1 to θ_p = 0.085 for x = 0.9). The effective magnetic moment μ_{eff} decreases from 7.37 μ_B for x = 0.1 to 3.56 μ_B for x = 0.9 due to Eu^{2+} site dilution by Ba^{2+} ions. However, the experimental value of μ_{eff} is slightly larger than theoretically expected values (7.23μ_B for x = 0.1 to 1.37 μ_B for x = 0.9).

We have measured magnetization while sweeping the field from 0 to 5 T and 5 T to 0 T at different temperatures for all compositions (x = 0.1 – 0.9). In Fig. 4.6 (a) – (d), we show $M(H)$ isotherms obtained at different temperatures for four selected composition (x = 0.1, 0.3, 0.5 and 0.9). Although T_N of x = 0.1 is 3.74 K, M increases nonlinearly with H up to ~ 24 K in the paramagnetic state and linear M-H dependence is seen only above 30 K. The nonlinear behavior of $M(H)$ in the paramagnetic state could arise from the fact that the ratio of the Zeeman energy to thermal energy is $gS\mu_B H/k_B T = 2.35$ for $\mu_0 H$ = 5 T, T = 10K and S = 7/2. Hence the magnetic field effectively align Eu:4f spins even above T_N. For x = 0.9, this ratio is

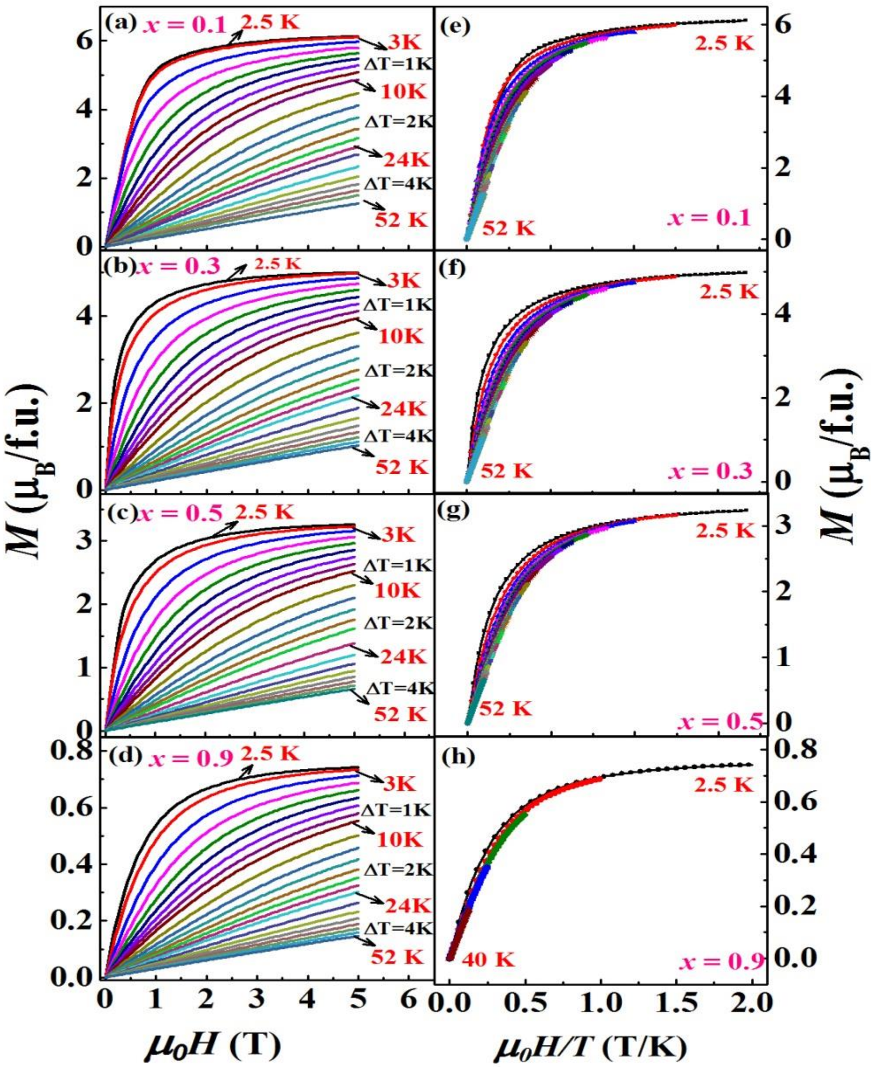

Figure 4.6 Left column: Magnetization isotherms at different temperatures for (a) *x* = 0.1, (b) *x* = 0.3, (c) *x* = 0.5 and (d) *x* = 0.9. Right column: *M* versus $\mu_0 H/T$ graphs for (e) *x* = 0.1, (f) *x* = 0.3, (g) *x* = 0.5 and (h) *x* = 0.9.

only 0.2 hence it behaves like a paramagnet. Classical (Langevin) or quantum mechanical model of paramagnetism predicts that magnetization curves measured at different temperatures should fall on a single curve when *M* is plotted against *H*/*T*. We show *M* versus *H*/*T* curves for *x* = 0.1, 0.3, 0.5 and 0.9 in Fig. 4.6 (e), (f), (g) and (h), respectively. For the highly spin diluted composition *x* = 0.9, all the curves almost fall on a single curve master curve. With decreasing *x*, deviation from the mater curve occurs below 30 K. For a given *H*/*T* values, the magnitude of *M* increases with lowering temperature and decreasing *x*. This is due to increase interaction between Eu-4f spins with lower temperature and with increasing magnetic field.

4.3.4 Ferroelectric properties

To study the ferroelectric properties of $Eu_{1-x}Ba_xTiO_3$, we measured capacitance (C) and dielectric loss ($tan\delta$) simultaneously for $Eu_{1-x}Ba_xTiO_3$ ($0.1 \leq x \leq 1.0$) samples with applying 1 V excitation voltage of various frequencies. From the measured capacitance, the dielectric constant (ε) was calculated using the relation, $= \frac{Ct}{\varepsilon_0 A}$, where t is the thickness, A is the cross section area of the sample and ε_0 is vacuum permittivity. Fig. 4.7 (a) and (b) show the temperature dependence of ε and $tan\delta$ for $x = 1.0$ i.e. $BaTiO_3$, respectively, measured while cooling from 450 K to 150 K. As one can see, $BaTiO_3$ exhibits a large value of ε for 1 kHz (ε_{max} ~ 6500 at T = 397 K), which decreases with increasing frequency. The $\varepsilon(T)$ for all frequencies display three anomalies at temperatures 397 K, 286 K and 194 K corresponding to cubic to tetragonal (C-T), tetragonal to orthorhombic (T-O) and orthorhombic to rhombohedra (O-R) phase transitions, respectively. The transition temperature values closely

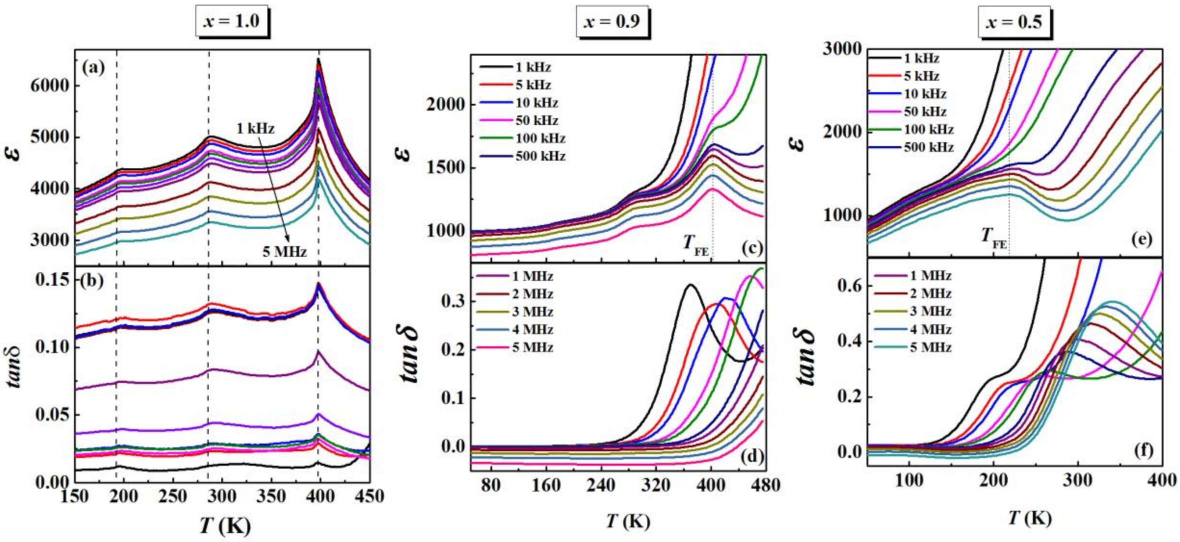

Figure 4.7 Temperature dependence of dielectric constant (ε) and dielectric loss ($tan\delta$) for (a) and (b) $x = 1.0$, (c) and (d) $x = 0.9$, (e) and (f) $x = 0.5$.

match with reported values shown in Fig. 1.2 (chapter 1) for this compound. We have noticed that the $tan\delta(T)$ also exhibits the peaks at exactly same temperature as observed in $\varepsilon(T)$.

Fig. 4.7 (c) and (d) show the temperature dependence of ε and $tan\delta$ for $x = 0.9$, respectively. Unlike $x = 1.0$, ε (T, f = 1kHz) for $x = 0.9$ decreases with decreasing temperature without showing any anomaly at high temperature. However, ε (T, f = 100 kHz) display a weak anomaly at T ~ 402 K corresponding to C-T transition, which becomes stronger as frequency increases. Another anomaly is noticed at T ~ 283 K for all frequencies corresponding to T-O transition. The temperature dependence of $tan\delta$ for $x = 0.9$ also show different behavior than that for $x = 1.0$. $tan\delta$ (T, f = 1 kHz) for $x = 0.9$ exhibits a peak at a temperature of 370 K, which shifts to higher temperature with increasing frequency. The temperature dependence of ε and $tan\delta$ for $x = 0.5$ is shown in Fig. 4.7 (e) and (f), respectively. The ε (T) for $x = 0.5$ shows a similar behavior to that for $x = 0.9$. The anomaly in ε (T, $f \geq$ 500 kHz) at T ~ 220 K indicates a C-T or ferroelectric transition in this compound, which was also reported earlier by Rushchanskii *et. al.*[186] and V. Goian *et. al.*[73] at T ~ 215 K. The $tan\delta$ (T, f = 1 kHz) for $x = 0.5$ also exhibits a hump at T ~ 194 K, which shifts to higher temperature as frequency increases and converts into a broad peak at f = 500 kHz. The absence of anomaly in ε (T) is noticed for low frequencies ($f \leq$ 100 kHz) in all $Eu_{1-x}Ba_xTiO_3$ samples except $BaTiO_3$. We also show the temperature dependence of ε for $x = 0.8$ and 0.7 in Fig. 4.8 (a) and (c), respectively, where ε (T, f = 1kHz) do not exhibit any anomaly. However, the anomaly appear at T ~ 340 K and f = 500 kHz for $x = 0.8$ and at T ~ 296 K and f = 50 kHz for $x = 0.7$. In addition, the temperature dependence of $tan\delta$ for $Eu_{1-x}Ba_xTiO_3$ ($0.95 \geq x \geq 0.1$) is different than that for $BaTiO_3$. The $tan\delta$ (T) for $Eu_{1-x}Ba_xTiO_3$ shows a peak, which shifts to higher temperature as frequency increases, while the peak position in $tan\delta$ (T) of $BaTiO_3$ is at

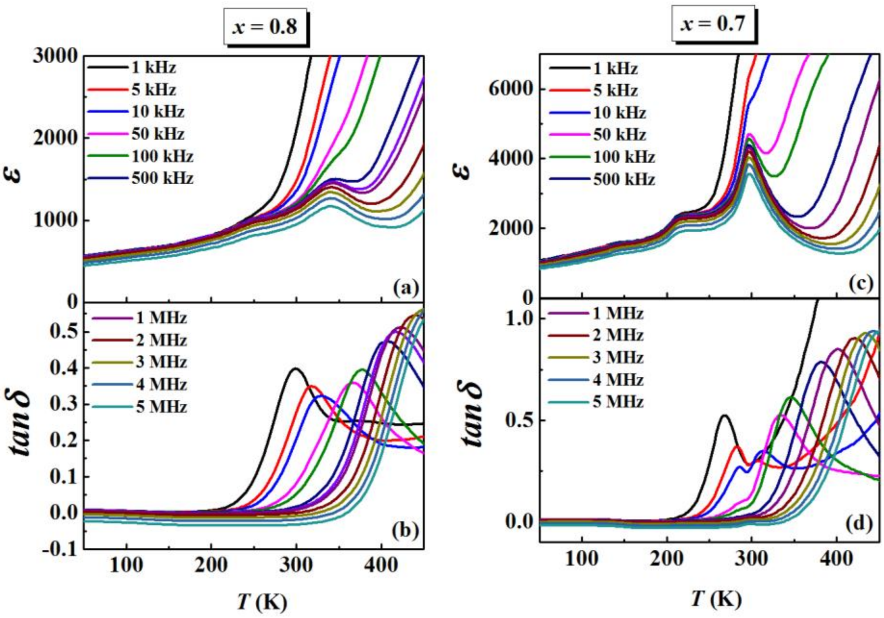

Figure 4.8 Temperature dependence of dielectric constant (ε) for (a) x = 0.8 and (c) x = 0.7, and dielectric loss (*tan*δ) for (b) x = 0.8 and (d) x = 0.7.

the same temperature for all frequencies. The shift in peak position of *tan*δ (T) in $Eu_{1-x}Ba_xTiO_3$ indicates the presence of dielectric relaxation in these compounds.

To compare the transition temperatures observed in $Eu_{1-x}Ba_xTiO_3$, we show temperature dependence of the normalized dielectric constant ($\varepsilon_N = \varepsilon(T)/\varepsilon$ (300K), where ε (300K) is the dielectric constant value at T = 300 K) for $Eu_{1-x}Ba_xTiO_3$ ($0.1 \leq x \leq 1.0$) at f = 1MHz in Fig. 4.9. For $0.7 \leq x \leq 1.0$, ε_N (T) displays three anomalies corresponding to C-T, T-O and O-R phase transitions, while only one anomaly corresponding to C-T is clearly visible for $0.4 \leq x \leq 0.6$. For $x \leq 0.30$, $\varepsilon_N(T)$ decreases monotonously with decreasing temperature and subsequently becomes temperature independent below 100 K for x = 0.10. The saturation behavior of $\varepsilon(T)$ could be due to the influence of quantum fluctuations as demonstrated in $EuTiO_3$ and other incipient ferroelectrics such as $SrTiO_3$. The exact transition temperature in $Eu_{1-x}Ba_xTiO_3$ ($0.4 \leq x \leq 1.0$) can be estimated from the inflection points of ε_N (T), *i.e.* the peak in $d\varepsilon/dT$. Fig. 4.10 shows the temperature dependence of $d\varepsilon/dT$ for few selected compounds. The C-T phase transition temperature (paraelectric to ferroelectric transition

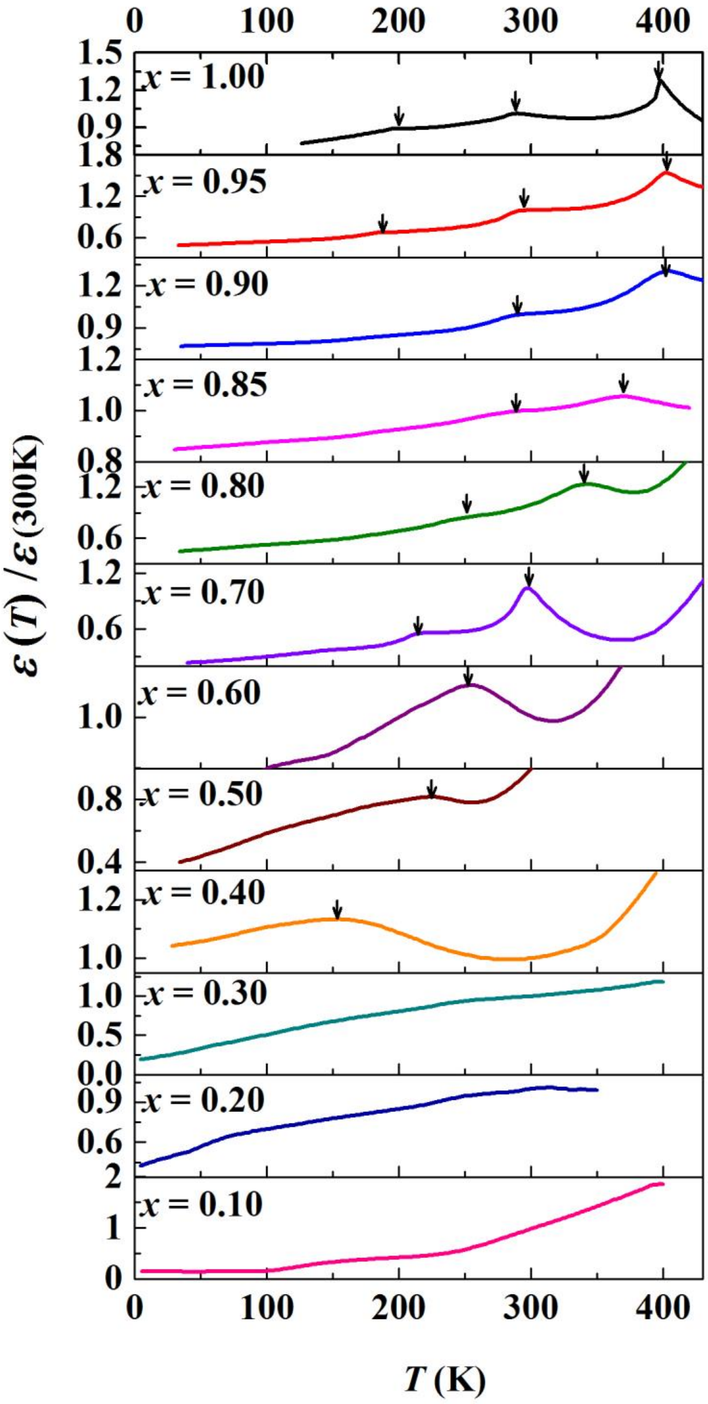

Figure 4.9 Temperature dependence of normalized dielectric constant ($\varepsilon(T)/\varepsilon(300\text{K})$, where $\varepsilon(300\text{K})$ is the dielectric constant value at T = 300 K) for $Eu_{1-x}Ba_xTiO_3$ ($0.1 \le x \le 1.0$).

temperature: T_{FE}) shifts towards lower temperature as x decreases from x = 1.0 (T_{FE} = 395 K) to x = 0.4 (T_{FE} = 150 K). Although the anomaly in dielectric constant is extensively used to determine the ferroelectric transition temperature in ferroelectrics, J. F. Scott stated that the dielectric anomalies could be also observed at nonferroelectric phase transition such as

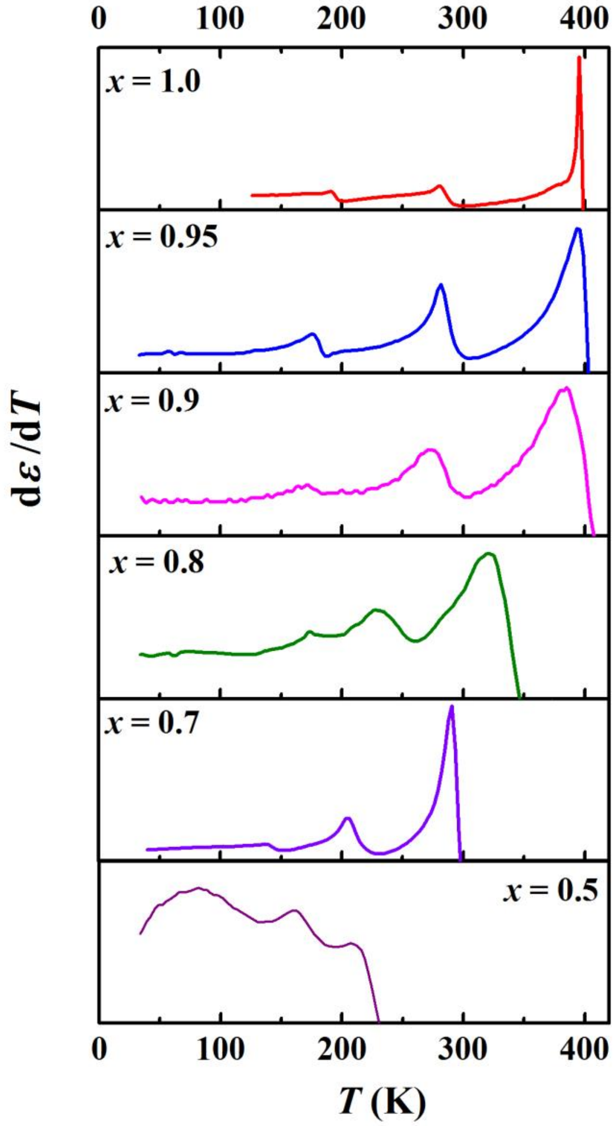

Figure 4.10 Temperature dependence of dε/dT for $Eu_{1-x}Ba_xTiO_3$ ($0.5 \le x \le 1.0$).

antiferrodistortive transition.[179] Heat capacity and pyroelectric current measurements as a function of temperature are also considered effective methods to determine the ferroelectric transition temperature. To verify T_{FE} obtained from the peak in dε/dT, we performed heat capacity and pyroelectric current measurements as a function of temperature for $x = 0.7$. The pyroelectric current was measured while heating the sample from 100 K to 320 K at the rate of 4 K/min after poling the sample under the electric field of 0.5 kV/cm.

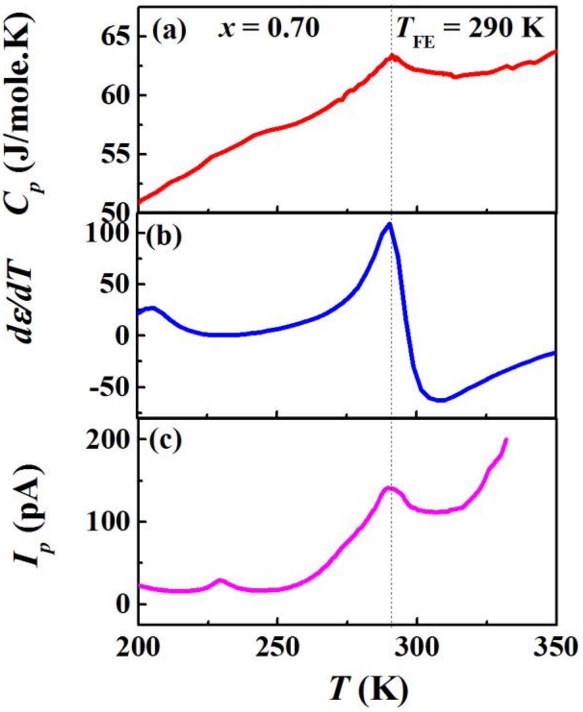

Figure 4.11 Temperature dependence of (a) heat capacity (C_p), (b) dε/dT and (c) pyroelectric current (I_p) for $x = 0.70$.

Fig. 4.11 (a), (b) and (c) show the temperature dependence of heat capacity (C_p), dε/dT and pyroelectric current (I_p), respectively for $x = 0.7$. The $C_p(T)$ monotonically increases as temperature increases and shows a λ like peak at $T = 290$ K. It is observed that the peak in $C_p(T)$appears at same temperature as peaks appear in dε/dT and $I_p(T)$. The I_p measurements were also carried out for $x = 0.5$ and 0.6 samples (not shown here) and the peak position in $I_p(T)$ closely matches with that in dε/dT.

4.3.5 Phase diagram of $Eu_{1-x}Ba_xTiO_3$

Fig. 4.12 shows the x dependence of phase transition temperatures T_{FE} (C-T), T_1 (T-O) and T_2 (O-R) estimated from the peak positions in dε/dT versus T curves. The T_{FE} decreases gradually as x decreases from x =1.0 (T_{FE} = 395 K) to x = 0.90 (T_{FE} = 385 K), while it decreases rapidly with further decreasing x from 0.85 (T_{FE} = 341 K) to 0.50 (T_{FE} = 210 K).

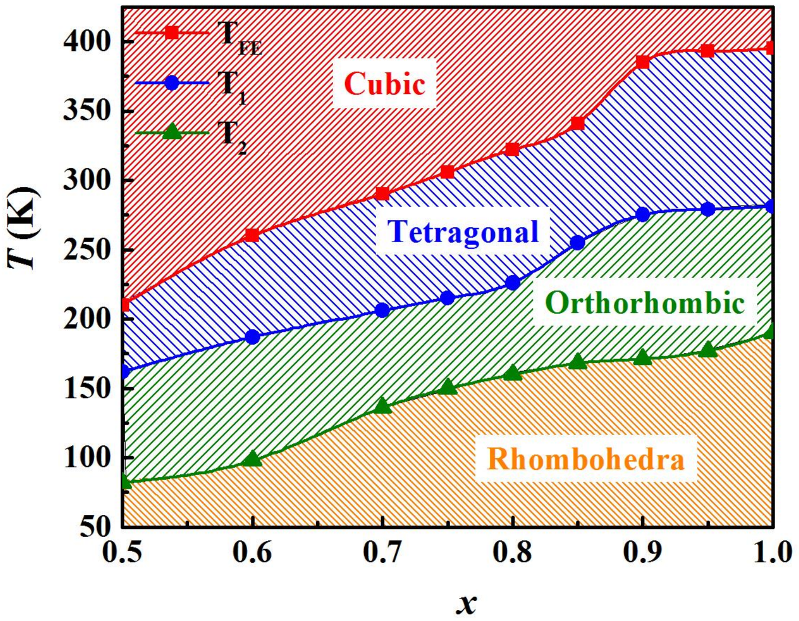

Figure 4.12 The phase transition temperatures T_{FE} (Cubic to tetragonal or paraelectric to ferroelectric transition), T_1 (Tetragonal to Orthorhombic) and T_2 (Orthorhombic to Rhombohedral) as a function of *x*. Shaded areas represent different phases.

The T_1 and T_2 both decrease monotonously as x decreases from $x = 1.0$ ($T_1 = 281$ K, $T_2 = 190$ K) to $x = 0.5$ ($T_1 = 162$ K, $T_2 = 82$ K). For $x = 0.4$, T_1 and T_2 do not appear, while $T_{FE} = 150$ K. To verify the structural transitions, the X-ray diffraction or Raman spectroscopy experiments as a function of temperature are needed.

On the basis of estimated magnetic transition temperatures (T_N and T_C) and ferroelectric transition temperature (T_{FE}), we established a sketch of phase diagram for $Eu_{1-x}Ba_xTiO_3$ ($0.0 \leq x \leq 1.0$) in the temperature-substitution (T-x) space as shown in Fig. 4.13. In Fig. 4.13, PM, AFM and FM represent paramagnetic, antiferromagnetic and ferromagnetic phases and PE and FE represent the paraelectric and ferroelectric phases. The left y-axis displays the magnetic transition temperature (T_N and T_C) and right y-axis represents the T_{FE}. For $x \geq 0.3$, the magnetic transition temperatures occur at lower temperature than the lowest temperature ($T = 2.5$ K) attained in our cryostat in NUS. The T_C for $x = 0.5$ was evaluated from the magnetization data measured using the micro Hall probe technique at University of

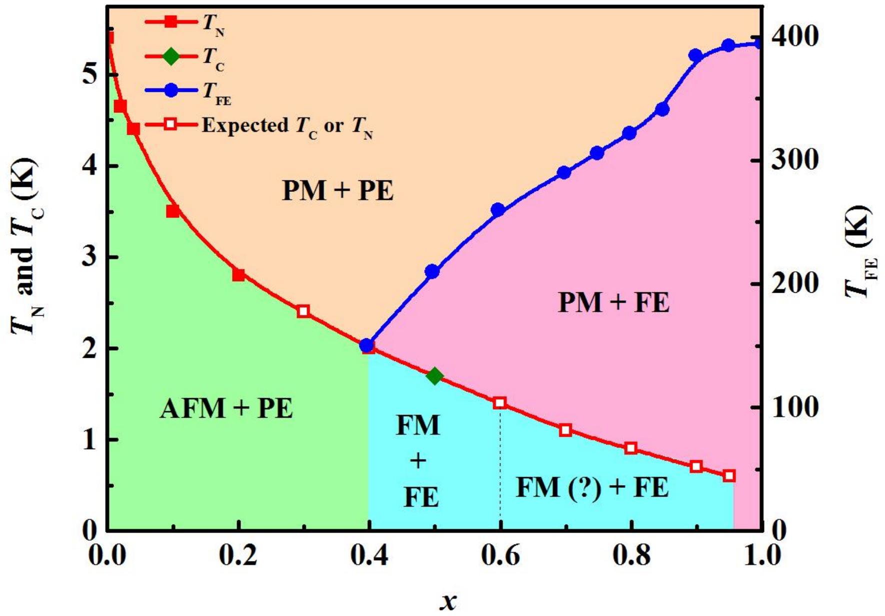

Figure 4.13 Phase diagram of $Eu_{1-x}Ba_xTiO_3$ (0.0 ≤ x ≤ 1.0). FE: Ferroelectric, PE: Paraelectric, AFM: Antiferromagnetic, FM: Ferromagnetic and PM: Paramagnetic. The magnetic transition temperatures for $x \geq 0.6$ are not measured experimentally but extrapolated values are initiated.

Zaragoza, Spain. To estimate the approximate T_N and T_C values for $x \geq 0.6$, we extrapolate the T_N and T_C versus T curve. As can be seen from Fig. 4.13, the two end compounds $x = 0.0$ and 1.0 are AFM+PE and PM+FE, respectively. As x increases from 0.0 to 1.0, $Eu_{1-x}Ba_xTiO_3$ transforms from AFM to FM and PE to FE at $x = 0.4$ and a multiferroic phase (FM + FE) can be realized for $Eu_{1-x}Ba_xTiO_3$ ($0.4 < x < 0.6$).

4.3.6 Magnetocaloric effect

4.3.6.1 Magnetic entropy change

From the measured magnetization isotherms, we have calculated the magnetic entropy change $\Delta S_m = S_m(H) - S_m(0)$ as described earlier in chapter 3. Suppression of spin fluctuation of $4f^7$ spins of Eu^{2+} ions by external magnetic field is responsible for the magnetic entropy change in $Eu_{1-x}Ba_xTiO_3$ (x = 0.1 - 0.9) compounds also. We plot the temperature dependence of $-\Delta S_m$ for all studied compositions (x = 0.1 - 0.9) and shown in Fig. 4.14 (a) - (i). When $\mu_0\Delta H = 0.5$ T, $-\Delta S_m$ for $x = 0.1$ is nearly zero above 50 K, but it decreases with lowering

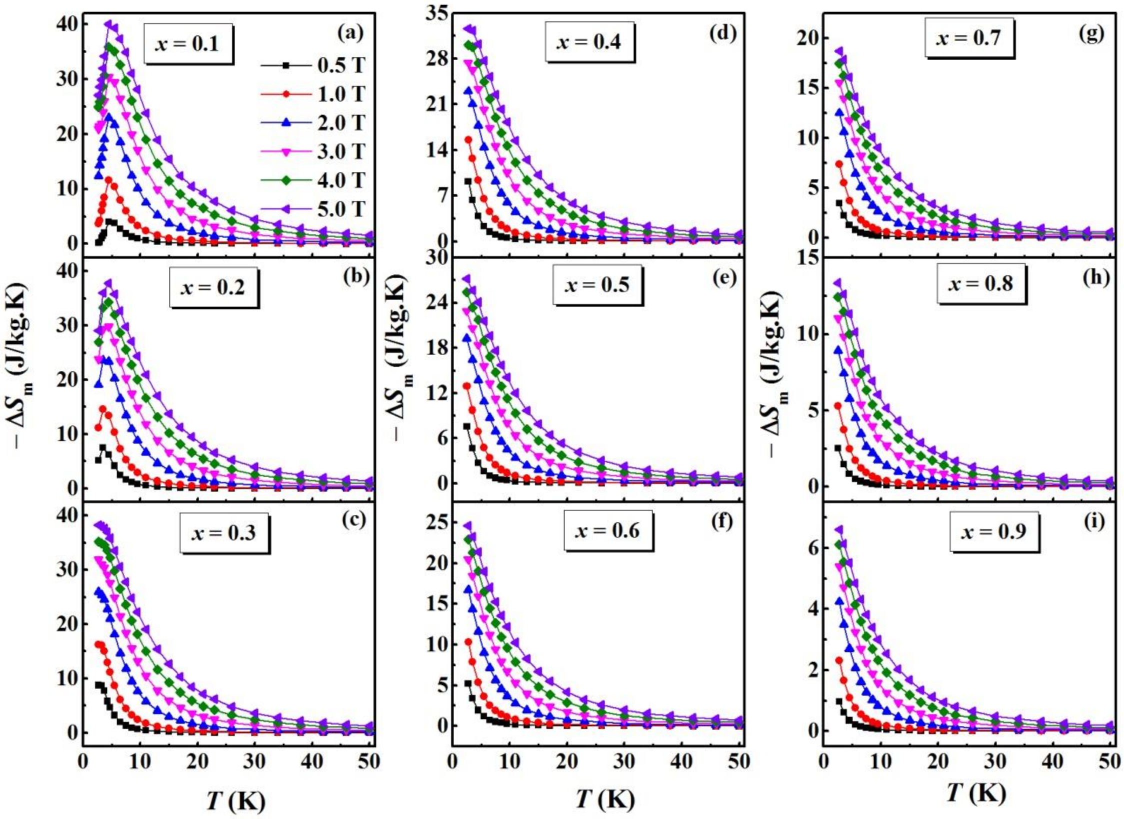

Figure 4.14 Temperature dependence of magnetic entropy change ($-\Delta S_m$) for (a) $x = 0.1$, (b) $x = 0.2$, (c) $x = 0.3$, (d) $x = 0.4$, (e) $x = 0.5$, (f) $x = 0.6$, (g) $x = 0.7$, (h) $x = 0.8$ and (i) $x = 0.9$ for a field change of $\mu_0\Delta H = 0.5$, 1, 2, 3, 4 and 5T.

temperature and shows a peak at $T = 4.5$ K, where it reaches a maximum value of 4.3 J.kg.K. The peak value of $-\Delta S_m$ increases with increasing value of ΔH ($-\Delta S_m = 11.60$, 21.89, 31.46 and 36.12 J/kg.K for $\mu_0\Delta H = 1$, 2, 3 and 4 T) and finally it reaches 40 J/kg.K for $\mu_0\Delta H = 5$ T. The position of the peak shows negligible shift (< 0.03 K) as the field changes from 0.5 T to 5 T. The observed value of the magnetic entropy is comparable to $EuTiO_3$ ($-\Delta S_m = 41$ J/kg.K for $\mu_0\Delta H = 5$ T), but higher than the maximum value of $-\Delta S_m = 16$ J/kg.K for $\mu_0\Delta H = 5$ T found for R = Dy among the rare earth titanates $RTiO_3$ (R = Dy, Ho, Er, Tm and Yb) series.[89] The observed $-\Delta S_m$ value is also higher than the maximum values reported in other Eu based materials such as EuO (17.5 J/kg.K, $T_C = 69$ K),[164] Eu_3O_4 (12.7 J/kg.K, $T_N = 5.3$ K),[165] $EuDy_2O_4$ (23 J/kg.K, $T_N = 5$ K),[167] $Eu_8Ga_{16}Ge_{30}$ – EuO composite (11.2 J/kg.K) [191] and $Eu_{0.45}Sr_{0.55}MnO_3$ (7 J/kg.K, $T_C = 120$ K),[192] EuSe (37.5 J/kg.K, $T_N = 4.6$

K)[166] and EuS (38 J/kg.K, T_C = 16 K) [193] for the same field change. The peak also occurs in x = 0.2 at T = 3.5 K but other compositions do not exhibit a peak since T_N decreases below the minimum temperature of 2.5 K reachable in our cryostat. The maximum value of $-\Delta S_m$ at the lowest temperature decreases with increasing Ba content. However, the most diluted sample (x = 0.9) shows a magnetic entropy change of $-\Delta S_m$ = 6.59 J/kg.K for $\mu_0\Delta H$ = 5 T, which is higher than the $-\Delta S_m$ = 1- 4 J/kg.K for the same field strength found in the majority of manganites exhibiting second order paramagnetic to ferromagnetic transitions.[9] The high values of $-\Delta S_m$ in present series of compounds compared to other Eu based oxides can be suggested to the following reasons: (1) Eu ions are mostly in the divalent state with large localized magnetic moments ($\mu = 7\mu_B$/Eu, S = 7/2, L = 0), (2) Thermal randomization of spins is negligible as T_N is below the liquid Helium temperature and hence the 4f spins easily align along the field direction as suggested by the M versus H/T plots. Hence, the applied field effectively suppresses the spin entropy of the 4f local moments leading to a giant magnetocaloric effect.

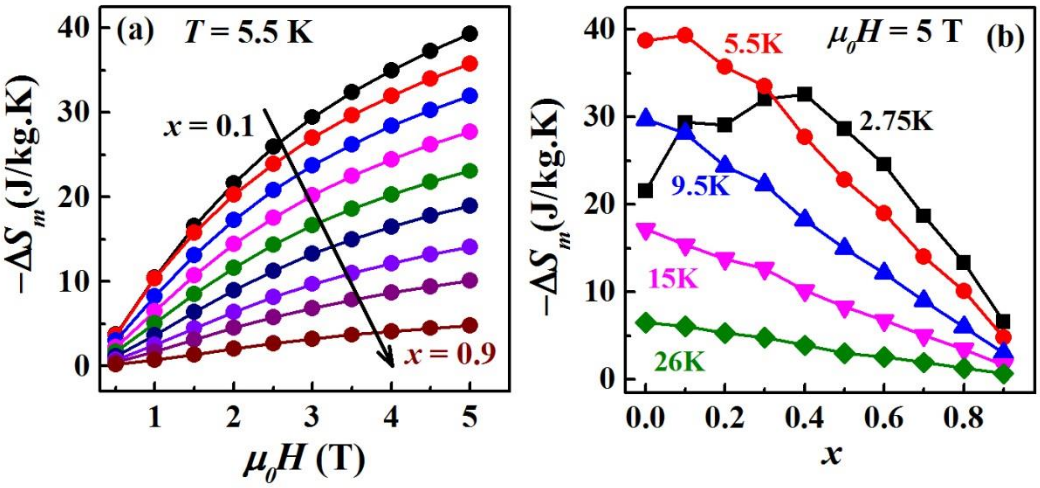

Figure 4.15 (a) Field dependence of $-\Delta S_m$ at T = 5.5 K for all compositions (x = 0.1-0.9). (b) Composition (x) dependence of $-\Delta S_m$ at T = 2.75 K, 5.5 K, 9.5 K, 15 K and 26 K.

Fig. 4.15 (a) shows the field dependence of $-\Delta S_m$ at T = 5.5 K for all the compositions (x = 0.1 – 0.9). As we can see, $-\Delta S_m$ increases superlinearly with increasing magnetic field for all the compositions and the largest change occurs for the x = 0.1 sample. We plot $-\Delta S_m$ as a function of Ba content (x) at five selected temperatures (T = 2.75, 5.5, 9.5, 15 and 26 K) in Fig. 4.15 (b). The $-\Delta S_m$ at T = 5.5, 9.5, 15 and 26 K decreases nearly linearly with increasing x whereas $-\Delta S_m$ at T = 2.75 K decreases below x = 0.3 due to the presence of antiferromagnetism in these samples.

4.3.6.2 Adiabatic temperature change in multiferroic $Eu_{0.5}Ba_{0.5}TiO_3$

To determine the adiabatic temperature change, we selected the half doped compound, $Eu_{0.5}Ba_{0.5}TiO_3$, which is ferroelectric below 210 K and ferromagnetic below 1.7 K. The main panel of Fig. 4.16(a) shows the temperature dependence of the heat capacity (C_p/R) at constant pressure normalized by the gas constant (R) under different magnetic fields upon cooling from 30 K to 0.35 K. The phonon contribution (dashed line) to the heat capacity can be described by the Debye model, which simplifies to a $C_L/R = aT^3$ dependence, where $a = 4.7 \times 10^{-5}$ K^{-3}. In the absence of an external magnetic field, the magnetic contribution (C_m) to C_p increases with decreasing temperature and goes through a peak value around T = 1.68 K (see the upper inset of Fig. 4.16(a) for clarity) which corresponds to the onset of ferromagnetic transition. As the applied magnetic field increases, the peak in C_m/R is rounded, decreased in amplitude and shifted to higher temperature (T = 1.6 K, 4.1 K, 8.7 K for $\mu_0 H$ = 0, 2 and 5 T). The maximum is no more visible for 7 T. The lower inset shows $C_p(T,H = 0)$ for T = 50-300 K. The heat capacity increases smoothly in the temperature range $T \approx$ 50- 200 K and shows a steplike change around 210 K. This anomaly is due to the onset of ferroelectric transition, which is supposed to occur at 210 K in this composition. We estimate the entropy (S) of the sample in a magnetic field H from the heat capacity data

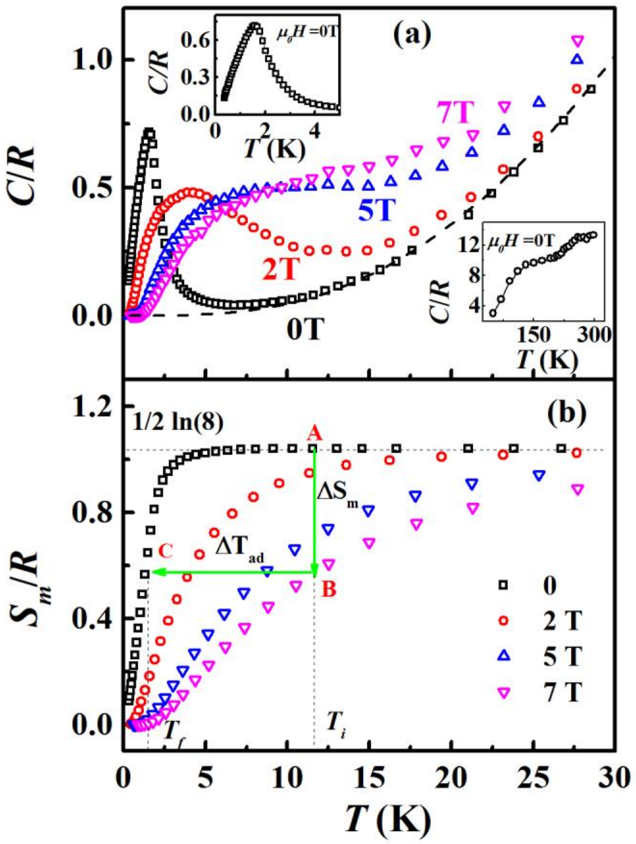

Figure 4.16 Main panels: Temperature dependence of (a) normalized heat capacity (C_p/R) under different magnetic fields (μ_0H = 0, 2, 5 and 7 T), together with the lattice contribution for $Eu_{0.5}Ba_{0.5}TiO_3$ (dashed line). $C_p(T, H = 0)/R$ for $T \leq 5$ K (upper inset) and T = 50-300 K. (b) Temperature dependence of normalized entropy (S/R) estimated from heat capacity data for μ_0H = 0, 2, 5 and 7 T. The dotted horizontal line indicates the high temperature limit of the spin entropy corresponding to complete disordering of 4f spins. The vertical line A → B represents decrease in entropy during isothermal magnetization. The horizontal line B → C represents the adiabatic demagnetization process in which the total entropy change is constant. The temperature of the sample decreases from T_i to T_f at the end of the adiabatic process.

using the relation $S(T,H) = \int_0^T \frac{C(T,H)}{T} dT$. The total entropy is $S = S_L + S_m + S_e$, where S_L, S_m and S_e are the lattice, magnetic, and electronic entropies, respectively. Since the titled compound is an insulator and shows no structural transition in the measured temperature range, it is the magnetic entropy (S_m) which dominates the other two contributions at low temperatures. The normalized entropy (S_m/R) is shown in Fig. 4.16(b). As the temperature increases from 0.35 K, $S_m(T,0)$ increases steeply until ~8 K and saturates above 10 K with a value $S_m/R = 1.04$. The spin entropy of localized $4f^7$ electrons attains a constant value in the paramagnetic state, where the spins are completely disordered. In this case, the spin entropy is given by S_m = $N R\ln(2s+1)$ where N is the number of magnetic atoms/unit cell, R is the gas constant and S = 7/2 for Eu^{2+} :$4f^7$ ion. The horizontal dotted line shows $S_m = 0.5R\ln 8 = 1.04R$ expected for $Eu_{0.5}Ba_{0.5}TiO_3$, which matches with the experimental values. $S_m(T,H)$ decreases below its zero field values over a temperature range with increasing external magnetic field because 4f spin fluctuations are quenched.

In section 4.3.6.1, the magnetic entropy change $\Delta S_m(T,\Delta H) = S_m(T,H) - S_m(T,0)$ for any field change $\Delta H = H \rightarrow 0$ was estimated from a set of M versus H isotherms using the Maxwell's equation $\Delta S_m = \int_0^H \left(\frac{\partial M}{\partial T}\right)_H dH$. Heat capacity under different magnetic fields provides a complete characterization of the magnetocaloric effect since we can estimate the both isothermal magnetic entropy change and adiabatic (isentropic) temperature change. We estimated ΔS_m from the heat capacity measured under different magnetic fields using the relation, $\Delta S(T,\Delta H) = \int_0^T \left[\frac{C(T,H)-C(T,0)}{T}\right] dT$. The estimation of the lattice contribution to the heat capacity is irrelevant in the present case since we deal with differences in total entropies in zero and at a fixed magnetic field H. Fig. 4.17 (a) shows ΔS_m versus T curves for $\mu_0\Delta H$ = 0 → 2 T, 0 → 5 T and 0 → 7 T. Symbols represent ΔS_m values calculated from the heat capacity and the solid line represents ΔS_m obtained from magnetization data, respectively. It can be seen that ΔS_m values calculated from both the methods closely match. The $-\Delta S_m$ $(T,\mu_0\Delta H = 2\text{ T})$ initially increases with decreasing temperature and goes through a peak around 2.3 K before decreasing at low temperatures. The peak value of $-\Delta S_m$ increases with increasing ΔH but the peak position shows only a small shift towards higher temperature. For example, while the position of the $-\Delta S_m$ peak shifts from T = 2.3 K to 2.9 K as $\mu_0\Delta H$ changes from 2 T to 7 T, the peak value increases from 20.21 J/kg.K to 31.32 J/kg.K.

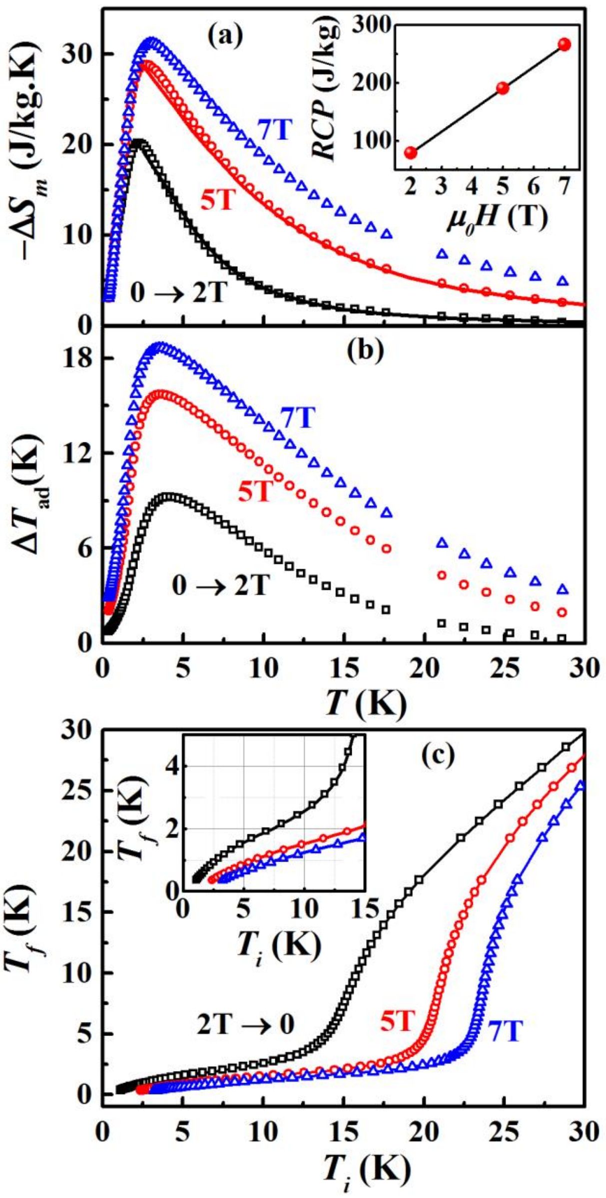

Figure 4.17 (a) Main panel: Temperature dependence of the entropy change $\Delta S(T,\Delta H) = S(T,H) - S(T,0)$ of $Eu_{0.5}Ba_{0.5}TiO_3$ for magnetization process $\Delta H = 0 \rightarrow H$, where $\mu_0 H$ = 2, 5 and 7 T. Symbol and line represent the ΔS data calculated from heat capacity and magnetization data respectively. Inset shows the relative cooling power (*RCP*) as a function of magnetic field. (b) Temperature dependence of the adiabatic temperature change $\Delta T_{ad}(T,\Delta H) = T_{ad}(T,H) - T_{ad}(T,0)$ for $\Delta H = 0 \rightarrow H$. (c) The temperature dependence of the final temperature (T_f) reachable from the initial temperature (T_i) of the demagnetization process B → C (see Figure 4.14).

The adiabatic temperature change $\Delta T_{ad}(T,\Delta H)= [T_i(T,H) - T_f(T,0)]_S$ for $\Delta H = H \rightarrow 0$ is obtained from S_m/R versus T curves. In an adiabatic demagnetization refrigerator, the sample is first magnetized isothermally at a temperature T_i, while its magnetic entropy decreases by ΔS_m, that is, from A to B along the vertical line in Fig. 4.15(b). The decrease in

S is compensated by an increase in the lattice entropy (phonon vibration) which raises the sample temperature. The excess heat generated in the sample is completely removed at point B by a coolant. In the isentropic process ($\Delta S = 0$) represented by the horizontal line B → C, the sample is isolated from the surrounding and the field is adiabatically decreased to zero, which causes the magnetic entropy to increase and lattice entropy to decrease in order to keep the total entropy change constant. Then, the final temperature of the sample decreases to T_f. The adiabatic temperature change $\Delta T_{ad} = T_i - T_f$ is estimated from the isentropic line in Fig.4.17(b) as the field is increased from value 0 to H and it is plotted in Fig. 4.15(b). Similarly to ΔS, ΔT_{ad} also goes through a peak and the peak value increases with increasing value of H. At the peak, ΔT_{ad} = 9.23 K, 15.75K and 18.68 K for $\mu_0\Delta H = 0 \rightarrow 2$ T, $0 \rightarrow 5$ T and $0 \rightarrow 7$ T, and the peak occurs at 4.2 K, 3.7 and 3.5 K, respectively. Figure 4.17(c) shows the final temperature reached by adiabatic removal of the magnetic field against the initial temperature. When T_i = 30 K, $T_f \approx T_i$ as the field is adiabatically reduced from 2 T to 0 T but T_f = 25 K if the field is changed from 7 T to 0 T. On the other hand if T_i = 25 K the final temperature reachable is 15 K for $\mu_0 H = 7$ T $\rightarrow 0$. The inset shows the expanded view of the low temperature region. It can be seen that with the initial temperature of 15(5) K, the final temperature attainable is 1.67(0.64) K for $\mu_0 H = 7$ T $\rightarrow 0$. This graph illustrates that $Eu_{0.5}Ba_{0.5}TiO_3$ could be a potential candidate for the magnetic refrigeration below 30 K. The ΔT_{ad} values observed in $Eu_{0.5}Ba_{0.5}TiO_3$ are larger than in other known promising materials for magnetic refrigeration below 30 K such as $Dy_3Ga_5O_{12}$ (ΔT_{ad} = 16 K for $\mu_0\Delta H$ = 7 T at T = 17 K)[194], $ErAl_2$ (ΔT_{ad} = 12 K for $\mu_0\Delta H$ = 5 T at T = 13 K)[168] and Gd_2 molecular cluster (ΔT_{ad} = 12.7 K for $\mu_0\Delta H$ = 7 T at T = 1.8 K)[195]. Among the rare earth titanates of the formula RTiO$_3$ (R = Ho, Dy, Er, Tm and Yb), $DyTiO_3$ exhibits the highest magnetic entropy change ($-\Delta S_m$ = 16 J/kg.K for $\mu_0\Delta H$ = 5 T) at the ferromagnetic transition of Ti sublattice.[89] Yu Su *et al.*[87] found ΔT_{ad} = 6.79 K, $-\Delta S_m$ =15.88 J/kg.K at T_C = 65 K in their single crystalline $DyTiO_3$ sample and attributed the large MCE observed to structural distortion that accompanies the magnetic phase transition. However, the magnetic entropy change in our sample ($-\Delta S_m = 29$ J/kg.K for $\mu_0\Delta H = 5$ T) surpasses that of $DyTiO_3$ and it originates not from the magnetic phase transition in the transition metal (Ti^{4+}) sublattice but from the suppression of spin fluctuations associated with the rare-earth 4f spins.

The relative cooling power ($RCP = \Delta S^{max} \times \Delta T_{FWHM}$, where ΔS^{max} is the maximum value of ΔS_m at the peak for a given ΔH, and ΔT_{FWHM} is the full width at half maximum in the temperature scale) is shown in the inset of Fig. 4.17(a),. The *RCP* increases with the magnetic field and reaches a maximum value of 343 J/kg (248 J/kg) for $\mu_0\Delta H = 7$ T (5 T). The *RCP* value in $Eu_{0.5}Ba_{0.5}TiO_3$ is higher than $EuHo_2O_4$ (275 J/kg at $T = 5$ K for $\mu_0\Delta H = 5$ T)[167], but smaller than EuSe (580 J/kg at $T = 4.6$ K for $\mu_0\Delta H = 5$ T)[166].

4.3.7 DC resistivity and magnetoresistance

Fig. 4.18 (a) shows the temperature dependence of four-probe dc resistivity (ρ_{dc}) for $x = 0.1$, 0.3, 0.5 and 0.6, measured while cooling from $T = 500$ K to 100 K. While $\rho_{dc}(T)$ for $x = 0.1$ increases monotonically with decreasing temperature, $\rho_{dc}(T)$ for $x = 0.3$, 0.5 and 0.6

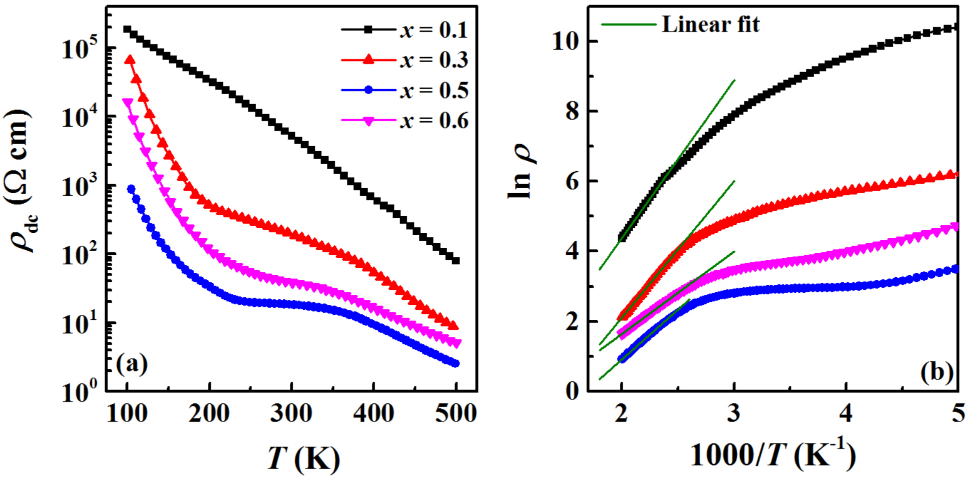

Figure 4.18 (a) Temperature dependence of four-probe dc resistivity (ρ_{dc}) under zero magnetic fields for $x = 0.10$, 0.30, 0.50 and 0.60. (b) lnρvs 1/T for all four compounds with linear fit.

samples shows a unusual behavior. $\rho_{dc}(T)$ for x = 0.3, 0.5 and 0.6 increases smoothly between 500 K and 350 K but shows a broad hump between 350 K and 250 K before increasing rapidly below 250 K. The $\rho_{dc}(T)$ of all samples follows thermally activated behavior $\rho = \rho_0 \exp\left(\frac{E_a}{k_B T}\right)$ in high temperature regime. Fig. 4.18(b) shows ln(ρ) versus 1/T plot in a temperature range, 500 K≤T ≤200 K. A nice linear fit is observed from T =500 K to T~ 400 K for all samples. The activation energy E_a calculated from the linear fit of ln(ρ) versus 1/T plot are 388, 335, 244 and 202 meV for x = 0.1, 0.3, 0.5 and 0.6, respectively. The activation energy of $Eu_{1-x}Ba_xTiO_3$ decreases with increasing x.

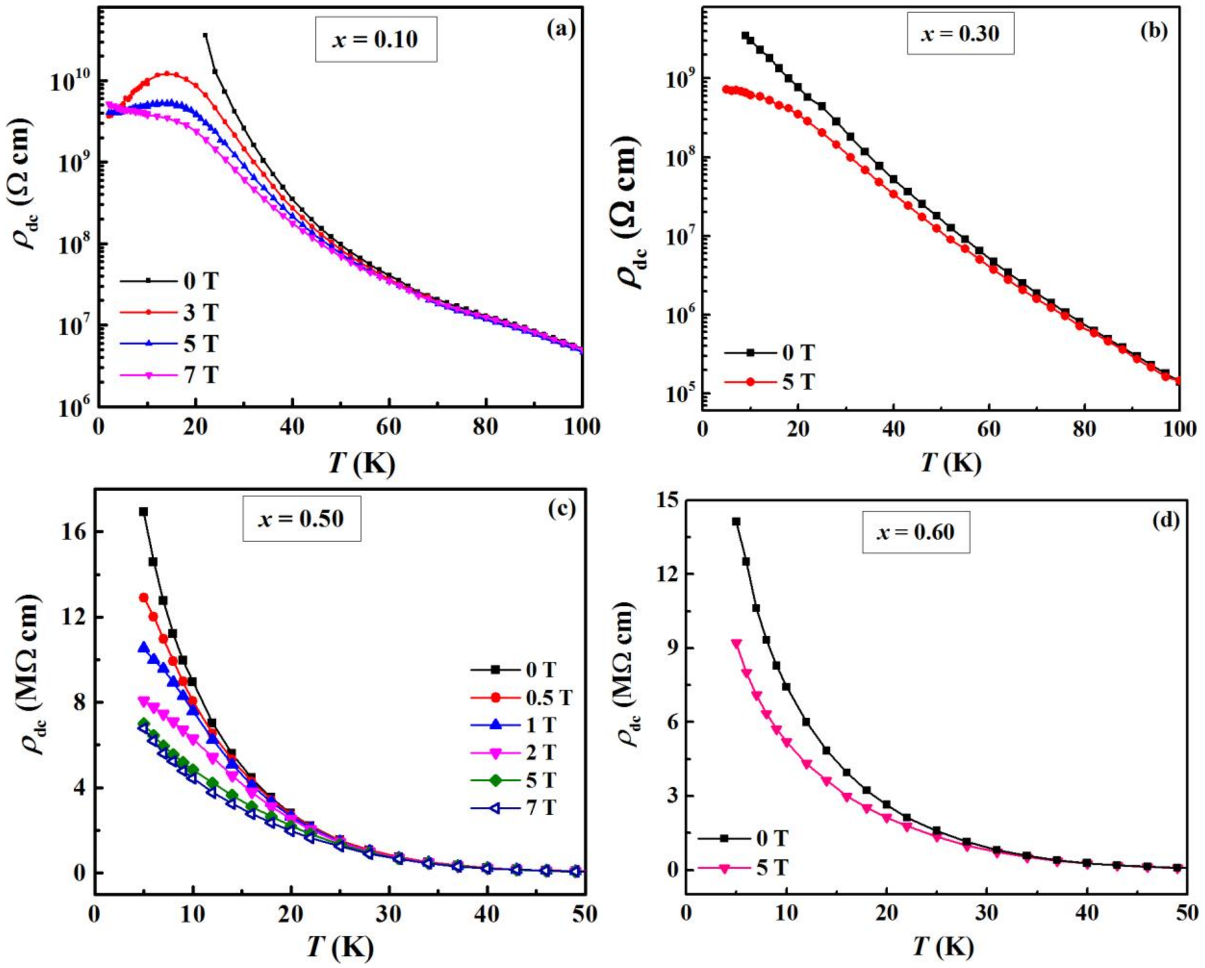

Figure 4.19 Temperature dependence of dc resistivity (ρ_{dc}) under different magnetic fields for (a) x = 0.10, (b) x = 0.30, (c) x = 0.50 and (d) x = 0.60.

Fig. 4.19 (a), (b), (c) and (d) show the temperature dependence of the two-probe dc resistivity (ρ_{dc}) for x = 0.10, 0.30, 0.50 and 0.60, respectively, measured at low temperatures (T = 100K – 2 K) under different magnetic fields. $\rho_{dc}(T)$ of x = 0.1 in zero field increases with decreasing temperature and it is not measurable below 20 K even with the electrometer. However, the application of magnetic field μ_0H = 3 T causes a maximum in ρ_{dc} at T = 14 K, below which ρ_{dc} decreases with decreasing temperature. The maximum sifts up by 1 K under 5 T. ρ_{dc} under 7T shows a tendency to increase below 15 K. $\rho_{dc}(T)$ of x = 0.30 in zero field also increase with decreasing temperature and it is measurable down to 5 K. ρ_{dc} decreases

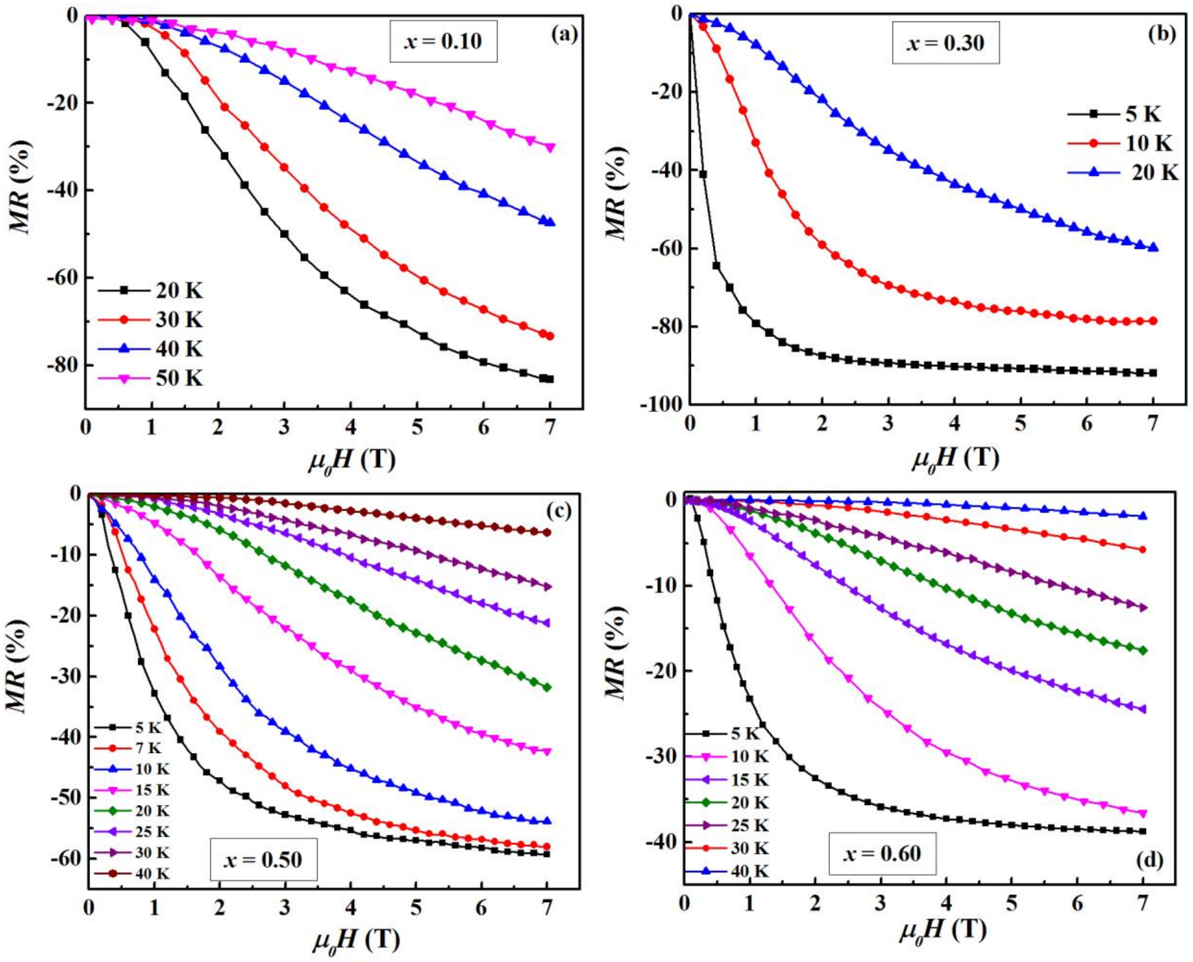

Figure 4.20 Magnetic field dependence of magnetoresistance (*MR*) at different temperatures for (a) *x* = 0.10, (b) *x* = 0.30, (c) *x* = 0.50 and (d) *x* = 0.60.

substantially below 40 K under 5 T and shows a tendency towards a maximum at 5 K. The zero field ρ_{dc} for x = 0.50 and 0.60 increases with decreasing temperature down to 5 K, where it reaches ρ_{dc} = 17 MΩ cm and 14 MΩ cm, respectively. The application of magnetic field decreases ρ_{dc} mostly below 30 K. field below 30 K. Here, we noticed that the zero field ρ_{dc} for x = 0.50 and 0.60 is lower than that for x = 0.10 and 0.30. The lower ρ_{dc} of x = 0.50 and 0.60 is most probably due to the presence of oxygen vacancies in these samples as observed from TGA.

Fig. 4.20 (a), (b), (c) and (d) show the field dependence of *MR* for x = 0.10, 0.30, 0.50 and 0.60, respectively, obtained from ρ_{dc} measured while varying the magnetic field at different temperatures. The *MR* for x = 0.10 is –83.5% at T = 20 K and μ_0H = 7 T, which decreases to –32.4% at 50 K. For x = 0.30, *MR* is –92%, –78% and –60 % at T = 5 K, 10 K and 20 K, respectively. The ρ_{dc} as a function of field for x = 0.50 and 0.60 is measured over wide temperature range (5 K – 40 K). At T = 5 K and μ_0H = 7 T, *MR* values are –59% and –39% for x = 0.50 and 0.60, respectively and it decrease to –6.3% and –1.8% at T = 40 K.

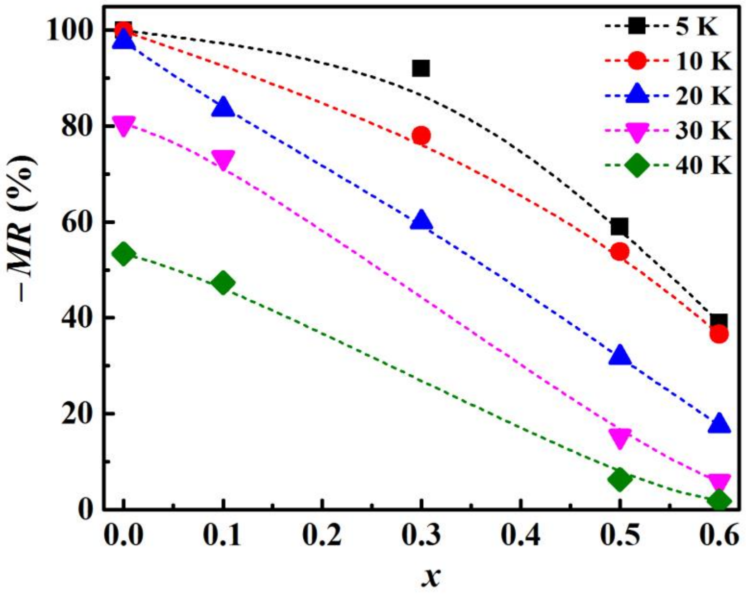

Figure 4.21 Magnetoresistance (*MR*) as a function of Ba contents (*x*) at different temperatures *T* = 5, 10, 20, 30 and 40 K.

Fig. 4.21 shows the negative magnetoresistance (−*MR*) as a function of Ba contents (x) at various temperatures under $\mu_0 H$ = 7T. As x increases, *MR* decreases in magnitude for all temperatures. At T = 5 K, *MR* decreases gradually from −99.98% for x = 0.00 to −92% for x = 0.30, while a rapid decrease is observed with further increasing x from 0.30 to 0.60 (*MR* = −59%). At T = 20 K, *MR* follows an almost linear decrease with x. However, *MR* decreases rapidly with increasing x for T = 30 K and 40 K and reaches 5.7% and 1.8%, respectively for x = 0.60.

In chapter 3, we have fitted the field dependence of *MR* of EuTiO$_3$ with a model proposed for *MR* in diluted semiconductors that explains the scattering of charge carriers with localized spins. According to the model, the negative resistance is given by[121]

$$MR = -a^2 \ln(1 + b^2 H^2) \tag{4.4}$$

where a and b are the fitting parameters and depend on the magnetization and density of states. We show field dependence of *MR* fitted with Eq. (4.4) for x = 0.10 and 0.60 in Fig. 4.22 (a) and (b), respectively. For x = 0.10, the experimental *MR* data fit very well in full

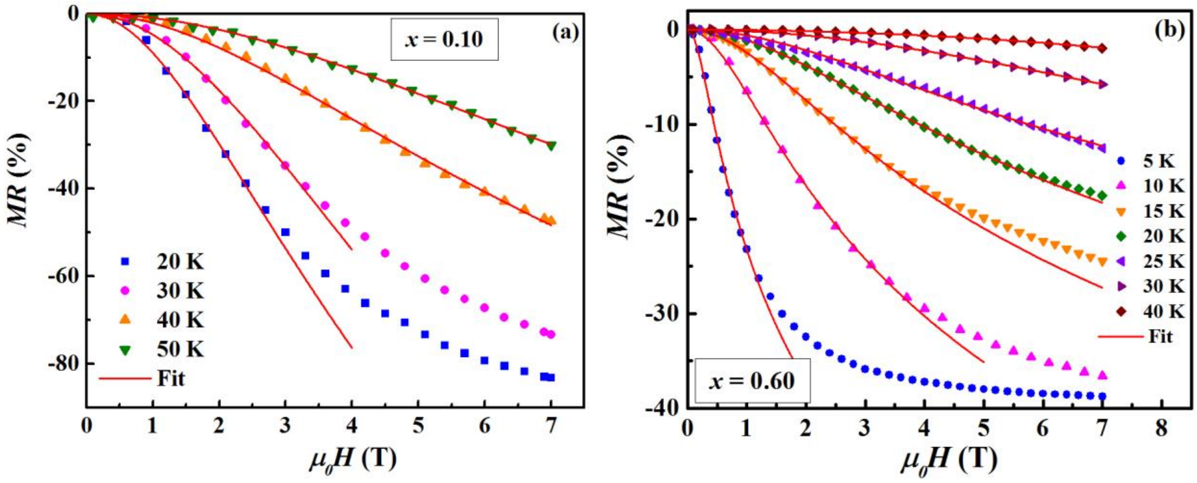

Figure 4.22 Symbols: Experimental *MR* as a function of magnetic field at different temperatures for (a) x = 0.10 and (b) x = 0.60. Solid line: Least-square fit of experimental *MR* to Eq. (4.4).

field range for T = 40 and 50 K, while deviation occurs around μ_0H = 3 T and 2.2 T for T =30 K and 20 K, respectively. In case of x = 0.60, experimental *MR* data agree well with Eq. (4.4) over full field range for $T \geq 25$ K. For T = 20 K, the calculated *MR* deviates from the experimental *MR* at μ_0H = 6 T, while this deviation is seen at μ_0H = 2.2 T for x = 0.10. Moreover, the experimental data for x = 0.60 fit well until the field of 3.5 T and 1.2 T for 10 K and 5 K, respectively. Similar fitting has been obtained for other compositions x = 0.30 and 0.50 (not shown here). Here, it is important to compare the fitting results of x = 0.10 and 0.60 with undoped compound $EuTiO_3$. In case of $EuTiO_3$, experimental *MR* data for T = 5 K completely disagree with Eq. (4.4) and fit only until μ_0H = 0.8 T and 2 T for T = 10 K and 20 K, respectively. Therefore, the magnetic field, where the deviation in experimental and calculated *MR* occurs, increases as x increases (μ_0H = 2 T, 2.2 T and 6 T for x = 0.00, 0.10 and 0.60, respectively at T = 20 K).

4.3.8 Magnetodielectric effect and ac magnetoresistance

4.3.8.1 Magnetic field dependence of dielectric constant and ac resistivity of lightly Ba doped $EuTiO_3$ ($Eu_{1-x}Ba_xTiO_3$, x = 0.02, 0.1 and 0.3)

Fig. 4.23 (a) and (b) show the temperature dependence of ε and ρ_{ac} for x = 0.02 under various magnetic fields (μ_0H = 0, 1, 3 and 5 T) from 60 K to 5 K for f = 1 kHz, respectively. In the absence of an external magnetic field, $\varepsilon(T)$ decreases rapidly between 60 K and 10 K and it is nearly temperature independent between 15 K and 5 K. The value of ε at 5 K is ~240. Application of an external magnetic field increases the value of ε over a limited temperature range. The ε at 5 K increases from ~ 240 in zero field to ~ 345 under 1 T magnetic field. As the temperature increases from 5 K, $\varepsilon(T)$ initially decreases and goes through a minimum around temperature ~ 10 K and then increases. Finally, $\varepsilon(T, \mu_0H = 1\text{ T})$ curve merges with $\varepsilon(T, \mu_0H = 0\text{ T})$ curve above 20 K. The minimum shifts to ~ 12 K under

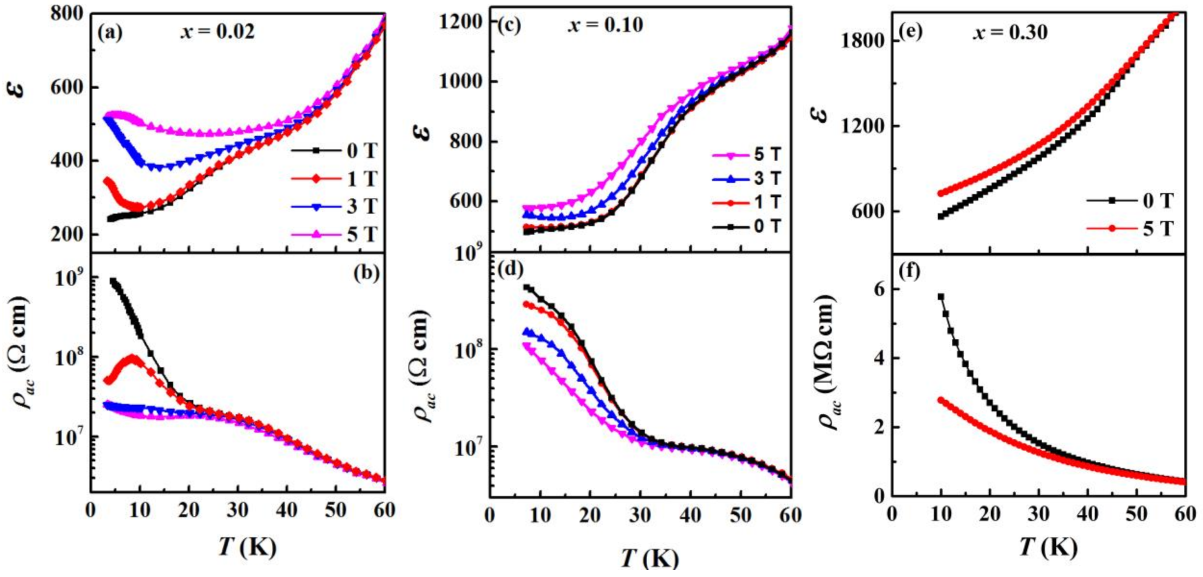

Figure 4.23 Temperature dependence of (a) dielectric constant (ε) and (b) ac resistivity (ρ_{ac}) for x = 0.02, (c) ε and (d) ρ_{ac} for x = 0.10, and (e) ε and (f) ρ_{ac} for x = 0.30.

3 T and to 20 K under 5 T. While the value of ε at 5 K for 3 T is enhanced compared to 1 T, enhancement is weak for 5 T. The ρ_{ac} for x = 0.02 (Fig 4.23(b)) in zero field increases rapidly below 20 K but its magnitude decreases under 1 T and shows a peak around ~10 K. The resistivity decreases further under 3 T magnetic field and $\rho_{ac}(T)$ shows a broad maximum around ~ 10 K. Although resistivity under 5 T also decreases in magnitude, the relative change between 3 and 5 T is much smaller than between 1 and 3 T. Strangely, $\rho_{ac}(T)$ under 5T increases below 10 K.

Fig. 4.23(c) and (d) show the temperature dependence of ε and ρ_{ac} for x = 0.10, respectively, under various magnetic fields ($\mu_0 H$ = 0, 1, 3 and 5 T) for f = 1kHz. In zero magnetic field, $\varepsilon(T)$ decreases rapidly as temperature decreases from 60 K to 25 K and it weakly depends on temperature below 25 K. Application of an external magnetic field leads to enhancement of ε value in a limited temperature range, but no minimum is observed. The ε at 10 K increases from ~ 500 in zero field to ~ 520 and 640 under 3 T and 7 T magnetic fields, respectively. The $\rho_{ac}(T)$ in zero field shows a rapid increase below 30 K. The value of ρ_{ac} decreases under the action of magnetic fields. For x = 0.30, we show the temperature dependence of ε and ρ_{ac} under the magnetic fields of 0 and 5 T in Fig. 4.23 (e) and (f), respectively. The zero field $\varepsilon(T)$ decreases rapidly as temperature decreases and reaches ~ 560 at T = 10 K. With application of magnetic field (5 T), ε value increases below 50 K. Here, we notice that the zero field ε value at low temperature increases with increasing x from 0.02 to 0.30. The zero field ρ_{ac} for x = 0.30 (~ MΩ cm) is much lower than that for x = 0.02 and 0.10 (~ GΩ cm). The lower resistivity could be due to the oxygen defects present in higher Ba doped samples. The $\rho_{ac}(T)$ in zero field shows a rapid increase below 60 K but it decreases in magnitude under 5 T and below 40 K.

Fig. 4.24 (a) and (b) show the magnetic field dependence of the percentage change of $MDE = \frac{\varepsilon(H)-\varepsilon(0)}{\varepsilon(0)}$ and $MR = \frac{\rho(H)-\rho(0)}{\rho(0)}$, respectively, for x = 0.02 at four selected temperatures. At 10 K, *MDE* varies less than 1% as the field increases from μ_0H= 0 to 1.5 T and then increases rapidly between 1.5 and 6 T and gradually between 6 T and 7 T. The *MDE*

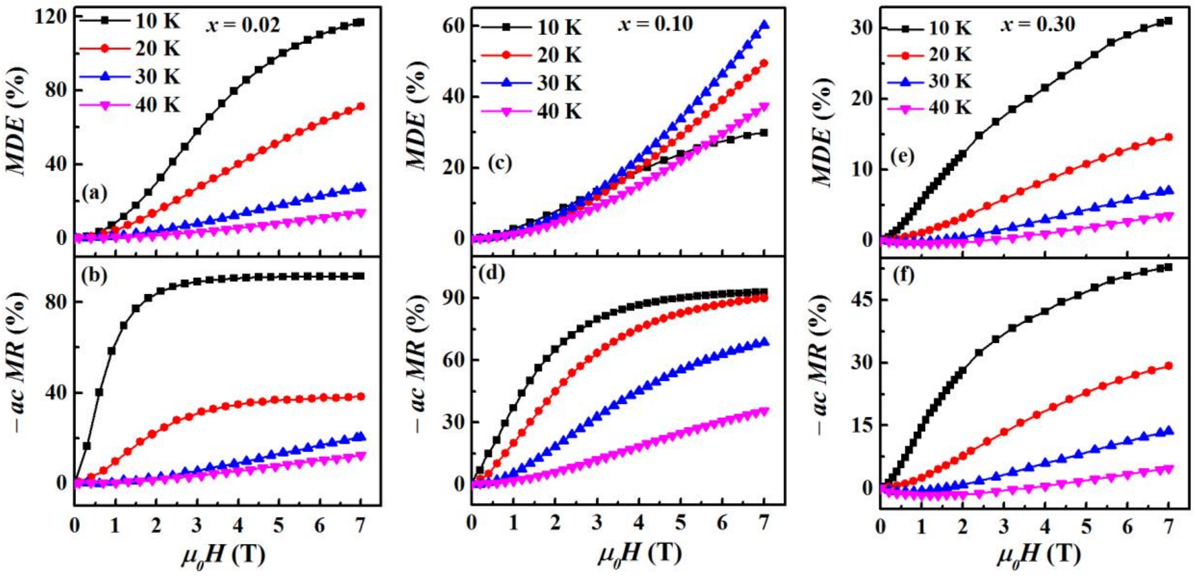

Figure 4.24 Magnetic field dependence of (a) magnetodielectric effect (*MDE*) and (b) negative ac magnetoresistance (− *ac MR*) for *x* = 0.02, (c) *MDE* and (d) − *ac MR* for *x* = 0.10, and (e) *MDE* and (f) − *ac MR* for *x* = 0.30 at *f* = 1kHz.

reaches 120% at 7 T. This is much larger than 7% *MDE* found at 2 K and 7T, well below the Neel temperature in single crystalline $EuTiO_3$ but lower than the 670 % *MDE* observed in polycrystalline $EuTiO_3$ at T = 10 K. The *MDE* data at 20 K, unlike that of 10 K, shows no tendency for saturation up to 7 T. The magnitude of the *MDE* falls with increasing temperature (*MDE* = 120, 76, 30, and 12% at 7 T for T = 10, 20, 30 and 40 K). In contrast to less than 1% change exhibited by *MDE* below 1.5 T, the –*MR* shows a dramatic increase of 80% at 1.5 T and 90 % at 3 T. It further increases by only 4 % as the field increases from 3 to 7 T. Thus, the field dependence of –*MR* is completely different from that of *MDE*. As the temperature increases, –*MR* also decreases (–*MR* = 94%, 30%, 20%, 12% at T = 10, 20, 30 and 40 K, respectively). The magnitude of *MR* (94 %) for $Eu_{0.98}Ba_{0.02}TiO_3$ at T = 10 K is lower than that for $EuTiO_3$ (99.88 %).

We show the field dependence of the *MDE* and the –*MR* of x = 0.10 in Fig. 4.24(c) and (d), respectively, at four different temperatures (T = 10, 20, 30 and 40 K) for f = 1kHz. At T = 10 K, the *MDE* increases gradually with magnetic field from $\mu_0 H$ = 0 T to 5 T, shows a tendency to saturate above 5 T and attains 30 % for $\mu_0 H$ = 7 T, which is larger than 3% *MDE* of single crystalline $Eu_{0.9}Ba_{0.1}TiO_3$ found well below the Neel temperature.[14] The *MDE* data at higher temperatures (20, 30 and 40 K), unlike that of 10 K, shows no tendency for saturation up to 7 T. At T= 30 K, *MDE* is 60 % and it is higher than its value (= 30%) at T = 40 K. In contrast to the small *MDE* observed below 1 T, the –*MR* shows a dramatic increase from 37% at 1 T to 80 % at 3 T and further 12 % increase between 3 and 7 T. As the temperature increases, the magnitude of *MR* decreases (–*MR* = 92 %, 69 % and 17 % at T = 10, 30 and 40 K, respectively). The field dependences of *MDE* and – *MR* for x = 0.30 are shown in Fig. 4.24 (e) and (f), respectively. The *MDE* and *MR* both increase in magnitude with increasing magnetic field in a similar manner. At T = 10 K, no saturation is observed in *MR* for high magnetic field in contrast to the field dependence of *MR* for x = 0.02 and 0.10.

The *MDE* = 31 % and – *MR* = 52 % at T = 10 K and μ_0H = 7 T. As temperature increases, *MDE* and – *MR* both decrease. Most importantly, the maximum values of *MDE* (120%, 60 % and 31 % for x = 0.02, 0.1 and 0.3, respectively) and *MR* (– 94%, – 92 % and – 52 % for x = 0.02, 0.1 and 0.3, respectively) decrease with increasing x.

4.3.8.2 Magnetic field dependence of dielectric constant and ac resistivity of $Eu_{1-x}Ba_xTiO_3$ (x = 0.5 and 0.6)

Fig. 4.25 (a) and (b) show the temperature dependence of ε and ac resistivity (ρ_{ac}) for x = 0.5, respectively, measured upon cooling from 50 K to 10 K under the field of 0 T and 5 T at f = 1kHz. The zero and 5 T fields data are represented with black square and red open circle symbols respectively. The $\varepsilon(T)$ decreases gradually as temperature decreases and shows a large value ~ 550 at T = 10 K. With an applied magnetic field of 5 T, the value of $\varepsilon(T)$ increases below 30 K. Conversely, $\rho_{ac}(T)$ increases with decreasing temperature and its value below 30 K decreases under 5T. Similar behavior is found for ε (T) and $\rho_{ac}(T)$ in x = 0.6 (Fig. 4.25(c) and (d)).

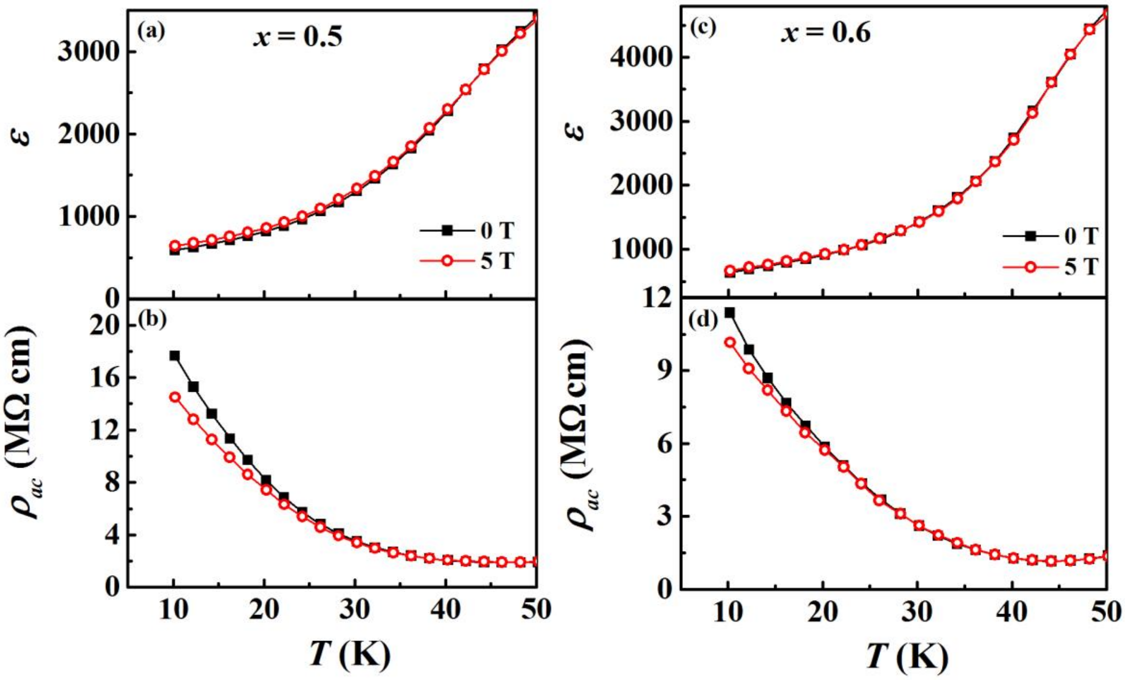

Figure 4.25 Temperature dependence of (a) dielectric constant (ε) and (b) ac resistivity (ρ_{ac}) for x = 0.5, and (c) ε and (d) ρ_{ac} for x = 0.6 at f = 1kHz.

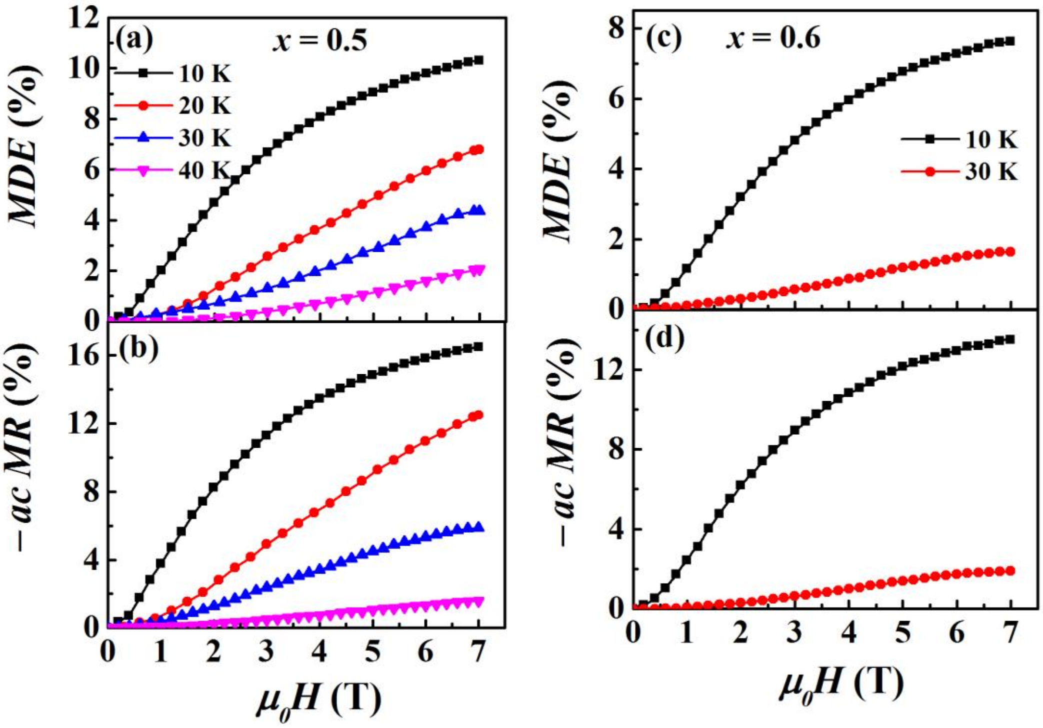

Figure 4.26 Magnetic field dependence of (a) magnetodielectric effect (*MDE*) and (b) negative magnetoresistance (–*MR*) for x = 0.5, and (c) *MDE* and (d) –*MR* for x = 0.6 at f = 1kHz.

Fig. 4.26 (a) and (b) show the field dependence of *MDE* and –*MR*, respectively for x = 0.5 at frequency f = 1 kHz and temperatures 10, 20, 30 and 40 K. The *MDE* at 10 K increases rapidly as the field is increased from μ_0H = 0 T to ~ 4T and then gradually above 4 T. Thus, the *MDE* is positive and it reaches +10% for μ_0H = 7 T at 10 K and it is smaller than + 31% *MDE* found in $Eu_{0.7}Ba_{0.3}TiO_3$ at T = 10 K. The −*MR* also increases with field and it shows the field dependence very similar to the *MDE*. The *MR* is −16.5% for 7 T at 10 K. Magnitudes of both *MDE* and *MR* decrease as the temperature increases (*MDE* = +2% and *MR* = −1.5 % at 40 K) and they become negligible above 40 K. Fig. 4.26 (c) and (d) show the field dependence of *MDE* and –*MR*, respectively for x = 0.6 at frequency f = 1 kHz and temperatures 10 and 30 K. At T = 10 K, *MDE* = 7.6% and *MR* = −13.5% for μ_0H = 7T. As temperature increases, *MDE* and *MR* both increase and reach +1.6% and −1.9%, respectively at T = 30K.

4.3.8.3 Correlation between *MDE* and ac *MR* of $Eu_{1-x}Ba_xTiO_3$ ($0.1 \leq x \leq 0.6$)

Fig. 4.27 (a), (b), (c) and (d) show the *MDE* versus –*MR* curves at different temperatures for $x = 0.10$, 0.30, 0.50 and 0.60, respectively. For $x = 0.10$, the *MDE* and – *MR* are highly non-linear at all temperatures. While *MDE* and –*MR* are approximately linear at 30 K and 40 K for $x = 0.30$, it is non-linear at $T = 10$ and 20 K. Furthermore, *MDE* and –*MR* are almost linear at all temperatures for $x = 0.50$ and 0.60.

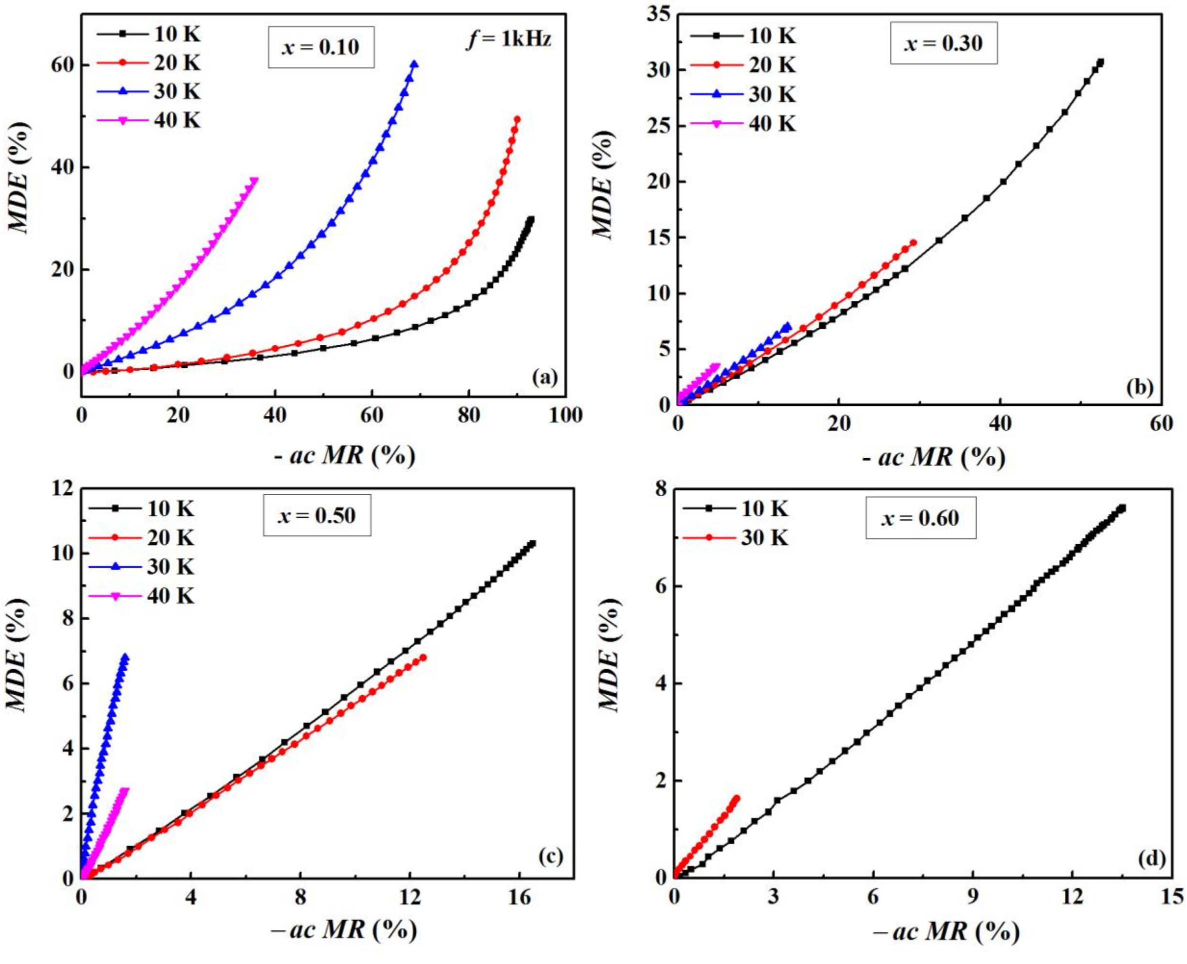

Figure 4.27 ***MDE*** **versus –*MR* curves at different temperatures for (a) $x = 0.10$, (b) $x = 0.30$, (c) $x = 0.50$ and (d) $x = 0.60$.**

4.3.8.4 *MDE* and ac *MR* as a function of Ba contents (x)

Fig. 4.28 displays the x dependence of maximum values of *MDE* and –*MR* at left and right y-axis respectively. As x increases, *MDE* and *MR* both decrease in magnitude. The

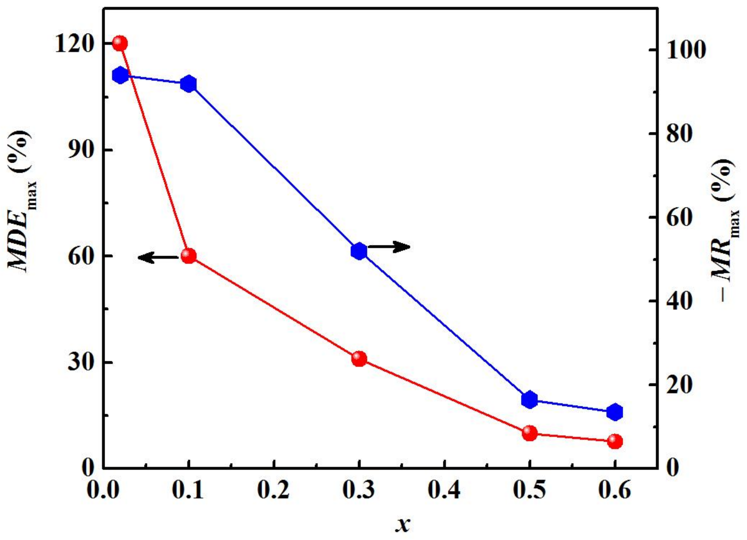

Figure 4.28 Maximum values of *MDE* (left y-axis) and – *ac MR* (right y-axis) as a function of Ba content (*x*).

MDE decreases from +120% for $x = 0.02$ to + 7.6% for $x = 0.6$. Therefore, the coupling between magnetism and dielectric constant decreases with Ba doping. The *MR* decreases from –94% for $x = 0.02$ to –13.5% for $x = 0.60$. As one can notice the values of ac and dc *MR* are same for $EuTiO_3$, while ac *MR* is much lower than the dc *MR* for $Eu_{1-x}Ba_xTiO_3$ ($x = 0.10 – 0.60$). The difference between ac and dc *MR* for $Eu_{1-x}Ba_xTiO_3$ increases as *x* increases.

4.3.8.6 Magnetodielectric loss

To investigate the magnetic field effect on dielectric loss, the capacitance (*C*) and dielectric loss (tanδ) have been measured simultaneously as a function of magnetic field at different temperatures and frequencies for $Eu_{1-x}Ba_xTiO_3$ ($x = 0.10 – 0.60$). Fig. 4.29 (a) and (b) show the field dependence of magnetodielectric loss (*MDL*) defined as $MDL = \frac{tan\delta(H) - tan\delta(0)}{tan\delta(0)}$ for $x = 0.10$ and 0.60, respectively at $f = 1$ kHz. The *MDL* is positive for all temperatures and frequencies and the field dependence of *MDL* is quite similar to that of *MDE*. For $x = 0.10$, *MDL* reaches +827% at $T = 10$ K and $\mu_0H = 7$ T, which is much larger than *MDE* value (+30%) at same temperature and field. *MDL* decreases with increasing

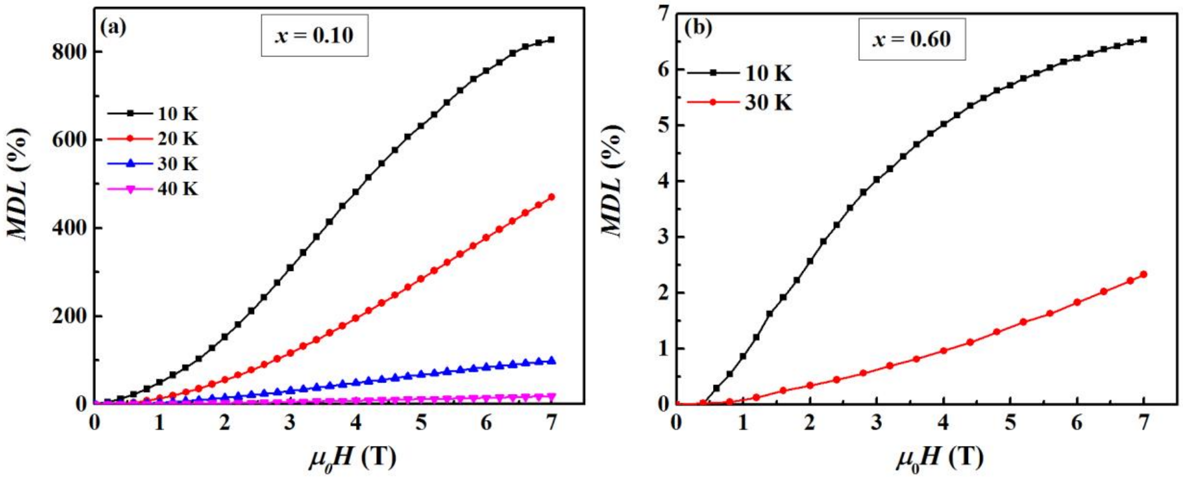

Figure 4.29 Magnetic field dependence of magnetodielectric loss (*MDL*) at various temperatures and *f* = 1kHz for (a) *x* = 0.10 and (b) *x* = 0.60.

temperature and it is +18% at $T = 40$ K. For $x = 0.60$, *MDL* is +6.5% at $T = 10$ K and $\mu_0 H = 7$ T, which is slightly smaller than *MDE* (+7.6%). For other compositions ($x = 0.3$ and 0.5), the *MDL* is positive for all temperatures (not shown here).

4.3.8.7 Origin of *MDE* in $Eu_{1-x}Ba_xTiO_3$

The observed *MDE* values for polycrystalline $Eu_{1-x}Ba_xTiO_3$ ($x = 0.1$ and 0.2) samples are much larger than that for single crystals (*MDE* = +3.5% for $x = 0.1$ and +2.8% for $x = 0.20$).[8] It is suggested that the coupling between magnetism and dielectric constant decreases with Ba doping. G. Catalan[148] predicted that a combination of negative magnetoresistance and Maxwell-Wagner relaxation effect can also lead to a positive magnetocapacitance effect. If the negative magnetoresistance arises from grains (core), *MDE* is expected to be positive and *MDL* is negative. On the other hand, if magnetoresistance is dominated by spin polarized tunneling across the grain boundaries, *MDE* is negative and *MDL* is positive. However, the signs of *MDE* and *MDL* are positive for all the frequencies for all polycrystalline $Eu_{1-x}Ba_xTiO_3$ samples. Therefore, *MDE* most likely arises from the intrinsic spin-phonon coupling rather than the combination of magnetoresistance and Maxwell Wagner relaxation. A quadratic dependence of *MDE* on magnetization (*M*) is an

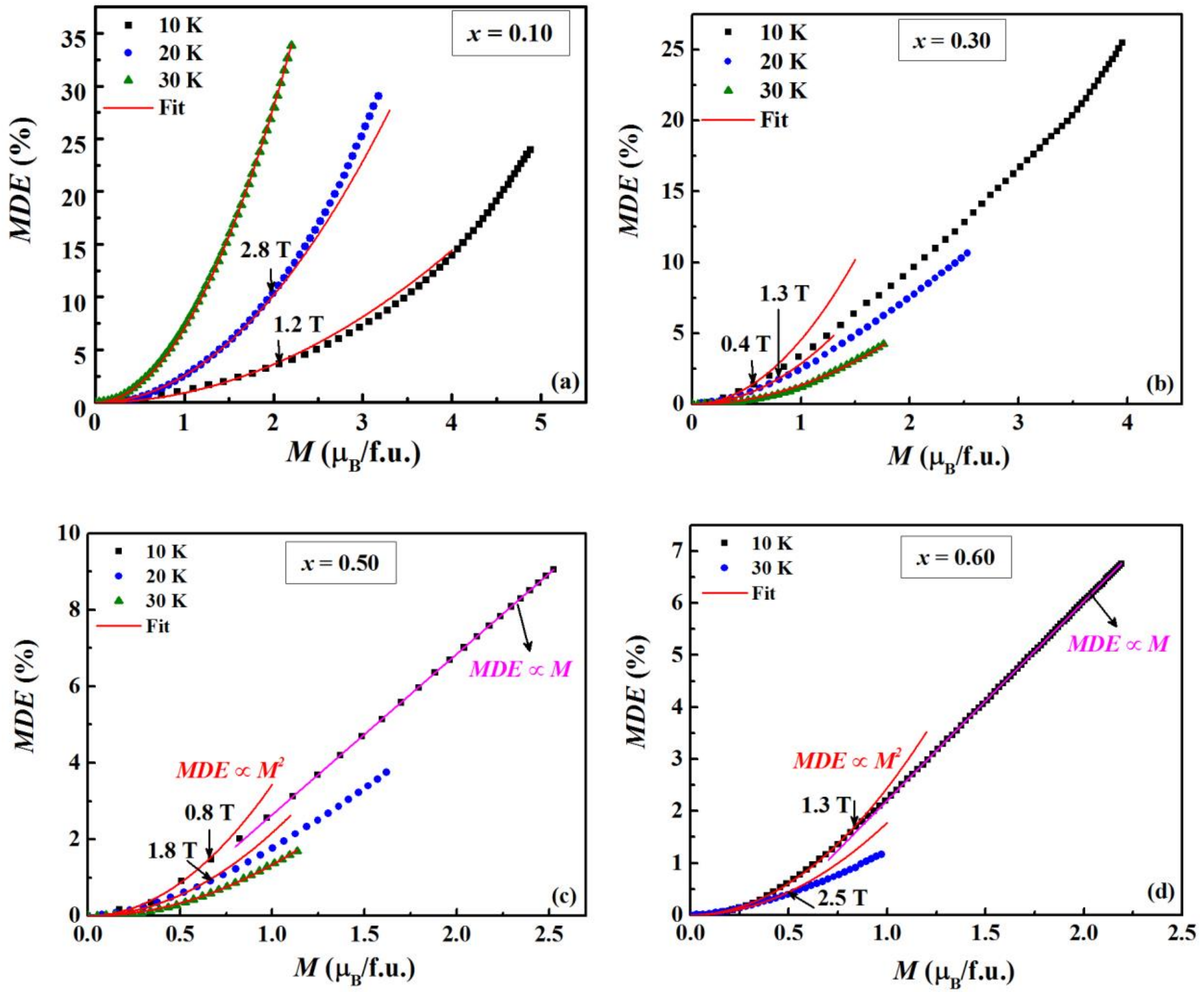

Figure 4.30 ***MDE*** **versus magnetization (*M*) at different temperatures for (a) *x* = 0.10, (b) *x* = 0.30, (c) *x* = 0.50 and (d) *x* = 0.60. Symbols and line represent the experimental data and fit.**

indication that *MDE* arises from the frequency shifts in the soft phonon mode induced by spin fluctuations and it was also found for polycrystalline EuTiO$_3$ (chapter 3).

$$\frac{\varepsilon(T,H)}{\varepsilon(T,0)} - 1 = \alpha M^2 \tag{4.5}$$

Fig. 4.30 (a), (b), (c) and (d) displays the *MDE* versus *M* curves fitted with Eq. (4.5) at frequency f = 1 kHz and at different temperatures for x = 0.10, 0.30, 0.50 and 0.60, respectively. For x = 0.10, the experimental *MDE* data fit nicely over full field range at T = 30K, while the data fit only for low magnetization (*i.e*. low magnetic field) at T = 20 K and 10 K. The deviation shifts to lower field as temperature decreases and found at μ_0H = 2.8 T and 1.2 T for T = 20 K and 10 K, respectively as depicted by arrows in Fig. 4.30 (a). Similar fitting results are obtained for x = 0.30 and deviation occurs at lower field than that for x = 0.10. For x = 0.50 and 0.60, *MDE* follow a quadratic dependence on M for low fields, while a linear dependence of *MDE* on M is found for high fields at T = 10 K.

4.4 Summary

Polycrystalline $Eu_{1-x}Ba_xTiO_3$ ($0.02 \leq x \leq 1.0$) samples were synthesized through solid state reaction method. The magnetic, dielectric, magnetocaloric, magnetoresistance and magnetodielectric properties were studied extensively. The important findings are:

1. The AFM transition temperature (T_N) shifts towards lower temperature with increasing Ba doping from x = 0.02 (T_N = 4.7 K) to x = 0.20 (T_N = 2.8 K) and turns into ferromagnetic for x = 0.50 (T_C = 1.7 K). The saturation magnetization follows a linear decrease with Ba doping (x).

2. Although $EuTiO_3$ is quantum paraelectric, ferroelectricity is induced for x = 0.4 at T_{FE} = 150 K. The ferroelectric transition temperature T_{FE} shifts towards higher temperature with increasing Ba doping and reaches at T_{FE} = 395 K for x = 1.0 ($BaTiO_3$). Ferroelectric transition around room temperature is found in $Eu_{0.3}Ba_{0.7}TiO_3$ (T_{FE} = 290 K) and $Eu_{0.25}Ba_{0.75}TiO_3$ (T_{FE} = 306 K).

3. A phase diagram is constructed for $Eu_{1-x}Ba_xTiO_3$ ($0.00 \leq x \leq 1.0$). The two end compounds x = 0.0 ($EuTiO_3$) and x = 1.0 ($BaTiO_3$) are AFM+PE and PM+FE, respectively. As x increases from 0.0 to 1.0, $Eu_{1-x}Ba_xTiO_3$ transforms from AFM to FM and PE to FE at x = 0.4 and a multiferroic phase (FM + FE) is realized for $Eu_{1-x}Ba_xTiO_3$ ($0.4 \leq x \leq 0.95$).

4. The magnetic entropy change is giant and it varies from $-\Delta S_m$ = 40 J/kg.K to 6.7 J/kg.K at T = 4.5 K for $\mu_0\Delta H$ = 5 T as x increases from 0.1 to 0.9 in the $Eu_{1-x}Ba_xTiO_3$ series. ΔS_m arises from the suppression of the spin fluctuations associated with Eu^{2+}:$4f^7$ electrons. The absence of hysteresis in the field dependences of magnetization with large magnetic entropy change is an added advantage of this series of compounds. In view of the observed giant magnetic entropy change, these compounds may be of interest for cryogenic magnetic refrigeration below 30 K.

5. It was found that the maximum adiabatic temperature change is ΔT_{ad} =18.68 K for $\mu_0\Delta H$ = 5 T in $Eu_{0.5}Ba_{0.5}TiO_3$, which is ferroelectric below ~ 215 K. The maximum isothermal magnetic entropy change is $-\Delta S_m$ = 31.32 J/kg.K and relative cooling power is RCP = 343 J/kg) a for a field change of 7 T.

6. Colossal negative magnetoresistance is observed in the series $Eu_{1-x}Ba_xTiO_3$ for x = 0.1 to 0.6) at temperature below 50 K. The magnetoresistance varies from MR = –85% (x = 0.0) to –20% (x = 0.6) at T = 20 K and $\mu_0 H$ = 7 T. The negative colossal magnetoresistance is suggested due to the suppression of $4f^7$ spin fluctuations by magnetic field which reduces the spin-disorder scattering.

7. The effect of magnetic field on dielectric constant and ac resistivity is studied simultaneously for $Eu_{1-x}Ba_xTiO_3$ ($0.02 \leq x \leq 0.6$) compounds. These compounds show large positive magnetodielectric effect together with negative magnetoresistance. The *MDE* and ac *MR* decreases with increasing Ba doping from x = 0.02 (*MDE* = 120% and *MR* = – 94%) to x = 0.60 (*MDE* = 7.6% and *MR* = –13.5%) at T = 10 K and $\mu_0 H$ = 7 T. While *MDE* versus –*MR* curves for x = 0.10 and 0.30 are highly non-linear, they are almost linear at all temperatures for x = 0.50 and 0.60.

8. The quadratic dependence of *MDE* on magnetization (*i.e.* $MDE \propto M^2$) for low fields indicates that the magnetodielectric effect is attributed to strong spin-lattice coupling in these compounds. However, a linear dependence of *MDE* on *M* is realized for x = 0.5 and 0.6 over high field range (2 T $\leq \mu_0 H \leq$ 7 T). First time, we observed a linear relation in *MDE* and *MR* for x = 0.5 and 0.6.

Chapter 5 Magnetic, Magnetocaloric and Magnetoresistance Properties of $Eu_{1-x}La_xTiO_3$ ($0.01 \leq x \leq 0.3$)

5.1 Introduction

In chapter 4, we study the isovalent substitution effect on magnetic, MCE and *MR* properties of $EuTiO_3$ through $Eu_{1-x}Ba_xTiO_3$ series, where magnetization, magnetic entropy change and *MR* reduce with increasing x. While the isovalent substitution does not dope any electron or hole in system, the substitution of trivalent rare earth ions (La^{3+} or Gd^{3+}) for Eu^{2+} dopes electrons into t_{2g} orbitals of Ti-3d band. Katsufuji and Takura[70] reported FM interaction with T_C = 8 K and metallic behavior in single crystalline $Eu_{0.9}La_{0.1}TiO_3$. The occurrence of negative magnetoresistance (*MR*) in $Eu_{0.9}La_{0.1}TiO_3$ single crystal and $Eu_{0.94}La_{0.06}TiO_3$ thin film has been reported by Katsufuji *et. al.*[70] and Takahashi *et. al.*[196] independently. Takahashi *et. al.* [196] also studied the anomalous Hall effect (AHE) for epitaxial thin films of $Eu_{1-x}La_xTiO_3$ ($0.01 \leq x \leq 0.06$) and found that the AHE can be controlled by doping concentration x of spin-polarized charge carriers. However, there is no report so far on the resistivity, magnetism and other physical properties of $Eu_{1-x}La_xTiO_3$ samples over wide composition range. Therefore, in this chapter we report magnetic, magnetocaloric and magnetoresistance properties of polycrystalline $Eu_{1-x}La_xTiO_3$ ($0.01 \leq x \leq 0.30$) samples.

5.2 Experimental details

Polycrystalline $Eu_{1-x}La_xTiO_3$ samples were synthesized through conventional solid-state reaction method using stoichiometric amount of Eu_2O_3, La_2O_3 and TiO_2 powders. were mixed, ground and annealed at 1200° C for 24 hours in reducing atmosphere (95% Ar and 5% H_2) to reduce Eu^{3+} into Eu^{2+}. After regrinding and annealing the powder at the same temperature twice, pellets were made with uniaxial pressure and sintered in the same atmosphere at 1300°C for 24 hours. Philips X'PERT MPD powder X-ray diffractometer was employed for structure characterization at room temperature using CuKα radiation. Rietveld refinement of the powder X-ray diffraction (XRD) pattern collected at room temperature was done using the Full Prof software. A Thermogravimetric analyzer (Discovery series, TA Instruments) was employed to determine the oxygen contents in $Eu_{1-x}La_xTiO_3$ samples. The temperature and field dependent magnetization were measured using a commercial vibrating sample magnetometer (VSM), equipped with PPMS, Quantum Design USA. Heat capacity was measured using relaxation technique in PPMS. The dc resistivity as a function of temperature and magnetic field was measured in PPMS using standard four-probe configuration.

5.3 Results and discussion

5.3.1 Structural characterization: X-ray diffraction

The main panel of Fig. 5.1 shows the powder X-ray diffraction patterns collected at room temperature for $Eu_{1-x}La_xTiO_3$ ($0.01 \leq x \leq 0.2$). All the samples were found to be in single phase. Fig. 5.2 (a) and (b) show the room temperature powder X-ray diffraction

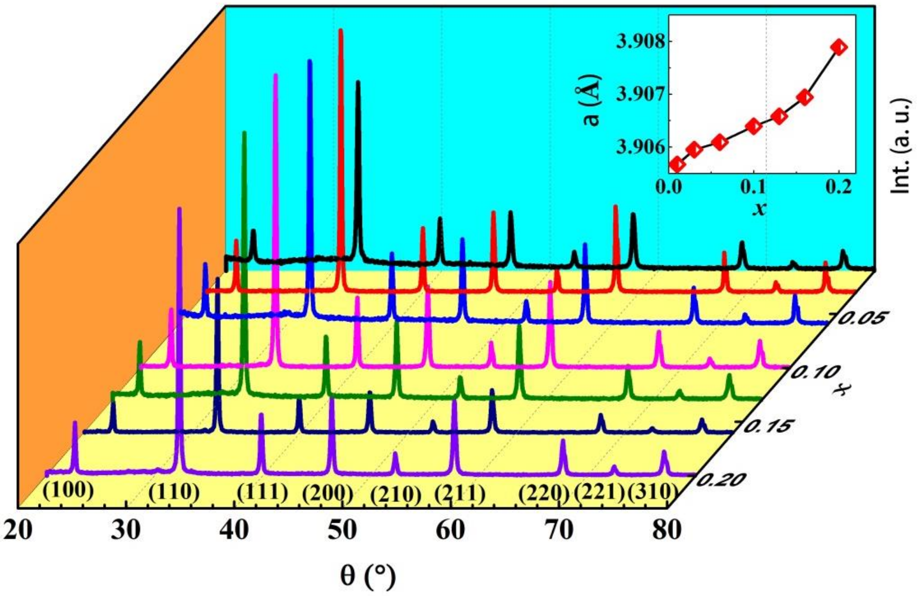

Figure 5.1 Main panel: Room temperature powder X-ray diffraction pattern for $Eu_{1-x}La_xTiO_3$ ($0.01 \leq x \leq 0.2$). Inset: The lattice constant (a) as a function of La content (x).

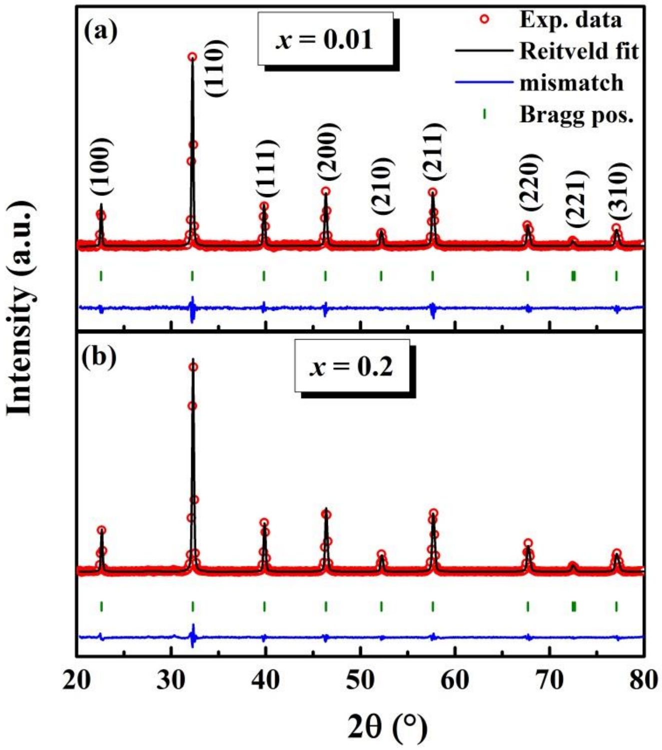

Figure 5.2 X-ray diffraction pattern of (a) $Eu_{0.99}La_{0.01}TiO_3$ and (b) $Eu_{0.80}La_{0.20}TiO_3$ samples with Reitveld fit.

patterns along with the Rietveld refinement for $x = 0.01$ and 0.2, respectively. Both samples crystallize in cubic structure with $Pm\overline{3}m$ space group. The intermediate compositions also possess the cubic structure. The inset of Fig. 5.1 shows the lattice constant (a) as a function of La content (x). The a value for $x = 0.01$ is 3.9056 Å, which is same as that of $EuTiO_3$ (a = 3.9056 Å).[197] The lattice constant increases with increasing x and a = 3.9082 Å for $x = 0.2$. Since the ionic radius of La^{3+} (1.032 Å) is smaller than that of Eu^{2+}(1.17 Å), the small increase in lattice constant is mainly due to the larger ionic radius of Ti^{3+} (0.670 Å) than Ti^{4+} (0.605Å).[198]

5.3.2 Thermogravimetric analysis

A Thermogravimetric analyzer (TGA) was employed to determine the oxygen contents in $Eu_{1-x}La_xTiO_3$ samples. It is known that perovskite $EuTiO_3$ oxidizes to pyrochlore

$Eu_2Ti_2O_7$ due to the oxidation of Eu^{2+} to Eu^{3+} following the Eq. (5.1) [160] and $LaTiO_3$ oxidizes to $La_2Ti_2O_7$ due to the oxidation of Ti^{3+} to Ti^{4+} following the Eq. (5.2) given below [37]

$$2\mathrm{Eu}^{(2+)}\mathrm{Ti}^{(4+)}\mathrm{O}_{3-\delta} + (\delta + 0.5)\mathrm{O}_2 \rightarrow \mathrm{Eu}_2^{(3+)}\mathrm{Ti}_2^{(4+)}\mathrm{O}_7 \tag{5.1}$$

$$2\mathrm{La}^{(3+)}\mathrm{Ti}^{(3+)}\mathrm{O}_{3-\delta} + (\delta + 0.5)\mathrm{O}_2 \rightarrow \mathrm{La}_2^{(3+)}\mathrm{Ti}_2^{(4+)}\mathrm{O}_7 \tag{5.2}$$

If the pyrochlore phases are considered as oxygen stoichiometric, oxygen contents of the perovskite phase can be assessed from the weight gain of the samples during oxidation on heating in air. Therefore, the oxygen nonstoichiometry parameter δ for $Eu_{1-x}La_xTiO_{3-\delta}$ samples can be determined using Eq. (5.3), which is derived from the combination of Eq. (5.1) and Eq. (5.2).

$$2M(\mathrm{Eu}_{1-x}\mathrm{La}_x\mathrm{TiO}_3) - 2\delta M(\mathrm{O}) = \frac{(1-x)M(\mathrm{Eu}_2\mathrm{Ti}_2\mathrm{O}_7) + xM(\mathrm{La}_2\mathrm{Ti}_2\mathrm{O}_7)}{100\% + \Delta m(\%)} \tag{5.3}$$

where M represents the molar mass and Δm is the weight gain.

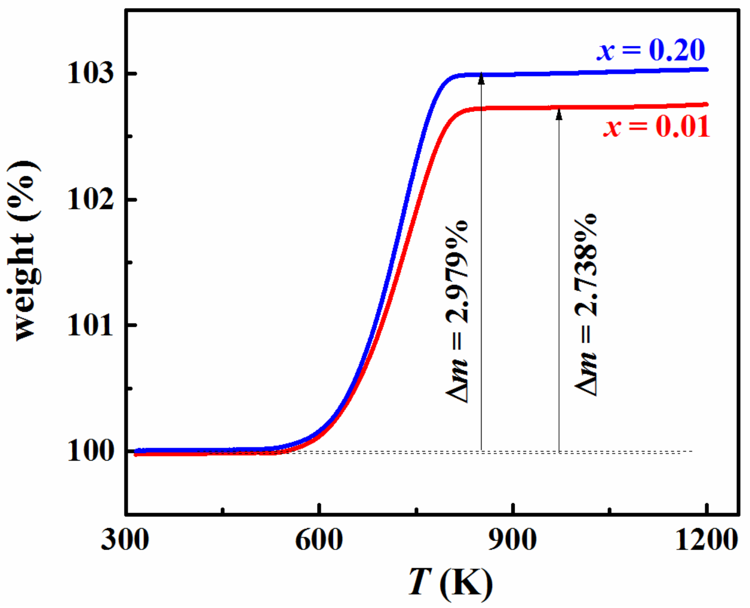

Figure 5.3 TGA traces of $Eu_{1-x}La_xTiO_3$ (x = 0.01 and 0.2) during oxidation in air.

Fig. 5.3 shows the TGA trace of the measured weight gain while heating $x = 0.01$ and 0.20 samples in air from room temperature to 1200 K at a rate of 5 K/min. From the weight gain of $\Delta m = 2.738\%$ and 2.979 % for $x = 0.01$ and 0.02, the calculated δ values are – 0.074 and – 0.042 for $x = 0.01$ and 0.2, respectively. The negative sign of δ indicates a slight excess of oxygen in the present samples. Hence, the compositions can be written as $Eu_{0.99}La_{0.01}TiO_{3.074}$ and $Eu_{0.8}La_{0.2}TiO_{3.042}$.

5.3.3 DC magnetization and susceptibility

The main panel of Fig. 5.4 shows the temperature dependence of magnetization, *M*(*T*), of $Eu_{1-x}La_xTiO_3$ $(0.01 \leq x \leq 0.2)$ samples in the low temperature range $2.5\ K \leq T \leq 30\ K$ under a magnetic field of $H = 1$ kOe. Although we measured *M*(*T*) from 300 K down to 2.5 K, data only below 30 K are shown here for clarity. The peak at $T = 5.2$ K ($= T_N$) in *M*(*T*) of $x = 0.01$ is the signature of AFM transition. The Neel temperature (T_N) of $x = 0.01$ is slightly lower than that of $EuTiO_3$ ($T_N = 5.5$ K). The peak is absent in *M*(*T*) for $x \geq 0.03$, which indicates strengthening of the FM interaction at the expense of weakening of the AFM

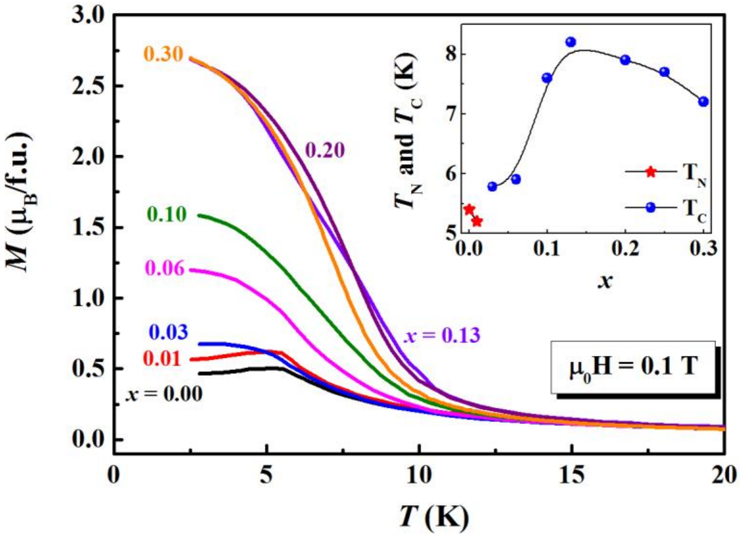

Figure 5.4 Main panel: Temperature dependence of magnetization under the applied field *H* = 1kOe. Inset shows the T_N and T_C as a function of La concentration (*x*).

coupling between Eu^{2+} ions. The FM Curie temperature (T_C) is identified from the position of the minimum in dM/dT curves. The inset of Fig. 5.4 displays T_N and T_C as a function of x. The T_C initially increases with x from $T_C = 5.7$ K for $x = 0.03$ to $T_C = 8.5$ K for $x = 0.13$ and then decreases for $x \geq 0.13$. It is predicted that AFM coupling among neighboring Eu^{2+}:$4f^7$ spins in $EuTiO_3$ is dominated by superexchange interactions involving Ti-3d(t_{2g}) empty states compared to superexchange interaction commonly encountered via O-2p orbitals in perovskite structure.[43] The substitution of La^{3+} for Eu^{2+} introduces t_{2g}^1 electrons in the empty Ti-3d band, which seems to suppress AFM interaction and promote FM interaction among neighboring Eu^{2+}:$4f^7$ spins.

We also measured the magnetization using the standard zero-field cooled (ZFC) and field cooled (FC) protocols under magnetic fields H = 50, 100, 200, 300 Oe and 1 kOe for x = 0.01– 0.30. We show ZFC and FC $M(T)$ data for four selected samples x = 0.01, 0.06, 0.10 and 0.20 in Fig 5.5 (a), (b), (c) and (d), respectively. The ZFC curve bifurcates from the FC

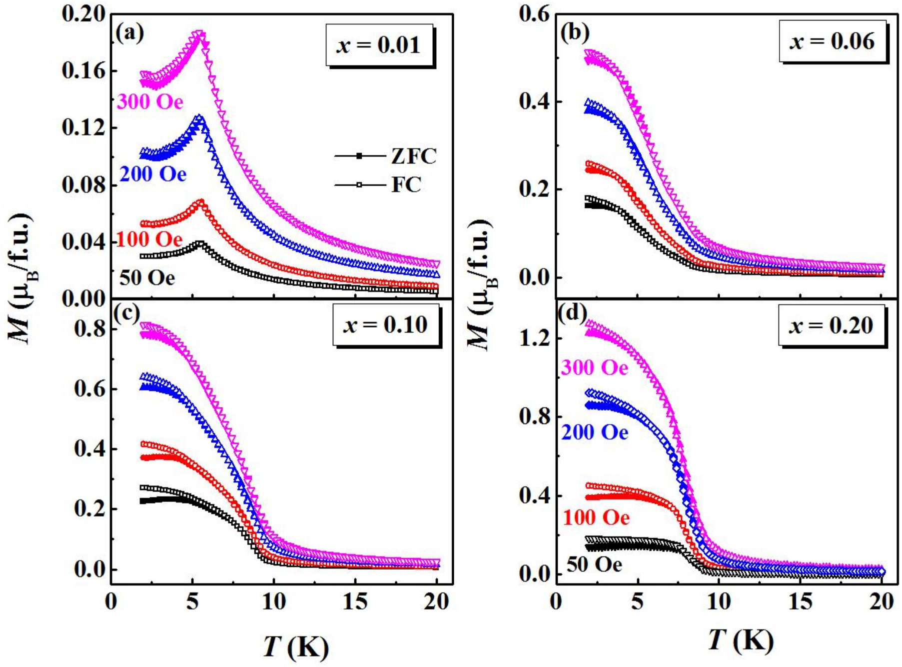

Figure 5.5 Temperature dependence of magnetization in zero-field cooled (ZFC) and field-cooled (FC) modes under different magnetic fields for (a) x = 0.01, (b) x = 0.06, (c) x = 0.10 and (d) x = 0.2. Solid and open symbols represent the ZFC and FC data, respectively.

curve for H = 50 Oe in all samples but the difference decreases as the strength of the magnetic field is increased. The ZFC and FC curves for $H \geq 500$ Oe virtually matched and hence we do not show them here. The small difference observed between ZFC and FC curves indicate the presence of weak ferromagnetic interaction in antiferromagnetic sample $x = 0.01$ and antiferromagnetic interaction in predominantly ferromagnetic sample $x \geq 0.06$ below 300 Oe. However, for fields $H \geq 1$ kOe, $x \geq 0.06$ samples can be considered as a homogeneous ferromagnet.

Fig. 5.6 shows the field dependence of magnetization for selected samples at $T = 2.5$ K measured while sweeping the magnetic field ($\mu_0 H = 0 \rightarrow +7$ T and $+7$ T$\rightarrow -7$ T $\rightarrow +7$ T). The $M(H)$ of $x = 0.01$ increases linearly with the magnetic field below 1 T and shows tendency to saturate above $\mu_0 H = 2$ T. The antiferromagnetic ground state of $x = 0.01$ changes into spin- flopped state for fields lower than 0.2 T and M increases linearly with increasing H when the spins in the spin-flopped state cants towards the field direction.[199] As can be noted from the Fig. 5.5, the linear field dependence of M is suppressed as x increases and $M(H)$ curves of $x = 0.13$ and 0.2 resemble that of a soft ferromagnet. The

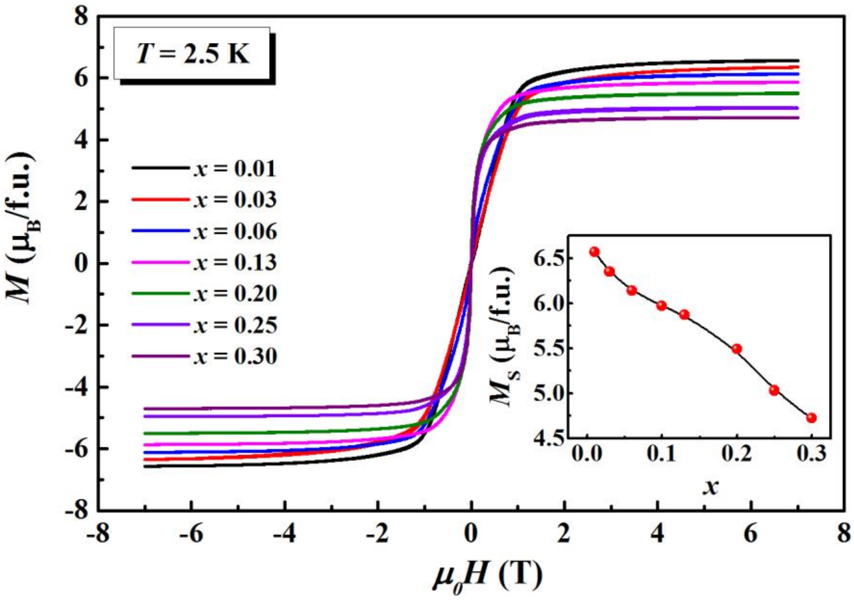

Figure 5.6 Main panel - Field dependence of magnetization for $Eu_{1-x}La_xTiO_3$ at T = 2.5 K. Inset: Saturation magnetization (M_S) as a function of La content (x).

saturation magnetization (M_S) at 5 T for $x = 0.01$ is 6.56 μ_B/f.u. for $x = 0.01$ and it decreases with increasing x, and reaches 4.72 μ_B/f.u. for $x = 0.3$. As x moles of Eu^{2+} (S = 7/2) ions are replaced by x moles of La^{3+} (S = 0) ions, x number of d^1 (S = 1/2) electrons are introduced in the Ti-3d(t_{2g}) conduction band. If the doped electrons are also fully aligned with the magnetic field, the saturation magnetization of $Eu_{1-x}La_xTiO_3$ is expected to be $M_S = (1- x)M(Eu^{2+}) + xM(Ti^{3+})$. The experimentally found M_s values at the highest field for $x = 0.2$ and $x = 0.3$ are 5.51 μ_B/f.u. and 4.7 μ_B/f.u., respectively, which are closer to the theoretical value of 5.6μ_B/f.u. and 4.9 μ_B/f.u. expected for contribution from the Eu^{2+} ions only than from 5.7μ_B/f.u. and 5.05 μ_B/f.u. expected for contributions from both Eu^{2+} and Ti^{3+} ions. It is likely that spins of doped d^1 electrons are not fully aligned in the available field range but they do mediate ferromagnetic interaction between the 4f spins of Eu^{2+} ions. We would like to remind that in the ferromagnetic $YTiO_3$ possessing Ti^{3+} ions, $M_s = 0.8$ μ_B/Ti instead of $M_s = 1\mu_B$/Ti expected theoretically and it was attributed to non-zero orbital contribution to the total angular momentum.[200, 201]

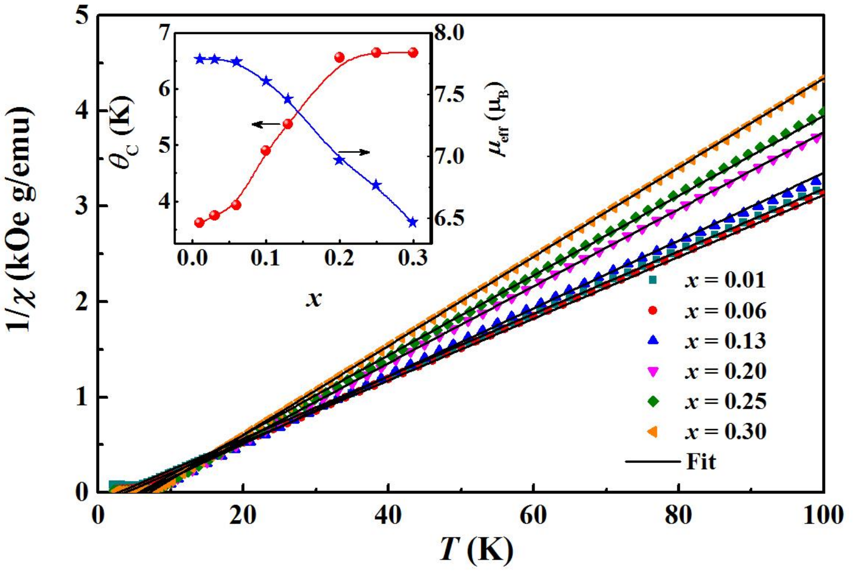

Figure 5.7 (a) Main panel: Temperature dependence of inverse susceptibility ($1/\chi$) for different compositions (x). Symbol and line represent the experimental data and Curie Weiss fit, respectively. Inset: Curie Weiss temperature (θ_{CW}) on the left hand scale and effective magnetic moment (μ_{eff}) on the right hand scale as a function of x.

The main panel of Fig. 5.7 shows the temperature dependence of the inverse susceptibility ($1/\chi$) for different x along with the Curie-Weiss fit ($\chi^{-1} = (T-\theta_c)/C$). The Curie-Weiss temperature (θ_c) and the effective magnetic moment ($\mu_{eff} = 2.83(C_M)^{1/2}$, where C_M is the Curie constant per gram molecular weight) estimated from the fits are shown in the inset of Fig. 5.7. The positive sign of θ_c indicates FM correlations among the 4f spins. The θ_c increases rapidly with increasing x from 3.61 K for $x = 0.01$ to 6.56 K for $x = 0.2$ and mostly saturates for $x \geq 0.2$. However, μ_{eff} decreases from 7.78μ_B for $x = 0.01$ to 6.47μ_B for $x = 0.3$ due to decrease in the Eu^{2+} content.

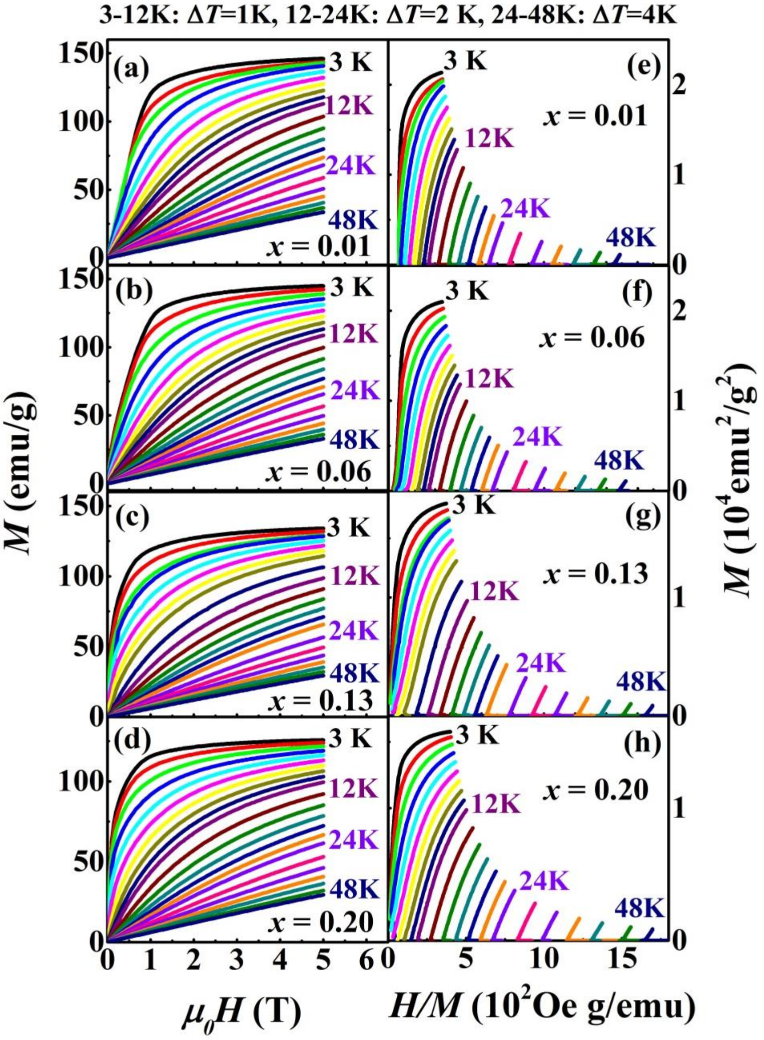

Figure 5.8 Magnetization isotherms $M(H)$ at different temperatures for (a) $x = 0.01$, (b) $x = 0.06$, (c) $x = 0.13$ and (d) $x = 0.20$. Arott plot (M^2 versus H/M curves) for (e) $x = 0.01$, (f) $x = 0.06$, (g) $x = 0.13$ and (h) $x = 0.20$.

Fig. 5.8(a), (b), (c) and (d) show the magnetization isotherms *M*(*H*) at different temperatures from 3 K to 48 K for $x = 0.01$, 0.06, 0.13 and 0.20, respectively. *M* increases nonlinearly with *H* for temperatures from 3 K to 24 K for all compositions, while a linear behavior is observed from 24 K to 48 K. Generally, analyzing the Arrott plot (M^2 versus H/M curves) is the easy way to determine the critical exponents, critical temperature and nature of the phase transition of materials.[202] According to the Landau theory of phase transition, M^2 vs H/M curve should be a straight line and cross the origin at T_C and the intercept of the curves on the H/M axis should be negative below T_C and positive above T_C. We show the Arrot plot (M^2 versus H/M curves) in Fig. 5.8 (e) – (h) for all the samples. In case of $Eu_{1-x}La_xTiO_3$ ($x = 0.13$ and 0.2), the M^2 versus H/M curves cross the origin around 7 K but the curves are not linear for all the temperatures. However, the positive slopes of the Arrot plot for all the samples indicate the second order nature of PM-AFM transition in $x = 0.01$ and PM-FM transition in $x = 0.06 – 0.20$.

5.3.4 Heat capacity

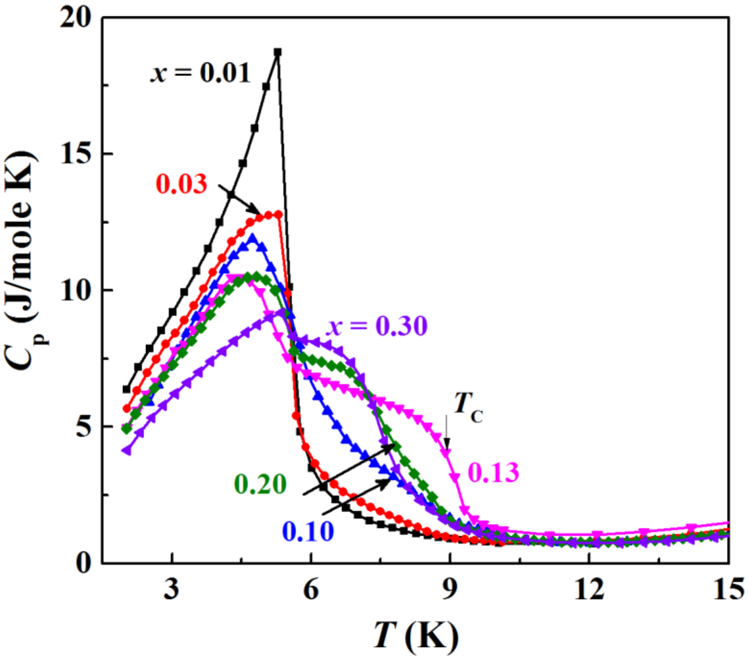

Figure 5.9 Temperature dependence of heat capacity (C_p) under zero magnetic field for $x = 0.01 – 0.30$. The downward arrow indicates T_C for $x = 0.13$ obtained from magnetization data.

Fig. 5.9 shows the temperature dependence of heat capacity (C_p) in low temperature regime (15 K – 2 K) for $Eu_{1-x}La_xTiO_3$ (x = 0.01 – 0.30). The data includes both magnetic and lattice contribution to the specific heat. The magnetic contribution to the heat capacity dominates that lattice contribution in all the samples below 10 K. The $C_p(T)$ of x = 0.01 shows a sharp increase followed by a peak at T = 5.3 K , which corresponds to the Neel temperature, T_N. The peak decreases in magnitude and rounded in x = 0.03. All other samples show two features: A step-like increase (shoulder) at a high temperature followed by a rounded peak at a lower temperature. The step-like increase is more pronounced in x = 0.13. We believe that this step-like increase is due to the onset of ferromagnetism. The arrow marks the T_C determined from *dM/dT* curve. The step like increase shifts to lower temperature as x increases from 0.13 to 0.30. This is in agreement with the trend of T_C inferred from $M(T)$ data, which suggests that T_C initially increases with La content, reaches a maximum value (T_C = 8.8 K) for x = 0.13 and then decreases. The rounded peak observed below the step is not necessarily an indication of a phase transition into antiferromagnetic state. Li *et al.*[64] also noticed the steplike and rounded peak features in $EuTi_{1-x}Nb_xO_3$ series for $0.1 \leq x \leq 0.16$ and suggested them to either a chemical inhomogeneity or the coexistence of two magnetic phases. On the other hand, $C_p(T)$ in single crystalline $Eu_{0.85}Nb_{0.15}TiO_3$ shows only one single sharp peak.[203]

Fig. 5.10(a), (b) and (c) show the magnetic heat capacity $C_m(T)$ obtained after subtracting the lattice contribution from the measured $C_p(T)$ together with $M(T)$ under H = 50 Oe measured in the zero-field cool (*ZFC*) mode for x = 0.1, 0.13 and 0.2 samples, respectively. It is seen that ZFC-$M(T)$ shows a cusp for each sample and the temperature corresponding to the cusp is very close to the position of the rounded peak in $C_m(T)$. The rounded peak in $C_m(T)$ could be due to a minor fraction of the antiferromagnetic phase-residue of $EuTiO_3$ coexist with the majority ferromagnetic phase in $Eu_{1-x}La_xTiO_3$. However,

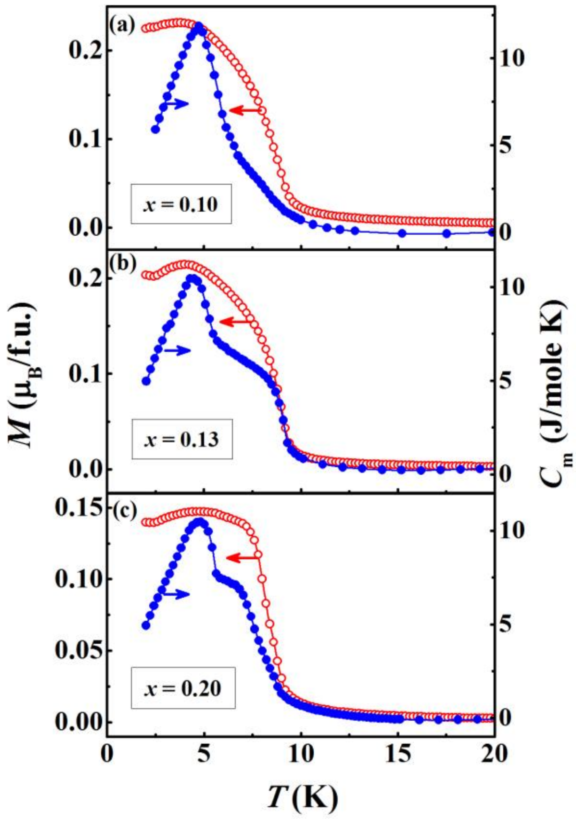

Figure 5.10 Temperature dependence of magnetization (*M*- left y axis) and magnetic heat capacity (C_m -right y axis) for (a) *x* = 0.10, (b) *x* = 0.013 and (c) *x* = 0.20.

this antiferromagnetic phase seems to change to ferromagnetic in magnetic fields of of 300 Oe and above. Another possibility is that the rounded peak represents the Schottky anomaly due to the crystal field splitting of 3d-states into t_{2g} and e_g levels. Further studies are needed to understand the exact origin of the rounded peak in the heat capacity of the La-substituted samples.

5.3.5 Magnetocaloric effect

5.3.5.1 Magnetic entropy change

The magnetic entropy change $\Delta S_m = S_m(H) - S_m(H = 0)$ is obtained by applying the Maxwell thermodynamic relation $-\Delta S_m = \int_0^H \left(\frac{\partial M}{\partial T}\right)_H dH$ to the set of *M*-*H* isotherms measured. We calculated ΔS_m using the numerical approximation to the Maxwell's relation: $-\Delta S_m(T,H) =$

$\sum_i \frac{M_{i+1}(T_{i+1},H_i)-M_i(T_i,H_i)}{T_{i+1}-T_i}\Delta H_i$. Fig. 5.11 (a), (b), (c) and (d) show the temperature dependence of ΔS_m for $x = 0.01$, 0.06, 0.13 and 0.20, respectively for different values of ΔH, where $\Delta H = 0 \rightarrow 5$ T means H is increased from 0 to 5 T. The $-\Delta S_m(T)$ raises with lowering temperature and goes through a peak value before decreasing on the low temperature side. While $-\Delta S_m$ shows a peak at $T = 5.5$ K for $x = 0.01$ and 0.06, the peak occurs at $T = 7.5$ K for $x = 0.13$ and 0.2. In the series $Eu_{1-x}Ba_xTiO_3$, the position of $-\Delta S_m$ peak shifts to lower temperature with increasing x,[75] but it shifts to higher temperature with increasing x in $Eu_{1-x}La_xTiO_3$ series because the magnetic transition temperature also shifts to higher temperature with increasing x.

Fig. 5.12 (a) shows the field dependence of the peak value of $-\Delta S_m$ ($-\Delta S_m^{max}$) for all compositions. The $-\Delta S_m^{max}$ increases with increasing value of ΔH but decreases with

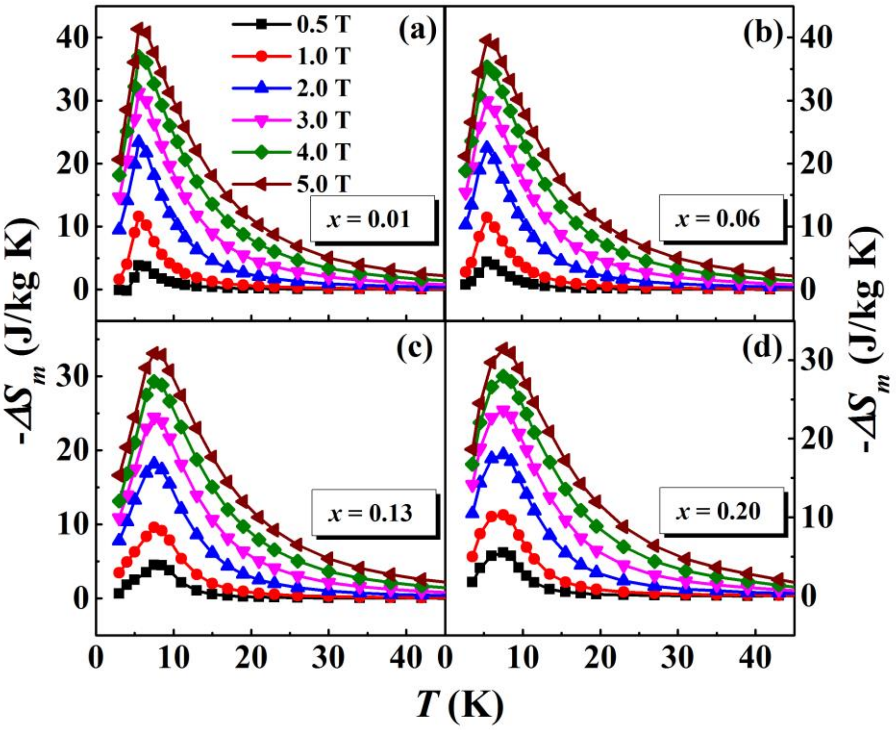

Figure 5.11 Temperature dependence of magnetic entropy change ($-\Delta S_m$) for (a) $x = 0.01$, (b) $x = 0.06$, (c) $x = 0.13$ and (d) $x = 0.20$.

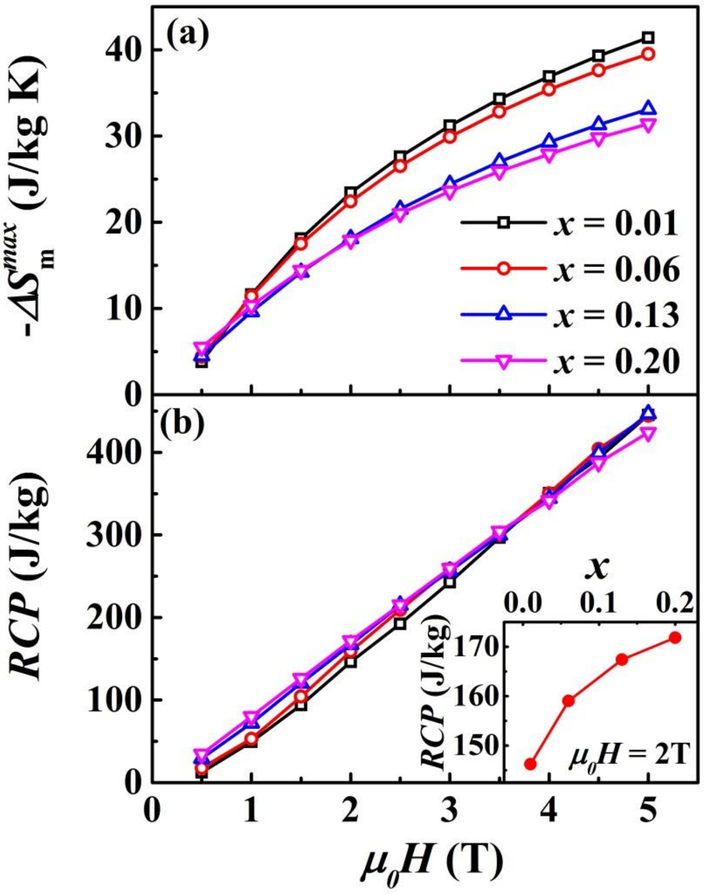

Figure 5.12 Field dependence of (a) maximum magnetic entropy change ($-\Delta S_m^{max}$) and (b) relative cooling power (*RCP*) for different compositions (*x*). Inset shows the *RCP* as a function of *x* with field change of $\mu_0\Delta H$ = 2 T.

increasing *x* ($-\Delta S_m$ = 41.38, 39.55, 33.10 and 31.41 J/kg.K for $\mu_0\Delta H$ = 5 T and for *x* = 0.01, 0.06, 0.13 and 0.20, respectively). The magnetic entropy change decreases by only 24% as *x* increases from 0.01 to 0.2. Besides a large ΔS_m value, a good magnetic refrigerator should show a large adiabatic temperature change (ΔT_{ad}) and relative cooling power (*RCP*). The *RCP* quantifies the amount of heat transferred between the cold and the hot reservoirs separated by a temperature difference δT_{FWHM} in an ideal Carnot cycle and it is defined as $RCP = -\Delta S_m^{max} \times \delta T_{FWHM}$, where δT_{FWHM} is the temperature span corresponding to the full width at half maximum of the ΔS_m versus *T* curve. The field dependences of *RCP* for different *x* are shown in the main panel of Fig. 5.12(b). The *RCP* increases with increasing field change for all the samples. For low field change 0.5 T ≤ $\Delta\mu_0 H$ ≤ 3 T, *RCP* value increases with increasing x, shows a same value for $\mu_0\Delta H$ = 3.5 T and decreases for $\mu_0\Delta H \geq$ 3.5 T. We noticed that ΔT_{FWHM} increases with increasing La concentration but $-\Delta S_m^{max}$ decreases. Therefore, introducing the electron in Ti-3d state directly affects the magnetocaloric properties of $\mathrm{EuTiO_3}$. The inset of Fig. 5.12 (b) shows the *RCP* values as a function of x for $\mu_0\Delta H$ = 2 T. For $\mu_0\Delta H$ = 2 T, *RCP* increases from 146 J/kg for x = 0.01 to 172 J/kg for x = 0.20. For $\mu_0\Delta H$ = 5 T, the maximum *RCP* is found 445 J/kg for x = 0.01.

5.3.5.1 Adiabatic temperature change

We have chosen the composition x = 0.01 and x = 0.20 to estimate the adiabatic temperature change (ΔT_{ad}) induced by the magnetic field. Fig. 5.13(a) shows the heat capacity, $C_p(T, H)$, in the low temperature regime (T = 40 K to 2.5 K) for $\mu_{□}\Delta H$ = 0, 2 and 5 T. The smooth decrease of C_p from 250 K down to ~9 K is due to softening of the phonon vibrations with lowering temperature. Below 9 K, the phonon contribution is overwhelmed by spin fluctuations, which contributes to extra heat capacity. As the temperature is lowered further C_p exhibits a sharp peak at $T = T_N$ = 5.28 K, which marks the antiferromagnetic ordering of 4f spins of $\mathrm{Eu^{2+}}$ ions. The peak in the heat capacity is very close to T_N = 5.2 K estimated from *dM/dT* curve. The peak decreases in amplitude, smears and shifts to high temperatures under the action of $\mu_0 H$ = 2 and 5T. The magnetic entropy $S_m(H)$ in a field H can be calculated using the equation $S_m(H) = \int_0^T \frac{C_p(T,H)}{T} dT$. We first subtracted the lattice contribution by fitting the high temperature zero-field heat capacity data with sum of Einstein and Debye models.[204] Fig. 5.13(b) shows $S_m(H,T)$ for $\mu_0 H$ = 0, 2 and 5 T. S_m (H = 0, T) is nearly constant above ~ 9 K and decreases rapidly at lower temperatures. The constant entropy above ~ 9 K indicates the maximum spin entropy expected for disordered 4f spins. Since the spins will be distributed equally among the $2S$+1 degenerate states in the

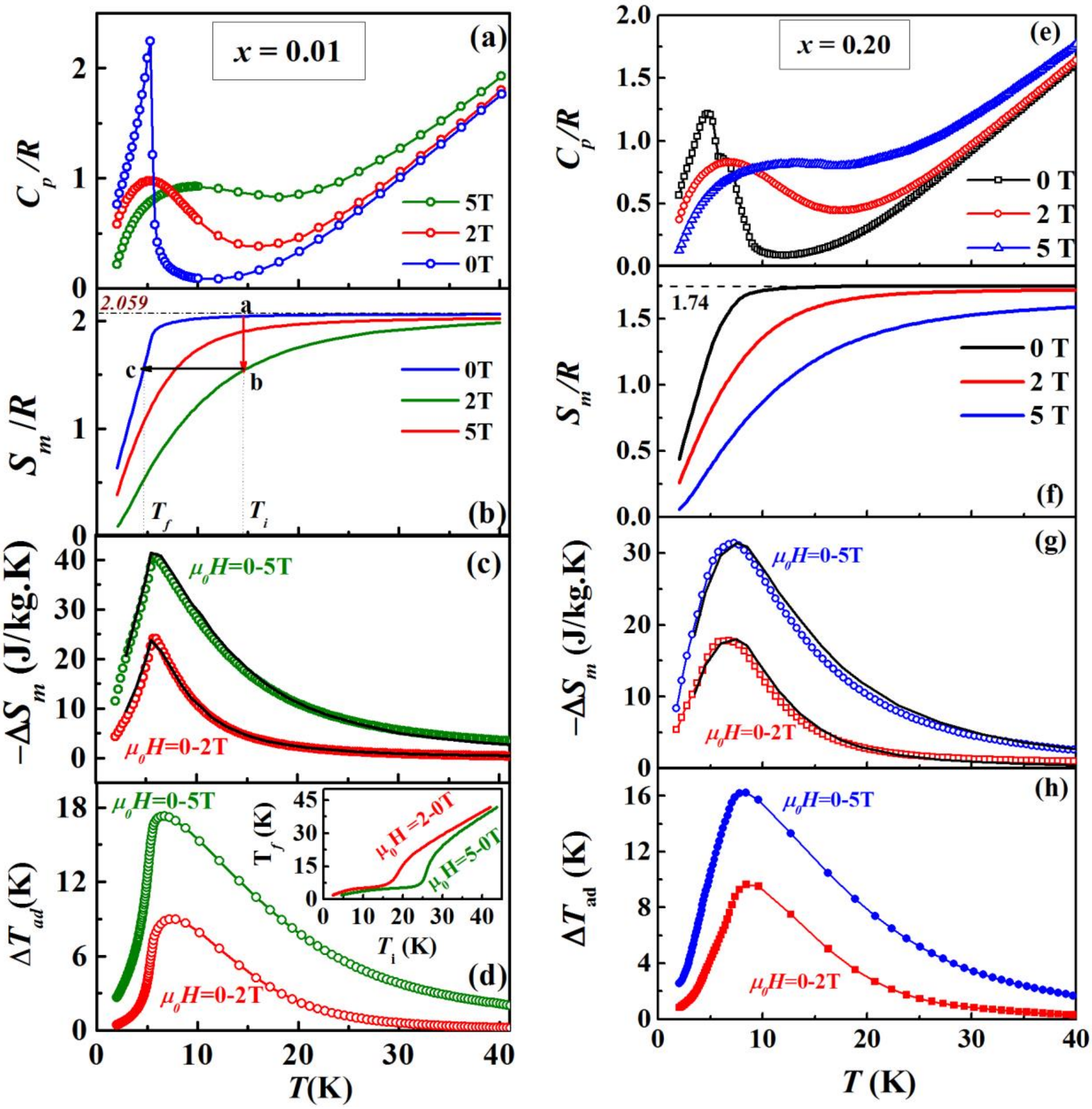

Figure 5.13 Left column- Main panels: Temperature dependence of (a) heat capacity (C_p), (b) magnetic entropy (S_m), (c) magnetic entropy change ($-\Delta S_m$) and (d) adiabatic temperature change (ΔT_{ad}) of $Eu_{0.99}La_{0.01}TiO_3$. Insets: (d) Final temperature (T_f) as a function of initial temperature (T_i) in the adiabatic demagnetization process for magnetic fields 2 T and 5 T. Right column - Temperature dependence of (e) C_p, (f) S_m, (g) $-\Delta S_m$ and (h) ΔT_{ad} of $Eu_{0.80}La_{0.20}TiO_3$.

paramagnetic state, the temperature independent spin entropy is given by $S_m/R=(1-x)\ln(2S+1) = 2.058$ for $x = 0.01$, where $S = 7/2$ and R is the gas constant. The loss of entropy below 9 K is due to increasing spin correlation and finally to spontaneous ordering of 4f moments in antiparallel configuration. Application of an external magnetic field causes S_m to decrease below its zero field values. Fig. 5.13(c) shows the temperature dependence of ΔS_m for μ_0H = 2 and 5 T extracted from the heat capacity (open symbol) and magnetization isotherms (solid line). The $-\Delta S_m$ values obtained by both the methods closely match. The $-\Delta S_m$ initially increases with decreasing temperature below 40 K and goes through a peak around 6 K. The peak increases in magnitude with increasing strength of the magnetic field. The adiabatic temperature change, ΔT_{ad}, which is the temperature change reached in isentropic process ($\Delta T_{ad} = [T_i(H_1) - T_f(H_2)]_S$) is shown in Fig. 5.13(d). We find that ΔT_{ad} = 17.28 K at 6.7 K for $H = 0 \rightarrow 5$ T. The inset in Fig. 5.13(d) where the final temperature (T_f) reachable by the adiabatic demagnetization is plotted against the starting temperature (T_i) illustrates that the lowest temperature T_f = 5.3 (2.1) K can be achieved by adiabatic removal of 5 T magnetic field at T_i = 20 (5) K. Moreover, T_f = 19.4 K at T_i = 27.6 K, which suggests that this material could be useful for hydrogen liquefaction.

Fig. 5.13 (e) and (f) show the temperature dependence of the normalized heat capacity (C_p/R) and magnetic entropy (S_m/R), respectively, under different magnetic fields μ_0H = 0 T, 2 T and 5 T. The zero field heat capacity shows a step like increase followed by a peak at lower temperature. The step like increase in $C_p(T)$ is the due to the onset of ferromagnetism, while the peak is due to the presence of weak antiferromagnetic interaction. As the magnetic field increases, peak decreases in amplitude, smears and shifts to high temperatures. The S_m (H = 0, T) is nearly constant above ~ 12 K and decreases rapidly at lower temperatures. The constant magnetic entropy above ~ 12 K indicates the maximum spin entropy expected for random Eu^{2+} ($4f^7$) and Ti^{3+} ($3d^1$) spins. The magnetic entropy of $Eu_{1-x}La_xTiO_3$ is expected to be $S_m = (1-x)S_m(Eu^{2+}) + xS_m(Ti^{3+})$. For x = 0.20, the experimental value of S_m (1.74R) closely matches with the theoretically calculated S_m (1.79R) for Eu-4f and Ti-3d spins. Fig. 5.13(g) shows the temperature dependence of the ΔS_m for μ_0H = 2 and 5 T extracted from the heat capacity (open symbol) and magnetization isotherms (solid line). The $-\Delta S_m$ is 31.34 (17.8)

J/kg.K for $\mu_0\Delta H = 5$ (2) T at $T = 7$ K. The temperature dependence of ΔT_{ad} for $x = 0.20$ is shown in Fig. 5.13 (h). The $\Delta T_{ad} = 16$ K for $\mu_0\Delta H = 5$ T and $T = 8.4$ K, which is slightly lower than that for $x = 0.01$.

We compare ΔT_{ad}, $-\Delta S_m^{max}$ and RCP of $Eu_{1-x}La_xTiO_3$ ($x = 0.01$ and 0.2) samples with other promising magnetocaloric materials in Table 5.1. Among these having magnetic transition temperature below 10 K (first 11 rows), $Eu_{0.99}La_{0.01}TiO_3$ shows the highest value of $-\Delta S_m^{max}$ (41.5 J/kg.K) for $\mu_0\Delta H = 5$ T. It is also found that $Eu_{0.80}La_{0.20}TiO_3$ shows smaller $-\Delta S_m^{max}$ value compared to $Eu_{0.80}Ba_{0.20}TiO_3$. The ΔT_{ad} value for $x = 0.01$ is also higher than other oxides except for $Gd_3Ga_5O_{12}$ and $Gd(HCOO)_3$. While ΔT_{ad} and $-\Delta S_m^{max}$ values for $x = 0.01$ are highest among all other Eu based materials (row 9 – 13), EuS shows the highest RCP value.

S. No.	Material	T_N / T_C (K)	ΔT_{ad} (K)		$-\Delta S_m^{max}$ (J/kg.K)		RCP (J/kg)		Ref.
			$\Delta H = 2$T	$\Delta H = 5$T	$\Delta H = 2$T	$\Delta H = 5$T	$\Delta H = 2$T	$\Delta H = 5$T	
1.	$Eu_{0.99}La_{0.01}TiO_3$	5.2	9	17.2	23	41.5	146	445	This work
2.	$Eu_{0.80}La_{0.20}TiO_3$	7.5	9.6	16	18	31.4	172	424	This work
3.	$Eu_{0.80}Ba_{0.20}TiO_3$	2.8	-	-	20	35	-	-	[75]
4.	$EuTiO_3$	5.4	10	16.5	22.3	40.4	110	440	[163]
5.	$Gd_3Ga_5O_{12}$	1	10	24	-	25	67	-	[169, 170]
6.	$Gd(HCOO)_3$	2	12	-	45	-	135	-	[171]
7.	HoCuSi	7	-	-	16.7	33.1	-	385	[205]
8.	ErRuSi	8	-	-	15	21.2	150	416	[206]
9.	EuSe	4.6	-	-	23.5	37.5	194	580	[166]
10.	Eu_3O_4	5.3	3.8	7.8	7.1	12.7	-	-	[165]
11.	$EuHo_2O_4$	5	3	~ 8	9	22.5	75	275	[167]
12.	EuO	69	3.2	6.8	8.5	17.5	-	-	[164]
13.	EuS	18.5	7.5	10.4	22	37	284	782	[193]
14.	$DyTiO_3$	65	4.14	6.79	9.6	15.9	174	470	[87]

Table 5.1 The transition temperature (T_N or T_C), ΔT_{ad}, $-\Delta S_m^{max}$ and RCP values for $\mu_0\Delta H = 2$ T and 5 T for $Eu_{1-x}La_xTiO_3$ ($x = 0.01$ and 0.2) with other potential magnetic refrigerant materials.

5.3.6 DC resistivity and magnetoresistance (*MR*)

5.3.6.1 Temperature dependence of dc resistivity under zero magnetic field for $Eu_{1-x}La_xTiO_3$ ($0.00 \leq x \leq 0.20$)

Fig 5.14 (a) and (b) show the temperature dependence of dc resistivity (ρ_{dc}) for x = 0.00, 0.01, 0.03 and 0.06 and x = 0.10, 0.13 and 0.20, respectively measured upon cooling from 300 K to 2 K. For parent compound (x = 0.0), the value of resistance below 20 K exceeds the instrument limit as described earlier in chapter 3. At T = 300 K, ρ_{dc} value of x = 0.01 (347 Ω cm)is larger than that for x = 0.00 (131 Ω cm) but it decreases 3 orders of magnitude for x = 0.03. While ρ_{dc} (T) for x = 0.00 increases gradually with decreasing temperature from 300 K to 60 K and rapidly below 60 K, ρ_{dc} (T) for x = 0.01 goes through a maximum around 64 K. The x = 0.03 and 0.06 do not show any maximum until 2K temperature unlikely to x = 0.01. The maximum again appear for x = 0.10, 0.13 and 0.20 (Fig. 5.14 (b)) at higher temperature than that for x = 0.01. We show the ρ_{dc} value at 300 K and

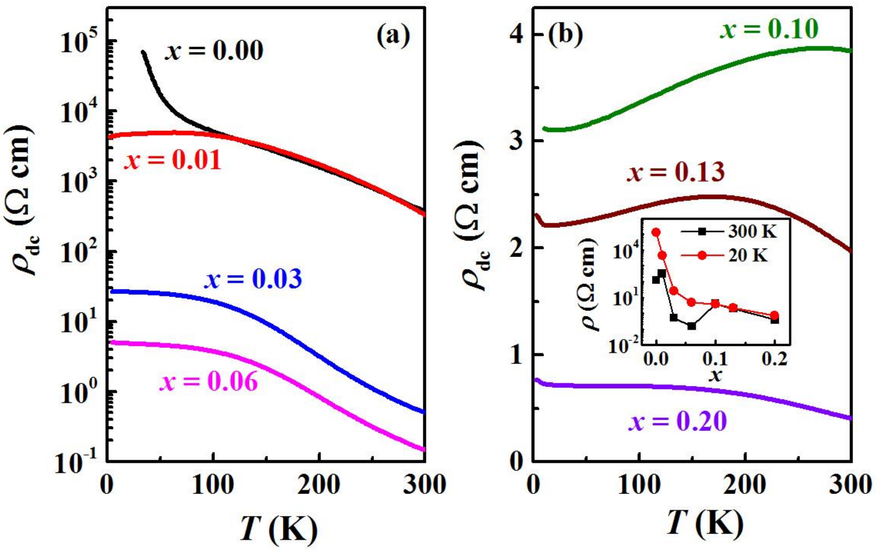

Figure 5.14 Temperature dependence of dc resistivity (ρ_{dc}) for (a) x = 0.00 – 0.06 and (b) x = 0.10 – 0.20 under zero magnetic field. Inset shows the ρ_{dc} as a function of x at temperatures 300 K and 20 K.

20 K as a function of x in inset of Fig. 5.14 (b). For T = 300 K, ρ_{dc} does not show a systematic trend with increasing x, while at T = 20 K, ρ_{dc} decreases rapidly as x increases from 0.00 to 0.03 and gradually for further increasing x from 0.03 to 0.20. The zero field resistivity for x = 0.01, 0.03 and 0.06 is completely different than that of the $Eu_{1-x}La_xTiO_3$ (x = 0.01 – 0.06) thin films grown on LSAT substrate.[196] The $Eu_{1-x}La_xTiO_3$ thin films show metallic behavior throughout temperature range and ρ_{dc} value is 3 orders of magnitude smaller than that of our $Eu_{1-x}La_xTiO_3$ polycrystalline samples. Although $Eu_{0.9}La_{0.1}TiO_3$ single crystal is metallic throughout temperature range and shows a kink at ferromagnetic transition temperature T_C = 8 K,[70] polycrystalline sample displays insulator-metal transition at T = 194 K and an upturn at T = 26 K, much above of T_C. Therefore, polycrystalline $Eu_{1-x}La_xTiO_3$ samples are distinctive than the thin films and single crystals in terms of electronic properties. However, the magnetic properties are quite similar.

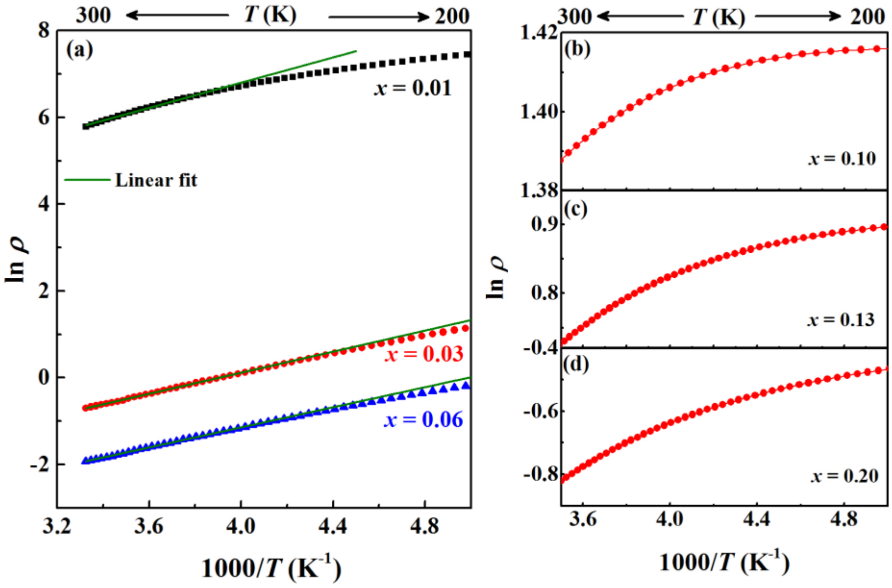

Figure 5.15 lnρ versus 1/T curves for (a) x = 0.01, 0.03 and 0.06, (b) x = 0.10, (c) x = 0.13 and (d) x = 0.20. Solid line in Fig. (a) represents the linear fit.

The ρ_{dc} for EuTiO$_3$ follows thermally activated behavior $\rho = \rho_0 \exp\left(\frac{E_a}{k_B T}\right)$ in the high temperature regime with activation energy, E_a = 217 meV (chapter 3). Therefore, we try to fit ρ_{dc} (T) data for Eu$_{1-x}$La$_x$TiO$_3$ with same relation. Fig. 5.15 (a) show ln(ρ) versus 1/T plot with linear fit for x = 0.01, 0.03 and 0.06 in temperature region 300 K < T < 200 K. The values of E_a calculated from the linear fit of ln(ρ) versus 1/T plot are 125 meV, 104 meV and 99.6 meV for x = 0.01, 0.03 and 006, respectively. Here, we noticed that the value of E_a for x = 0.01 (125 meV) is smaller than that for x = 0.00 (217 meV) and it decreases with increasing x. ln(ρ) versus 1/T plots for x = 0.10, 0.13 and 0.20 are shown in Fig. 5.15 (b), (c) and (d), respectively. As one can see, ln(ρ) versus 1/T plots for x = 0.10 - 0.20 are highly non-linear for full temperature range. So, ρ(T) for x = 0.10 – 0.20 do not follow thermal activation behavior.

5.3.6.2 Magnetic field dependence of dc resistivity of lightly doped Eu$_{1-x}$La$_x$TiO$_3$ (x = 0.01)

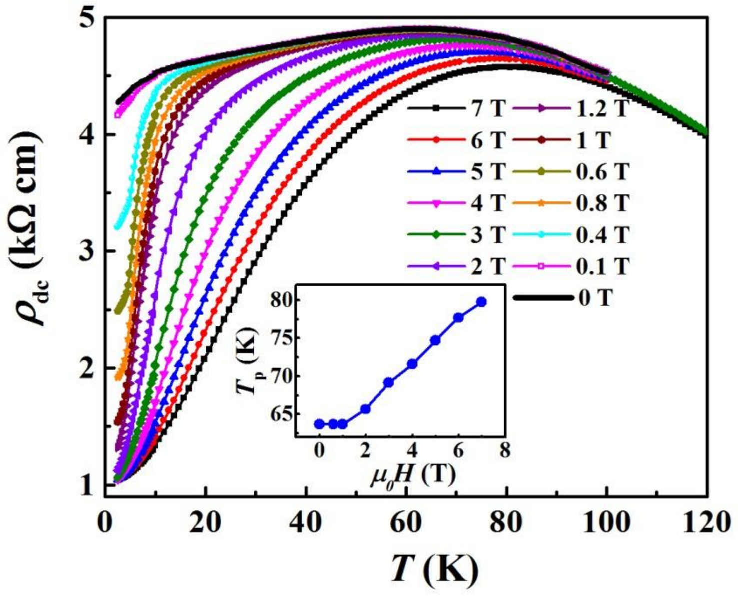

Figure 5.16 Temperature dependence of dc resistivity (ρ_{dc}) under different magnetic fields for x = 0.01. Inset shows the peak position of ρ_{dc}(T) as a function of magnetic field.

The main panel of Fig. 5.16 shows the temperature dependence of ρ_{dc} measured upon cooling from 100 K to 2 K under different magnetic fields for x = 0.01. The zero-field ρ_{dc} shows a broad maximum (I-M transition) around 64 K. Upon application of a magnetic field, the value of ρ_{dc} decreases. The effect is prominent below 10 K for low magnetic fields ($H <$ 0.5 T). As the strength of magnetic field increases, ρ_{dc} decreases substantially up to 80 K. The I-M transition temperature as a function of magnetic field is shown in the inset of Fig. 5.16. The I-M transition is found at same temperature as magnetic field increases from 0 to 1 T, while it shifts to higher temperature with increasing magnetic field from 1 T to 7 T.

The magnetoresistance (MR) is calculated from the temperature dependent ρ_{dc} data shown in Fig. 5.16 using formula $MR = \frac{\rho(H,T)-\rho(0,T)}{\rho(0,T)}$, where $\rho(0,T)$ and $\rho(H,T)$ are the resistivity values under zero and H magnetic field, respectively at temperature T and shown in Fig. 5.17(a). The MR is negative and its magnitude increases with decreasing temperature and increasing magnetic field. With application of $\mu_0 H \leq 1$ T, MR increases gradually from 120 K to 20 K, rapidly below 20 K and it reaches –70 % at T = 2 K for $\mu_0 H$ = 1 T. For $\mu_0 H \geq$ 2 T, MR saturates at –75 % at T = 2K. We also measured the dc-resistance (R_{dc}) while

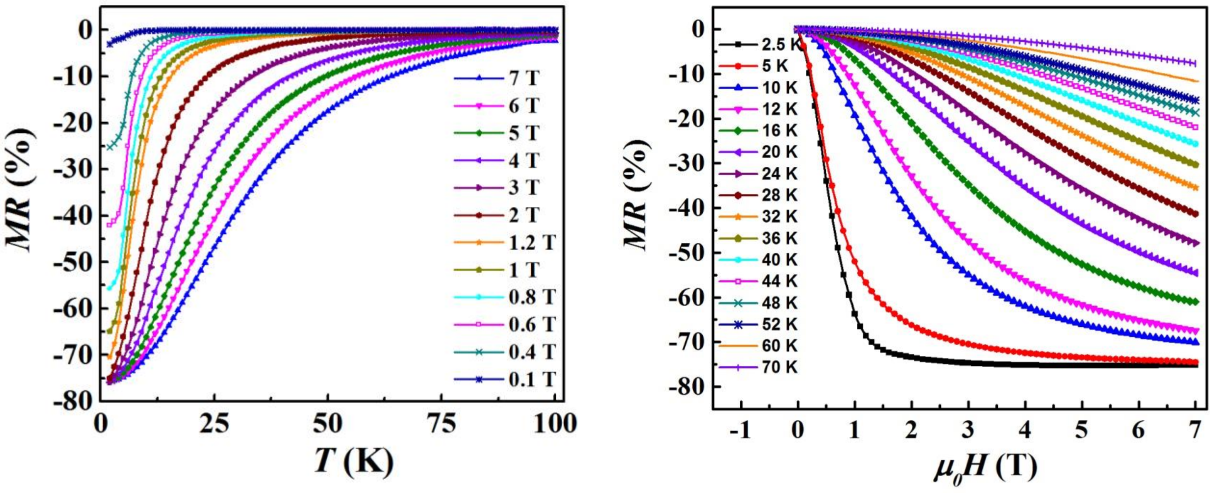

Figure 5.17 (a) Temperature dependence of magnetoresistance (*MR*) for various magnetic fields and (b) Magnetic field dependence of *MR* at different temperatures for *x* = 0.01.

varying the magnetic field at fixed temperatures and calculated MR. The MR as a function of magnetic field is shown in Fig. 5.17(b). At T = 2 K, MR increases rapidly as applied magnetic field increases from 0 to 1 T, reaches –70 % at μ_0H = 1 T, increases gradually from 1 T to 3 T and saturates for higher field μ_0H > 3 T. The maximum value of MR is –75 % at T = 2 K and μ_0H = 7 T, which is smaller than that of $EuTiO_3$ (–99.98 %) as shown in chapter 3. For $T \geq 5$ K, MR increases in magnitude continuously with increasing magnetic field without saturation and decreases in magnitude with increasing temperature. Appreciable MR (–5 % for μ_0H = 7 T) occurs at T = 70 K, which is far above T_N = 5.2 K.

5.3.6.3 Magnetic field dependence of dc resistivity of $Eu_{1-x}La_xTiO_3$ (x = 0.03 and 0.06)

Fig. 5.18 (a) and (b) show the temperature dependence of dc resistivity (ρ_{dc}) of x = 0.03 and 0.06, respectively, measured while cooling from 50 K to 2 K under different magnetic fields. For x = 0.03, the zero field ρ_{dc} (T) shows a kink or maxima at T = 5 K, which becomes broader and shifts towards higher temperature as magnetic field increases. The maximum occurs at T = 40 K when μ_0H = 7T. A large magnetic field effect is observed at low temperature (T < 20 K). While a peak is seen in zero field ρ_{dc} (T) of x = 0.03, zero field

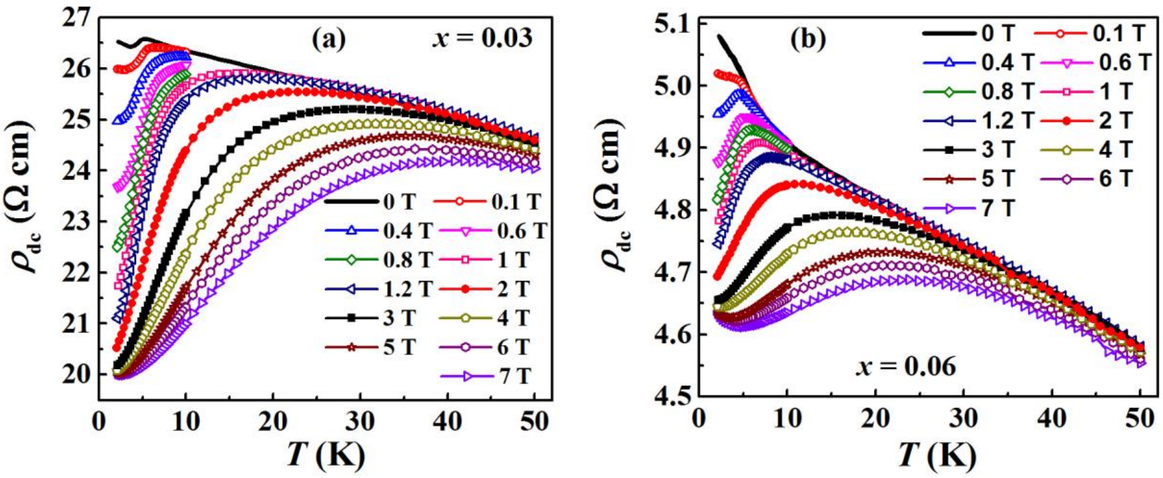

Figure 5.18 Temperature dependence of dc resistivity (ρ_{dc}) for (a) x = 0.03 and (b) x = 0.06 under various magnetic fields.

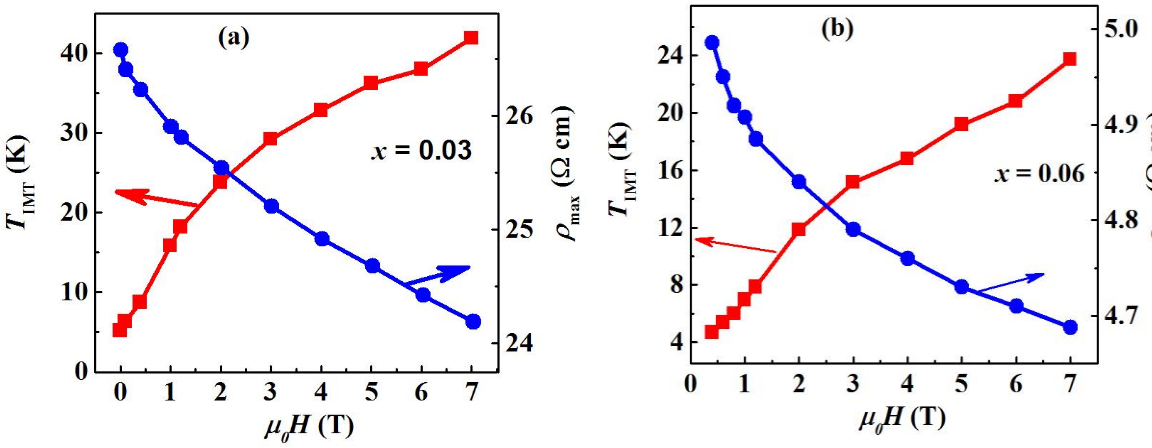

Figure 5.19 The magnetic field dependence of insulator-metal transition temperature (T_{IMT}) on left y-axis and maximum dc resistivity on right y-axis for (a) $x = 0.03$ and (b) $x = 0.06$.

ρ_{dc} of $x = 0.06$ increases rapidly with decreasing temperature without showing any transition. However, the application of magnetic field induces a peak (insulator-metal transition) in ρ_{dc} for $x = 0.06$, similar to $EuTiO_3$. The peak becomes broader and shifts towards higher temperature with increasing magnetic field. The maximum resistivity and I-M transition temperature as a function of magnetic field are shown in Fig. 5.19 (a) and (b) for $x = 0.03$ and 0.06, respectively. The I-M transition temperature increases with increasing magnetic field,

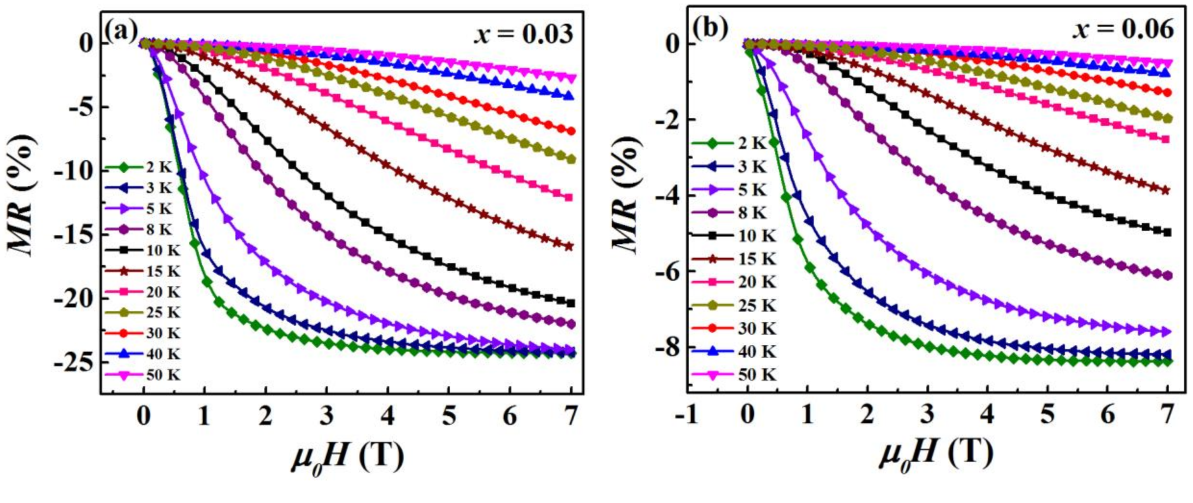

Figure 5.20 Magnetoresistance (*MR*) as a function of magnetic field at different temperatures for (a) $x = 0.03$ and (b) $x = 0.06$.

while the maximum ρ_{dc} decreases for both compounds. Whereas, the variation in I-M transition temperature with magnetic field for $x = 0.03$ is much larger than that for $x = 0.06$. For $x = 0.03$, T_{IMT} increases from 5.2 K at $\mu_0 H = 0$ T to 42 K at $\mu_0 H = 7$T and for $x = 0.06$, it increases from 4.8 K at $\mu_0 H = 0.1$ T to 24 K at $\mu_0 H = 7$T.

Fig. 5.20 (a) and (b) show the magnetic field dependence of *MR* for $x = 0.03$ and 0.06, respectively, at various temperatures. At $T = 2$K, *MR* shows a large change for $\mu_0 H < 1$ T and the change is only incremental for fields above 3 T i.e. it nearly saturates. *MR* is – 25 % for $x = 0.03$ and – 8.5 % for $x = 0.06$ at $T = 2$ K and $\mu_0 H = 7$ T. For $T > 5$ K, no saturation is observed in *MR* for higher magnetic fields. The *MR* decreases with increasing temperature and reaches – 2% for $x = 0.03$ and – 0.3 % for $x = 0.06$ at $T = 50$ K and $\mu_0 H = 7$ T.

5.3.6.4 Magnetic field dependence of dc resistivity of $Eu_{1-x}La_xTiO_3$ ($0.10 \leq x \leq 0.20$)

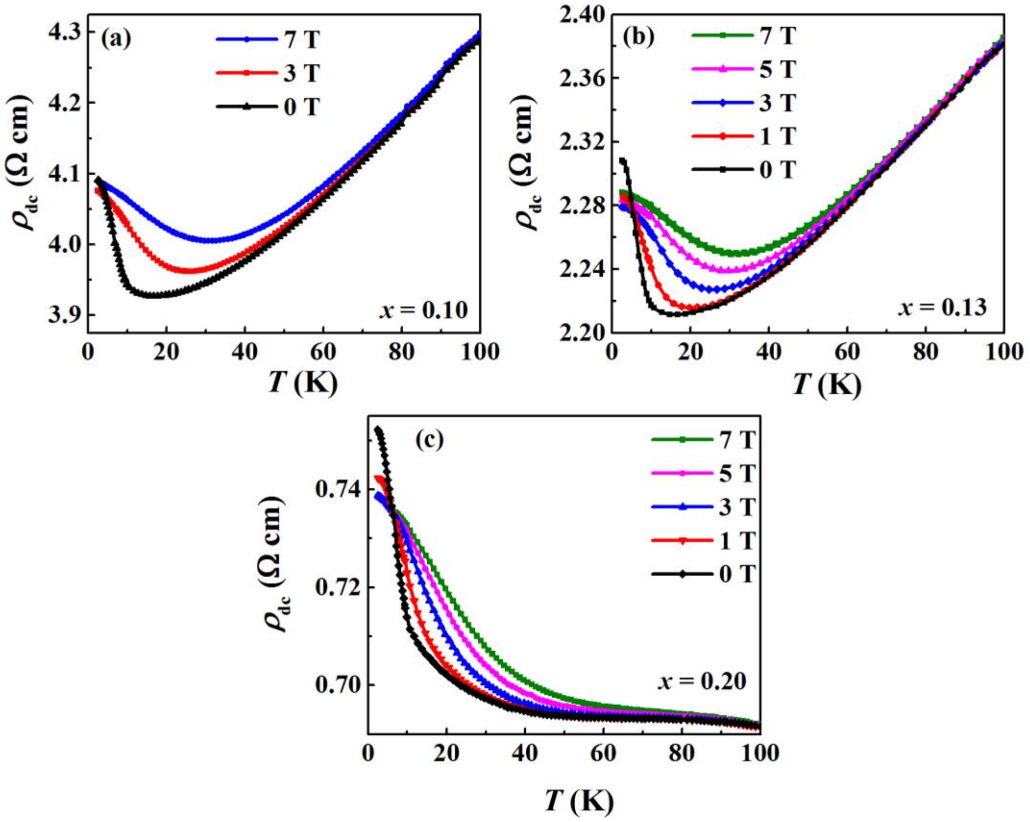

Figure 5.21 Temperature dependence of dc resistivity ρ_{dc} under different magnetic fields for (a) $x = 0.10$, (b) $x = 0.13$ and $x = 0.20$.

Fig. 5.21 (a), (b) and (c) show the temperature dependence of ρ_{dc} for x = 0.10, 0.13 and 0.20, respectively in temperature range T = 100 K - 2 K under different magnetic fields. The zero-field $\rho_{dc}(T)$ of x = 0.10 decreases with decreasing temperature from 100 K to ~ 20 K and shows an upturn at T = 17 K. Application of an external magnetic field shifts this upturn towards higher temperature (25 K for $\mu_0 H$ = 3 T and 30 K for $\mu_0 H$ = 7T) and increases the value of ρ_{dc} over a limited temperature range (60 K – 5 K). However, ρ_{dc} is suppressed under an external magnetic field at the lowest temperature. The ρ_{dc}(T) under fields 3 T and 7 T crosses the zero field ρ_{dc}(T) at T = 4.5 K and 3 K, respectively, and the value of ρ_{dc} decreases. For x = 0.13, $\rho_{dc}(T)$ displays exactly same trend as x = 0.10, except the upturn at T = 32 K and crossover at T = 4.5 K for $\mu_0 H$ = 7 T. The $\rho_{dc}(T)$ for x = 0.20 is completely different than that for x = 0.10 and 0.13. While the zero-field $\rho_{dc}(T)$ is nearly temperature independent from 100 K to 40 K, it shows a rapid upturn at T = 40 K. As magnetic field increases, the upturn shifts towards higher temperature, $\rho_{dc}(T)$ increases over a limited temperature range. Below 6 K, the $\rho_{dc}(T)$ decreases with an application of magnetic field. Here, it is noticed that the crossover between $\rho_{dc}(T)$ with field and zero field shifts to higher temperatures as x increases.

Fig. 5.22 (a), (b) and (c) show the temperature dependence of *MR* under various magnetic fields for x = 0.10, 0.13 and 0.20, respectively. All samples exhibit crossover from positive *MR* (PMR) to negative *MR* (NMR) as temperature decreases. For x = 0.10, PMR increases with decreasing temperature from 100 K and shows a maximum value (+2.3 %) at 10 K for $\mu_0 H$ = 3 T. The maximum in PMR shifts to higher temperature with increasing magnetic field strength. The NMR is observed below 4.5 K and it increases in magnitude as temperature decreases. The highest NMR is –0.45 % at T = 2 K for $\mu_0 H$ = 3 T. Similar trends of PMR and NMR are observed for x = 0.13, and 0.20. The positions of the maximum in

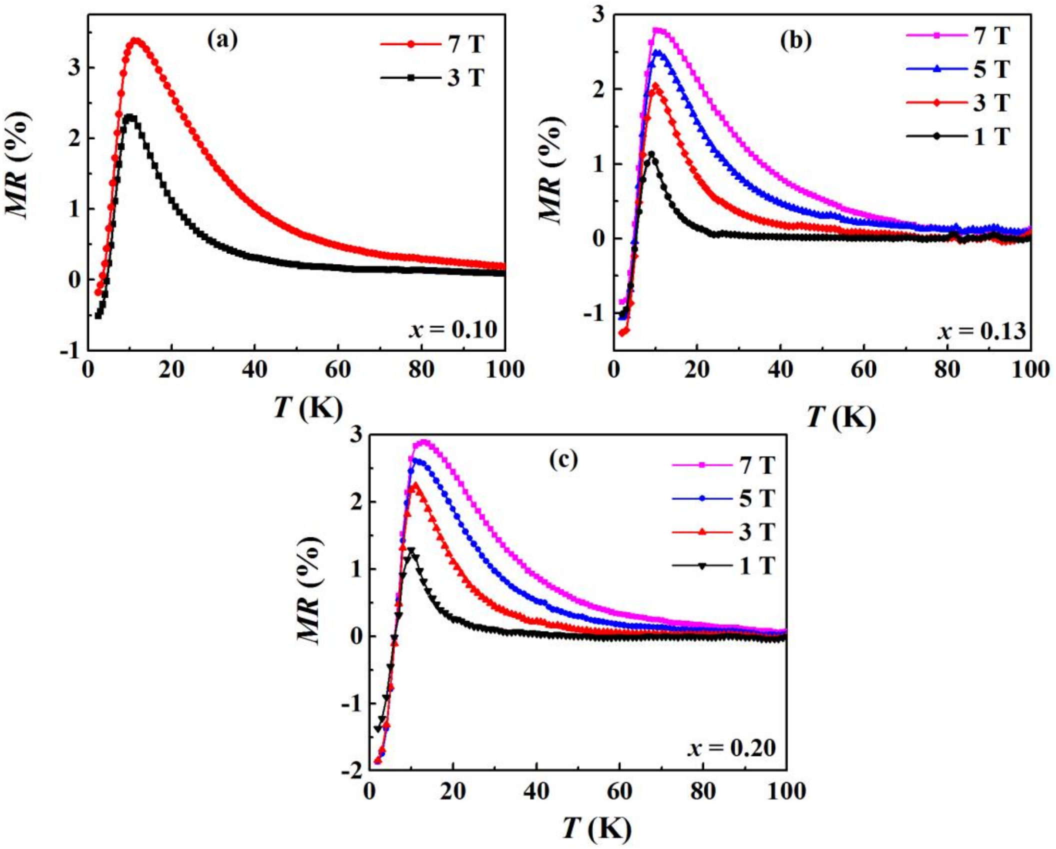

Figure 5.22 Temperature dependence of magnetoresistance (*MR*) at different magnetic fields for (a) *x* = 0.10, (b) *x* = 0.13 and (c) *x* = 0.20.

PMR for $x = 0.13$ exactly matches with $x = 0.10$, while it shifts to $T = 13$ K for $x = 0.20$, 0.25 and 0.30 under $\mu_0H = 7$ T. We observed a similar temperature dependence of *MR* for $x =$ 0.25 and 0.30 (not shown here).

Fig. 5.23 (a), (b) and (c) show *MR* as a function of magnetic field for $x = 0.10$, 0.13 and 0.20, respectively, at selected temperatures from 2 K to 30 K. At $T = 2$K, all samples show NMR. The NMR at 2 K exhibits a completely different trend than that of lightly doped $Eu_{1-x}La_xTiO_3$ ($x = 0.01$, 0.03 and 0.06). For $x = 0.10$, the noticed features in NMR are: (i) it initially increases rapidly with increasing magnetic field from 0 T to 0.3 T, (ii) increases gradually from 0.3 T to 1.9 T, (iii) becomes field independent from 1.9 T to 3 T and (iv) decreases as field increases from 3 T to 7 T. For comparison, we display *MR* for $x = 0.10$, 0.13 and 0.20 at $T = 2$K in Fig. 5.23 (d). While the trend of *MR* at $T = 2$ K is quite similar for all three samples, the position of the maximum value of NMR shifts towards higher field with

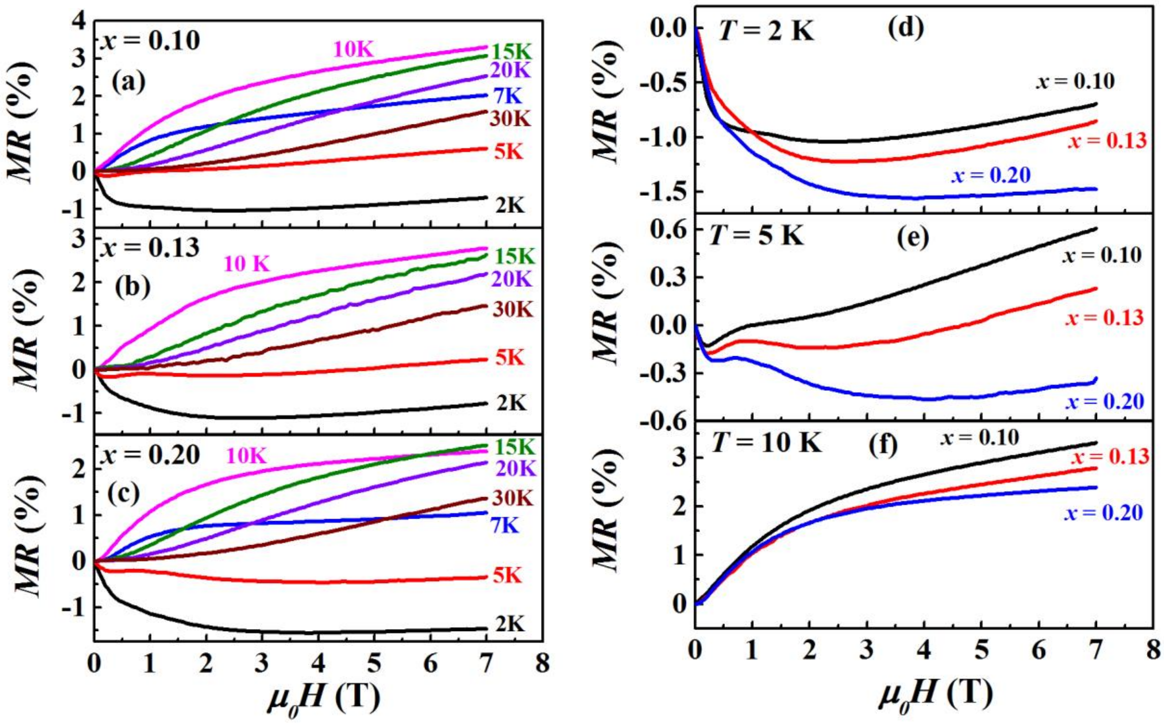

Figure 5.23 Magnetic field dependence of magnetoresistance (*MR*) at different temperatures for (a) *x* = 0.10, (b) *x* = 0.13 and (c) *x* = 0.20; and for various *x* values at temperatures (d) *T* = 2 K, (e) *T* = 5 K and (f) *T* = 10 K.

increasing *x*. The *MR* value increases in magnitude with increasing *x* value and reaches from – 0.70 % for *x* = 0.10 to −1.5 % for *x* = 0.20 at $\mu_0 H$ = 7 T. From Fig. 5.23 (e), *MR* at *T* = 5 K displays a crossover from negative to positive for *x* = 0.10 and 0.13, but it remains negative for *x* = 0.20 in full field range. For *T* ≥ 7 K, *MR* is positive for all the samples. While the highest value of PMR is found at *T* = 10 K over full field range for *x* = 0.10 and 0.13, for *x* = 0.20, PMR for *T* = 15 K exceeds that for *T* = 10 K at $\mu_0 H$ = 5.75 T. From Fig. 5.23 (f), PMR at *T* = 10 K decreases with increasing *x* value and it is +3.3%, +2.7% and +2.4% for *x* = 0.10, 0.13 and 0.20, respectively, at $\mu_0 H$ = 7 T. Even the maximum PMR (2.5 %) at *T* = 15 K for *x* = 0.20 is lower than that at *T* = 10 K for *x* = 0.13. The PMR decreases as temperature increases and PMR = 1.6 %, 1.45 % and 1.35 % for *x* = 0.10, 0.13 and 0.20, respectively, at *T* = 30 K and $\mu_0 H$ = 7 T.

5.3.6.5 *MR* as a function of *x* in $Eu_{1-x}La_xTiO_3$ ($0.00 \le x \le 0.30$)

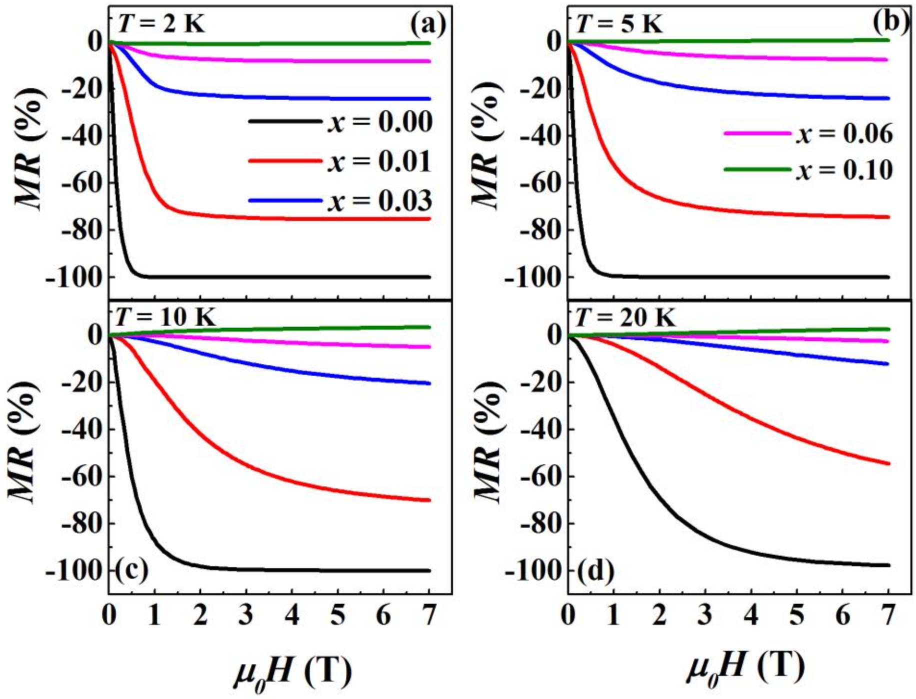

Figure 5.24 Magnetic field dependence of magnetoresistance (*MR*) for different La contents (*x*) at temperatures (a) *T* = 2 K, (b) *T* = 5 K, (c) *T* = 10 K and *T* = 20 K.

Fig. 5.24 (a), (b), (c) and (d) show the magnetic field dependence of *MR* for *x* = 0.00 – 0.10 at temperatures *T* = 2 K, 5 K, 10 K and 20 K, respectively. The value of *MR* decreases as *x* increases for all temperatures. At *T* = 2 K, *MR* for *x* = 0.00 increases rapidly for field below 0.5 T and saturates above 0.7 T. As *x* increases, the field where *MR* starts to saturate increases and no saturation is observed for *x* = 0.06 and 0.10. Similar trend is observed for *T* = 5K and 10 K, while there is no saturation of *MR* at *T* = 20 K for all samples. Fig. 5.25 show the *MR* as a function of La content (*x*) at temperatures *T* = 2 K and 20 K. The dotted line represents the zero value of *MR*. At *T* = 2K, the negative *MR* decreases rapidly as *x* increases from 0.00 to 0.03 and gradually from 0.03 to 0.10 and almost saturates above *x* = 0.10. For *T* = 20 K, *MR* as a function of *x* exhibits a similar trend, but *MR* becomes positive for *x* ≥ 0.10.

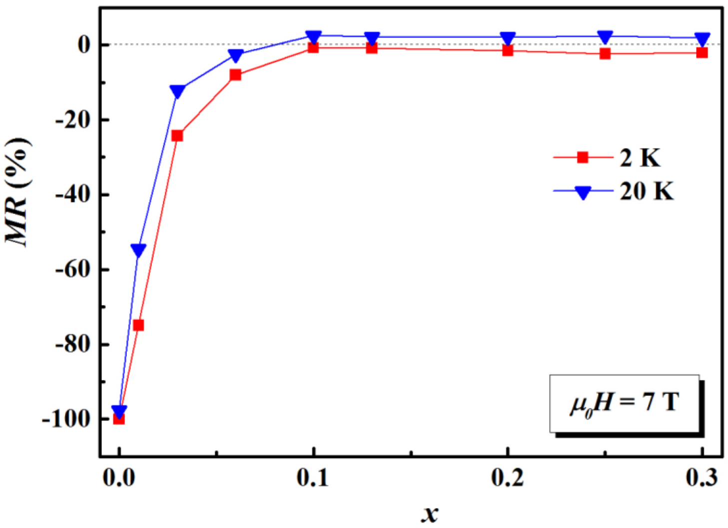

Figure 5.25 Magnetoresistance (*MR*) as a function of *x* at different temperatures for $\mu_0 H$ = 7T. Dotted line represents the zero value of *MR*.

5.3.7 Origin of magnetoresistance (*MR*) in $\mathrm{Eu}_{1-x}\mathrm{La}_x\mathrm{TO}_3$

Near and above the magnetic transition temperature, the scattering of charge carriers with spin fluctuations can be suppressed by magnetic field, leading to the negative *MR* in $\mathrm{Eu}_{1-x}\mathrm{La}_x\mathrm{TiO}_3$. If there is a scattering of charge carriers with spin fluctuations, the low field magnetoresistance scales with square of the ratio of field-induced magnetization and saturation magnetization[118] i.e.

$$MR = C\left(\frac{M}{M_{sat}}\right)^2 \tag{5.4}$$

Fig. 5.26 (a) shows the negative *MR* versus $(M/M_{\max})^2$ curves at different temperatures with linear fit. $M_{\max}$ is the magnetization at 5 T magnetic field for corresponding temperatures. For T = 70 K, *MR* is perfectly linear with $(M/M_{\max})^2$ for full magnetization regime, while the *MR* deviates from linearity for $T \leq 52$ K. The deviation from the linearity shifts towards lower magnetization as temperature decreases and the curve is not anymore linear for T = 5 K, below T_N. The scaling factor *C*, which is related to the coupling between charge carriers and the localized magnetic moments, is determined from the slope of linear fit in Fig. 5.26 (a) and shown in Fig. 5.26 (b). The *C* value is small (0.04) at T = 70 K and

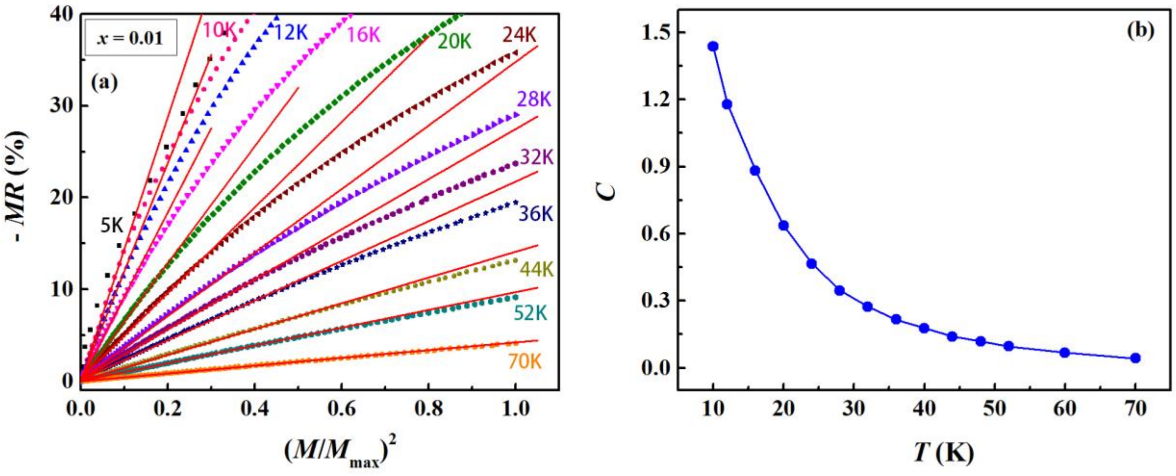

Figure 5.26 (a) Symbols - Negative *MR* versus $(M/M_{max})^2$ at different temperatures and Red Line - Linear fit for $Eu_{0.99}La_{0.01}TiO_3$. (b) Temperature dependence of the coupling coefficient *C*.

increases with decreasing temperature. The highest *C* value is 1.44 at *T* = 10 K, which is much lower than that value for$La_{1-x}Ca_xMnO_3$ (*C* = 6-8)[118, 207] and $Eu_{0.95}Gd_{0.05}Se$ (*C* = 5-15)[93, 118], but comparable to $La_{1-x}Sr_xCoO_3$ (*C* = 1.2)[208]. The observed relation between *MR* and magnetization indicates that the field-induced suppression of the spin fluctuation is major origin of the *MR* in $Eu_{0.99}La_{0.01}TiO_3$.

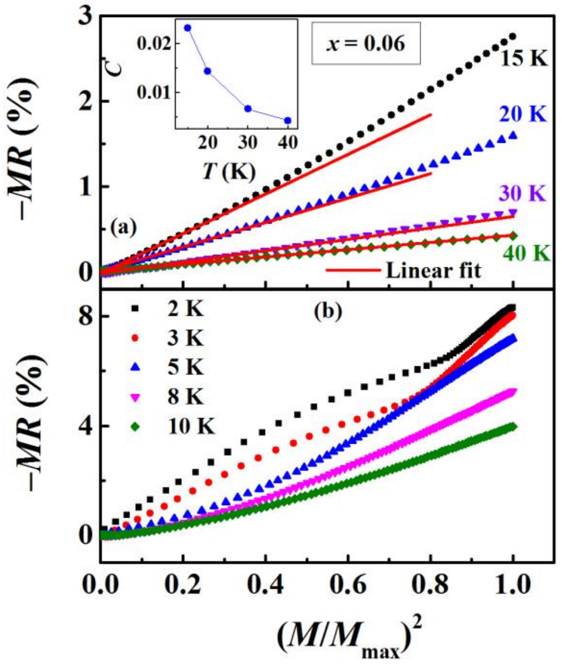

Figure 5.27 (a) Symbols - Negative *MR* versus $(M/M_{max})^2$ at temperatures *T* = 15, 20, 30 and 40 K, and Red Line - Linear fit for *x* = 0.06. Inset: Temperature dependence of the coupling coefficient *C*. (b) Negative *MR* versus $(M/M_{max})^2$ at temperatures *T* = 2, 3, 5, 8 and 10 K.

The *MR* versus $(M/M_{\max})^2$ curves for $x = 0.06$ are shown in main panels of Fig. 5.27 (a) and (b). From Fig. 5.27 (a), *MR* is linear $(M/M_{\max})^2$ for full magnetization regime at $T = 40$ K, while the deviation from linearity occurs for $T \leq 30$ K. The deviation shifts to lower magnetization value as temperature decreases and no linear relation is observed for $T \leq 10$ K. The observed value of *C* for $x = 0.06$ is shown in the inset of Fig. 5.27 (a). The smaller value of *C* for $x = 0.06$ ($C = 0.014$ at $T = 20$ K) than $x = 0.01$ ($C = 0.64$ at $T = 20$) indicates that the effective coupling between charge carriers and local spins reduces as *x* increases. P. Majumdar and P. Littlewood [118] predicted that the coupling coefficient *C* is related to the charge carrier concentration, i.e. $C \propto n^{-2/3}$, where *n* is the charge carrier density. As *x* increases, the charge carrier density increases and therefore the coupling between charge carriers and local spins reduces.

Since the *MR* data for $x = 0.01$ and 0.06 do not follow Eq. (5.4) for temperatures $T < 15$ K, we fit *MR* data for $0.01 \leq x \leq 0.06$ with Eq. (5.5) proposed to explain the *MR* for diluted magnetic semiconductors due to spin disorder scattering.

$$MR = -a^2 \ln(1 + b^2 H^2) \tag{5.5}$$

The *MR* data for $x = 0.01$ is fitted with Eq. (5.5) and shown in Fig. 5.28 (a). The experimental

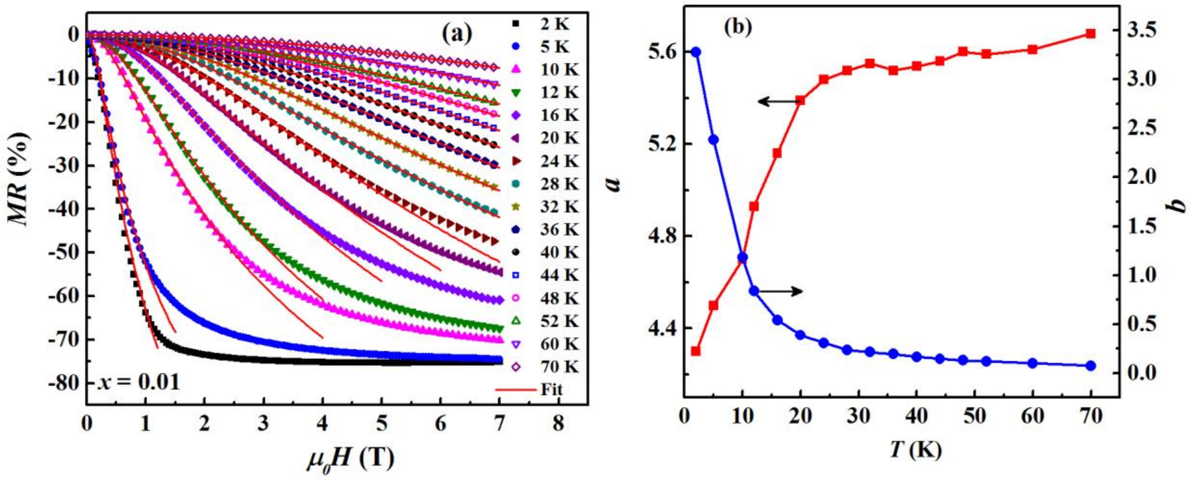

Figure 5.28 (a) Symbols: Experimental *MR* as a function of magnetic field at different temperatures for *x* = 0.01. Solid line: Least-squares fit of experimental *MR* to Eq. 5.5. (b) Temperature dependence of coefficients a (left y-axis) and b (right y-axis) in Eq. 5.5.

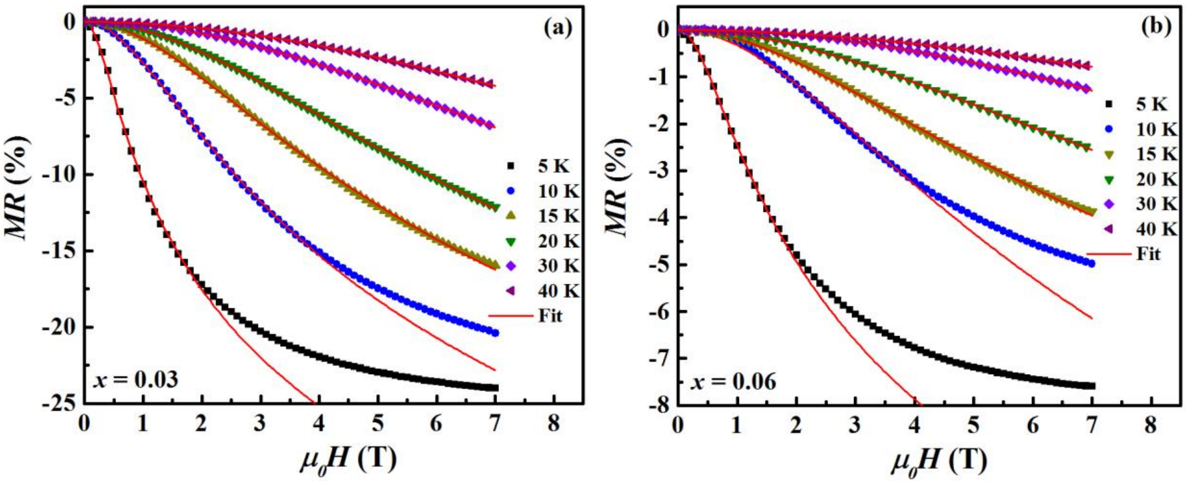

Figure 5.29 (a) Least-squares fit of the negative *MR* to Eq. (5.5) for (a) *x* = 0.03 and (b) *x* = 0.06.

MR data fit very well in full field range for $T \geq 28$ K, while the deviation occurs for $T \leq 24$ K. As can be seen from Fig. 5.28(a), the field where deviation occurs in experimental and calculated MR decreases with decreasing temperature. The coefficients *a* and *b* are shown at the left and right y-axis, respectively in Fig. 5.28 (b). As temperature decreases, the coefficient *a* decreases, while the coefficient *b* increases. We also fitted *MR* data for $x = 0.03$ and 0.06 with Eq. (5.5) and shown in Fig. 5.29 (a) and (b), respectively. The fitting parameters *a* and *b* are summarized in Table 5.2 for samples $x = 0.01$, 0.03 and 0.06. It is found that *a* and *b* both have temperature and La doping dependence. While *a* increases with increasing temperature, *b* decreases. It has been discussed that the substitution of La^{3+} for Eu^{2+} introduces t_{2g}^{1} electrons in the empty 3d band, it means the charge carrier concentration increases as *x* increases. Hence, the parameters *a* and *b* both increases with increasing dopant (*x*) and carrier concentration.

***T*(K)**	***x* = 0.01**		***x* = 0.03**		***x* = 0.06**	
	a	***b***	***a***	***b***	***a***	***b***
5	4.501	3.538	2.374	2.319	1.382	1.634
10	4.712	1.180	2.692	0.670	1.471	0.447
20	5.390	0.387	2.921	0.257	1.640	0.179
40	5.532	0.166	3.270	0.098	1.481	0.093

Table 5.2 Values of the fitting parameters *a* and *b* to the Eq.(5.2) for *x* = 0.01, *x* = 0.03 and *x* = 0.06 at few selected temperatures.

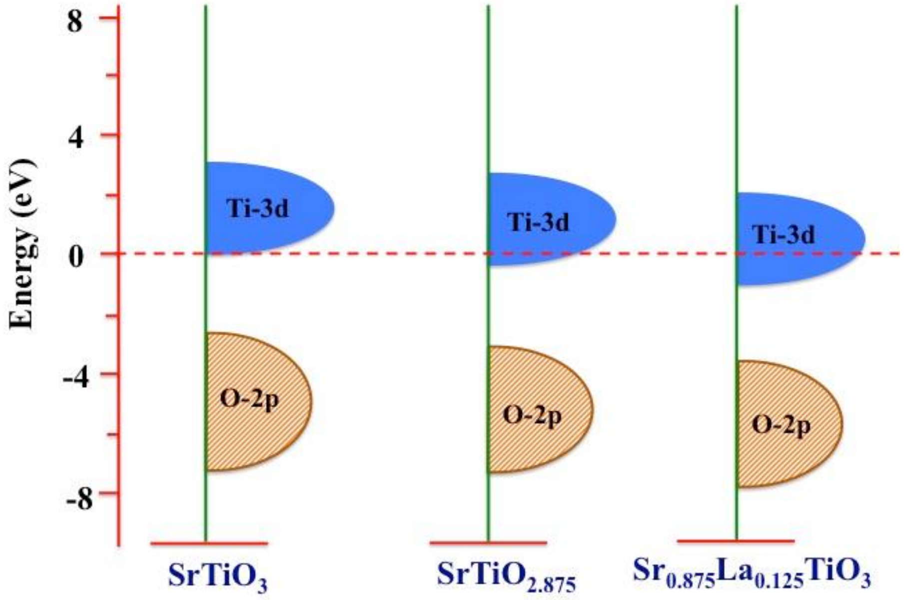

Figure 5.30 Schematic of electronic band structure of $SrTiO_3$, $SrTiO_{3-\delta}$ and $Sr_{1-x}La_xTiO_3$.

To explain the positive *MR* for $Eu_{1-x}La_xTiO_3$ (x = 0.10 - 0.20), a two band model can be utilized. In this model, hybridization between two bands (Example: p-d band mixing in InMnSb)[123] leads to the spin splitting of the bands and gives rise to a positive magnetoresistance. In case of $EuTiO_3$, valance band consists of occupied O-2p band and conduction band has Ti-3d and Eu-5d bands, while localized Eu-4f band exist near to Fermi level.[43] N. Shanthi and D. D. Sharma has investigated the electronic structure of electron-doped $SrTiO_{3-\delta}$ and $Sr_{1-x}La_xTiO_3$ within *ab* initio band-structure approach.[209] It is found that in case of $Sr_{1-x}La_xTiO_3$, the conduction band (Ti-3d band) moves towards Fermi level due to electron doping as shown in Fig. 5.30. A similar concept can be applied to $Eu_{1-x}La_xTiO_3$, where Ti-3d band moves to the Fermi level and mixes with Eu-4f band (Fig. 5.31). This f-d hybridization leads to spin splitting of Ti-3d band into two subbands with different spin polarized carriers. For a two-band model the positive *MR* is given by

$$MR = \frac{c^2H^2}{(1 + d^2H^2)} \tag{5.6}$$

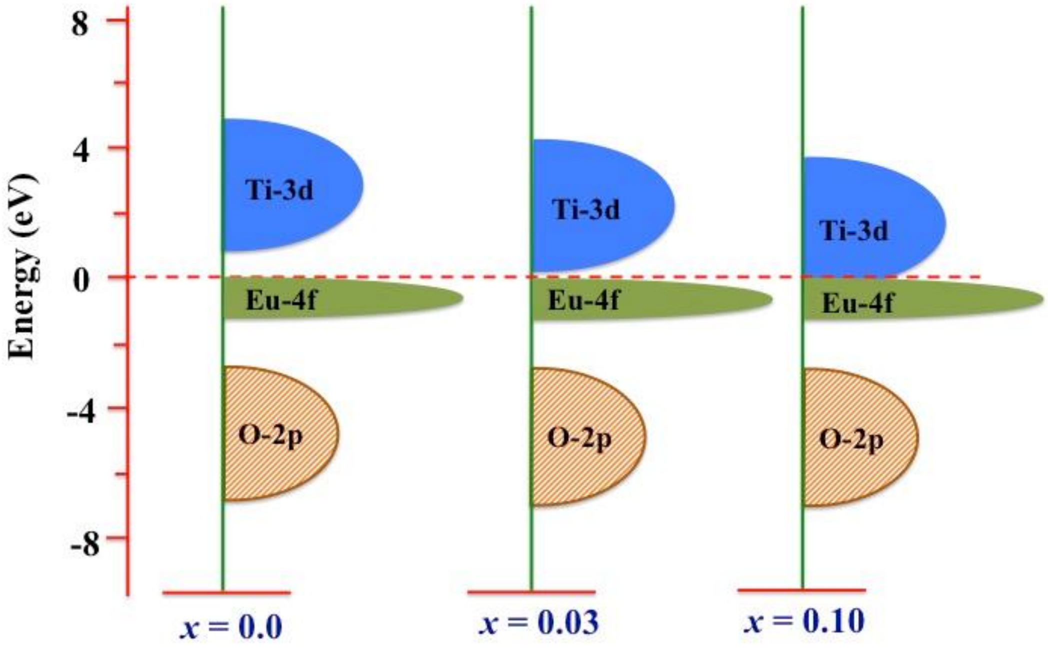

Figure 5.31 Schematic of electronic band structure of $Eu_{1-x}La_xTiO_3$.

where c and d are related to the conductivity and mobility of carriers in the two spin-split bands and are given by

$$c^2 = \frac{\sigma_1\sigma_2(\mu_1 + \mu_2)^2}{(\sigma_1 + \sigma_2)^2} \tag{5.7}$$

and

$$d^2 = \frac{(\sigma_1\mu_2 - \sigma_2\mu_1)^2}{(\sigma_1 + \sigma_2)^2} \tag{5.8}$$

where σ_1 (σ_2) and μ_1(μ_2) are the conductivity and mobility of the majority spin (minority spin) carriers in two band, respectively.

To determine the band splitting responsible for the observed positive *MR* in $Eu_{1-x}La_xTiO_3$ (x = 0.10 – 0.20), we fit experimental *MR* data to the Eq. (5.6). The fitted *MR* data for x = 0.10 and 0.20 are shown in Fig. 5.31 (a) and (b), respectively. The experimental *MR* data fit quite well for $T \geq 20$ K, but deviation occur for T = 15 K for both samples. Similar fits were also obtained for x = 0.13 (not shown here). *MR* at T = 10 K for all samples does not

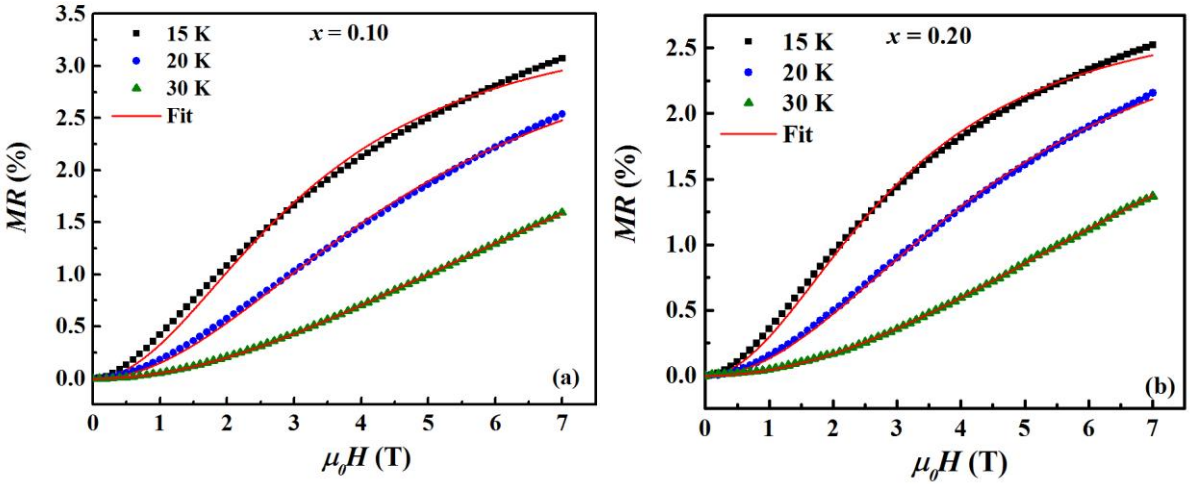

Figure 5.32 Least-squares fit of the positive *MR* to Eq. (5.6) for (a) *x* = 0.10 and (b) *x* = 0.20.

fit with Eq. (5.6) even in low field range. The value of fitting parameters *c* and *d* are given in Table 5.3 for *x* = 0.10, 0.13 and 0.20. The conductivity and mobility of the charge carriers can be obtained from the *c* and *d* values if total conductivity and mobility is known.

***T* (K)**	***x* = 0.10**		***x* = 0.13**		***x* = 0.20**	
	c	***d***	***c***	***d***	***c***	***d***
20	5.390	0.387	2.921	0.257	1.640	0.179
30	5.532	0.166	3.270	0.098	1.481	0.093

Table 5.3 Values of the fitting parameters *c* and *d* for *x* = 0.10, *x* = 0.13 and *x* = 0.20 at temperatures *T* = 20 and 30 K.

For *T* = 2 K, we performed a least square fitting of our data to the combination of Eq. (5.5) and (5.6), which is given by

$$MR = -a^2 \ln(1 + b^2 H^2) + \frac{c^2 H^2}{(1 + d^2 H^2)} \tag{5.9}$$

The fitted *MR* data for *x* = 0.10, 0.13 and 0.20 at *T* = 2 K is shown in Fig. 5.30. The fitted *MR* agrees very well with the experimental data for all three samples. The fitting parameters *a*, *b*, *c* and *d* are summarized in Table 5.4. While the parameter *a* increases with increasing *x*, the parameters *b*, *c* and *d* decrease.

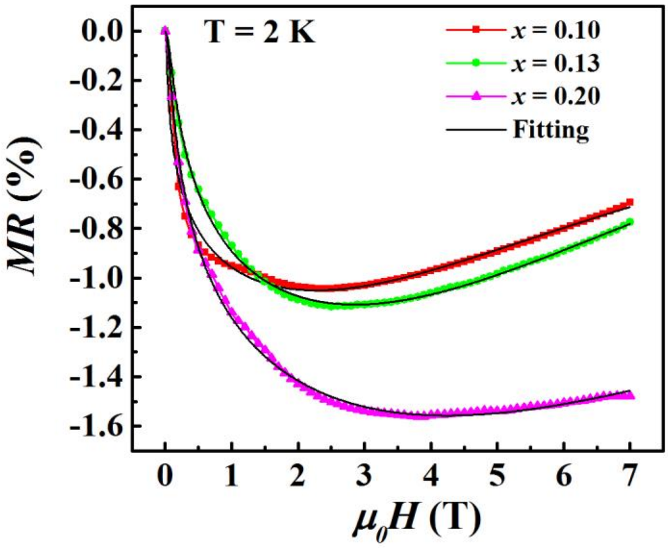

Figure 5.33 Least-squares fit of the *MR* at *T* = 2 K to Eq. (5.9) for *x* = 0.10, 0.13 and 0.20.

Sample	*a*	*b*	*c*	*d*
***x* = 0.10**	0.348	57.888	0.167	0.130
***x* = 0.13**	0.434	11.380	0.165	0.105
***x* = 0.20**	0.464	1.309	0.121	0.078

Table 5.4 Values of the fitting parameters *a*, *b*, *c* and *d* to the Eq. (5.9) for *x* = 0.10, *x* = 0.13 and *x* = 0.20 at temperature *T* = 2 K.

5.4 Summary

In summary, polycrystalline $Eu_{1-x}La_xTiO_3$ samples over wide compositions ($0.01 \le x \le 0.30$) were prepared using standard solid-state reaction method. The magnetic, magnetocaloric and electrical properties were investigated with increasing La concentration. The important findings are:

1. The ground state of $Eu_{1-x}La_xTiO_3$ changes from antiferromagnetic for $x = 0.01$ (T_N = 5.2 K) to ferromagnetic for $x \ge 0.03$. The ferromagnetic Curie temperature increases

as x increases from $x = 0.03$ ($T_C = 5.7$ K) to $x = 0.13$ ($T_C = 8.8$ K) and then decreases with further increasing x ($T_C = 7.2$ K for $x = 0.30$).

2. The $x = 0.01$ sample shows a large reversible isothermal magnetic entropy change of $-\Delta S_m = 23$ (41.5) J/kg.K and adiabatic temperature change, $\Delta T_{ad} = 9$ (17.2) K around 6.7 K for a field change of $\mu_0 \Delta H = 2$ (5) Tesla. Although the peak value of $-\Delta S_m$ decreases as La content increases, it is impressive even in $x = 0.2$($-\Delta S_m = 31.41$ J/kg.K at $T = 7.5$ K for $\mu_0 \Delta H = 5$ T).
3. For $x = 0.01$, adiabatic removal of 5 T magnetic field at 20 K will result in the final temperature of 5.3 K or removal of field at 27 K will result in 19 K.
4. The $x = 0.01$ shows a colossal negative magnetoresistance ($MR = -75$ % at $T = 2$ K for $\mu_0 H = 7$T). The I-M transition in this composition occurs around 80 K, which is far above the magnetic phase transition temperature and the magnetic field has significant impact on the resistivity even at temperature as high as 90 K. The negative MR decreases drastically with increasing La contents. For $x \geq 0.10$, the sign of MR changes to positive as temperature increases above 5 K. The positive MR is not quadratic in H.
5. Spin disorder scattering mechanism is suggested as the possible origin of the colossal negative MR in $Eu_{1-x}La_xTiO_3$. The occurrence of positive MR in $Eu_{1-x}La_xTiO_3$ ($x \geq 0.10$) could be due to the hybridization of Eu-4f and Ti-3d bands, which leads to the spin splitting of Ti-3d band. Theoretical prediction for the electronic structure of $Eu_{1-x}La_xTiO_3$ will be helpful to verify the suggested mechanism for negative and positive MR.

Chapter 6 Conclusions and Scope of Future Work

The important findings in this thesis work have already been discussed in the summary section of each chapter. In this chapter, overall view of the present work is summarized along with the future scope of this work.

6.1 Summary

In this thesis, we have studied the magnetic, electrical, magnetocaloric, magnetoresistance and magnetodielectric properties of three systems: (i) $EuTiO_3$, (ii) $Eu_{1-x}Ba_xTiO_3$ and (iii) $Eu_{1-x}La_xTiO_3$ in detail. $EuTiO_3$ in which Eu^{2+} spins ordered antiferromagnetically below 5.4 K exhibits multiple exciting phenomena such as giant magnetocaloric effect, insulator-metal transition, colossal magnetoresistance and magnetodielectric effect. $Eu_{1-x}Ba_xTiO_3$ and $Eu_{1-x}La_xTiO_3$ systems provide a great opportunity to study the effect of dilution of Eu^{2+} spins on the magnetic, magnetocaloric, magnetoresistance and magnetodielectric properties. While the isovalent Ba^{2+} substitution for Eu^{2+} does not dope any electron or hole in system, the substitution of aliovalent La^{3+} for Eu^{2+} dopes electrons into t_{2g} orbital of Ti-3d band of $EuTiO_3$.

6.1.1 Magnetic properties

$EuTiO_3$ shows antiferromagnetic (AFM) ordering due to Eu^{2+} magnetic moments below $T_N = 5.42$ K. While the compounds $x \leq 0.2$ in $Eu_{1-x}Ba_xTiO_3$ remains AFM, the ground state of $Eu_{1-x}La_xTiO_3$ changes from AFM for $x = 0.01$ to ferromagnetic (FM) for $x \geq 0.03$. The FM interaction is also observed in $Eu_{0.5}Ba_{0.5}TiO_3$ below $T_C = 1.7$ K. The magnetic transition temperature in $Eu_{1-x}Ba_xTiO_3$ shifts to lower temperature as Ba content increases. In $Eu_{1-x}La_xTiO_3$, the FM Curie temperature increases as x increases from $x = 0.03$ ($T_C = 5.7$ K) to $x = 0.13$ ($T_C = 8.8$ K) and then decreases with further increasing x ($T_C = 7.2$ K for $x = 0.30$). The antiferromagnetic coupling among neighboring Eu^{2+}: $4f^7$ spins in $EuTiO_3$ is dominated by superexchange interaction involving Ti-3d(t_{2g}) empty states compared to superexchange interaction via O-2p orbitals, which is nominally encountered in perovskite oxides. The substitution of La^{3+} for Eu^{2+} introduces t_{2g} electrons in the empty Ti-3d band, which seems to suppress AFM coupling and promote FM interaction between 4f spins of neighboring Eu^{2+} through RKKY like interaction.

6.1.2 Ferroelectric properties

While $EuTiO_3$ remains paraelectric (PE) down to low temperature, the substitution of Ba induces ferroelectricity in $Eu_{1-x}Ba_xTiO_3$ for $x \geq 0.4$. The ferroelectric (FE) transition temperature T_{FE} shifts towards higher temperature with increasing Ba doping from $x = 0.40$ (T_{FE} = 150 K) to $x = 1.0$ (T_{FE} = 395 K). We have constructed a phase diagram for $Eu_{1-x}Ba_xTiO_3$ ($0.00 \leq x \leq 1.0$). The two end compounds $x = 0.0$ ($EuTiO_3$) and $x = 1.0$ ($BaTiO_3$) are AFM+PE and PM+FE, respectively. As x increases from 0.0 to 1.0, $Eu_{1-x}Ba_xTiO_3$ transforms from AFM to FM and PE to FE at $x = 0.4$ and a multiferroic phase (FM + FE) is realized for $Eu_{1-x}Ba_xTiO_3$ ($0.4 \leq x \leq 0.95$).

6.1.3 Magnetocaloric effect

The magnetocaloric effect (MCE) is investigated for $EuTiO_3$, $Eu_{1-x}Ba_xTiO_3$ ($0.1 \leq x \leq 0.9$) and $Eu_{1-x}La_xTiO_3$ ($0.01 \leq x \leq 0.20$) by means of magnetization and heat capacity measurements. We listed the isothermal magnetic entropy change ($-\Delta S_m$), adiabatic temperature change (ΔT_{ad}) and refrigeration cooling power (RCP) for few selected compounds in Table 6.1. $EuTiO_3$ shows a giant magnetocaloric effect around T_N = 5.4 K. $-\Delta S_m$, ΔT_{ad} and RCP are 49(40.4) J/kg.K, 21(16.5) K and 540(440) J/kg, respectively, for a field change of 7(5) T at T_N. The magnetic entropy change varies from $-\Delta S_m$ = 40 J/kg.K to 6.7 J/kg.K at T = 4.5 K for $\mu_0 \Delta H$ = 5 T as x increases from 0.1 to 0.9 in the $Eu_{1-x}Ba_xTiO_3$

Compound	**$-\Delta S_m$ (J/kg.K)**	**ΔT_{ad} (K)**	***RCP* (J/kg)**	**T_N/T_C (K)**
$EuTiO_3$	41	16.5	440	5.4
$Eu_{0.9}Ba_{0.1}TiO_3$	40	-	-	3.5
$Eu_{0.5}Ba_{0.5}TiO_3$	29	15.7	360	1.7
$Eu_{0.1}Ba_{0.9}TiO_3$	6.6	-	-	-
$Eu_{0.99}La_{0.01}TiO_3$	41.5	17.2	445	5.2
$Eu_{0.8}La_{0.2}TiO_3$	31	16	430	7.5

Table 6.1 List of magnetic entropy change (ΔS_m), adiabatic temperature change ($-\Delta T_{ad}$) and relative cooling power (*RCP*) for selected compound studied in thesis.

series. Half doped compound $Eu_{0.5}Ba_{0.5}TiO_3$ exhibits $-\Delta S_m$ = 31.32 J/kg.K, ΔT_{ad} =18.68 K and *RCP* = 343 J/kg for $\mu_0\Delta H$ = 7 T. In $Eu_{1-x}La_xTiO_3$ series, the x = 0.01 sample shows a large $-\Delta S_m$ = 41.5 J/kg.K and ΔT_{ad} = 17.2 K around 6.7 K for a field change of $\mu_0\Delta H$ = 5 T. Although the peak value of $-\Delta S_m$ and ΔT_{ad} decreases as La content increases, it is impressive in x = 0.2($-\Delta S_m$ = 31.41 J/kg.K and ΔT_{ad} = 16 K at T = 7.5 K for $\mu_0\Delta H$ = 5 T). The giant magnetocaloric effect in these compounds arises from the suppression of the spin fluctuations associated with Eu^{2+}:$4f^7$ electrons. The absence of hysteresis in the field dependences of magnetization with large magnetic entropy and adiabatic temperature changes is an added advantage. In view of the observed large values of $-\Delta S_m$, ΔT_{ad} and *RCP*, these compounds may be of interest for cryogenic magnetic refrigeration below 30 K.

6.1.4 DC resistivity and magnetoresistance

The impact of magnetic field on the dc resistivity is studied for $EuTiO_3$, $Eu_{1-x}Ba_xTiO_3$ ($0.1 \leq x \leq 0.6$) and $Eu_{1-x}La_xTiO_3$ ($0.01 \leq x \leq 0.30$). $EuTiO_3$ is an insulator under zero magnetic field, while the application of a magnetic field drives an insulator to metal (I-M) transition in paramagnetic region. The I-M transition shifts towards higher temperature (T = 22 K >> T_N for μ_0H = 7 T) with increasing strength of the magnetic field. $EuTiO_3$ shows a colossal negative magnetoresistance, $MR = \Delta\rho/\rho(0) = -99.15\%$ under a small magnetic field of $\mu_0 H = 0.5$ T at $T = 2$ K and $MR = -45\%$ under 7 T at $T = 45$ K ($>>T_N$). This is first observation of colossal negative MR among the rare earth titanates.

The negative MR value of $EuTiO_3$ reduces with Ba^{2+} and La^{2+} substitution for Eu^{2+}. In $Eu_{1-x}Ba_xTiO_3$ series, the negative MR varies from $MR = -85\%$ ($x = 0.1$) to -20% ($x = 0.6$) at $T = 20$ K and $\mu_0 H = 7$ T. However, the negative MR decreases drastically with increasing La contents in $Eu_{1-x}La_xTiO_3$ series. For $Eu_{0.99}La_{0.01}TiO_3$, $MR = -75$ % at $T = 2$ K for $\mu_0 H = 7$T. For $x \geq 0.10$ in $Eu_{1-x}La_xTiO_3$, the sign of MR changes to positive as temperature increases above 5 K.

The negative colossal magnetoresistance in $EuTiO_3$ as well as in $Eu_{1-x}La_xTiO_3$ and $Eu_{1-x}La_xTiO_3$ is suggested due to the suppression of $4f^7$ spin fluctuations by magnetic field, which reduces the spin-disorder scattering. The occurrence of positive MR in $Eu_{1-x}La_xTiO_3$ ($x \geq 0.10$) could be due to the hybridization of Eu-4f and Ti-3d bands, which leads to the spin splitting of Ti-3d band. The additional experiments and theoretical calculation for electronic structure are needed to verify the suggested mechanism for negative and positive MR.

6.1.5 Magnetodielectric effect

The effect of magnetic field on dielectric constant and ac resistivity is studied simultaneously for $EuTiO_3$ and $Eu_{1-x}Ba_xTiO_3$ ($0.02 \leq x \leq 0.6$) compounds. Polycrystalline $EuTiO_3$ shows a giant positive magnetodielectric effect ($MDE = \Delta\varepsilon/\varepsilon(0) = 670$ % under 7 T at $T = 10$ K), which is much larger than that observed in $EuTiO_3$ single crystal ($\Delta\varepsilon/\varepsilon(0) = 7$ % under 1.5 T at $T = 2$ K) and thin film ($\Delta\varepsilon/\varepsilon(0) = 3$ % under 1.5 T at $T = 2$ K). $EuTiO_3$ exhibits a colossal negative ac MR ($MR = -99.9\%$ at $T = 10$ K for $\mu_0 H = 7$ T). A simultaneous occurrence of positive MDE and negative ac MR indicates that the large MDE in polycrystalline $EuTiO_3$ could be due to the Maxwell-Wagner relaxation mechanism. Impedance spectroscopy data confirms the presence of Maxwell-Wagner relaxation in this compound above 15 K. However, the occurrence of positive magnetodielectric loss excludes this mechanism as the origin of *MDE*. The quadratic dependence of *MDE* on magnetization (*i.e.* $MDE \propto M^2$) for low fields indicates that *MDE* is attributed to strong spin-lattice coupling in this material.

The compounds of $Eu_{1-x}Ba_xTiO_3$ series also show large positive magnetodielectric effect together with negative magnetoresistance up to $x = 0.6$. The *MDE* and ac *MR* decreases with increasing Ba doping from $x = 0.02$ ($MDE = 120\%$ and $MR = -94\%$) to $x = 0.60$ ($MDE = 7.6\%$ and $MR = -13.5\%$) at $T = 10$ K and $\mu_0 H = 7$ T. While *MDE* versus $-MR$ curves for $x = 0.10$ and 0.30 are highly non-linear, they are almost linear at all temperatures for $x = 0.50$ and 0.60. $MDE \propto M^2$ for low fields indicates that the magnetodielectric effect is due to the spin-lattice coupling in these compounds. However, a linear dependence of *MDE* on *M* is realized for $x = 0.5$ and 0.6 over high field range ($2 \text{ T} \leq \mu_0 H \leq 7$ T). First time, we observed a linear relation in *MDE* and *MR* for $x = 0.5$ and 0.6.

6.2 Future scope

6.2.1 Electrocaloric effect in $Eu_{1-x}Ba_xTiO_3$

The electrocaloric effect (ECE), an analogous to magnetocaloric effect, is a phenomenon in which a reversible temperature of a material changes with application of an electric field. Besides magnetocaloric materials, electrocaloric materials also have attracted specific attention because the easy tunability of ferroelectric phase transition by chemical substitution could be exploited for refrigeration over a broad temperature range. Multiferroics are of special interest. Not only they can show caloric effects in response to electrical and magnetic fields independently, but also the presence of magneto-electric interaction may enhance the caloric effect and allow tunability of magnetocaloric effect by electric field, and vice versa.

The compounds of $Eu_{1-x}Ba_xTiO_3$ series provide a great opportunity to study the electrocaloric effect around their ferroelectric transition temperature as well as the impact of electric field on the magnetocaloric effect. Recently, a giant electrocaloric effect (ΔT = 15-20 K) is predicted in $EuTiO_3$ nanowires around room temperature.[210] However, there is no experimental report so far available on the ECE in $EuTiO_3$. Since $x = 0.7$ and 0.75 compounds of $Eu_{1-x}Ba_xTiO_3$ series exhibit ferroelectric transition at T_{FE} ~ 290 K and 306 K, respectively, they could show a large ECE near room temperature.

6.2.2 Thermoelectric effect in $Eu_{1-x}La_xTiO_3$

Thermoelectric effect (or seebeck effect) is a phenomenon in which a temperature gradient between two ends of a material produces a voltage difference between that ends. Seebeck coefficient (or thermopower) is defined as

$$\alpha = \frac{\Delta V}{\Delta T}$$

where ΔT is temperature gradient and ΔV is voltage difference.

$EuTiO_3$ exhibits a large Seebeck coefficient (~1000μV/K) at room temperature.[211] The impact of magnetic field on the Seebeck coefficient of $EuTiO_3$ at low temperature could be interesting. Since the resistivity of $EuTiO_3$ is very high (~ 10^9 Ω-cm) at low temperature, the thermopower measurements will not be reliable. However, the substitution of La^{3+} for Eu^{2+} reduces the resistivity of $Eu_{1-x}La_xTiO_3$. Therefore, the study of thermopower and magnetothermopower in $Eu_{1-x}La_xTiO_3$ will be impressive. Magnetothermopower in $Eu_{1-x}La_xTiO_3$ will shed light on possible origin of *MR*.

6.2.3 GdTiO$_3$ and Eu$_{1-x}$Gd$_x$TiO$_3$

A Mott insulator GdTiO$_3$ is ferromagnetic below T_C = 30 K.[32] While EuTiO$_3$ has only Eu^{2+}:4f^7 spins, GdTiO$_3$ has an additional spin Ti^{3+}:3d^1 with Gd^{3+}:4f^7. A giant magnetocaloric effect could be expected in GdTiO$_3$ due to the suppression of Ti^{3+}:3d^1 and Gd^{3+}:4f^7 spins fluctuations under the magnetic field. However, no one has studied the magnetocaloric properties in GdTiO$_3$ experimentally and theoretically till now.

Unlike Eu$_{1-x}$Ba$_x$TiO$_3$ and Eu$_{1-x}$La$_x$TiO$_3$, Eu$_{1-x}$Gd$_x$TiO$_3$ is a system where Eu^{2+}:4f^7 spins are replaced by Gd^{3+}:4f^7 spins. Additionally, substitution of Gd^{3+} for Eu^{2+} will introduce t$_{2g}$ electrons in Ti-3d band, which could suppress antiferromagnetism and promote ferromagnetic interaction between neighboring Eu^{2+}:4f^7 spins through RKKY like interaction. The study of magnetization, magnetocaloric effect, magnetoresistance and magnetothermopower in Eu$_{1-x}$Gd$_x$TiO$_3$ series will be very exciting.

In view of *MR* observed in Eu$_{1-x}$Ba$_x$TiO$_3$ system, it will be interesting to study the effect of different alkaline earth ions such as Sr^{2+} and Ca^{2+} on the magnetoresistance of EuTiO$_3$. Finally, a detail investigation of band structure of EuTiO$_3$ with and without magnetic field is needed instantly to understand the origin of *MR* in this compound.

Bibliography

[1] J.G. Bednorz, K.A. Müller, *Possible highTc superconductivity in the Ba−La−Cu−O system*, Zeitschrift für Physik B Condensed Matter, 64 (1986) 189-193.

[2] A. Schilling, M. Cantoni, J.D. Guo, H.R. Ott, *Superconductivity above 130 K in the Hg-Ba-Ca-Cu-O system*, Nature, 363 (1993) 56-58.

[3] R. Mahendiran, R. Mahesh, A.K. Raychaudhuri, C.N.R. Rao, *Room-temperature giant magnetoresistance in* $La_{1-x}Pb_xMnO_3$, Journal of Physics D-Applied Physics, 28 (1995) 1743-1745.

[4] A. Urushibara, Y. Moritomo, T. Arima, A. Asamitsu, G. Kido, Y. Tokura, *Insulator-metal transition and giant magnetoresistance in* $La_{1-x}Sr_xMnO_3$, Physical Review B, 51 (1995) 14103-14109.

[5] Y. Tokura, A. Urushibara, Y. Moritomo, T. Arima, A. Asamitsu, G. Kido, N. Furukawa, *Giant magnetotransport phenomena in filling-controlled kondo-lattice system* $La_{1-x}Sr_xMnO_3$, Journal of the Physical Society of Japan, 63 (1994) 3931-3935.

[6] R. Mahendiran, A. Raychaudhuri, *Magnetoresistance of the spin-state-transition compound* $La_{1-x}Sr_xCoO_3$, Physical Review B, 54 (1996) 16044.

[7] A.C. Masset, C. Michel, A. Maignan, M. Hervieu, O. Toulemonde, F. Studer, B. Raveau, J. Hejtmanek, *Misfit-layered cobaltite with an anisotropic giant magnetoresistance:* $Ca_3Co_4O_9$, Physical Review B, 62 (2000) 166-175.

[8] D.M. Repaka, T. Tripathi, M. Aparnadevi, R. Mahendiran, *Magnetocaloric effect and magnetothermopower in the room temperature ferromagnet* $Pr_{0.6}Sr_{0.4}MnO_3$, Journal of Applied Physics, 112 (2012) 123915.

[9] M.-H. Phan, S.-C. Yu, *Review of the magnetocaloric effect in manganite materials*, Journal of Magnetism and Magnetic Materials, 308 (2007) 325-340.

[10] K.A. GschneidnerJr, V. Pecharsky, A. Tsokol, *Recent developments in magnetocaloric materials*, Reports on Progress in Physics, 68 (2005) 1479.

[11] Z.J. Huang, Y. Cao, Y.Y. Sun, Y.Y. Xue, C.W. Chu, *Coupling between the ferroelectric and antiferromagnetic orders in* $YMnO_3$, Physical Review B, 56 (1997) 2623-2626.

[12] T. Kimura, S. Kawamoto, I. Yamada, M. Azuma, M. Takano, Y. Tokura, *Magnetocapacitance effect in multiferroic* $BiMnO_3$, Physical Review B, 67 (2003).

[13] J. Wang, J.B. Neaton, H. Zheng, V. Nagarajan, S.B. Ogale, B. Liu, D. Viehland, V. Vaithyanathan, D.G. Schlom, U.V. Waghmare, N.A. Spaldin, K.M. Rabe, M. Wuttig, R.

Ramesh, *Epitaxial $BiFeO_3$ Multiferroic Thin Film Heterostructures*, Science, 299 (2003) 1719-1722.

[14] T. Katsufuji, H. Takagi, *Coupling between magnetism and dielectric properties in quantum paraelectric $EuTiO_3$*, Physical Review B, 64 (2001) 054415.

[15] J.H. Lee, L. Fang, E. Vlahos, X.L. Ke, Y.W. Jung, L.F. Kourkoutis, J.W. Kim, P.J. Ryan, T. Heeg, M. Roeckerath, V. Goian, M. Bernhagen, R. Uecker, P.C. Hammel, K.M. Rabe, S. Kamba, J. Schubert, J.W. Freeland, D.A. Muller, C.J. Fennie, P. Schiffer, V. Gopalan, E. Johnston-Halperin, D.G. Schlom, *A strong ferroelectric ferromagnet created by means of spin-lattice coupling*, Nature, 466 (2010) 954-U972.

[16] H.D. Megaw, *Crystal structure of barium titanate*, Nature, 155 (1945) 484-485.

[17] A. von Hippel, *Ferroelectricity, Domain Structure, and Phase Transitions of Barium Titanate*, Reviews of Modern Physics, 22 (1950) 221-237.

[18] B. Matthias, A. Vonhippel, *Domain structure and dielectric response of barium titanate single crystals*, Physical Review, 73 (1948) 1378-1384.

[19] M.I. Desheng Fu, *Role of Ca off-centering in tuning the ferroelectric phase transitions in $Ba(Zr,Ti)O_3$ system*, (2015).

[20] J.F. Schooley, W.R. Hosler, M.L. Cohen, Superconductivity in Semiconducting $SrTiO_3$, Physical Review Letters, 12 (1964) 474-475.

[21] F.W. Lytle, *X‐Ray Diffractometry of Low‐Temperature Phase Transformations in Strontium Titanate*, Journal of Applied Physics, 35 (1964) 2212-2215.

[22] S.K. Mishra, D. Pandey, *Low temperature x-ray diffraction study of the phase transitions in $Sr_{1-x}Ca_xTiO_3(x=0.02,0.04)$: Evidence for ferrielectric ordering*, Applied Physics Letters, 95 (2009) 232910.

[23] E. Tosatti, R. Martoňák, *Rotational melting in displacive quantum paraelectrics, Solid State Communications*, 92 (1994) 167-180.

[24] K.A. Müller, H. Burkard, *$SrTiO_3$: An intrinsic quantum paraelectric below 4 K*, Physical Review B, 19 (1979) 3593-3602.

[25] H.M. Christen, J. Mannhart, E.J. Williams, C. Gerber, *Dielectric properties of sputtered $SrTiO_3$ films*, Physical Review B, 49 (1994) 12095-12104.

[26] M. Itoh, R. Wang, Y. Inaguma, T. Yamaguchi, Y.J. Shan, T. Nakamura, *Ferroelectricity Induced by Oxygen Isotope Exchange in Strontium Titanate Perovskite*, Physical Review Letters, 82 (1999) 3540-3543.

[27] J.G. Bednorz, K.A. Müller, *$Sr_{1-x}Ca_xTiO_3$: An XY Quantum Ferroelectric with Transition to Randomness*, Physical Review Letters, 52 (1984) 2289-2292.

[28] J.H. Haeni, P. Irvin, W. Chang, R. Uecker, P. Reiche, Y.L. Li, S. Choudhury, W. Tian, M.E. Hawley, B. Craigo, A.K. Tagantsev, X.Q. Pan, S.K. Streiffer, L.Q. Chen, S.W. Kirchoefer, J. Levy, D.G. Schlom, *Room-temperature ferroelectricity in strained* $SrTiO_3$, Nature, 430 (2004) 758-761.

[29] H. Uwe, T. Sakudo, *Stress-induced ferroelectricity and soft phonon modes in* $SrTiO_3$, Physical Review B, 13 (1976) 271-286.

[30] H.W. Jang, A. Kumar, S. Denev, M.D. Biegalski, P. Maksymovych, C.W. Bark, C.T. Nelson, C.M. Folkman, S.H. Baek, N. Balke, C.M. Brooks, D.A. Tenne, D.G. Schlom, L.Q. Chen, X.Q. Pan, S.V. Kalinin, V. Gopalan, C.B. Eom, *Ferroelectricity in Strain-Free* $SrTiO_3$ *Thin Films*, Physical Review Letters, 104 (2010) 197601.

[31] D.A. MacLean, H.-N. Ng, J.E. Greedan, *Crystal structures and crystal chemistry of the* $RETiO_3$ *perovskites: RE = La, Nd, Sm, Gd, Y*, Journal of Solid State Chemistry, 30 (1979) 35-44.

[32] J.E. Greedan, *The rare earth-titanium (III) perovskite oxides—An isostructural series with a remarkable variation in physical properties*, Journal of the Less Common Metals, 111 (1985) 335-345.

[33] T. Katsufuji, Y. Taguchi, Y. Tokura, *Transport and magnetic properties of a Mott-Hubbard system whose bandwidth and band filling are both controllable:* $R_{1-x}Ca_xTiO_{3+y/2}$, Physical Review B, 56 (1997) 10145-10153.

[34] M. Masahito, I. Masatoshi, *Orbital physics in the perovskite Ti oxides*, New Journal of Physics, 6 (2004) 154.

[35] M. Mochizuki, M. Imada, *G-type Antiferromagnetism and Orbital Ordering due to the Crystal Field from the Rare-Earth Ions Induced by the* $GdFeO_3$*-type Distortion in* $RTiO_3$ *Where R=La, Pr, Nd and Sm*, Journal of the Physical Society of Japan, 73 (2004) 1833-1850.

[36] Y. Okimoto, T. Katsufuji, Y. Okada, T. Arima, Y. Tokura, *Optical spectra in* $(La,Y)TiO_3$*: Variation of Mott-Hubbard gap features with change of electron correlation and band filling*, Physical Review B, 51 (1995) 9581-9588.

[37] J.P. Goral, J.E. Greedan, D.A. MacLean, *Magnetic behavior in the series* $La_xY_{1-x}TiO_3$, Journal of Solid State Chemistry, 43 (1982) 244-250.

[38] Y. Tokura, Y. Taguchi, Y. Okada, Y. Fujishima, T. Arima, K. Kumagai, Y. Iye, *Filling dependence of electronic properties on the verge of metal-Mott-insulator transition in* $Sr_{1-x}La_xTiO_3$, Physical Review Letters, 70 (1993) 2126-2129.

[39] Y. Taguchi, Y. Tokura, T. Arima, F. Inaba, *Change of electronic structures with carrier doping in the highly correlated electron system* $Y_{1-x}Ca_xTiO_3$, Physical Review B, 48 (1993) 511-518.

[40] J. Brous, I. Fankuchen, E. Banks, *Rare earth titanates with a perovskite structure*, Acta Crystallographica, 6 (1953) 67-70.

[41] T. McGuire, M. Shafer, R. Joenk, H. Alperin, S. Pickart, *Magnetic structure of* $EuTiO_3$, Journal of Applied Physics, 37 (1966) 981-982.

[42] C.L. Chien, Debenede.S, F.D.S. Barros, *Magnetic properties of* $EuTiO_3$, Eu_2TiO_4, *and* $Eu_3Ti_2O_7$, Physical Review B, 10 (1974) 3913-3922.

[43] H. Akamatsu, Y. Kumagai, F. Oba, K. Fujita, H. Murakami, K. Tanaka, I. Tanaka, *Antiferromagnetic superexchange via 3d states of titanium in* $EuTiO_3$ *as seen from hybrid Hartree-Fock density functional calculations*, Physical Review B, 83 (2011).

[44] T. Birol, C.J. Fennie, *Origin of giant spin-lattice coupling and the suppression of ferroelectricity in* $EuTiO_3$ *from first principles*, Physical Review B, 88 (2013) 094103.

[45] J.H. Lee, X. Ke, N.J. Podraza, L.F. Kourkoutis, T. Heeg, M. Roeckerath, J.W. Freeland, C.J. Fennie, J. Schubert, D.A. Muller, P. Schiffer, D.G. Schlom, *Optical band gap and magnetic properties of unstrained* $EuTiO_3$ *films*, Applied Physics Letters, 94 (2009) 212509.

[46] H. Wu, W.Z. Shen, *Magnetoelectric effect in perovskite quantum paraelectric* $EuTiO_3$, Solid State Communications, 133 (2005) 487-491.

[47] H. Wu, Q. Jiang, W.Z. Shen, *Coupling between the magnetism and dielectric properties in* $Eu_{1-x}Ba_xTiO_3$, Physical Review B, 69 (2004) 014104.

[48] S. Kamba, V. Goian, M. Orlita, D. Nuzhnyy, J. Lee, D. Schlom, K. Rushchanskii, M. Ležaić, T. Birol, C. Fennie, *Magnetodielectric effect and phonon properties of compressively strained* $EuTiO_3$ *thin films deposited on* $(001)(LaAlO_3)_{0.29}$-$(SrAl_{1/2}Ta_{1/2}O_3)_{0.71}$, Physical Review B, 85 (2012) 094435.

[49] S. Kamba, D. Nuzhnyy, P. Vanek, M. Savinov, K. Knizek, Z. Shen, E. Santava, K. Maca, M. Sadowski, J. Petzelt, *Magnetodielectric effect and optic soft mode behaviour in quantum paraelectric* $EuTiO_3$ *ceramics*, Epl, 80 (2007).

[50] C.J. Fennie, K.M. Rabe, *Magnetic and Electric Phase Control in Epitaxial* $EuTiO_3$ *from First Principles*, Physical Review Letters, 97 (2006) 267602.

[51] A.N. Morozovska, M.D. Glinchuk, R.K. Behera, B. Zaulychny, C.S. Deo, E.A. Eliseev, *Ferroelectricity and ferromagnetism in* $EuTiO_3$ *nanowires*, Physical Review B, 84 (2011) 205403.

[52] A. Bussmann-Holder, J. Kohler, R.K. Kremer, J.M. Law, *Relation between structural instabilities in* $EuTiO_3$ *and* $SrTiO_3$, Physical Review B, 83 (2011).

[53] M. Allieta, M. Scavini, L.J. Spalek, V. Scagnoli, H.C. Walker, C. Panagopoulos, S.S. Saxena, T. Katsufuji, C. Mazzoli, *Role of intrinsic disorder in the structural phase transition of magnetoelectric* $EuTiO_3$, Physical Review B, 85 (2012).

[54] D.S. Ellis, H. Uchiyama, S. Tsutsui, K. Sugimoto, K. Kato, D. Ishikawa, A.Q.R. Baron, *Phonon softening and dispersion in* $EuTiO_3$, Physical Review B, 86 (2012) 220301.

[55] K.Z. Rushchanskii, N.A. Spaldin, M. Ležaić, *First-principles prediction of oxygen octahedral rotations in perovskite-structure* $EuTiO_3$, Physical Review B, 85 (2012) 104109.

[56] V. Goian, S. Kamba, O. Pacherova, J. Drahokoupil, L. Palatinus, M. Dusek, J. Rohlicek, M. Savinov, F. Laufek, W. Schranz, A. Fuith, M. Kachlik, K. Maca, A. Shkabko, L. Sagarna, A. Weidenkaff, A.A. Belik, *Antiferrodistortive phase transition in* $EuTiO_3$, Physical Review B, 86 (2012).

[57] P.G. Reuvekamp, R.K. Kremer, J. Kohler, A. Bussmann-Holder, *Evidence for the first-order nature of the structural instability in* $EuTiO_3$ *from thermal expansion measurements*, Physical Review B, 90 (2014).

[58] Z. Guguchia, H. Keller, R.K. Kremer, J. Köhler, H. Luetkens, T. Goko, A. Amato, A. Bussmann-Holder, *Spin-lattice coupling induced weak dynamical magnetism in* $EuTiO_3$ *at high temperatures*, Physical Review B, 90 (2014) 064413.

[59] L.J. Spalek, S.S. Saxena, C. Panagopoulos, T. Katsufuji, J.A. Schiemer, M.A. Carpenter, *Elastic and anelastic relaxations associated with phase transitions in* $EuTiO_3$, Physical Review B, 90 (2014) 054119.

[60] P.G. Reuvekamp, R.K. Kremer, J. Kohler, A. Bussmann-Holder, *Spin-lattice coupling induced crossover from negative to positive magnetostriction in* $EuTiO_3$, Physical Review B, 90 (2014).

[61] R. Patrick, C. Kevin, G. Zurab, K. Hugo, K.K. Reinhard, S. Arndt, K. Jürgen, B.-H. Annette, *Tiny cause with huge impact: polar instability through strong magneto-electric-elastic coupling in bulk* $EuTiO_3$, Journal of Physics: Condensed Matter, 27 (2015) 262201.

[62] B.J. Kennedy, G. Murphy, E. Reynolds, M. Avdeev, H.E.R. Brand, T. Kolodiazhnyi, *Studies of the antiferrodistortive transition in* $EuTiO_3$, Journal of Physics-Condensed Matter, 26 (2014).

[63] T. Yamamoto, R. Yoshii, G. Bouilly, Y. Kobayashi, K. Fujita, Y. Kususe, Y. Matsushita, K. Tanaka, H. Kageyama, *An Antiferro-to-Ferromagnetic Transition in* $EuTiO_{3-x}H_x$ *Induced by Hydride Substitution*, Inorganic Chemistry, 54 (2015) 1501-1507.

[64] L. Li, H. Zhou, J. Yan, D. Mandrus, V. Keppens, *Research Update: Magnetic phase diagram of* $EuTi_{1-x}B_xO_3$ *(B = Zr, Nb)*, APL Mater., 2 (2014) 110701.

[65] D. Akahoshi, H. Horie, S. Sakai, T. Saito, *Ferromagnetic behavior in mixed valence europium* (Eu^{2+}/Eu^{3+}) *oxide* $EuTi_{1-x}M_xO_3$ ($M = Al^{3+}$ *and* Ga^{3+}), Applied Physics Letters, 103 (2013) 172407.

[66] Z.-J. Mo, Z.-H. Hao, J. Shen, L. Li, J.-F. Wu, F.-X. Hu, J.-R. Sun, B.-G. Shen, *Observation of giant magnetocaloric effect in* $EuTi_{1-x}Cr_xO_3$, Journal of Alloys and Compounds, 649 (2015) 674-678.

[67] L. Li, J.R. Morris, M.R. Koehler, Z.L. Dun, H.D. Zhou, J.Q. Yan, D. Mandrus, V. Keppens, *Structural and magnetic phase transitions in* $EuTi_{1-x}Nb_xO_3$, Physical Review B, 92 (2015).

[68] T. Kolodiazhnyi, K. Fujita, L. Wang, Y. Zong, K. Tanaka, Y. Sakka, E. Takayama-Muromachi, *Magnetodielectric effect in* $EuZrO_3$, Applied Physics Letters, 96 (2010) 252901.

[69] H. Akamatsu, K. Fujita, H. Hayashi, T. Kawamoto, Y. Kumagai, Y. Zong, K. Iwata, F. Oba, I. Tanaka, K. Tanaka, *Crystal and Electronic Structure and Magnetic Properties of Divalent Europium Perovskite Oxides* $EuMO_3$ *(M = Ti, Zr, and Hf): Experimental and First-Principles Approaches*, Inorganic Chemistry, 51 (2012) 4560-4567.

[70] T. Katsufuji, Y. Tokura, *Transport and magnetic properties of a ferromagnetic metal:* $Eu_{1-x}R_xTiO_3$, Physical Review B, 60 (1999) R15021-R15023.

[71] K. Yoshii, M. Mizumaki, A. Nakamura, H. Abe, *Structure and magnetism of* $Eu_{1-x}Dy_xTiO_3$, Journal of Solid State Chemistry, 171 345-348.

[72] Z. Guguchia, H. Keller, A. Bussmann-Holder, J. Köhler, K.R. Kremer, *The low temperature magnetic phase diagram of* $Eu_xSr_{1-x}TiO_3$, The European Physical Journal B, 86 (2013) 1-4.

[73] V. Goian, S. Kamba, D. Nuzhnyy, P. Vanek, M. Kempa, V. Bovtun, K. Knizek, J. Prokleska, F. Borodavka, M. Ledinsky, I. Gregora, *Dielectric, magnetic and structural properties of novel multiferroic* $Eu_{0.5}Ba_{0.5}TiO_3$ *ceramics*, Journal of Physics-Condensed Matter, 23 (2011).

[74] N.L. Henderson, X. Ke, P. Schiffer, R.E. Schaak, *Solution precursor synthesis and magnetic properties of* $Eu_{1-x}Ca_xTiO_3$, Journal of Solid State Chemistry, 183 (2010) 631-635.

[75] K. Rubi, P. Kumar, D.V. Maheswar Repaka, R. Chen, J.-S. Wang, R. Mahendiran, *Giant magnetocaloric effect in magnetoelectric* $Eu_{1-x}Ba_xTiO_3$, Applied Physics Letters, 104 (2014).

[76] W.F. Giauque, D.P. MacDougall, *Attainment of Temperatures Below 1 Absolute by Demagnetization of* $Gd_2(SO_4)_3.8H_2O$, Physical Review, 43 (1933) 768-768.

[77] G.V. Brown, *Magnetic heat pumping near room temperature*, Journal of Applied Physics, 47 (1976) 3673-3680.

[78] J. Lyubina, R. Schäfer, N. Martin, L. Schultz, O. Gutfleisch, *Novel design of La (Fe, Si) 13 alloys towards high magnetic refrigeration performance*, Advanced Materials, 22 (2010) 3735-3739.

[79] E. Brück, *Developments in magnetocaloric refrigeration*, Journal of Physics D: Applied Physics, 38 (2005) R381.

[80] I. Dubenko, M. Khan, A.K. Pathak, B.R. Gautam, S. Stadler, N. Ali, *Magnetocaloric effects in Ni–Mn–X based Heusler alloys with X= Ga, Sb, In*, Journal of Magnetism and Magnetic Materials, 321 (2009) 754-757.

[81] D.V.M. Repaka, T.S. Tripathi, M. Aparnadevi, R. Mahendiran, *Magnetocaloric effect and magnetothermopower in the room temperature ferromagnet* $Pr_{0.6}Sr_{0.4}MnO_3$, Journal of Applied Physics, 112 (2012).

[82] K. Kamiya, H. Takahashi, T. Numazawa, H. Nozawa, T. Yanagitani, *Hydrogen liquefaction by magnetic refrigeration*, Cryocoolers, 14 (2007) 637.

[83] V.K. Pecharsky, K.A. Gschneidner Jr, *Magnetocaloric effect and magnetic refrigeration*, Journal of Magnetism and Magnetic Materials, 200 (1999) 44-56.

[84] P. Wikus, E. Canavan, S.T. Heine, K. Matsumoto, T. Numazawa, *Magnetocaloric materials and the optimization of cooling power density*, Cryogenics, 62 (2014) 150-162.

[85] T. Numazawa, K. Kamiya, T. Utaki, K. Matsumoto, *Magnetic refrigerator for hydrogen liquefaction*, Cryogenics, 62 (2014) 185-192.

[86] J.A. Barclay, W.A. Steyert, *Materials for magnetic refrigeration between 2 K and 20 K*, Cryogenics, 22 (1982) 73-80.

[87] Y. Su, Y. Sui, X. Wang, J. Cheng, Y. Wang, W. Liu, X. Liu, *Large magnetocaloric properties in single-crystal dysprosium titanate*, Materials Letters, 72 (2012) 15-17.

[88] Y. Su, Y. Sui, J. Cheng, X. Wang, Y. Wang, W. Liu, X. Liu, *Large reversible magnetocaloric effect in* $HoTiO_3$ *single crystal*, Journal of Applied Physics, 110 (2011) 083912.

[89] Y. Su, Y. Sui, J.-G. Cheng, J.-S. Zhou, X. Wang, Y. Wang, J. Goodenough, *Critical behavior of the ferromagnetic perovskites* $RTiO_3$ *(R= Dy, Ho, Er, Tm, Yb) by magnetocaloric measurements*, Physical Review B, 87 (2013) 195102.

[90] V.K. Pecharsky, K.A. Gschneidner, A.O. Pecharsky, A.M. Tishin, *Thermodynamics of the magnetocaloric effect*, Physical Review B, 64 (2001) 144406.

[91] W. Thomson, *On the Electro-Dynamic Qualities of Metals: Effects of Magnetization on the Electric Conductivity of Nickel and of Iron*, Proceedings of the Royal Society of London, 8 (1856) 546-550.

[92] M.N. Baibich, J.M. Broto, A. Fert, F.N. Van Dau, F. Petroff, P. Etienne, G. Creuzet, A. Friederich, J. Chazelas, *Giant Magnetoresistance of (001)Fe/(001)Cr Magnetic Superlattices*, Physical Review Letters, 61 (1988) 2472-2475.

[93] S. Von Molnar, S. Methfessel, *Giant Negative Magnetoresistance in Ferromagnetic* $Eu_{1-x}Gd_xSe$, Journal of Applied Physics, 38 (1967) 959-964.

[94] R. von Helmolt, J. Wecker, B. Holzapfel, L. Schultz, K. Samwer, *Giant negative magnetoresistance in perovskitelike* $La_{2/3}Ba_{1/3}MnO_x$ *ferromagnetic films*, Physical Review Letters, 71 (1993) 2331-2333.

[95] S. Jin, T.H. Tiefel, M. McCormack, R.A. Fastnacht, R. Ramesh, L.H. Chen, *Thousandfold Change in Resistivity in Magnetoresistive La-Ca-Mn-O Films*, Science, 264 (1994) 413-415.

[96] B.T. Matthias, R.M. Bozorth, J.H. Van Vleck, *Ferromagnetic Interaction in EuO*, Physical Review Letters, 7 (1961) 160-161.

[97] H.G. Bohn, W. Zinn, B. Dorner, A. Kollmar, *Neutron scattering study of spin waves and exchange interactions in ferromagnetic and paramagnetic EuS*, Journal of Applied Physics, 52 (1981) 2228-2230.

[98] Y. Shapira, S. Foner, N.F. Oliveira, *Effect of antiferromagnetic ordering on the resistivity of EuTe*, Physics Letters A, 32 (1970) 323-324.

[99] R. Griessen, M. Landolt, H.R. Ott, *A new antiferromagnetic phase in EuSe below 1.8 K*, Solid State Communications, 9 (1971) 2219-2223.

[100] A. Mauger, C. Godart, *The magnetic, optical, and transport properties of representatives of a class of magnetic semiconductors: The europium chalcogenides*, Physics Reports, 141 (1986) 51-176.

[101] M.R. Oliver, McWhorte.Al, J.O. Dimmock, T.B. Reed, *Conductivity studies in europium oxide*, Physical Review B, 5 (1972) 1078.

[102] Y. Shapira, S. Foner, T.B. Reed, *EuO. 1. Resistivity and hall-effect in field up to 150 kOe*, Physical Review B, 8 (1973) 2299-2315.

[103] J.B. Torrance, M.W. Shafer, T.R. McGuire, *Bound magnetic polarons and insultor-metal transition in EuO*, Physical Review Letters, 29 (1972) 1168.

[104] Y. Shapira, H.E. Stanley, H. Birecki, S. Foner, T.B. Reed, *Dependence of insulator-metal transition in EuO on magnetic order*, Physics Letters A, A 41 (1972) 471.

[105] P. Liu, J.K. Tang, *A magnetic polaron model for the enhanced Curie temperature of EuO$_{1-x}$*, Journal of Physics-Condensed Matter, 25 (2013).

[106] S. Sullow, I. Prasad, M.C. Aronson, S. Bogdanovich, J.L. Sarrao, Z. Fisk, *Metallization and magnetic order in EuB$_6$*, Physical Review B, 62 (2000) 11626-11632.

[107] P.G. Steeneken, L.H. Tjeng, I. Elfimov, G.A. Sawatzky, G. Ghiringhelli, N.B. Brookes, D.J. Huang, *Exchange Splitting and Charge Carrier Spin Polarization in EuO*, Physical Review Letters, 88 (2002) 047201.

[108] Y. Shapira, R.L. Kautz, T.B. Reed, *Positive magnetoresistance due to conduction-band splitting in EuSe and EuTe*, Physics Letters A, 47 (1974) 39-40.

[109] Y. Shapira, R.L. Kautz, *Effect of spin splitting of the conduction band on the resistivity and Hall coefficient: Model for the positive magnetoresistance in EuSe*, Physical Review B, 10 (1974) 4781-4794.

[110] R. Bachmann, K.N. Lee, T.H. Geballe, A. Menth, *Spin Scattering and Magnetic Ordering in EuB$_6$*, Journal of Applied Physics, 41 (1970) 1431-1432.

[111] Z. Fisk, D.C. Johnston, B. Cornut, S. von Molnar, S. Oseroff, R. Calvo, *Magnetic, transport, and thermal properties of ferromagnetic EuB$_6$*, Journal of Applied Physics, 50 (1979) 1911-1913.

[112] J.Y. Chan, S.M. Kauzlarich, P. Klavins, R.N. Shelton, D.J. Webb, *Colossal negative magnetoresistance in an antiferromagnet*, Physical Review B, 57 (1998) R8103-R8106.

[113] C.S. Snow, S.L. Cooper, D.P. Young, Z. Fisk, A. Comment, J.-P. Ansermet, *Magnetic polarons and the metal-semiconductor transitions in (Eu,La)B$_6$ and EuO: Raman scattering studies*, Physical Review B, 64 (2001) 174412.

[114] V.G. Storchak, D.G. Eshchenko, E. Morenzoni, T. Prokscha, A. Suter, N. Ingle, W. Heiss, T. Schwarzl, G. Springholz, R.L. Kallaher, S. von Molnar, *Magnetic polarons in Eu-based films of magnetic semiconductors*, Physical Review B, 81 (2010).

[115] J.M.D. Teresa, M.R. Ibarra, P.A. Algarabel, C. Ritter, C. Marquina, J. Blasco, J. Garcia, A. del Moral, Z. Arnold, *Evidence for magnetic polarons in the magnetoresistive perovskites*, Nature, 386 (1997) 256-259.

[116] P.G. De Gennes, J. Friedel, *Anomalies de résistivité dans certains métaux magníques*, Journal of Physics and Chemistry of Solids, 4 (1958) 71-77.

[117] C. Haas, *Spin-Disorder Scattering and Magnetoresistance of Magnetic Semiconductors*, Physical Review, 168 (1968) 531-538.

[118] P. Majumdar, P.B. Littlewood, *Dependence of magnetoresistivity on charge-carrier density in metallic ferromagnets and doped magnetic semiconductors*, Nature, 395 (1998) 479-481.

[119] K. Kubo, N. Ohata, *A Quantum Theory of Double Exchange. I*, Journal of the Physical Society of Japan, 33 (1972) 21-32.

[120] Y. Shimakawa, Y. Kubo, T. Manako, *Giant magnetoresistance in* $Ti_2Mn_2O_7$ *with the pyrochlore structure*, Nature, 379 (1996) 53-55.

[121] R.P. Khosla, J.R. Fischer, *Magnetoresistance in Degenerate CdS: Localized Magnetic Moments*, Physical Review B, 2 (1970) 4084-4097.

[122] J.A. Peters, B.W. Wessels, *Magnetoresistance of InMnAs magnetic semiconductors, Physica E: Low-dimensional Systems and Nanostructures*, 42 (2010) 1447-1450.

[123] J.A. Peters, N.D. Parashar, N. Rangaraju, B.W. Wessels, *Magnetotransport properties of InMnSb magnetic semiconductor thin films*, Physical Review B, 82 (2010) 205207.

[124] S.M. Watts, S. Wirth, S. von Molnár, A. Barry, J.M.D. Coey, *Evidence for two-band magnetotransport in half-metallic chromium dioxide*, Physical Review B, 61 (2000) 9621-9628.

[125] S. Ye, P. Klar, T. Henning, M. Lampalzer, W. Stolz, W. Heimbrodt, *Influence of codoping on the magnetoresistance of paramagnetic (Ga,Mn)As*, Journal of superconductivity, 16 (2003) 159-162.

[126] T. Andrearczyk, J. Jaroszyński, G. Grabecki, T. Dietl, T. Fukumura, M. Kawasaki, *Spin-related magnetoresistance of n-type ZnO:Al and* $Zn_{1-x}Mn_xO$*:Al thin films*, Physical Review B, 72 (2005) 121309.

[127] Y. Shapira, R.L. Kautz, *Effect of spin splitting of conduction-band on resistivity and hall-coefficient - model for positive magntoresistance in EuSe*, Physical Review B, 10 (1974) 4781-4794.

[128] Y. Shapira, R.L. Kautz, T.B. Reed, *Positive magnetoresistance due to conduction-band splitting in EuSe and EuTe*, Physics Letters A, A 47 (1974) 39-40.

[129] W. Eerenstein, N.D. Mathur, J.F. Scott, *Multiferroic and magnetoelectric materials*, Nature, 442 (2006) 759-765.

[130] R. Ramesh, N.A. Spaldin, *Multiferroics: progress and prospects in thin films*, Nat Mater, 6 (2007) 21-29.

[131] C.N.R. Rao, C.R. Serrao, *New routes to multiferroics*, Journal of Materials Chemistry, 17 (2007) 4931-4938.

[132] J.F. Scott, *Data storage: Multiferroic memories*, Nat Mater, 6 (2007) 256-257.

[133] E. Ascher, H. Rieder, H. Schmid, H. Stössel, *Some Properties of Ferromagnetoelectric Nickel- Iodine Boracite, $Ni_3B_7O_{13}I$*, Journal of Applied Physics, 37 (1966) 1404-1405.

[134] W. Schnelle, H. Schmid, *Magnetic and structural phase transitions of multiferroic boracites $M_3B_7O_{13}X$ (M=3d transition metal Cr–Zn or Mg; X=halogen Cl, Br, I)*, Physical Review B, 91 (2015) 184411.

[135] I. Nomoto, H. Sato, T. Fukui, Y. Narumi, K. Kindo, S. Nakamura, Y. Tsunoda, *Structure and Magnetic Properties of New Trigonal Iron-Boracite, $Fe_3B_7O_{13}(OH)$*, Journal of the Physical Society of Japan, 80 (2010) 014801.

[136] N.A. Hill, *Why Are There so Few Magnetic Ferroelectrics?*, The Journal of Physical Chemistry B, 104 (2000) 6694-6709.

[137] G.A. Smolenskii, V.A. Isupov, A.I. Agranovskaya, *A new group of ferroelectrics - (with layered structure)*, Soviet Physics-Solid State, 1 (1959) 149-150.

[138] V.A. Bokov, I.E. Mylnikova, G.A. Smolenskii, *Ferroelectric antiferromagnetics*, Soviet Physics Jetp-Ussr, 15 (1962) 447-449.

[139] F. Sugawara, S. Iiida, Y. Syono, S.-i. Akimoto, *Magnetic Properties and Crystal Distortions of $BiMnO_3$ and $BiCrO_3$*, Journal of the Physical Society of Japan, 25 (1968) 1553-1558.

[140] N.A. Hill, K.M. Rabe, *First-principles investigation of ferromagnetism and ferroelectricity in bismuth manganite*, Physical Review B, 59 (1999) 8759-8769.

[141] I. Sosnowska, T.P. Neumaier, E. Steichele, *Spiral magnetic ordering in bismuth ferrite*, Journal of Physics C: Solid State Physics, 15 (1982) 4835.

[142] T. Zhao, A. Scholl, F. Zavaliche, K. Lee, M. Barry, A. Doran, M.P. Cruz, Y.H. Chu, C. Ederer, N.A. Spaldin, R.R. Das, D.M. Kim, S.H. Baek, C.B. Eom, R. Ramesh, *Electrical control of antiferromagnetic domains in multiferroic BiFeO3 films at room temperature*, Nat Mater, 5 (2006) 823-829.

[143] B. Ponomarev, S. Ivanov, Y.F. Popov, V. Negrii, B. Red'Kin, *Magnetoelectric properties of some rare earth molybdates*, Ferroelectrics, 161 (1994) 43-48.

[144] I. Dzyaloshinskii, *On the magneto-electrical effect in antiferromagnets*, 1960, 628-629.

[145] D. Astrov, *The magnetoelectric effect in antiferromagnetics*, Sov. Phys. JETP, 11 (1960) 708-709.

[146] G. Lawes, A.P. Ramirez, C.M. Varma, M.A. Subramanian, *Magnetodielectric effects from spin fluctuations in isostructural ferromagnetic and antiferromagnetic systems*, Physical Review Letters, 91 (2003).

[147] G. Lawes, T. Kimura, C.M. Varma, M.A. Subramanian, N. Rogado, R.J. Cava, A.P. Ramirez, *Magnetodielectric effects at magnetic ordering transitions*, Progress in Solid State Chemistry, 37 (2009) 40-54.

[148] G. Catalan, *Magnetocapacitance without magnetoelectric coupling*, Applied Physics Letters, 88 (2006).

[149] V. Bobnar, P. Lunkenheimer, M. Paraskevopoulos, A. Loidl, Separation of grain boundary effects and intrinsic properties in perovskite-like $Gd_{0.6}Y_{0.4}BaCo_2O_{5.5}$ using high-frequency dielectric spectroscopy, Physical Review B, 65 (2002).

[150] D.C. Sinclair, T.B. Adams, F.D. Morrison, A.R. West, *$CaCu_3Ti_4O_{12}$: One-step internal barrier layer capacitor,* Applied Physics Letters, 80 (2002) 2153-2155.

[151] T. Bonaedy, Y.S. Koo, K.D. Sung, J.H. Jung, *Resistive magnetodielectric property of polycrystalline gamma- Fe_2O_3*, Applied Physics Letters, 91 (2007).

[152] A.R. Von Hippel, *Dielectrics and Waves*, Artech House, 1954.

[153] M. Mario, *Interface-driven magnetocapacitance in a broad range of materials*, Journal of Physics: Condensed Matter, 20 (2008) 322202.

[154] Y. Chen, X.-Y. Zhang, C. Vittoria, V.G. Harris, *Giant magnetodielectric effect and magnetic field tunable dielectric resonance in spinel MnZn ferrite*, Applied Physics Letters, 94 (2009) 102906.

[155] T. Penney, M.W. Shafer, J.B. Torrance, *Insulator-metal trnasition and long range magnetic order in EuO*, Physical Review B, 5 (1972) 3669-&.

[156] T. Ito, Y. Shimada, T. Katsufuji, *Magnetoresistance in a doped Mott-Hubbard system: $RTiO_3$*, Physical Review B, 91 (2015) 024411.

[157] J.P. Goral, J.E. Greedan, *The magnetic structures of $LaTiO_3$ and $CeTiO_3$*, Journal of Magnetism and Magnetic Materials, 37 (1983) 315-321.

[158] S. Maekawa, T. Tohyama, S.E. Barnes, S. Ishihara, W. Koshibae, G. Khaliullin, *Physics of transition metal oxides*, Springer Science & Business Media, 2013.

[159] B.P. Alho, A.M.G. Carvalho, P.J. von Ranke, *Anisotropic magnetocaloric effect in antiferromagnetic systems: Application to $EuTiO_3$*, Journal of Applied Physics, 116 (2014).

[160] L. Sagarna, S. Populoh, A. Shkabko, J. Eilertsen, A.E. Maegli, R. Hauert, M. Schrade, L. Karvonen, A. Weidenkaff, *Influence of the Oxygen Content on the Electronic Transport Properties of $Sr_xEu_{1-x}TiO_{3-\delta}$*, Journal of Physical Chemistry C, 118 (2014) 7821-7831.

[161] B.K. Banerjee, *On a generalised approach to first and second order magnetic transitions*, Physics Letters, 12 (1964) 16-17.

[162] P.J. von Ranke, B.P. Alho, E.P. Nóbrega, V.S.R. de Sousa, T.S.T. Alvarenga, A.M.G. Carvalho, N.A. de Oliveira, *The influence of magnetic and electric coupling properties on the magnetocaloric effect in quantum paraelectric* $EuTiO_3$, Journal of Magnetism and Magnetic Materials, 324 (2012) 1290-1295.

[163] A. Midya, P. Mandal, K. Rubi, R. Chen, J.-S. Wang, R. Mahendiran, G. Lorusso, M. Evangelisti, *Large adiabatic temperature and magnetic entropy changes in* $EuTiO_3$, Physical Review B, 93 (2016) 094422.

[164] K. Ahn, A. Pecharsky, K. Gschneidner, V. Pecharsky, *Preparation, heat capacity, magnetic properties, and the magnetocaloric effect of EuO*, Journal of applied physics, 97 (2005) 3901.

[165] K. Ahn, V. Pecharsky, K. Gschneidner, *The magnetothermal behavior of mixed-valence* Eu_3O_4, Journal of Applied Physics, 106 (2009) 3918.

[166] D. Li, T. Yamamura, S. Nimori, Y. Homma, F. Honda, D. Aoki, *Giant and isotropic low temperature magnetocaloric effect in magnetic semiconductor EuSe*, Applied Physics Letters, 102 (2013) 2409.

[167] A. Midya, N. Khan, D. Bhoi, P. Mandal, *Giant magnetocaloric effect in magnetically frustrated* $EuHo_2O_4$ *and* $EuDy_2O_4$ *compounds*, Applied Physics Letters, 101 (2012) 132415.

[168] P. Von Ranke, V. Pecharsky, K. Gschneidner, *Influence of the crystalline electrical field on the magnetocaloric effect of* $DyAl_2$, $ErAl_2$, *and* $DyNi_2$, Physical Review B, 58 (1998) 12110.

[169] R. Levitin, V. Snegirev, A. Kopylov, A. Lagutin, A. Gerber, *Magnetic method of magnetocaloric effect determination in high pulsed magnetic fields*, Journal of magnetism and magnetic materials, 170 (1997) 223-227.

[170] A.C.S. Hamilton, G.I. Lampronti, S.E. Rowley, S.E. Dutton, *Enhancement of the magnetocaloric effect driven by changes in the crystal structure of Al-doped GGG,* $Gd_3Ga_{5-x}Al_xO_{12}$ $(0 < x < 5)$, Journal of Physics: Condensed Matter, 26 (2014) 116001.

[171] G. Lorusso, J.W. Sharples, E. Palacios, O. Roubeau, E.K. Brechin, R. Sessoli, A. Rossin, F. Tuna, E.J.L. McInnes, D. Collison, M. Evangelisti, *A Dense Metal–Organic Framework for Enhanced Magnetic Refrigeration*, Advanced Materials, 25 (2013) 4653-4656.

[172] L. Sagarna, A. Shkabko, S. Populoh, L. Karvonen, A. Weidenkaff, *Electronic structure and thermoelectric properties of nanostructured* $EuTi_{1-x}Nb_xO_{3-\delta}$ $(x = 0.00;\ 0.02)$, Applied Physics Letters, 101 (2012).

[173] N.F.S. Mott, *Metal-insulator transitions* / N. F. Mott, Taylor & Francis ; Barnes & Noble Books, London : New York, 1974.

[174] H. Yi, N.H. Hur, J. Yu, *Anomalous spin susceptibility and magnetic polaron formation in the double-exchange systems*, Physical Review B, 61 (2000) 9501-9505.

[175] N. Mannella, C.H. Booth, A. Rosenhahn, B.C. Sell, A. Nambu, S. Marchesini, B.S. Mun, S.H. Yang, M. Watanabe, K. Ibrahim, E. Arenholz, A. Young, J. Guo, Y. Tomioka, C.S. Fadley, *Temperature-dependent evolution of the electronic and local atomic structure in the cubic colossal magnetoresistive manganite* $La_{1-x}Sr_xMnO_3$, Physical Review B, 77 (2008).

[176] H.D. Zhou, E.S. Choi, J.A. Souza, J. Lu, Y. Xin, L.L. Lumata, B.S. Conner, L. Balicas, J.S. Brooks, J.J. Neumeier, C.R. Wiebe, *Magnetic-polaron-driven magnetoresistance in the pyrochlore* $Lu_2V_2O_7$, Physical Review B, 77 (2008) 020411.

[177] M. Ryazanov, R.K. Kremer, A. Simon, H. Mattausch, *Metal-nonmetal transition and colossal negative magnetoresistance in the gadolinium hydride halides* $GdIH_x$ $(0.67 < x < 1)$, Physical Review B, 73 (2006).

[178] L.M. Wang, H.E. Horng, H.C. Yang, *Anomalous magnetotransport in* $SrRuO_3$ *films: A crossover from Fermi-liquid to non-Fermi-liquid behavior*, Physical Review B, 70 (2004).

[179] J. Scott, *Dielectric anomalies in nonferroelectric phase-transitions*, JETP Lett, 49 (1989).

[180] A. Bussmann-Holder, J. Köhler, R.K. Kremer, J.M. Law, *Relation between structural instabilities in* $EuTiO_3$ *and* $SrTiO_3$, Physical Review B, 83 (2011) 212102.

[181] T.D. Sparks, M.C. Kemei, P.T. Barton, R. Seshadri, E.-D. Mun, V.S. Zapf, *Magnetocapacitance as a sensitive probe of magnetostructural changes in* $NiCr_2O_4$, Physical Review B, 89 (2014) 024405.

[182] R. Tackett, G. Lawes, B.C. Melot, M. Grossman, E.S. Toberer, R. Seshadri, *Magnetodielectric coupling in* Mn_3O_4, Physical Review B, 76 (2007) 024409.

[183] R. Schmidt, J. Ventura, E. Langenberg, N.M. Nemes, C. Munuera, M. Varela, M. Garcia-Hernandez, C. Leon, J. Santamaria, *Magnetoimpedance spectroscopy of epitaxial multiferroic thin films*, Physical Review B, 86 (2012).

[184] P. Lunkenheimer, S. Krohns, S. Riegg, S.G. Ebbinghaus, A. Reller, A. Loidl, *Colossal dielectric constants in transition-metal oxides*, Eur. Phys. J. Spec. Top., 180 (2009) 61-89.

[185] D.L. Janes, R.E. Bodnar, A.L. Taylor, *Europium barium titanate - magnetic ferroelectric compound*, Journal of Applied Physics, 49 (1978) 1452-1454.

[186] K.Z. Rushchanskii, S. Kamba, V. Goian, P. Vanek, M. Savinov, J. Prokleska, D. Nuzhnyy, K. Knizek, F. Laufek, S. Eckel, S.K. Lamoreaux, A.O. Sushkov, M. Lezaic, N.A.

Spaldin, *A multiferroic material to search for the permanent electric dipole moment of the electron*, Nature Materials, 9 (2010) 649-654.

[187] J.M. Wesselinowa, *Origin of the multiferroicity in* $Eu_{0.5}Ba_{0.5}TiO_3$, physica status solidi (b), 249 (2012) 615-619.

[188] T. Wei, Q.J. Zhou, X. Yang, Q.G. Song, Z.P. Li, X.L. Qi, J.M. Liu, *Competition between quantum fluctuation and ferroelectric order in* $Eu_{1-x}Ba_xTiO_3$, Applied Surface Science, 258 (2012) 4601-4606.

[189] M. Evangelisti, A. Candini, A. Ghirri, M. Affronte, E.K. Brechin, E.J.L. McInnes, *Spin-enhanced magnetocaloric effect in molecular nanomagnets*, Applied Physics Letters, 87 (2005) 072504.

[190] W.W. Li, R. Zhao, L. Wang, R.J. Tang, Y.Y. Zhu, J.H. Lee, H.X. Cao, T.Y. Cai, H.Z. Guo, C. Wang, L.S. Ling, L. Pi, K.J. Jin, Y.H. Zhang, H.Y. Wang, Y.Q. Wang, S. Ju, H. Yang, *Oxygen-Vacancy-Induced Antiferromagnetism to Ferromagnetism Transformation in* $Eu_{0.5}Ba_{0.5}TiO_{3-\delta}$ *Multiferroic Thin Films*, Scientific Reports, 3 (2013).

[191] A. Chaturvedi, S. Stefanoski, M.-H. Phan, G.S. Nolas, H. Srikanth, *Table-like magnetocaloric effect and enhanced refrigerant capacity in* $Eu_8Ga_{16}Ge_{30}$*-EuO composite materials*, Applied Physics Letters, 99 (2011).

[192] G.J. Liu, J.R. Sun, J.Z. Wang, T.Y. Zhao, B.G. Shen, *A comparison study of the entropy changes in materials with and without short-range magnetic order*, Journal of Physics: Condensed Matter, 19 (2007) 466215.

[193] D.X. Li, T. Yamamura, S. Nimori, Y. Homma, F. Honda, Y. Haga, D. Aoki, *Large reversible magnetocaloric effect in ferromagnetic semiconductor EuS*, Solid State Communications, 193 (2014) 6-10.

[194] H. Kimura, H. Maeda, M. Sato, *Single crystals growth and magneto-thermal properties of* $Dy_3Ga_5O_{12}$ *garnet*, Journal of Materials Science, 23 (1988) 809-813.

[195] M. Evangelisti, O. Roubeau, E. Palacios, A. Camón, T.N. Hooper, E.K. Brechin, J.J. Alonso, *Cryogenic Magnetocaloric Effect in a Ferromagnetic Molecular Dimer*, Angewandte Chemie International Edition, 50 (2011) 6606-6609.

[196] K.S. Takahashi, M. Onoda, M. Kawasaki, N. Nagaosa, Y. Tokura, *Control of the Anomalous Hall Effect by Doping in* $Eu_{1-x}La_xTiO_3$ *Thin Films*, Physical Review Letters, 103 (2009) 057204.

[197] D. Bessas, K.Z. Rushchanskii, M. Kachlik, S. Disch, O. Gourdon, J. Bednarcik, K. Maca, I. Sergueev, S. Kamba, M. Ležaić, R.P. Hermann, *Lattice instabilities in bulk* $EuTiO_3$, Physical Review B, 88 (2013) 144308.

[198] http://abulafia.mt.ic.ac.uk/shannon/ptable.php.

[199] V.V. Shvartsman, P. Borisov, W. Kleemann, S. Kamba, T. Katsufuji, *Large off-diagonal magnetoelectric coupling in the quantum paraelectric antiferromagnet* $EuTiO_3$, Physical Review B, 81 (2010).

[200] M. Tsubota, F. Iga, T. Takabatake, N. Kikugawa, T. Suzuki, I. Oguro, H. Kawanaka, H. Bando, *Low-field magnetic anisotropy in Mott-insulating ferromagnet* $Y_{1-x}Ca_xTiO_3$ (x⍰ 0.1), Physica B: Condensed Matter, 281 (2000) 622-624.

[201] W. Knafo, C. Meingast, A.V. Boris, P. Popovich, N.N. Kovaleva, P. Yordanov, A. Maljuk, R.K. Kremer, H.v. Löhneysen, B. Keimer, *Ferromagnetism and lattice distortions in the perovskite* $YTiO_3$, Physical Review B, 79 (2009) 054431.

[202] A. Arrott, *Criterion for Ferromagnetism from Observations of Magnetic Isotherms*, Physical Review, 108 (1957) 1394-1396.

[203] S. Roy, N. Khan, P. Mandal, *Giant low-field magnetocaloric effect in single-crystalline* $EuTi_{0.85}Nb_{0.15}O_3$, APL Mater., 4 (2016) 026102.

[204] A.J. Dos santos-García, E. Climent-Pascual, J.M. Gallardo-Amores, M.G. Rabie, Y. Doi, J. Romero de Paz, B. Beuneu, R. Sáez-Puche, *Synthesis and magnetic properties of the high-pressure scheelite-type* $GdCrO_4$ *polymorph*, Journal of Solid State Chemistry, 194 (2012) 119-126.

[205] J. Chen, B.G. Shen, Q.Y. Dong, F.X. Hu, J.R. Sun, *Giant reversible magnetocaloric effect in metamagnetic HoCuSi compound*, Applied Physics Letters, 96 (2010) 152501.

[206] S.B. Gupta, K.G. Suresh, *Giant low field magnetocaloric effect in soft ferromagnetic ErRuSi*, Applied Physics Letters, 102 (2013) 022408.

[207] P. Schiffer, A.P. Ramirez, W. Bao, S.W. Cheong, *Low Temperature Magnetoresistance and the Magnetic Phase Diagram of* $La_{1-x}Ca_xCoO_3$, Physical Review Letters, 75 (1995) 3336-3339.

[208] S. Yamaguchi, H. Taniguchi, H. Takagi, T. Arima, Y. Tokura, *Magnetoresistance in Metallic Crystals of* $La_{1-x}Sr_xCoO_3$, Journal of the Physical Society of Japan, 64 (1995) 1885-1888.

[209] N. Shanthi, D.D. Sarma, *Electronic structure of electron doped* $SrTiO_3$: $SrTiO_{3-\delta}$ *and* $Sr_{1-x}La_xTiO_3$, Physical Review B, 57 (1998) 2153-2158.

[210] X. Wang, R. Chu, Z.C. Dong, C.G. Zhong, Y.Y. Huang, Y. Min, M. Wang, P.X. Zhou, G.Q. Yuan, S. Wei, *The giant electrocaloric effect in EuTiO3 nanowires near room temperature*, Journal of Alloys and Compounds, 649 (2015) 261-266.

[211] L. Sagarna, K.Z. Rushchanskii, A. Maegli, S. Yoon, S. Populoh, A. Shkabko, S. Pokrant, M. Ležaić, R. Waser, A. Weidenkaff, *Structure and thermoelectric properties of* $EuTi(O,N)_{3\pm\delta}$, Journal of Applied Physics, 114 (2013) 033701.